FULL-SPECTRUM SOLAR ENERGY HARVESTING USING NANOTECHNOLOGY-ENABLED PHOTOVOLTAIC/THERMOELECTRIC HYBRID SYSTEM

A thesis submitted to Cardiff University in the candidature
for the degree of
Doctor of Philosophy

By
Hasan Talib Hashim,
BSc., MSc.

Institute of Energy
School of Engineering
Cardiff University
September 2015

SUMMARY

Carbon emissions, climate change and the finite resource of fossil fuels are driving an increasing need for renewable energy, and in particular, an interest in photovoltaic (PV) cells. Most PV cells operate in temperatures above 25 ^{o}C, and the performance of PV cells reduces with increased operation temperature. This research aims to resolve some engineering issues by integrating PV cells with a thermoelectric generator (TEG). Integrating TEG with PV cells helps to transfer heat from the PV through the TEG to an actively or passively cooled heat sink. The temperature difference established across the TEG can generates additional electrical power by the Seebeck effect.

The main objective of this research is to investigate the feasibility of developing a PV/TEG hybrid system that can offer better performance than that can be obtained from each individual system. The key parameters, which are crucial to the development of efficient hybrid system, were investigated. These include the temperature coefficient of PV cells, geometry of TEGs and thermal coupling between the PV and TEG. It was found that the dye sensitised solar cells (DSC) has a preferred temperature coefficient that are the most suitable for use in a PV/TEG system. In this work, a theoretical model was also developed for determination of the optimal geometry of the TEG for PV/TEG hybrid systems.

A special type of DSCs was designed and fabricated which employ titanium as the counter electrode (other than conventional FTO-glass) to improve the thermal coupling between the PV and TEG. A unique DSC/TEG hybrid system was constructed using this special type of DSC and its generating performance was studied in comparison with a similar system that uses conventional FTO-glass counter electrode. The experimental results show that the power output and efficiency of the hybrid PV/TEG system with Ti counter electrode is significantly higher than the similar system with a conventional FTO-glass electrode due to an improved thermal coupling between the DSC and TEG. It is concluded that a hybrid PV/TEG system can provide improved performance beyond that of each individual system. However, the improvement can only be achieved with appropriate type of PV cells, optimised TEGs and advanced structures for integration, such as Ti counter electrode.

DECLARATION AND STATEMENTS

DECLARATION

This work has not previously been accepted in substance for any degree and is not concurrently submitted in candidature for any degree.

Signed…….... (Hasan Talib Hashim) Date…….

STATEMENT 1

This thesis is being submitted in partial fulfilment of the requirements for the degree of Doctor of Philosophy (PhD).

Signed ……. (Hasan Talib Hashim) Date…….

STATEMENT 2

This thesis is the result of my own independent work/investigation, except where otherwise stated. Other sources are acknowledged by explicit references.

Signed ……. (Hasan Talib Hashim) Date…….

STATEMENT 3

I hereby give consent for my thesis, if accepted, to be available for photocopying and for inter-library loan, and for the title and summary to be made available to outside organisations.

Signed …… (Hasan Talib Hashim) Date……..

ACKNOWLEDGEMENTS

First and foremost I am thankful to my God “Allah (swt)” for providing me with the patience and strength to go on and complete this task.

I would like to thank my supervisor, Dr Gao Min, for the continuous help and guidance he gave me during my PhD; I am sincerely grateful to him. His invaluable guidance, excellent research attitude and knowledge about the field of study always encouraged me.

I also would like to express gratitude to my second supervisor, Dr Kensuke Yokoi for his encouragement during my study at Cardiff University.

Special thanks go to Dr Jorge García-Cañadas for his effort and time spent with me, especially for the use of AUTOLAB. I would like to thank Dr John Bomphrey, Dr Tracy Sweet, Dr Matthew Phillips, Dr Martin Prest and Dr Tanuj Singh for their feedback and comments on the thesis chapters.

Special thanks go to my colleagues Lourdes Garcia and Mateusz Augustyniak for the helpful discussion during the time of manufacturing of dye sensitised solar cells.

I would like to acknowledge Dr Ross Kynch in the Mechanical Engineering department at Cardiff University for his help in Matlab® coding and simulation.

The Centre for Solar Energy Research in Glyndŵr University, Wales, UK is acknowledged for providing the cadmium telluride solar cells.

I would also like to thank the Republic of Iraq, especially the Ministry of Higher Education (MOHE) and Scientific Research for providing the financial support.

My acknowledgment goes also to my parents, brother and sister. This thesis would have been simply impossible to complete without their support.

My deepest appreciation goes to my beloved wife, Hawraa, for her constant care, love and support, and for always standing beside me during happy and sad moments. Thanks also to lovely son Mujtaba. They have suffered the most from my absence during their most difficult times.

Lastly, I offer my regards and gratitude to all of those who supported me in any aspect during the completion of this thesis, in particular my close friend computer system engineer Ghassan Saraf.

PUBLICATIONS

H. Hashim, J. J. Bomphrey, and G. Min, “Model for geometry optimisation of thermoelectric devices in a hybrid PV/TE system,” *Renew. Energy*, vol. 87, pp. 458–463, 2016.

Hashim.Hasan and G. Min, “Enhance the Performance of Hybrid Dye Sensitised Solar Cell /Thermoelectric System,” in *Photovoltaic Science applications and Technology, PVSAT-9,10–12 April,Swansea University,UK*, 2013, pp. 141–144.

CONTENTS

LIST OF SYMBOLS

Symbol	Definition	Unit
A_{act}	Active area of PV cells	m^2
A_C	Cross sectional area of a thermoelement	m^2
A_{PV}	Device area of the PV cells	m^2
A_{TE}	Total area of thermoelectric module	m^2
c_p	Specific heat at constant pressure	J/kg.K
G	Solar radiation	W/m^2
h_{cov}	Convection heat transfer coefficient	$W/m^2.K$
I_{SC}	Short circuit current	mA
J	Current density	A/m^2
k	Thermal conductivity of Bismuth telluride	W/m.K
k_g	Thermal conductivity of glass	W/m.K
L_c	Thickness of the ceramic	m
L_g	Thickness of the glass	m
L_{TE}	Thermoelement length	m
M	Molarity	mol/L
n	Electrical contact parameter	mm
P	Electrical Power Output	W
Q	Heat losses	W
r	Thermal contact parameter	
R	Resistance	Ohm
R_i	Internal resistance of thermoelement	Ohm
s	The ratio of the load resistance to the internal resistance of the thermoelectric generator	

t	Time	Second
T_{amb}	Ambient temperature	K
T_C	Cold side temperature of the thermoelectric generator	K
T_{cell}	PV cell temperature	K
T_H	Hot side temperature of the thermoelectric generator	K
T_M	Mean temperature	K
U_t	Heat transfer coefficient by convection and conduction	$W/m^2.K$
V	Volume	m^3
V	Voltage	Volt
V_C	Closed circuit voltage	Volt
V_O	Open circuit voltage	Volt
ZT	Dimensionless figure of mert	
α	Seebeck coefficient	μV/K
β	Thomson coefficient	V/K
β_0	Temperature coefficient of PV cells	%/K
η_{PV}	Efficiency of PV cells	%
η_{TE}	Efficiency of TEG	%
π	Peltier coefficient	W/A
ρ	The electrical resistivity	Ω.cm
ΔT	Temperature difference	K
ΔT_c	Closed circuit temperature difference	K
ΔT_o	Open circuit temperature difference	K
ΔT_s	Short circuit temperature difference	K

ABBREVIATIONS

amb	Ambient
con	Convection
DSC	Dye sensitised solar cells
EGT	Evacuated glass tubular
FGM	Functionally graded material
HTC	Hybrid tandem cell
n	Nanofluid
OC	Open circuit
P_{max}	Maximum power output
PSC	Polymer solar cell
PV cell	Photovoltaic cell
PV/TEG	Photovoltaic/thermoelectric hybrid system
rad	Radiative
SC	Short circuit
SEM	Scanning electron microscope
SSA	Solar selective absorber
TC	Thermoelectric cell
TCO	Transparent Conductive Oxide
TE	Thermoelectric
TEC	Thermoelectric cooler
TEG	Thermoelectric generator
Ti	Titanium

LIST OF FIGURES

LIST OF TABLES

CHAPTER 1 – INTRODUCTION

1.1 Historical Development of Photovoltaic/Thermoelectric Systems

A major challenge in the 21st century is to provide a sustainable supply of energy that is environmentally friendly and cost effective. Solar energy, as the most abundant energy source on earth, has been converted into electricity using solar cells and into heat using solar heating panels. Solar energy conversion is a very promising renewable technology, but its wide-scale applications rely on further increases in efficiency and reductions in cost. The interest in renewable energy has increased significantly in recent years because of the problems associated with fossil fuels (e.g., limited resources, increasing prices and serious environmental impact).

Photovoltaic (PV) cells, although still expensive, are attracting more and more attention due to their ability to convert freely-available light into electricity. A solar cell is a solid state device made from two types (n and p) of semiconductors, which is capable of converting solar energy directly into electrical energy. However, a large proportion of solar energy is converted to waste heat in a PV cell, due to thermalisation of the excited, high energy electrons and absorption of low energy photons. This results in an increase in the temperature of the PV cell and leads to a loss of power output because the power output of PV cells decreases with increasing the operating temperature. Therefore, there has been considerable interest in cooling PV cells using a number of passive or active cooling techniques[1][2], including the use of thermoelectric (TE) coolers [3][4]. Thus, the operating temperature of solar cells can be maintained at an acceptable level to ensure sufficient power output.

An alternative approach is to use the TE device as a generator to convert waste heat to electricity. The principles of utilising the PV cell and thermoelectric generator (TEG) in a hybrid system have been discussed since 1986 [5] when a solar–TEG hybrid system

was installed at Northern Forestry as a power source. Later a hybrid solar PV/TEG system was proposed by Vorobiev et al [6]. The system comprised a concentrator system, a PV cell and a TEG. A hybrid PV/TEG system was introduced as a renewable energy source to operate hybrid electrical vehicles [7]. The incorporation of different types of PV cells (such as DSC) with TEG has been studied in the literature [8][9][10][11][12][13]. A hybrid tandem cell including DSC and TEG has been reported [9], as shown in Figure 1.1. The hybrid system was characterised based on connecting the two devices in series, in parallel or separately. The experimental results demonstrated that matching the load between the DSC and TEG is important to achieve the best results in the case of connecting them in series also, the hybrid system recorded a 10 % improvement in contrast with the single cell.

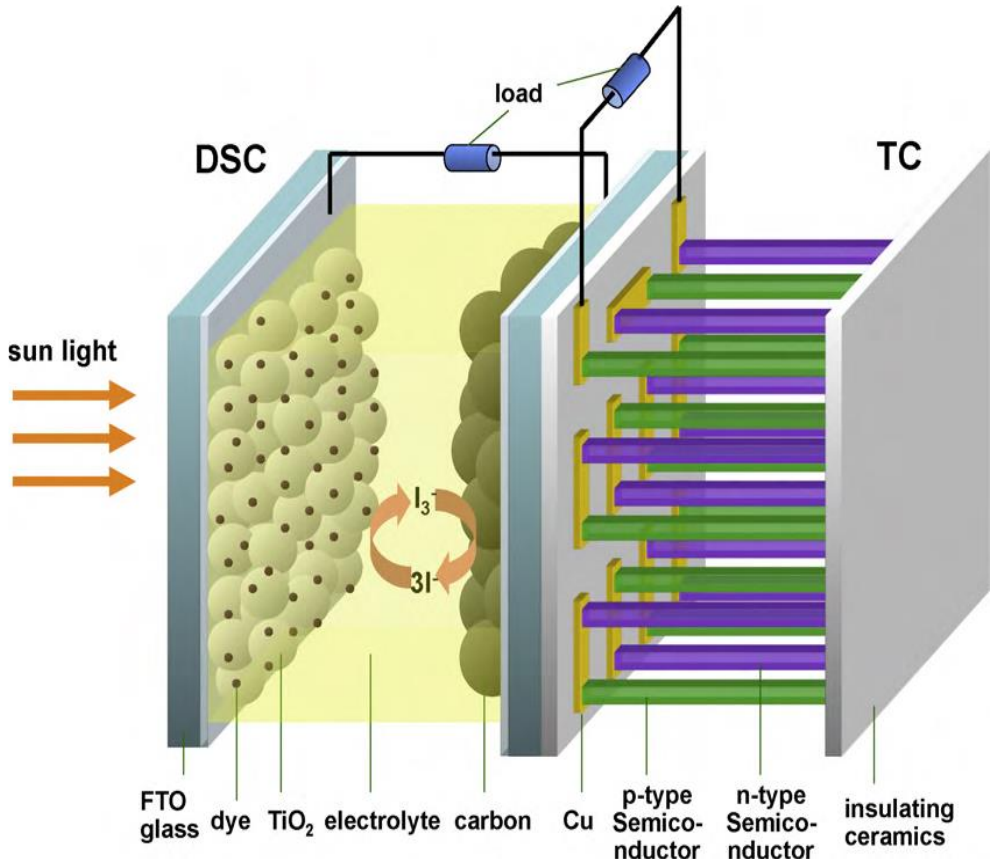

Figure 1. 1 A schematic diagram for the hybrid tandem cell [9]

1.2 Background to the Present Research

Integrating TEG with solar cells can help the solar cells to transfer excess heat and reduce their operating temperature. In addition, a temperature difference across thermoelectric devices between the hot side (solar cells) and the cold side (heat sink) will lead to extra electrical power generation from the TEG by the Seebeck effect.

Conventionally, TEG was integrated directly with different types of PV cells without investigating the best type, i.e. the technology that wastes the least amount of power due to the thermal resistance and increases in the operating temperature of the PV cell. Optimisation of the number of thermoelement is crucial for the efficiency of both the TEG and the PV cell.

In this work, an experimental study was conducted to investigate the candidate solar cells for a hybrid PV/TEG system. Six different types of PV cells were tested under fixed light intensity and different temperatures, and the drop in open-circuit voltage, short-circuit current, fill factor, maximum power output (P_{max}) and conversion efficiency (η_{PV}) of the PV cells were analysed. To date, very few studies have focussed on the geometric optimisation of the TEG to improve the performance of a hybrid PV/TEG system. In this work, an analytical model for a PV/ TEG hybrid system is derived in order to study the effect of increasing the number of thermoelements on the power generation of the PV cell and the TEG in a closed circuit condition. Integration of TEG with PV cells, in particular DSC, has been reported in the literature [8][9][10][11][12][13]. However, the addition of a TEG directly to the FTO-glass counter electrode of a DSC makes the thermal coupling between them less effective. Therefore, the heat transfer between the TEG and DSC is improved by fabricating a unique hybrid tandem cell (HTC), comprising a metallic DSC, TEG and an active heat sink.

1.3 Aim and Objectives

The main objective of the work in this thesis is to investigate fundamental science and technological aspects that are crucial to the realisation of the PV/TEG hybrid system. The key tasks include:

1) To identify suitable types of solar cells for this proposed application through in-depth characterisation of power generating performance and, in particular, the dependence of performance on temperature.

2) To characterise different types of solar energy conversion devices, e.g. silicon solar cell, cadmium telluride, copper indium selenium, DSC and TEG.

3) To establish theoretical model and carry out simulation for investigating system optimisation in order to determine appropriate geometries for a PV cell, TEG and heat exchanger in a hybrid system.

4) To design and construct a prototype of the proposed hybrid system, including the selection and fabrication of key components, such as the development of high thermal performance DSC with metallic electrode.

5) To investigate experimentally the performances of the prototype system and evaluate the potential of PV/TE hybrid system as a promising future renewable energy technology.

1.4 Thesis Outline

Chapter one

This introductory chapter provides background information about PV/TEG hybrid systems. It gives a brief description of historical developments of thermal management of PV cells by passive and active cooling. Typical PV/TEG designs are introduced and the methods of integration are described. Also, this chapter includes a background to the present research, describes the aim and objectives and outline of the thesis.

Chapter two

The second chapter gives an overview of solar energy technology and a review of the methods available for harvesting solar energy. It focuses on the state-of-the-art research in the fields of PV cells, TE devices and combined systems. A detailed review of research in the field of combined PV/thermal collectors is presented, which shows that most effort to date has focused on flat plate collectors using water or air as the working fluid. A review of concentrator PV applications is undertaken, which shows that most applications use Fresnel lenses, aluminium foil and reflective mirrors. The technology to incorporate PV cells with TE devices is then evaluated. This chapter also examines the current research efforts in developing effective PV cooling systems using nanofluids.

Chapter three

The chapter explains the equipment and experimental procedure that was used to collect the experimental results. This is followed by a description of an experimental investigation on the temperature coefficients of the six different types of solar cells under fixed light intensity. This work represents the most systematic research to date, which covers all 6 types of the state-of-the-art solar cells. The results from this study provide

useful information and convincing evidence in the selection of appropriate candidate solar cells for integrating with TEG in a hybrid system.

Chapter four

This chapter describes the modelling of a PV/TEG hybrid system. The construction of the model based on energy balance equation of the PV/TEG hybrid system is explained, followed by calculating the parameters for both the PV cell and the TEG. To validate the theoretical results predicted from the model, a test rig of compound PV and TEG is designed and constructed. The details of the test rig design are illustrated. The experimental measuring technique for the apparatus and its temperature measuring techniques are discussed, including the equipment and procedures. The results obtained from the experiments are then compared with the theoretical calculations. A unique aspect of this model is that the simulation of the power output of TEG is performed under closed circuit, which significantly improves the accuracy of the simulation and consequently the optimal geometry for maximum power output of TEGs.

Chapter five

This chapter investigates the factors that influence the performance of the PV/TEG hybrid system. These include: (1) The effect of light intensity increasing on the PV/TEG hybrid system by fabricating a solar dish parabolic concentrator; (2) The effect of changing the mass flow rate of the water in the cooling system on the of the PV/TEG hybrid system.

Chapter six

This chapter briefly describes the procedure of DSC fabrication in the laboratory, including the challenges, the obstacles, and the experiences gained. Two types of counter electrodes for DSC were also investigated: the conventional FTO-glass and a metallic counter electrode. Also included is an investigation of different metallic materials for the metallic counter electrode. The DSC with metallic counter electrode was specifically developed to improve the thermal coupling between PV and TEG in a PV/TEG hybrid system. The performance of the hybrid system employing DSC with metallic counter electrode was investigated and compared with that using an FTO-glass counter electrode. In addition, the optimum TEG geometry for an integrated DSC/TEG hybrid system was also investigated using three TEG modules of different dimensions.

Chapter seven

This chapter summarises the major achievements of this work and recommendations of future development

CHAPTER TWO - LITERATURE REVIEW

2.1 Introduction

This chapter gives an overview of solar energy and technologies of harvesting energy from the sun. This includes single systems such as PV, TEG and also combined systems such as photovoltaic/thermal (PV/T) and photovoltaic/thermoelectric (PV/TE). Several experimental and theoretical studies have focused on optimisation of PV/T system design. Some theoretical investigations have examined the cooling of the PV by using thermoelectric cooler (TEC). Only few papers have discussed the integration of thermoelectric generator (TEG) with PV cells and the optimisation of the hybrid system and these are discussed in this chapter. The effectiveness of nanofluid as a coolant in PV/T system is also reviewed.

2.2 Overview of Solar Energy

There is current demand for the use of solar energy due to it being a silent, no moving part and low maintains costs [14] and environmentally friend source of energy [15]. The most exploited sources of energy at present are fossil fuels, even though the earth receives a higher amount of solar energy from the Sun than is generated by fossil fuels. The various types of fossil fuel (such as coal, gas, and oil) emit high amounts of carbon dioxide, which exacerbates environmental issues such as the threat of global warming [16]. It is therefore thought that solar energy will begin to dominate over the next three decades (as shown in Figure 2.1 [17]**)** as fossil fuels diminish and the global energy demand increases**.**

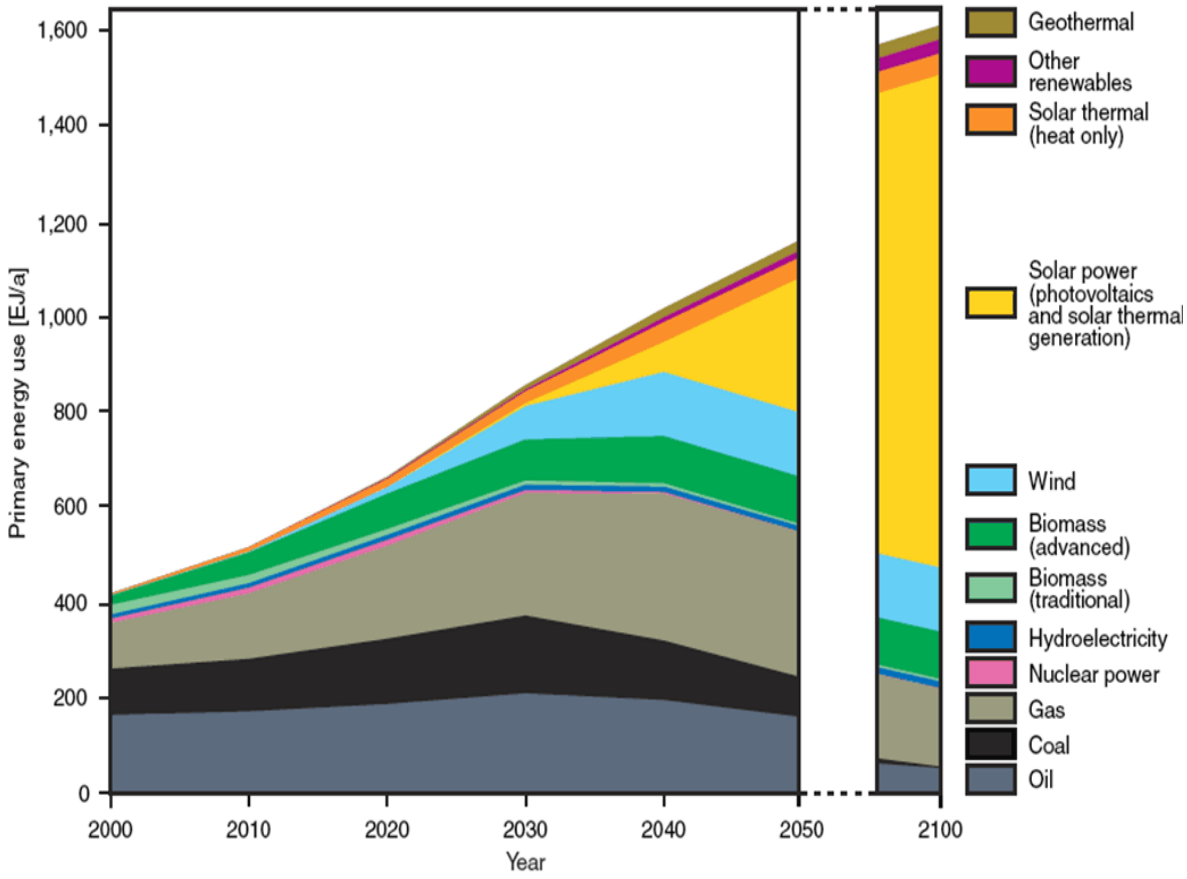

Figure 2. 1 Predicted global energy production. Solar will be the largest source of energy beyond 2050 [17]

2.3 Methods of harvesting solar energy

There are several different methods for harvesting solar energy. Some methods are indirect, such as wind energy, hydroelectric energy and so on. Others are direct, such as PV cells, solar thermal, combined systems, thermoelectric devices and recently integrated hybrid systems of PV cells and TEG and so on. This research will review the direct methods of harvesting solar energy only.

2.3.1 Photovoltaic (PV) cell

A PV cell is a device which converts solar energy (photons) into electrical energy (volts) by photovoltaic effect. Solar conversion efficiency is an important parameter to evaluate

the performance of PV cells. It is highly affected by the semiconductor material and the operating temperature of the PV cell. Today, there are many types of PV cells in the market and they are classified according to their semiconductor material. Examples include silicon solar cells, gallium arsenide (GaAs), indium phosphide (InP), and DSC [18]. The DSC solar cell has attracted many scientists and engineers aiming to develop and increase its efficiency because of its potential low-cost of production [19][20][21]. The structure of DSC contains five components: the working electrode, a thin layer of semiconductor, a dye sensitiser, electrolyte, and a counter electrode [18]. A schematic diagram for the structure is presented in Figure 2.2 [22].

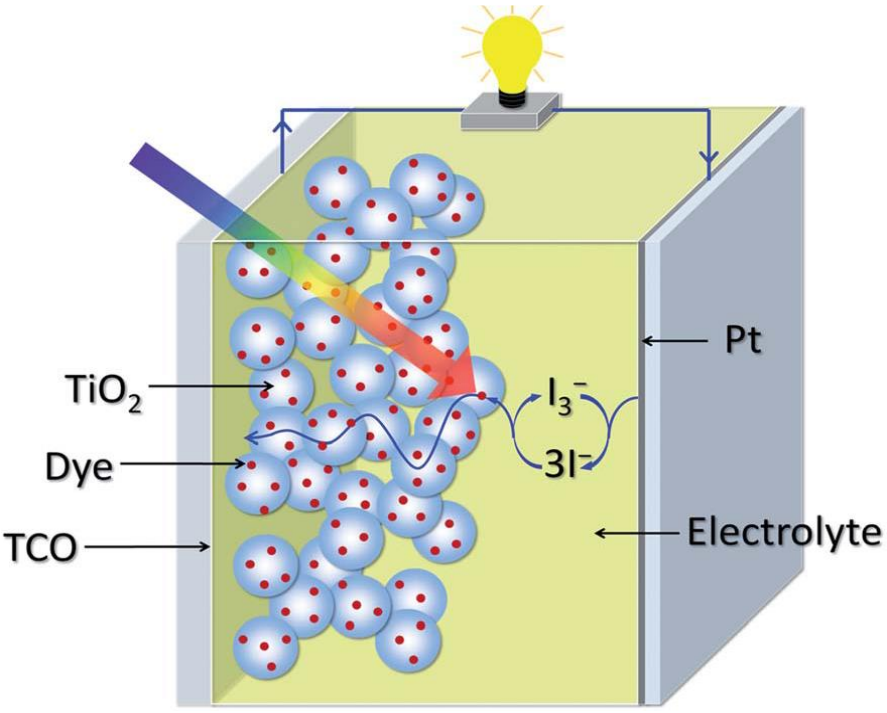

Figure 2. 2 The structure of a DSC [22]

DSC also offers the potential to fabricate the cell in a flexible design [23][24] by using a plastic counter electrode, as shown in Figure 2.3 [25].

Generally, PV cells are characterised by measuring their current–voltage (I-V) curves.

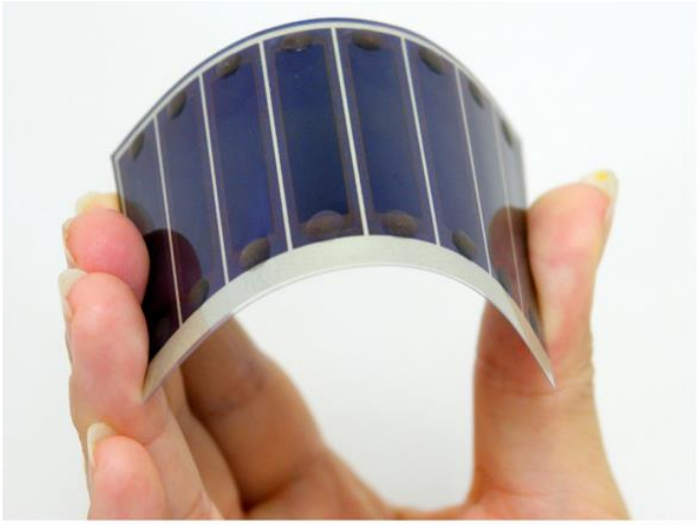

Figure 2. 3 A photograph of 5 x 10 cm2 flexible PV cell [25]

Using the I-V curves, the maximum power can be determined by the product of the current at the maximum power point (I_{MP}) and the voltage at the maximum power point (V_{MP}). Figure 2.4 is a typical I-V and P-V curves for PV cells [15].

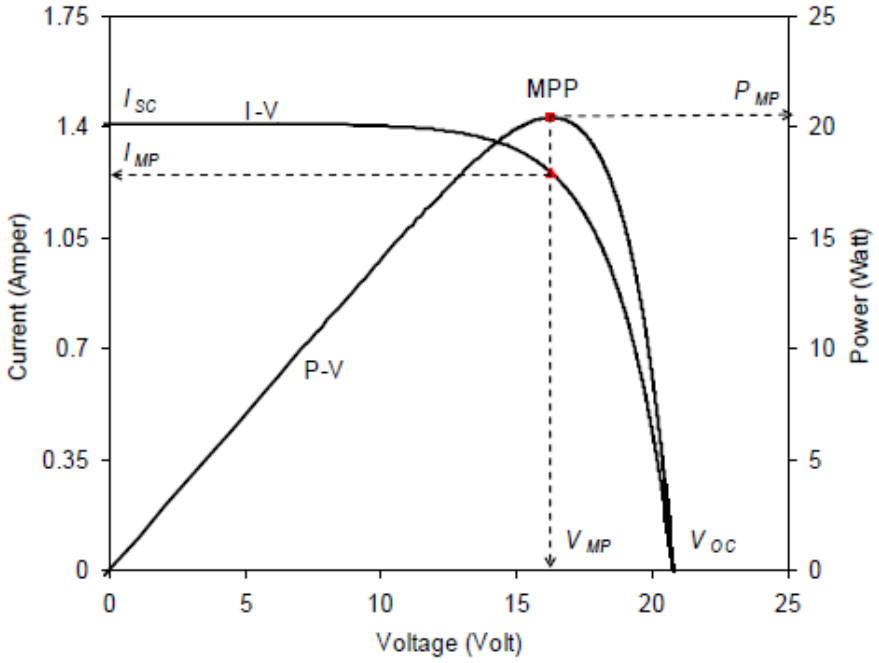

Figure 2. 4 Typical I-V and P-V curves for a PV module [15]

Consequently, the conversion efficiency of a PV cell (η_{pv}) can be calculated by:

$$\eta_{pv} = \frac{I_{MP}V_{MP}}{GA_{pv}}, \quad 2.1$$

where, G (W.m^{-2}) is the solar radiation intensity and A_{PV} (m^2) is the PV cell area. Another useful parameter to evaluate the quality of a solar cell is the fill factor, which is defined as:

$$FF = \frac{I_{MP}V_{MP}}{I_{SC}V_{OC}}, \quad 2.2$$

where, I_{SC} is the short circuit current and V_{OC} is the open circuit voltage (see Figure 2.4). The effect of temperature on PV cells has been investigated [26], [27]. It was found that the maximum power output (P_{max}) of PV cells decreases with increasing temperature [28], [29]. Figure 2.5 shows the power output of crystalline solar cells as a function of the output voltage for different operating temperatures at 28 ^{0}C, 40 ^{0}C, 60 ^{0}C, and 80 ^{0}C, respectively [30]. It has been established that the conversion efficiency of silicon PV cells (η_{PV}) decreases linearly with increasing temperature [31], as shown in Figure 2.6 [32]. However, DSC showed an interesting increase in η_{PV} with increasing temperature between (20 ^{0}C – 35 ^{0}C), in contrast with silicon and other PV technologies [33].

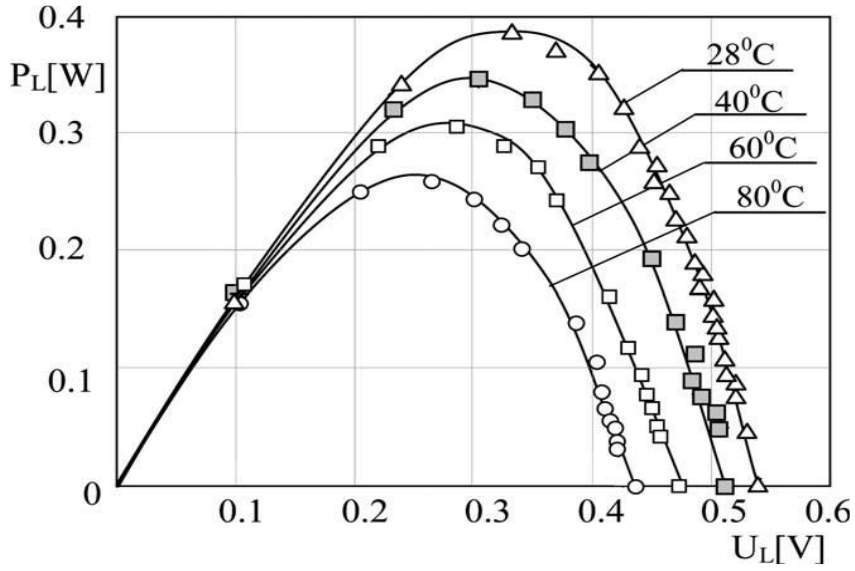

Figure 2. 5 The output power as a function of temperature for a crystalline solar cell [30]

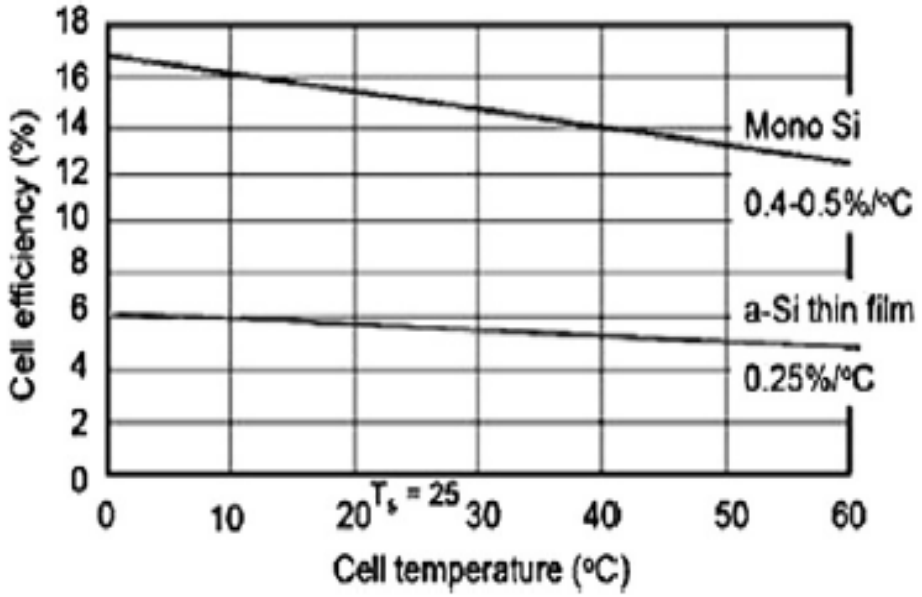

Figure 2. 6 The relation between PV cell efficiency and temperature [32]

2.3.2 Thermoelectric (TE) device

2.3.2.1 Thermoelectric effects

Thermoelectric power generation is a solid state energy source which converts heat into electricity [34], [35], utilising electrons as a working fluid. It is environmentally friendly [36], with no moving parts and produces no noise [37]. It is essentially consists of three effects: the Seebeck effect, the Peltier effect and the Thomson Effect [38], which is described below.

The Seebeck Effect

The Seebeck effect is the phenomenon of producing voltage due to a temperature difference by connecting two dissimilar materials in series electrically and in parallel thermally [39], as shown in Figure 2.7.

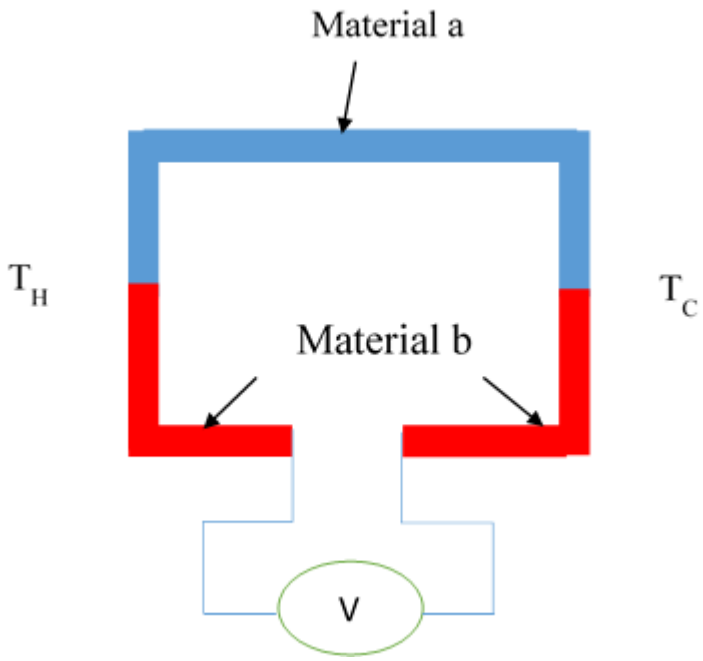

Figure 2. 7 The Seebeck effect: a voltage generated by the temperature difference across two dissimilar materials

The voltage generated can be calculated by:

$$V = \alpha_{ab} \Delta T, \quad 2.3$$

where, V is the voltage generated from the TE device, α_{ab} is the difference in Seebeck coefficient of the two materials, and ΔT is the temperature difference between the hot junction (T_H) and the cold junction (T_C).

The Peltier Effect

The Peltier effect is the phenomenon of generating temperature difference across the junctions of two dissimilar semiconductors as shown in Figure 2.8. The heat is absorbed at one junction and rejected at another junction by applying an external current [40]. The rate of heat removed ($\dot{Q}$) from one side to another side can be calculated as:

$$\dot{Q} = \pi_{ab} I, \quad 2.4$$

where, π_{ab} is the Peltier coefficient and I is the electrical current.

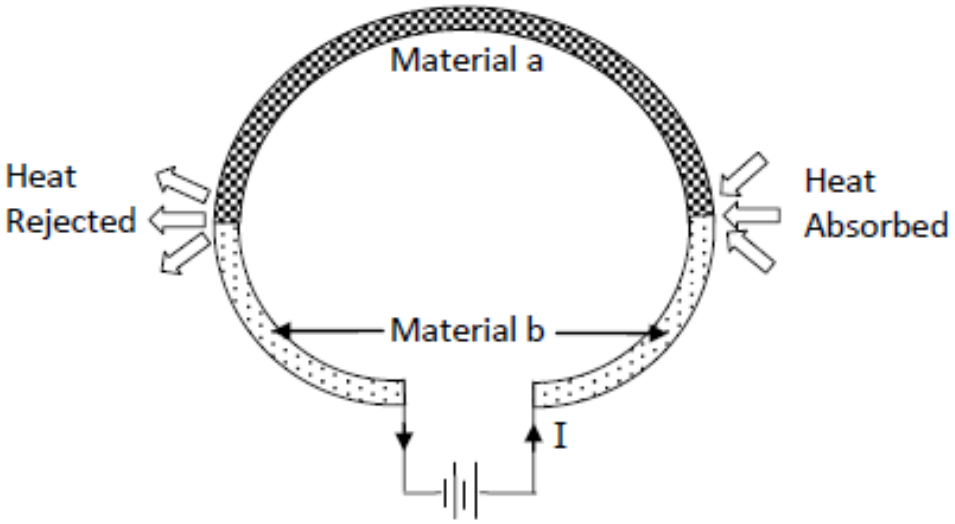

Figure 2. 8 Heat absorption at junctions because of the current applied [40]

Thomson Effect

The Thomson effect appears in all TE devices and is the phenomenon of heat absorption or dissipation due to current flow and temperature differences [41]. Figure 2.9 shows a single material subjected to ΔT and current [40].

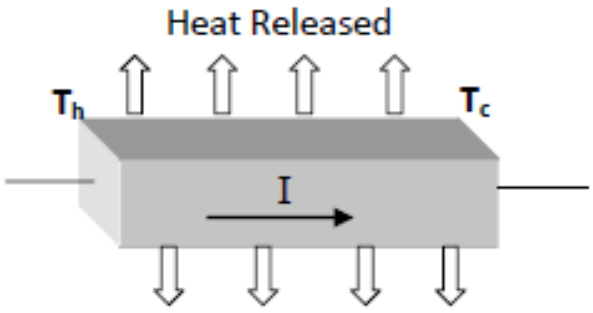

Figure 2. 9 Thomson Effect [40]

The total rate of heat absorption ($\dot{Q}_T$) is given as:

$$\dot{Q}_T = \beta I \Delta T, \quad 2.5$$

where, β is the Thomson coefficient.

The three coefficients are connected by the Kelvin relationships as described in the following equations [42]:

$$\pi_{ab} = \alpha_{ab} T, \quad 2.6$$

$$\frac{d\alpha_{ab}}{dT} = \frac{\beta_a - \beta_b}{T} \quad 2.7$$

2.3.2.2 Solar thermoelectric system

Solar thermoelectric is another method of converting solar energy into electric energy[43]. Gao [44] developed a theory to calculate the electric power output from TEG based on a known temperature difference. In the new formula, if the solar thermal energy is applied to the surface of a known collector then power output can be calculated directly from the solar radiation. A solar concentrator system utilising TEG was experimentally tested in [45]. The system was constructed with 6 TEGs (4 cm x 4 cm x 0.5 cm) in a hybrid system. The source of the heat was solar radiation while the cold side was provided by a water circulation system. The hot side temperature of the TE device reached 200 °C at midday, while the cold side almost 50 °C. The total power generated from the system was 220 W, which includes the electrical and thermal power. This system could be competitive with the PV/Thermal system (PV/T), see Figure 2.10.

Figure 2. 10 Concentrator, hybrid thermoelectric-solar system [45]

A design using evacuated tubular solar collector (ETSC) was reported in [46]. It consisted of a parabolic trough concentrator and TEG modules to generate both hot water and electric power. The hot side of the TEG device was integrated with a solar selective absorber (SSA), while the cold side was integrated with a heat sink. The whole system was operating under vacuum conditions as can be seen in Figure 2.11.

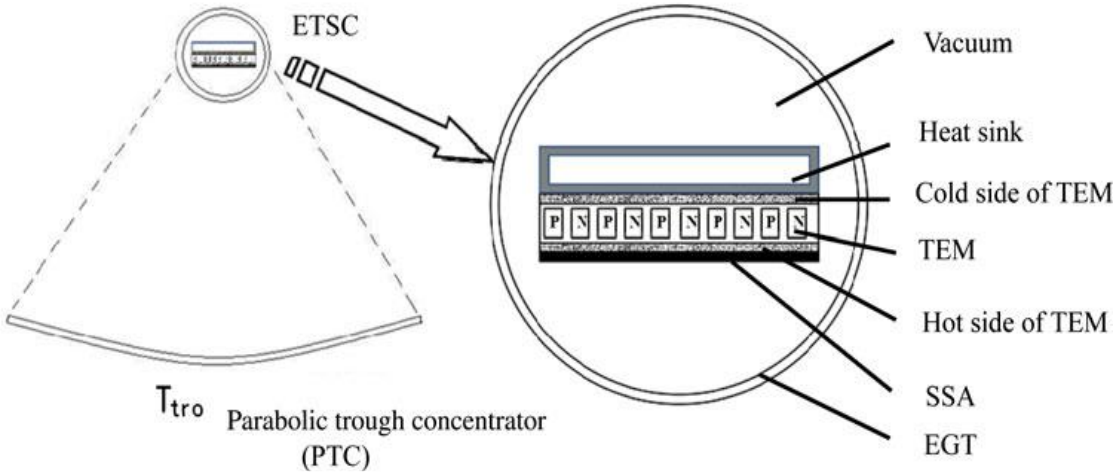

Figure 2. 11 Schematic diagram of the solar thermoelectric generator with a magnified view of the evacuated tubular [46]

A solar thermoelectric power generation plant was design using the TRANSYS software tool [47]. The input parameters for the software were the characterisation of the TEG device, the temperature for the hot side of TEG and the power output required. The simulation was experimentally validated by two small scale units where the source of heat was either an electrical heater or a compound parabolic collector utilising solar energy. Various design for the slope and angle of the compound parabolic collector were discussed. The measurement results agreed with the model and the TRANSYS software was therefore considered a useful tool for such a hybrid system.

A study into the modelling and optimisation of hybrid solar thermoelectric (HSTE) systems was also reported [48]. The main components of the system were a solar selective

material coated on TEG, a thermosyphon and a parabolic trough mirror concentrator, as shown in Figure 2.12. The concentrator was used to increase the light intensity in order to heat the hot side of TEG and the thermosyphon was used to enhance the heat transfer from thermoelectric to the condenser. The study investigated the effect of different thermoelectric materials and working fluids. The optimisation showed that a system efficiency (heat + power) up to 52.6 % is possible under 100 suns.

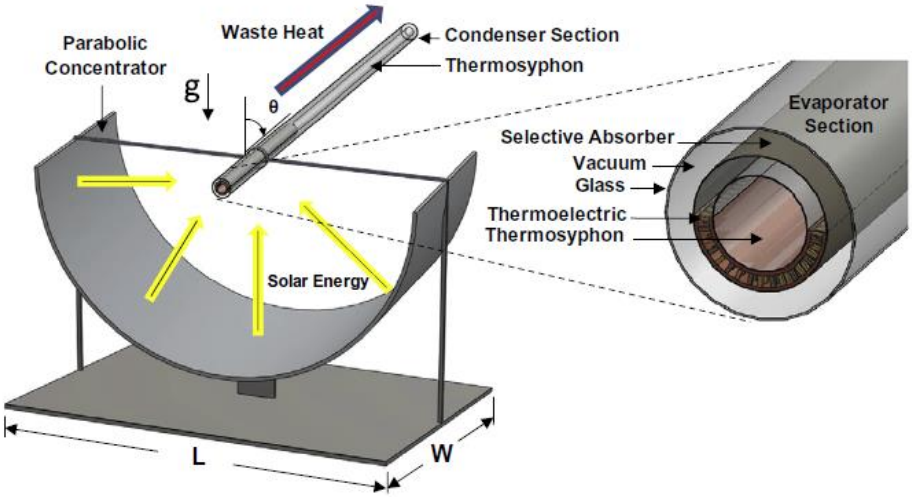

Figure 2. 12 Schematic diagram of the hybrid solar thermoelectric system [48]

An innovative solar thermoelectric generator (STEG) design is shown in Figure 2.13[49].

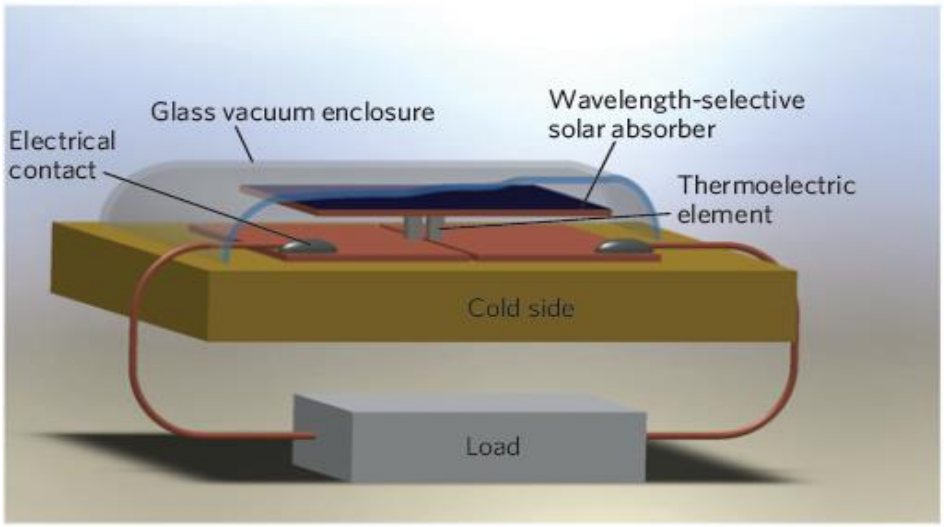

Figure 2. 13 Schematic diagram of the hybrid Solar thermoelectric [49]

The electric conversion efficiency was 4.6 % under 1 $kW.m^{-2}$ which was 7- 8 times higher the other STEG systems which were reported elsewhere. The nanostructured thermoelectric material inmproved the performance of the system [49]**.**

2.4 Combined Systems

Combined systems utilise the heat associated with electrical power production in PV cells in a hybrid design. The heat generated as a by-product could be used for domestic uses such as central heating [50], hot water [51] or to generate electricity in a supplementary stage by TEG [52] (using the Seebeck effect). Combined systems prevent the drop in electrical efficiency of the PV cell due to transfer the excessive heat in PV cell [53][54]. Adding the thermal power recovered from the system to the electrical power will also increase the total system power output [55]. Combining two systems uses a wide range of the solar spectrum, whereas the individual systems can only use part of it [52]. The heat extraction approach determines the type of combined system. For example cooling can be achieved by air [56], water [57], heat pipe [58], phase change material (PCM) [59] and thermoelectric cooler (TEC) [4] .

2.4.1 Photovoltaic/Thermal (PV/T) Hybrid System

Photovoltaic thermal technology (PV/T) is an integrated system that produces both heat and electricity. A solar cell produces electricity by converting solar radiation, while the thermal collector absorbs the heat from the solar cells and transfers it to warm a fluid. Meanwhile, the temperature of the PV cell will be reduced and stabilised, maintaining constant power production. PV/T is classified, according to the working fluid, into two main categories: air based PV/T and water based PV/T.

Air-based PV/T collectors.

Air cooled PV/T collectors are fabricated by integrating air heat channels, usually at the rear of the PV cell. The air circulates inside the channel either by force [60]or by the natural convection of heat transfer [61]. The PV/T system using forced convection has better performance than that with passsive cooling [62]. However, power is consumed when using the pump to circulate the fluid, and hence the net electrical power generation reduces [62]. Various designs of the PV/T system using air cooling were discussed in the literature [63][64].

The enhancement in both thermal and electrical power generation associated with a PV/T air collector was studied by Bambrook and Sproul [65]. An open-loop single pass duct with a fan was used for cooling to extract the heat from PV cells. The electrical efficiency achieved was 10.6 and 12.2 % while the thermal efficiency was 28 and 55 % [65].

A hybrid PV/T system using air collector for different operating parameters was designed, and a steady-state thermal model of the system was developed based on the energy balance equations [66]. The thermal and electrical efficiencies of the system were determined to be 42 and 8.4 %, respectively. Figure 2.14 shows a photograph of the system.

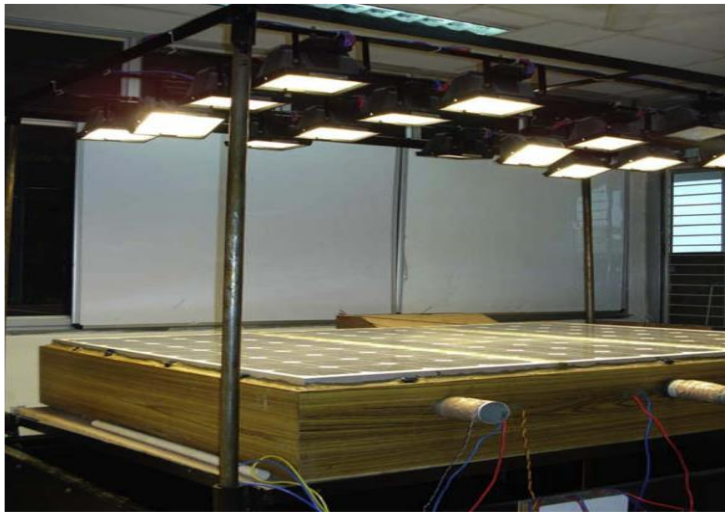

Figure 2. 14 Photograph of PV/T solar heater [66]

An analytical model was developed by Dubey et al. [67]. The model studied four different configurations. The glass-to-glass PV module with duct showed a higher performance and higher outlet air temperature. The system presented 10.41 % average annual efficiency for glass-to-glass type PV modules with duct and 9.75 % for the module without duct.

Jin et al. [68] developed a PV/T system using single-pass air collector with a rectangular tunnel absorber as shown in Figure 2.15. The rectangular tunnel was located on the rear of the PV panel. The PV/T system was tested under a solar simulator. The electrical, thermal and total efficiencies of the PV/T were obtained for the illumination intensity level of 817.4 W/m^2, mass flow rate of 0.0287 kg/s and ambient temperature of 25 $^{\circ}$C. It was concluded that the hybrid PV/T with a rectangular heat absorber tunnel showed the best performance in contrast with the conventional PV/T system [68].

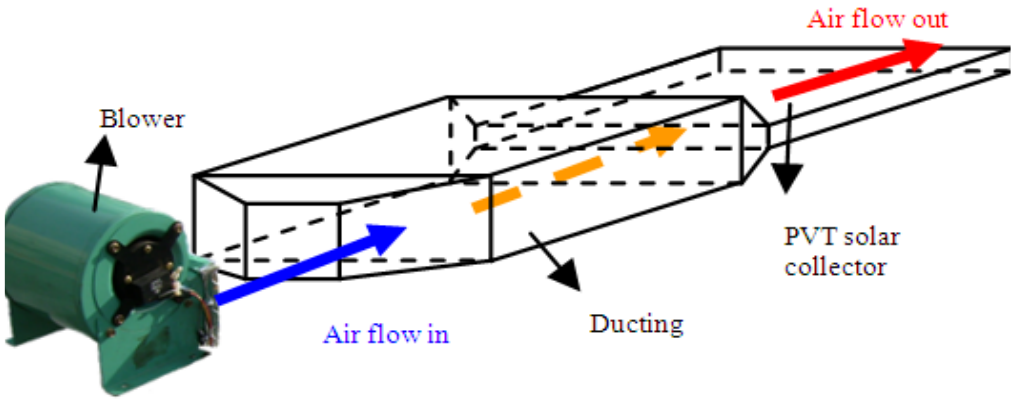

Figure 2. 15 Ducting connected to blower and photovoltaic thermal collector [68]

Light concentrator systems are used to achieve two important effects: firstly an increase in the electric power output, and secondly a reduction in cost by replacing the expensive semiconductor material with cheapest material such as mirrors, lenses and Fresnel lances [69]. Silicon and GaAs solar cells have been used widely for making concentrated PV (CPV) cells[70][71]. However, each solar cell working under a concentrator system needs cooling technology because the temperature of the solar cell will increase during

operation. A cooling system extracts the heat from solar cells and transfers it to the heat sink, heat pipe, thermal system or to a TE device. The PV module temperature should be kept as low as possible in order to maintain an acceptable level of conversion efficiency, as electricity production from PV/T hybrid system decreases with increasing temperature of the air flow [72]. Therefore, a compromise must be made between the electricity production and the useful hot air. Figure 2.16 shows a concentrator system cooled by air.

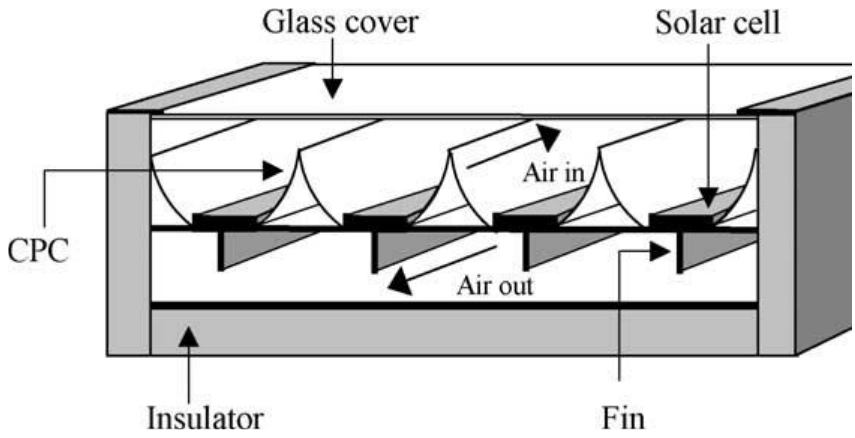

Figure 2. 16 A schematic model of a double-pass photovoltaic thermal solar collector with CPC and fins [72]

Different reflector materials were analysed for fill factor improvements in a low–concentrating PV system, see Figure 2.17 [73]. These included anodized aluminium, rolled aluminium foil, and mirror reflectors. The compound parabolic collector element was also examined with different reflector materials. The economic value of concentrator-PV systems has been studied, and it has been shown that the cost of each unit of energy produced by the concentrator PV system decreases with increasing concentration ratio if both electrical and thermal outputs are collected for useful purposes [74]. The PV/T air collector represents a simple technique to reduce the temperature of the PV cell. However, the physical properties of air limited the performance, making other methods of cooling preferable [75].

Figure 2. 17 The truncated compound parabolic concentrator showing removable reflectors and a 10-cell module string [73]

Water based PV/T collectors

The concept of a water cooled PV/T hybrid system was first discussed by Kern and Russell [76], and it was considered as one of the most efficient methods to harvest solar energy [77]. A hybrid of PV/T systems was simulated by the TRANSYS tool, which produces hot water for domestic applications in addition to generate electrical power [78]. A silicon PV module was integrated with a water heat extraction unit, as it can be seen in Figure 2.18. The study was carried out at three locations: Nicosia, Athens and Madison. The proposed system had the ability to produce a remarkable amount of thermal and electrical energy [78].

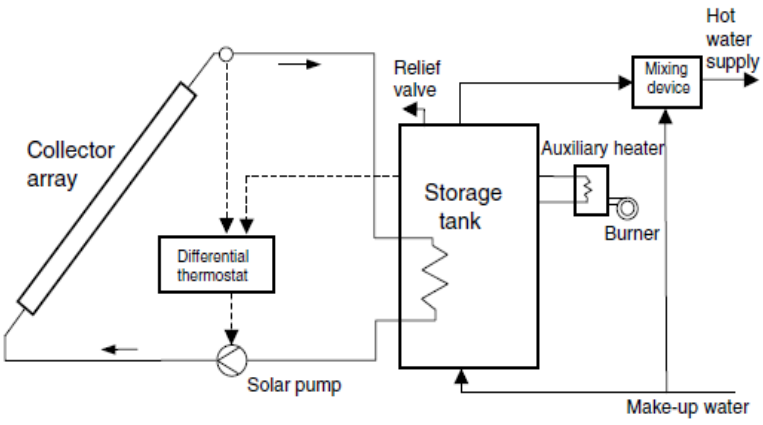

Figure 2. 18 Schematic diagram for the PV/T hybrid system [78]

Different kinds of PV panel materials such as c-Si, a-Si and $CuInSe_2$ have also been examined [79]. The study also evaluated the influence of thermal contact between the PV panel and the collector. It was found that the commercial PV panels were unable to provide a good thermal contact with the heat collector due to the poor thermal conductivity of the panel substrate material. Different materials and constructions utilised to improve the thermal contact between the PV panel and the collector. It was noted that the power output of the PV panel increased 10 % with the optimised design.

Three types of crystal silicon PV cell arrays and the GaAs cell array have been tested, as shown in Figure 2.19 [80]. The experimental results indicated that the electrical performance of the system with the GaAs cell array was better than that of the crystal silicon PV cell arrays. Furthermore, the system with crystal silicon PV cell arrays showed a better performance in terms of the thermal output power.

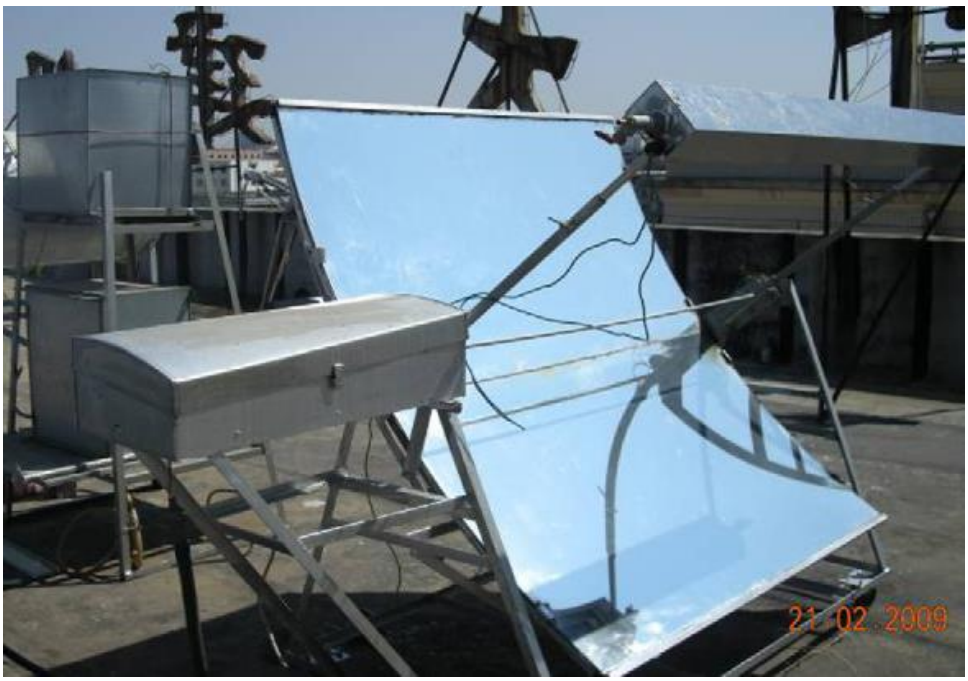

Figure 2. 19 The trough concentrated solar PV/T system [80]

PV/Heat-pipe

Another method to cool the PV cell, which utilised a heat pipe, was patented by Russell [81]. A hybrid system of PV/heat-pipe comprised three main parts, namely: the evaporator, the adiabatic section, and the condenser section [75]. A heat pipe was used to cool a concentrated PV unit which usually worked at high temperature. A row of PV cells were integrated on the surface of the heat pipe. The heat exchanger in the heat system can reomove the heat away for the PV effectively with circulating fluid inside heat pipe [81].

2.4.2 Photovoltaic/Thermoelectric (PV/TE) Hybrid System

The incorporation of TEG with PV cells has been investigated in the last ten years as it can recover the waste heat from the PV and generate electricity in a supplementary stage [82][83] [84][85]. A silicon thin film solar cell (STC) was integrated with TEG and a heat collector in a hybrid generation system (HGS) as shown in Figure 2.20. The heat collector worked by collecting the unwanted heat from the solar cells and transferring it to the hot side of the TEG [84].

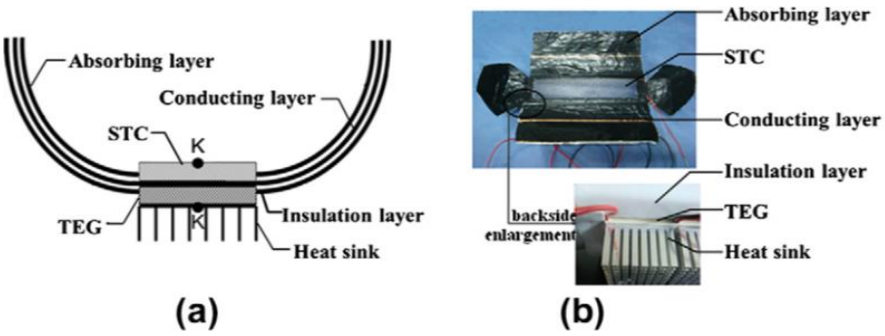

Figure 2. 20 A hybrid generation system; (a) Schematic diagram, and (b) photograph [84]

The distribution of heat across the TEG was analysed in this study by finite element method (FEM). The total power generated from the hybrid system was 393 mW which

was more than the individual system. A hybrid CPV/TEG was utilised to store the heat and use it as the heat source for the hot side of TEG, as in Figure 2.21 [85].

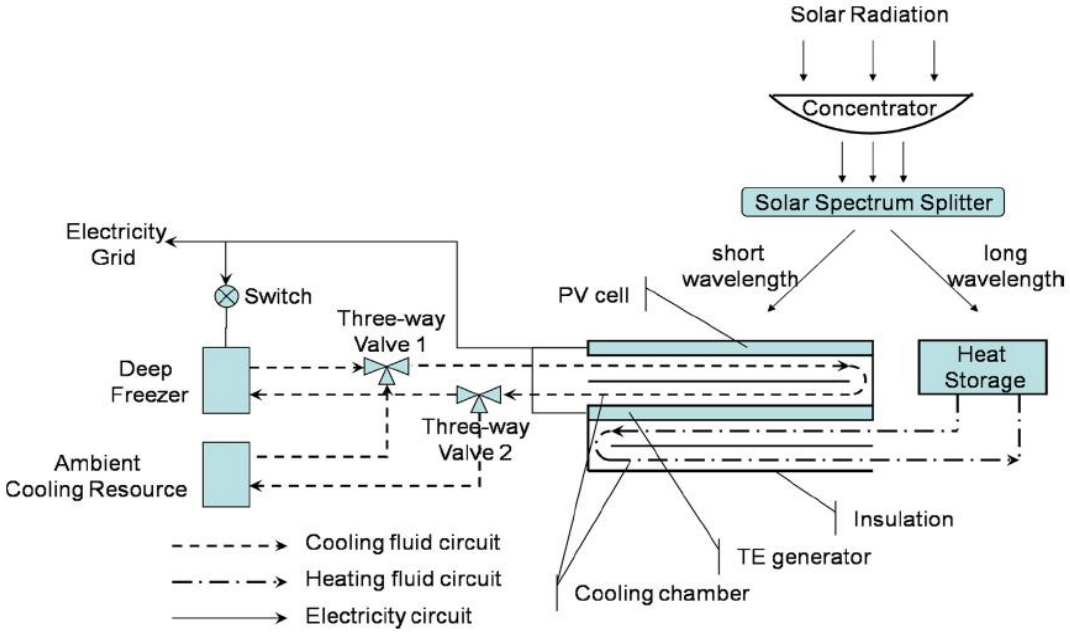

Figure 2. 21 A Schematic diagram for a hybrid generation system [85]

The solar spectrum splitter divided the solar spectrum into two regions: the short wavelength and the long wavelength. The short wavelength light was focused on the PV cell, while the long wavelength was used to heat the fluid in the heat storage media and used it later, as a heat source to operate the TEG [85].

An experimental study used a hot mirror to separate the near infrared light and focus it on the TEG by Mizoshiri, et al [86], as shown in Figure 2.22.

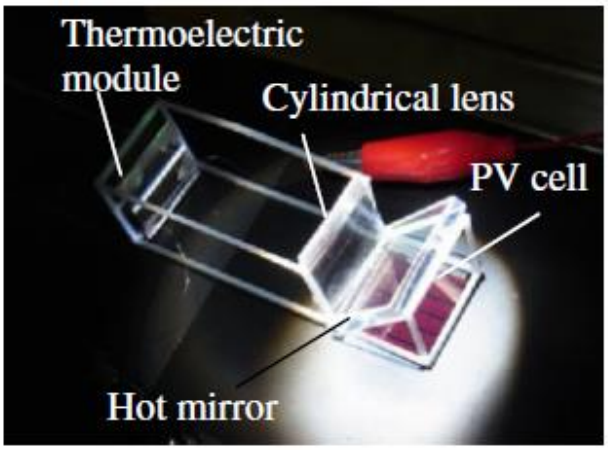

Figure 2. 22 A photograph of the hybrid system [86]

The experimental results indicated that there was a top up voltage from the TEG and that the total V_{OC} of the system was increased by 1.3 %.

Yang and Yin [87] designed a hybrid system containing PV cells, a TEG, and hot water (HW). Theoretically, they showed that the hybrid system produces higher electrical output power. However, they did not observe these advantages in the experiment, and the reason for this was related to the material of the TEG device. Therefore, the study recommended the use of nanotechnology to improve the material properties of TEG, thereby increasing the total efficiency of the hybrid system, as shown in Figure 2.23.

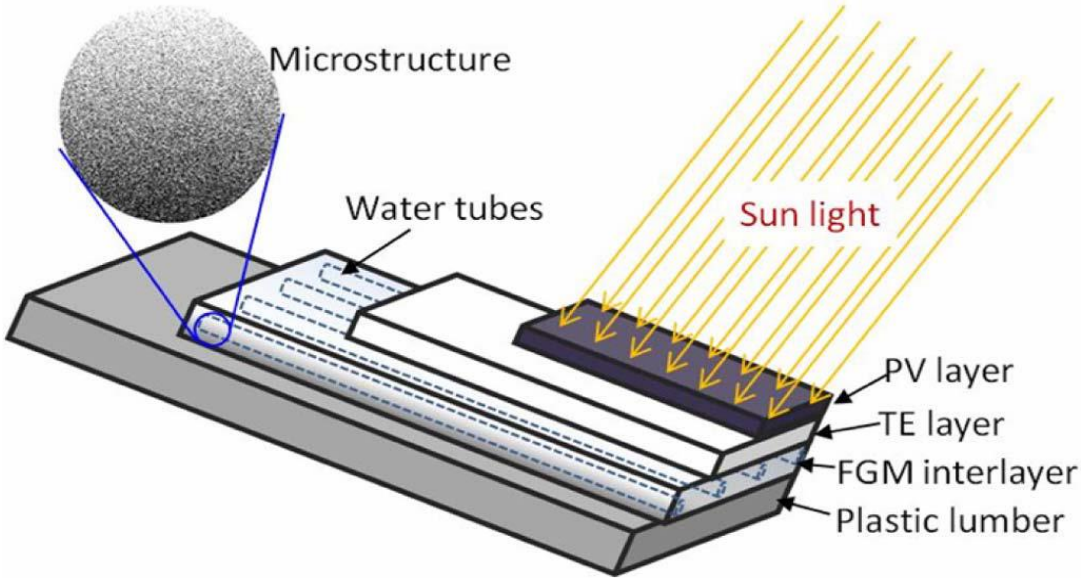

Figure 2. 23 A Schematic diagram of the novel hybrid solar panel [87]

More recently, a study which modelled a hybrid system, including PV cells and TEG, has analysed the effect of increasing the number of elements. The effect on the power output from PV and TEG was analysed [88]. The number of TE modules to generate the maximum power was discussed and the power output from the TEG was calculated.

The first polymer solar cell integrated with TEG in a hybrid system was reported in [89]. The overall power generation of the hybrid PV/TEG system was investigated experimentally. A schematic diagram of the system is presented in Figure 2.24. The

results indicate that the hybrid system is more efficient in generating electricity than using a singular system [89].

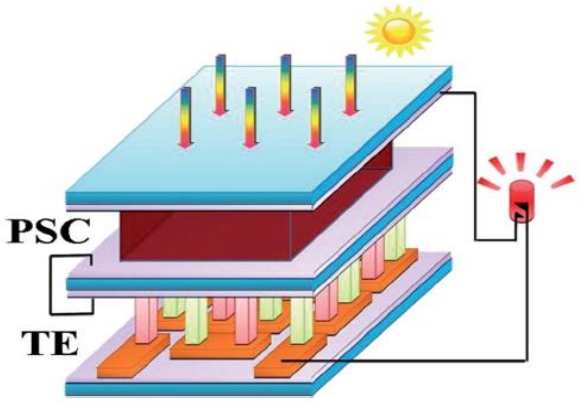

Figure 2. 24 A schematic diagram of the polymer solar cell and TEG [89]

The power losses due to the incorporation of TEG with PV in hybrid PV/TEG system were considered in [90]. The study suggested the use of low internal resistance for both devices and a large number of legs for TEG to increase the output voltage.

Since, the DSC is introduced in 1991, as a solar cell [19], the conversion efficiency increased gradually by time [91]. A DSC is able to use part of solar spectrum (short wavelength) and convert it to electricity, while the other part of solar spectrum (long wavelength) converted to heat as a waste heat inside the DSC [9]. As a results, the temperature of DSC increased and the conversion efficiency decreased. Thermoelectric generator can use this heat as a source of power and convert it to electricity by making temperature difference across it [92]. There have been some attempt to integrate TEG with DSC [8][9][10][11][12][13]. None of them has investigated the using of metallic counter electrode of DSC to integrate with TEG.

A thin film of CuO was coated on a TEG to improve the heat transfer by conduction in the hybrid system. The coating resulted in an increase in the conversion efficiency of TEG

by 10 % and in the total power output by 2.35 %. A nanofluid has also been used for cooling in this hybrid system to enhance the heat absorption [10]. The experimental results indicated that the power output from TEG was increased [12].

The TE device was also used as a cooler (via the Peltier effect) for PV in a hybrid PV/TE system [3]. The hybrid system included PV, TEC, aluminium sheet and a heat sink, as it can be seen in Figure 2.25.

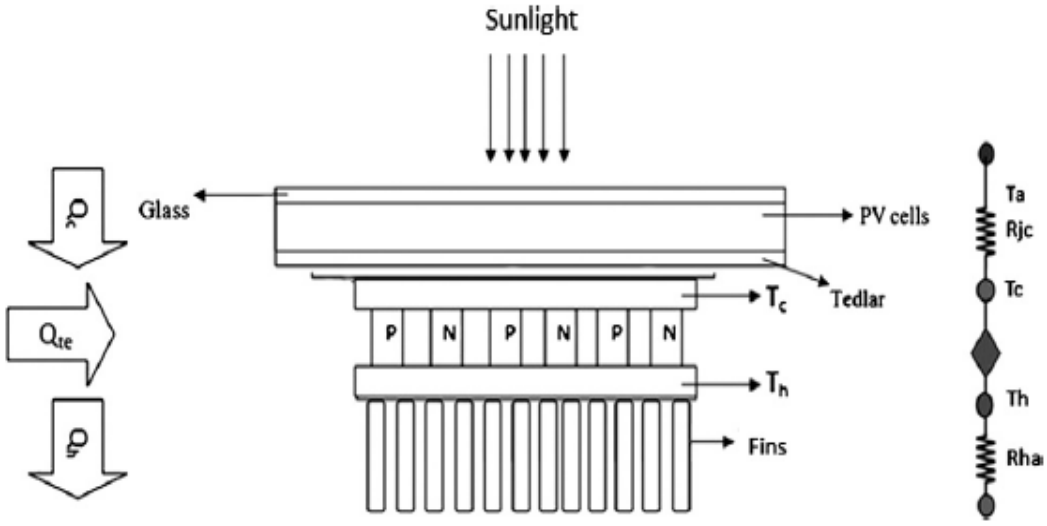

Figure 2. 25 A Schematic diagram of the hybrid PV/TE system [3]

The power supply for the TEC was generated by the PV device. It was found that additional power could be generated due to cooling of PV cell. Also, the study reveal that the figure of merit of the TE module strongly affected the performance of the system. However, the practical validation and economical study were not considered. The TEC was utilised in a building integrating PV system (BIPV) [4]. A dynamic model of BIPV was introduced to improve the performance of PV panels when TEC attached to the rear of a PV panel in a building. The results indicated that the temperature of the PV panel reduced by 10 °C without loss of power, and maintained the operating temperature of the PV panel at low level, increasing its life time.

2.4.3 Using Nanofluid in PV/T Hybrid Systems

Hybrid PV/T systems have been widely studied in the literature either theoretically or experimentally utilising water or air as coolant. Recently, some works have been done to investigate the use of nanofluid as a working fluid in PV/T hybrid system [93]. Figure 2.26 shows a schematic diagram for a PV/T hybrid system using nanofluid as the cooling media [94].

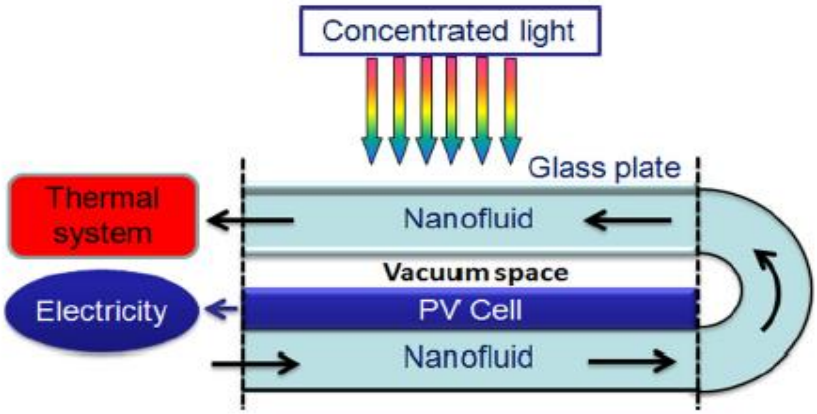

Figure 2. 26 A Schematic diagram for the hybrid PV/TE system [94]

Nanofluid optical filter utilised in solar energy application, which is fabricated from thin film or solid material [95]. Nanofluid optical filter is used to filter the wavelength of solar spectrum and permit only the useful solar energy for PV cell to go through it, while take in the unwanted energy in the solar spectrum [96].

A nanofluid was dispersed in the optical filter in order to use it, as the heat transfer and thermal storage medium [95]. The nanofluid was used to absorb the heat and transfer it away from the PV cells. Figure 2.27 shows a schematic diagram of the PV/T system integrated with the nanofluid optical filter.

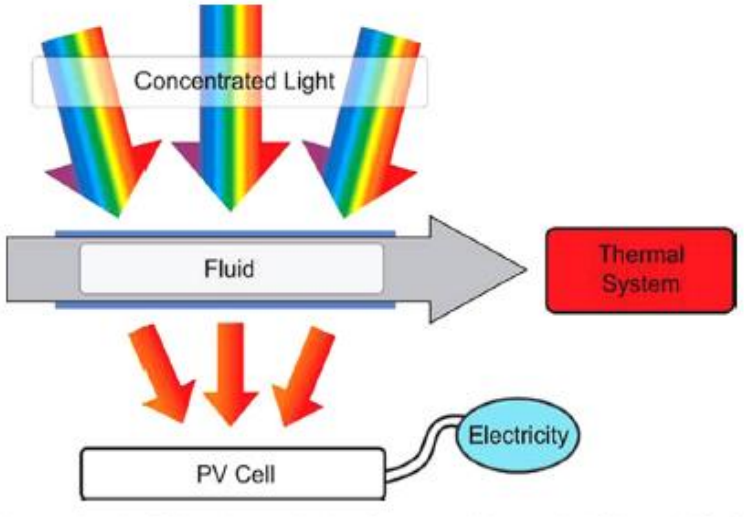

Figure 2. 27 Schematic diagram of the PV/T and optical filter [95]

Innovative ideas have been proposed involving magnetocaloric technologies. The main components of the proposed system include CPV cells, microchannel heat exchanger, and a magnetocalaric fluid as shown in Figure 2.28. In this system the CPV was cooled without consuming power for the pump. The advantages and disadvantages of the system were highlighted in [97].

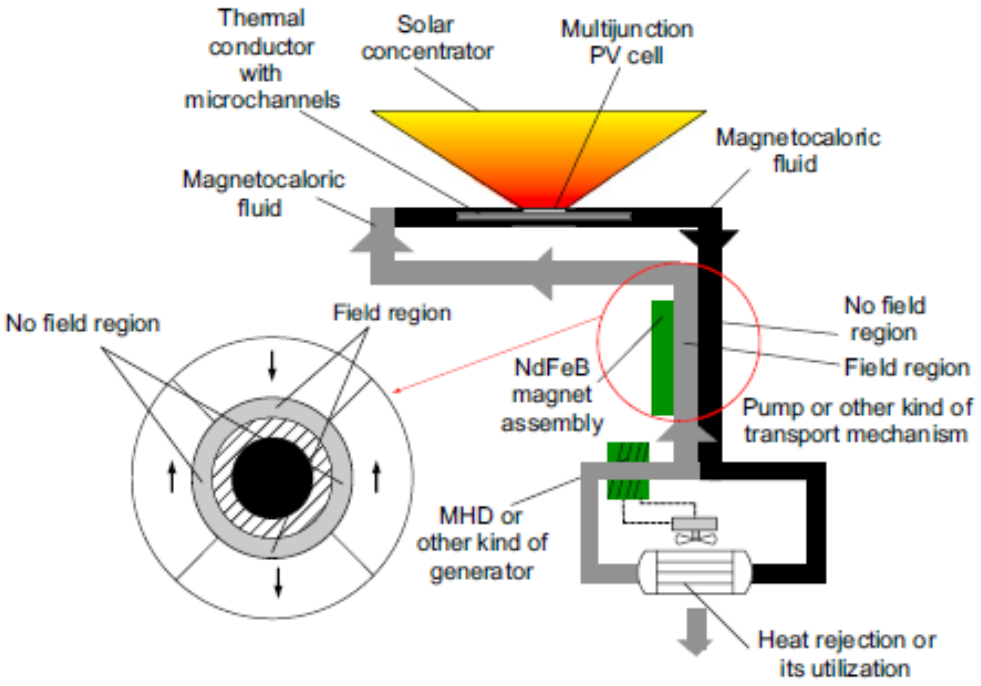

Figure 2. 28 Schematic diagram of the proposed system [97]

In summary, the methods of harvesting solar energy were reviewed and analysed here. Many studies have attempted to overcome the challenge of energy demand and to reduce their carbon footprint. Several researchers have studied the PV/T hybrid system experimentally and theoretically with different designs. In addition, the advantages, disadvantages and design requirements have been noted. Some studies focused on utilising TEC to maintain the operating temperature of PV at a certain value in order to avoid the reduction in P_{max} and η_{PV}, but the cost and economic studies are missing.

The technology of integrating a PV cell with TEG is a promising technique to utilise a wide range of the solar spectrum and to remove the heat from PV cells. However, researchers have not studied the best technology for incorporation. In addition, the optimisation study of the PV/TEG hybrid system was in an open circuit condition, without experimental validation. Finally, some attempts have been made to integrate DSC with TEG in a hybrid system, but improving the thermal coupling between the counter electrode of the DSC and the TEG by using a metallic DSC has not been reported yet.

CHAPTER THREE – TESTING THE CANDIDATE PV CELL FOR INTEGRATING WITH TEG MODULES

3.1 Introduction

The objective of this chapter is to identify the types of PV cells that are suitable for developing PV/TEG hybrid systems. The ideal PV cell for such systems should have an efficiency that would not decrease with increasing temperature. This chapter describes the instruments and experimental setups established for studying the influence of temperature on the performance of six types of PV cells. A Peltier device was used to accurately control and stabilise the PV cell temperature. The level of light was kept constant at 1000 W/m^2 for charaterisation of each PV cell. The voltage (V) and current (I) were measured using an Auto Lab System. The temperature dependence of P_{max} and η_{PV} for six types of PV cells was investigated.

3.2 Sensors and Instruments

This section describes the key components and equipment employed for the study of temperature dependence of PV cells.

3.2.1 Solar simulator

A solar simulator type ABB (Oriel LCS-100 94011A) was used as the light source to provide the light in the experiments. The solar simulator was located inside a Faraday cage. A photograph for the solar simulator presented in Figure 3.1

Figure 3. 1 A photograph of the solar simulator

3.2.2 Pyranometer

A calibrated Kipp and Zonen pyranometer (CM11-SN-048544) was used to measure the light intensity, which was provided by the solar simulator. The distance between the pyranometer sensor and the solar simulator was calibrated to get 1000 W/m^2, before the PV cell placed for characterisation. A photograph for the pyranometer is shown in Figure 3.2.

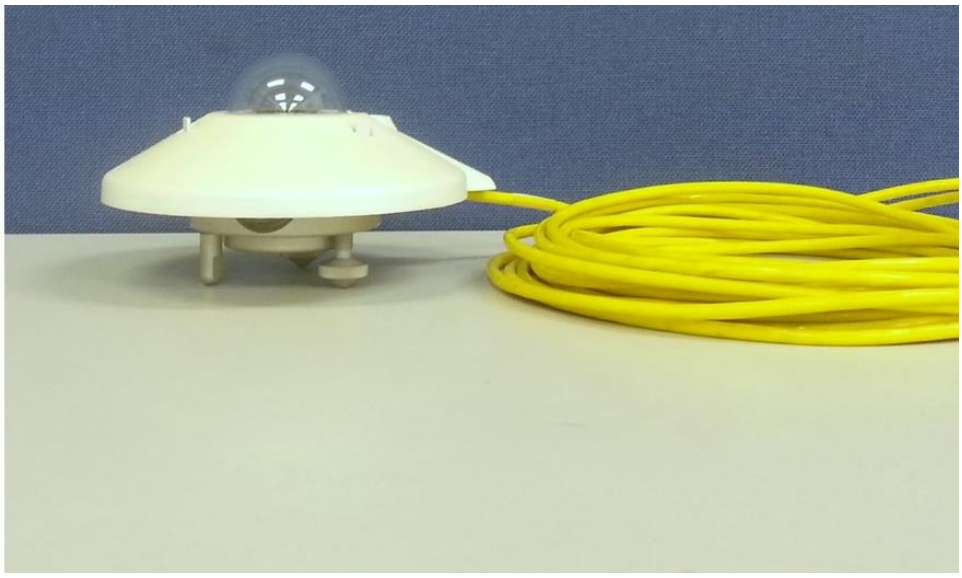

Figure 3. 2 Kipp and Zonen pyranometer

3.2.3 Peltier module

A Peltier module was used to control the temperature, for which characteristics are given in Table 3.1 and a photograph is shown in Figure 3.3.

Table 3. 1 Specifications of Peltier Device

Total area	40 mm X 40 mm
Number of elements	256
Cross section area of the element	1.4mmX 1.4mm
The length of the elements	1.2 mm

This device can function either as a cooler to keep the temperature of the PV cells at 25 ^{0}C or as a heater to increase the temperature of the PV cells up to 65 ^{0}C by reversing the polarity of Peltier device. A schematic diagram of the Peltier device circuit is shown in Figure 3.4.

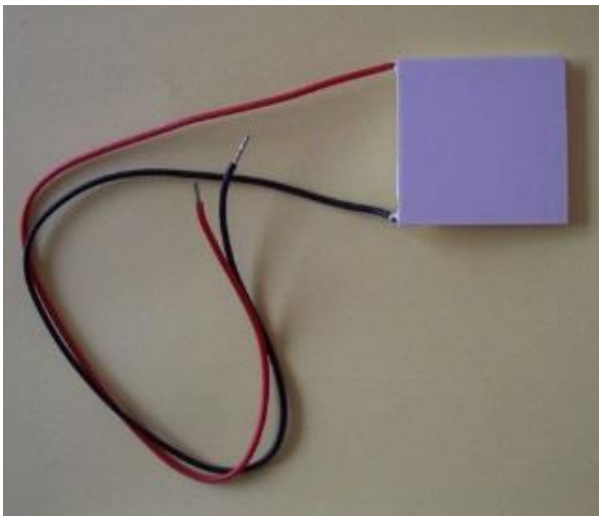

Figure 3. 3 Peltier device

The Peltier device was connected to a DC Power supply (EP-925). By changing the voltage of the power supply, the temperature of the PV cells that is mounted on the top surface of the Peltier module can be controlled.

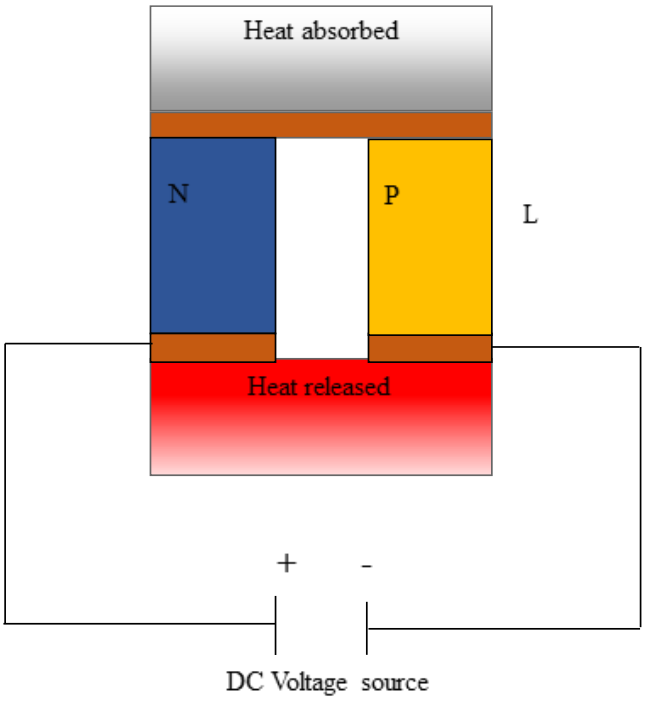

Figure 3. 4 Peltier device circuit

In order to dissipate the heat from the bottom side of the Peltier module effectively, the module is mounted on the top of heat exchanger.

3.2.4 Thermocouples

K-type thermocouples procured from RS Components, UK (RS 3630250) were used to measure the temperatures of the hot and cold sides of the PV/TE hybrid system. Also, the inlet and outlet fluid temperature in chapter five. The specifications of the thermocouple are shown in Table 3.2.

Table 3. 2 Specifications of K type thermocouples

Characteristic	Type K
Maximum Temperature	350 °C
Minimum Temperature	-60 °C
Termination Type	Miniature Plug
Cable Length	1m

The thermocouples were connected to an eight channel data logger (Pico technology limited, T-08 RS Components, UK 205-7572). Each channel was compatible with K-type thermocouples. The software package comes with the data logger, and the interface recorded the data to the computer. Figure 3.5 shows a photograph of the thermocouple sensors and data logger.

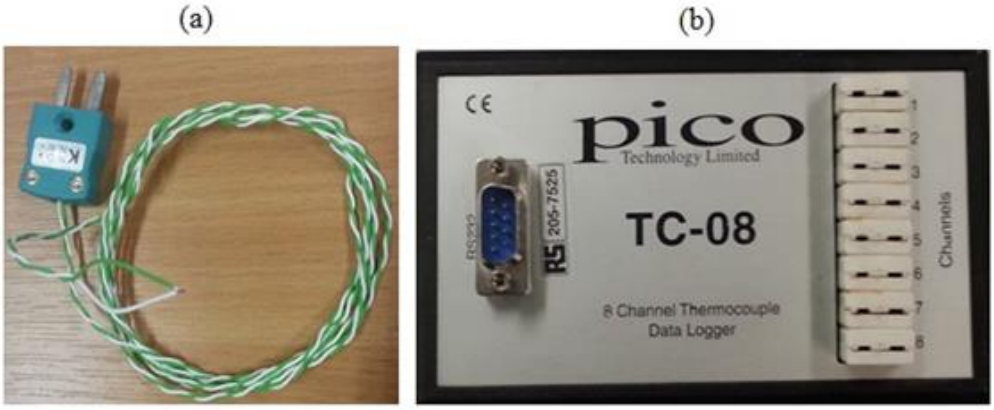

Figure 3. 5 Tools for temperature measurement; Thermocouple sensor (a), and data logger (b)

3.2.5 Heat Exchanger

A water-cooled aluminium heat exchanger (8 cm x 8 cm x 3 cm), as shown in Figure 3.6. It was used to take the heat away from the Peltier device by connecting it to tap water. A thin uniform layer of heat sink compound with a thermal conductivity of 2.9 W/m.K (RS-217-3835) used between the heat exchanger and the Peltier device.

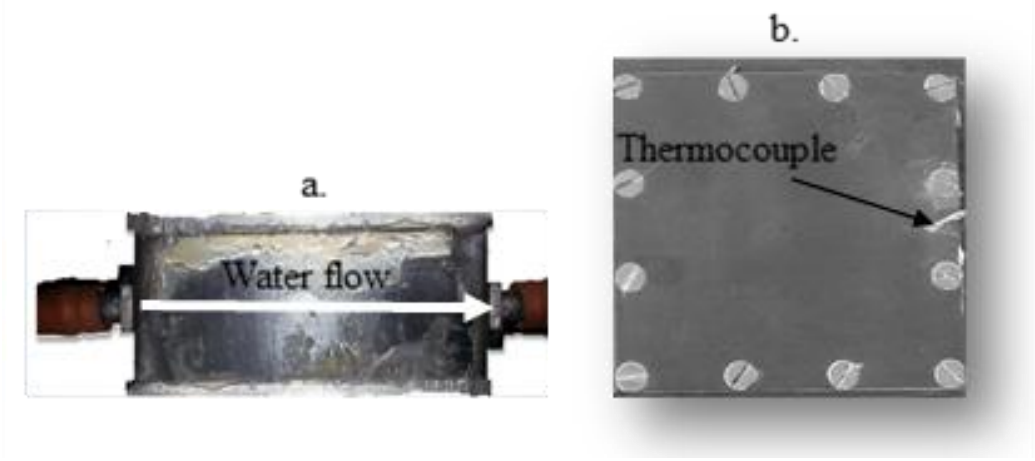

Figure 3. 6 Aluminium heat exchanger, (a) side view and (b) top view

3.2.6 AUTO LAB system

The AUTO LAB system was used to record the voltage and current of the I-V and P-V curves. The software provided with the AUTO LAB system facilitates easy setup of measurement requirements and record the data in Microsoft Excel. A photograph for the AUTO LAB and Faraday cage presented in Figure 3.7. An example of measurement commands is illustrated by a screenshot presented in Appendix.1, together with a measured I-V curve in Appendix.2.

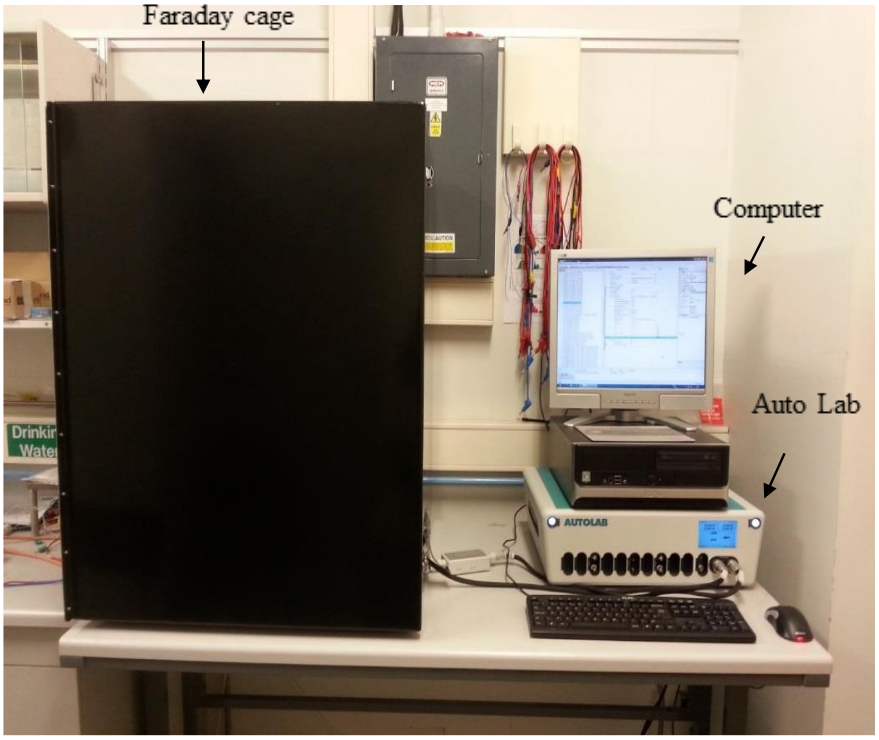

Figure 3. 7 A Photograph of solar simulator housed the Faraday cage and AUTO LAB system

3.2.7 PV cells

The PV cells investigated in this study include 4 types of commercial products: monocrystalline silicon (m-Si, Cheng Nuo Lamp Company), polycrystalline silicon (p-Si, GuangZhou Keaiwen Electronic Technology Company), amorphous silicon (a-Si, Trony-SC4040S-3NA) and copper indium selenium (CIS, MOPS-Electric,

271020888710). In addition, the cadmium telluride cells (CdTe), an early-stage prototype, was supplied by the Centre for Solar Energy Research in Glyndŵr University, Wales, UK. The dye-sensitised solar cells (DSCs) were prepared in-house at the Cardiff Thermoelectric Laboratory. Figure 3.8 shows an example of the active area (A_{act}) and total area (A_t) and a photograph of all 6 types of PV cells is presented in Appendix.3.

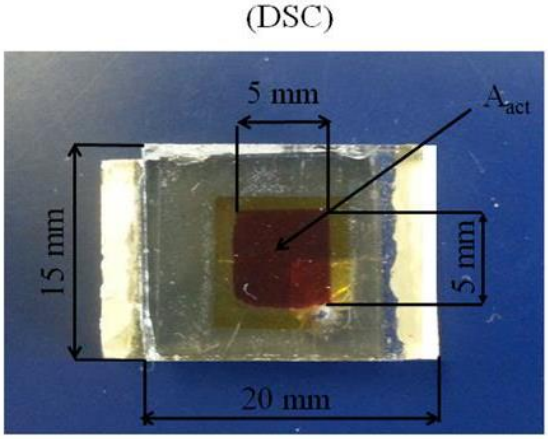

Figure 3. 8 A Photographs of (a) DSC; (b) m-Si showed the active area and total area

Table 3. 3 Specifications of the PV cells measured at standard test conditions

PV technology	A_{PV} (cm^2)	Active area (cm^2)	V_{OC} (V)	I_{SC} (mA)	FF (%)	η_{PV} (%)
m-Si	9	6.25	0.6	180	67.1	11.6
p-Si	20	12.95	1.8	130	77.4	14
a-Si	16	16	2.6	53.9	59.4	5.2
CIS	36	31.36	4.8	69	47.3	5
CdTe	30	25	4.1	64	46.7	4.9
DSC	3	0.25	0.78	3.1	41.4	4

Table 3.3 shows their specifications including the module area, active area, V_{OC}, I_{SC}, FF and η_{PV}.

3.3 Experimental setup

A schematic diagram of the experimental setup is shown in Figure 3.9 and a photograph in Figure 3.10. The PV cell absorbs the light from the solar simulator. Part of light is converted into heat in the PV cell, which can result in an increase in the operating temperature of the PV cell. In order to maintain the temperature of the PV unchanged, a temperature control system is employed which consists of a Peltier module and water heat exchanger. Two K-type thermocouples were used to measure the temperature of the PV cell. The top thermocouple was attached to the surface of the solar cell, or placed inside the glass electrode by drilling a hole from the side when possible. Another thermocouple was fixed inside a copper plate, which acted as a thermal conductor and homogeniser.

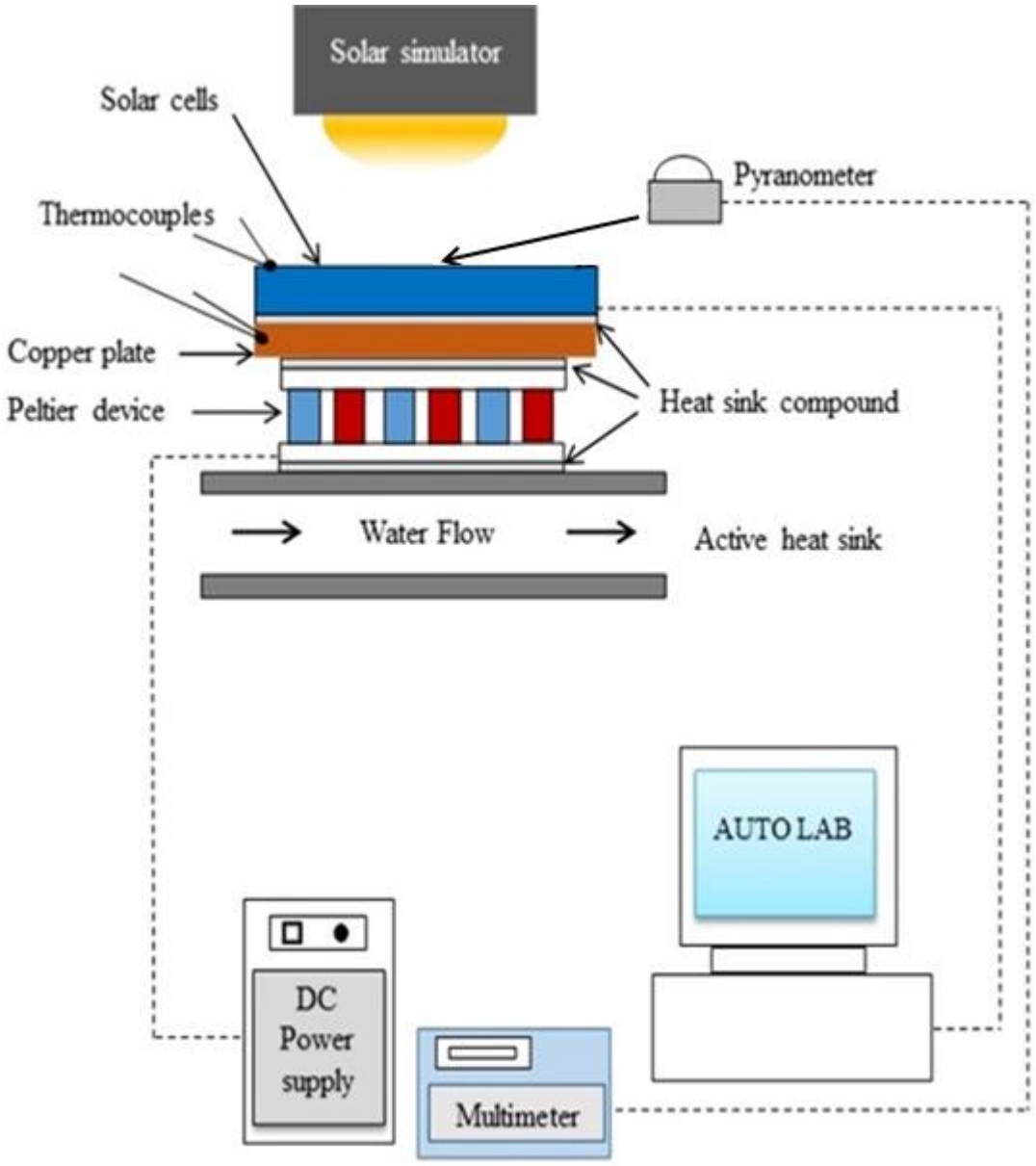

Figure 3. 9 Schematic diagram for experimental set up of the solar cell assembled with the Peltier cooling device

A thin uniform layer of heat sink compound was applied between the copper sheet and the rear of the PV cell to provide a good thermal contact. The operating temperature of the cell was considered to be the average of the two thermocouple measurements. A Peltier device was placed between the copper plate and the heat sink using the same heat sink compound. The I-V and P-V curves were obtained at stable PV cell temperatures of 25 °C, 35 °C, 45 °C, 55 °C and 65 °C.

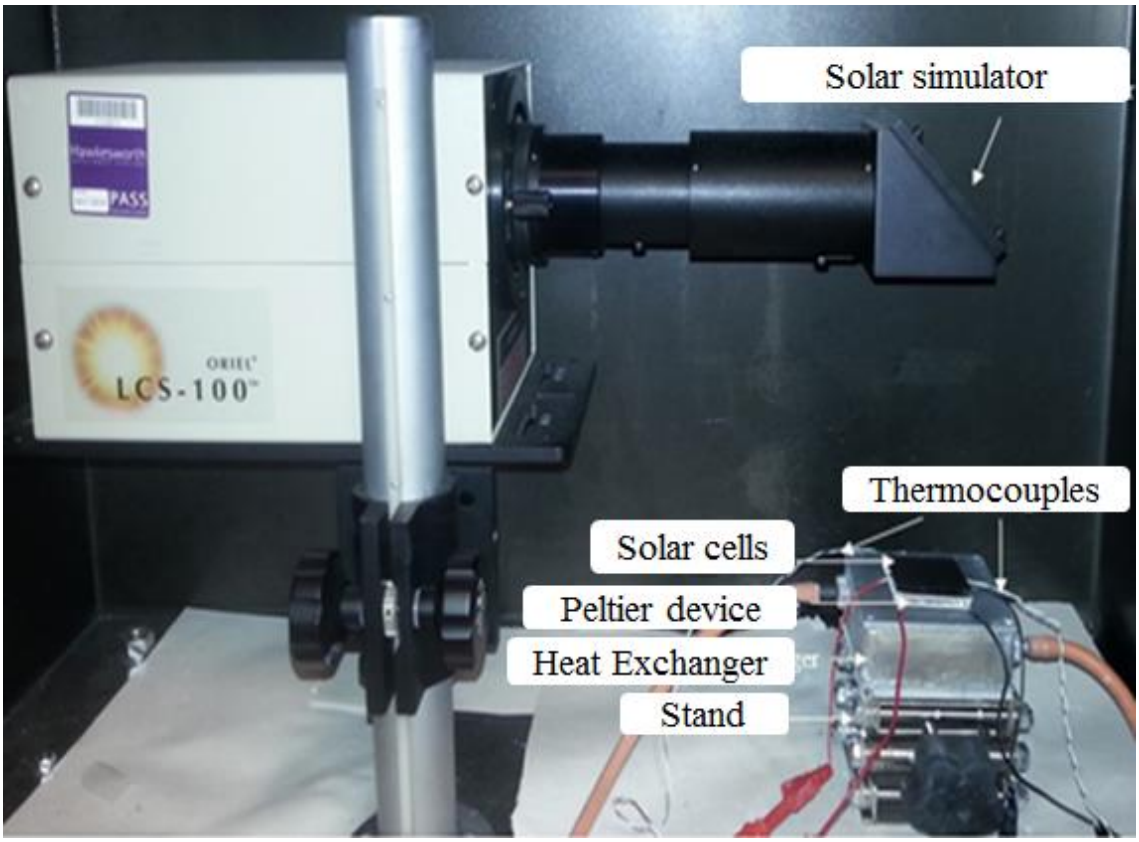

Figure 3. 10 A Photograph of the experimental set up of the solar cell assembled with the Peltier cooling device

3.4 Results and Discussion

The I-V curves for the 6 different types of PV cells are shown in Figure 3.11. It can be observed that increasing the operational temperature from 25 ^{o}C to 65 ^{o}C leads to a significant decrease in V_{OC} for all types and a slight increase in short circuit current (I_{SC}) except for DSC where, the I_{SC} was almost constant when the operational temperature increased from 25 ^{o}C to 45 ^{o}C than started to drop after the temperature passed 45 ^{o}C.

The decrease in V_{OC} results in a net reduction in P_{max} for all of the devices tested except for DSC, as shown in Figure 3.12.

In DSC, P_{max} increases with increasing temperature initially from 25 ^{o}C to 35 ^{o}C and then start to decreases with further increasing temperature.

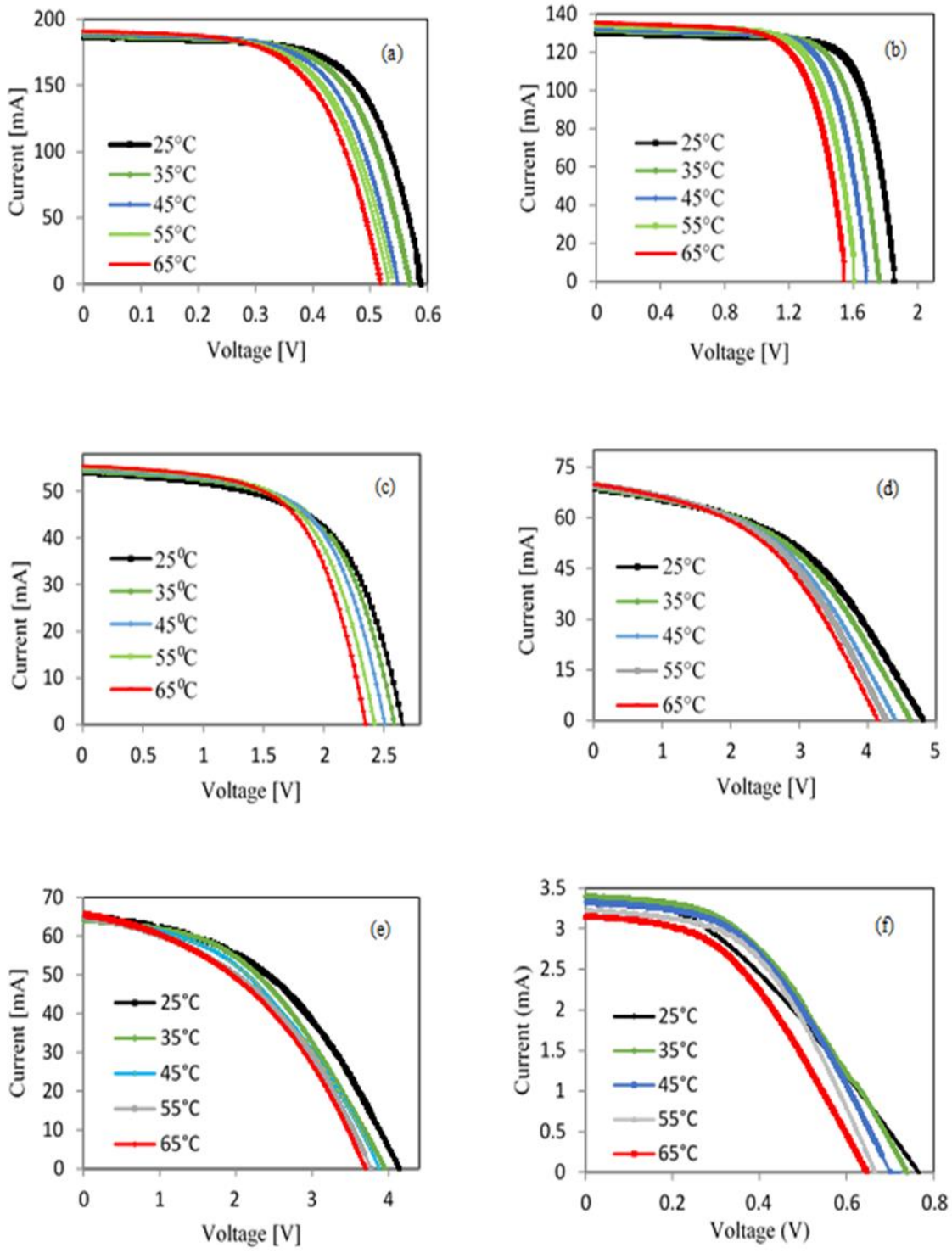

Figure 3. 11 I-V curves for (a) m-Si (b) p-Si (c) a-Si (d) CIS (e) CdTe and (f) DSC

This trend is unique and differs significantly from the other 5 types. It is thought that this is because the recombination losses stay constant for this period, and after that the change is started when the temperature became over 45 ^{o}C.

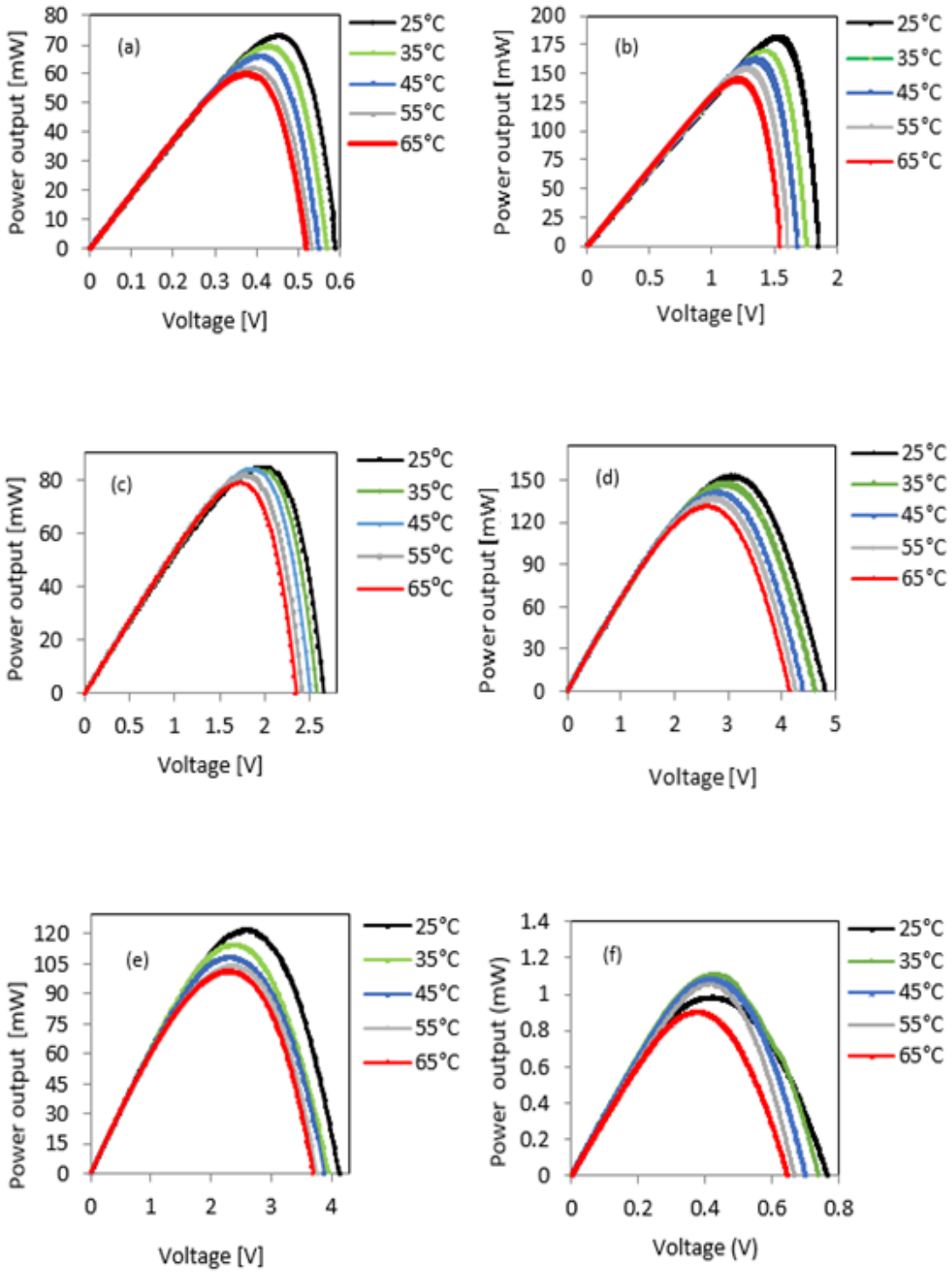

Figure 3. 12 P-V curves for (a) m-Si (b) p-Si (c) a-Si (d) CIS (e) CdTe and (f) DSC

The temperature dependence of the P_{max} in a solar cell is usually measured so-called the temperature coefficient, which is defined by [30]:

$$\frac{1}{P_{max}}\frac{\Delta P_{max}}{\Delta T} \qquad 3.1$$

It was found that the values determined from our experiment for m-Si (0.45 % / K) and p-Si (0.51 % / K) were in good agreement with the published data of the crystalline solar cells (0.65 %/K) [30].

The temperature dependence of I_{SC} and V_{OC} for different cells can be better illustrated by plotting them as a function of temperature as shown in Figure 3.13. It can be seen that an increase in the temperature caused a decrease in the V_{OC} for all PV cells. However, there was a slight increase in I_{SC} for all the PV cells except for DSC where it stayed constant from 25 ^{o}C to 45 ^{o}C and then decreased.

The P_{max} as a function of temperature for each PV cell was measured three times and the three measurements are presented in Figure 3.14. The standard deviation of the P_{max} output was calculated using the following equation [98]:

$$\sigma = \sqrt{\frac{1}{M}\sum_{i=1}^{M}(x_i - \bar{x})^2} \qquad 3.2$$

where, σ is the standard deviation, M is the number of measurements, x_i is the element and $\bar{x}$ is the mean of the measurements. Table A.4 in Appendix.3 presents the standard deviation associated with the measurement of the P_{max} for each type of PV cells over the temperature range: 25 ^{o}C, 35 ^{o}C, 45 ^{o}C, 55 ^{o}C and 65 ^{o}C. The results show that the data presented exhibits good repeatability.

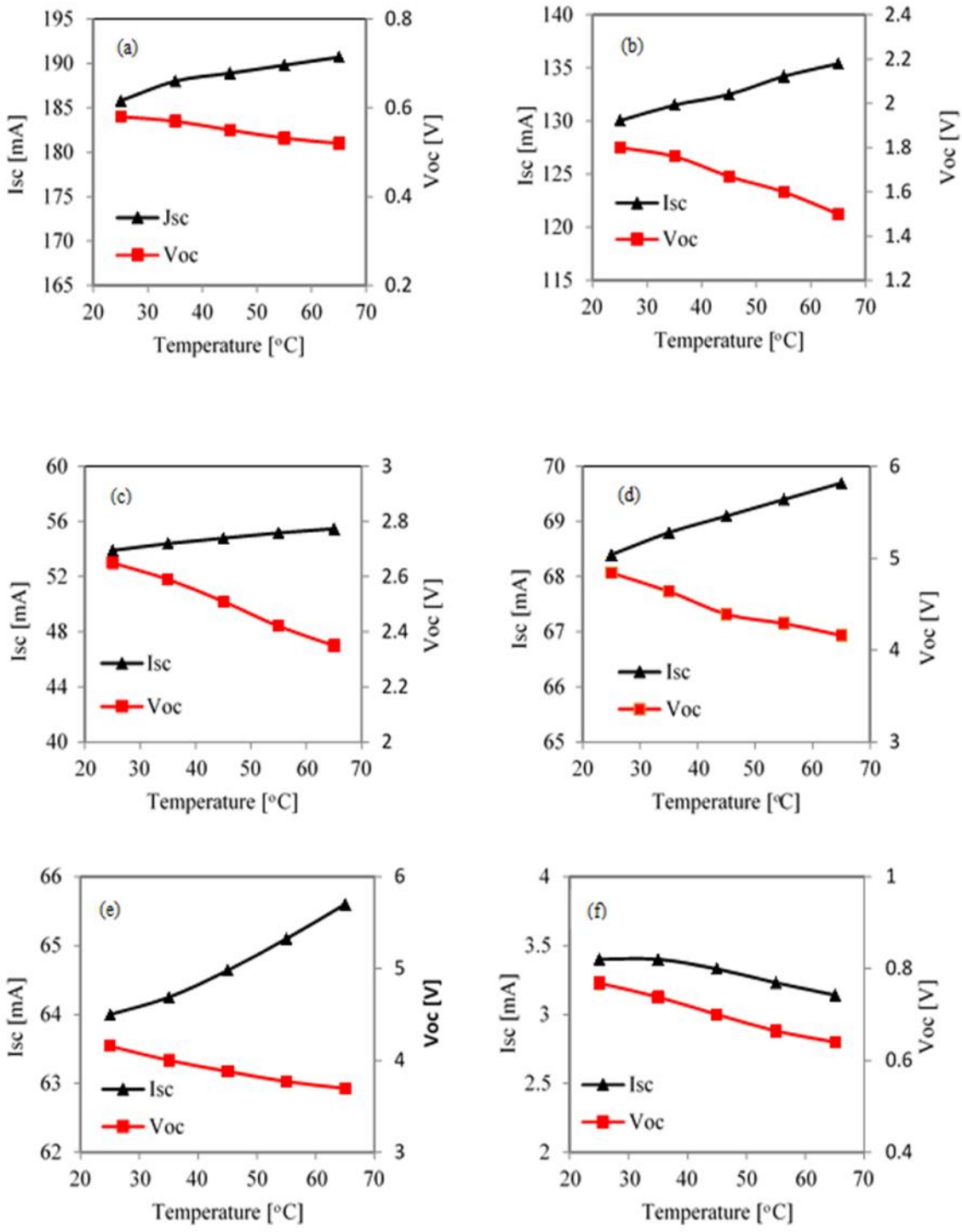

Figure 3. 13 I_{sc} & V_{oc} curves for (a) m-Si (b) p-Si (c) a-Si (d) CIS (e) CdTe and (f) DSC

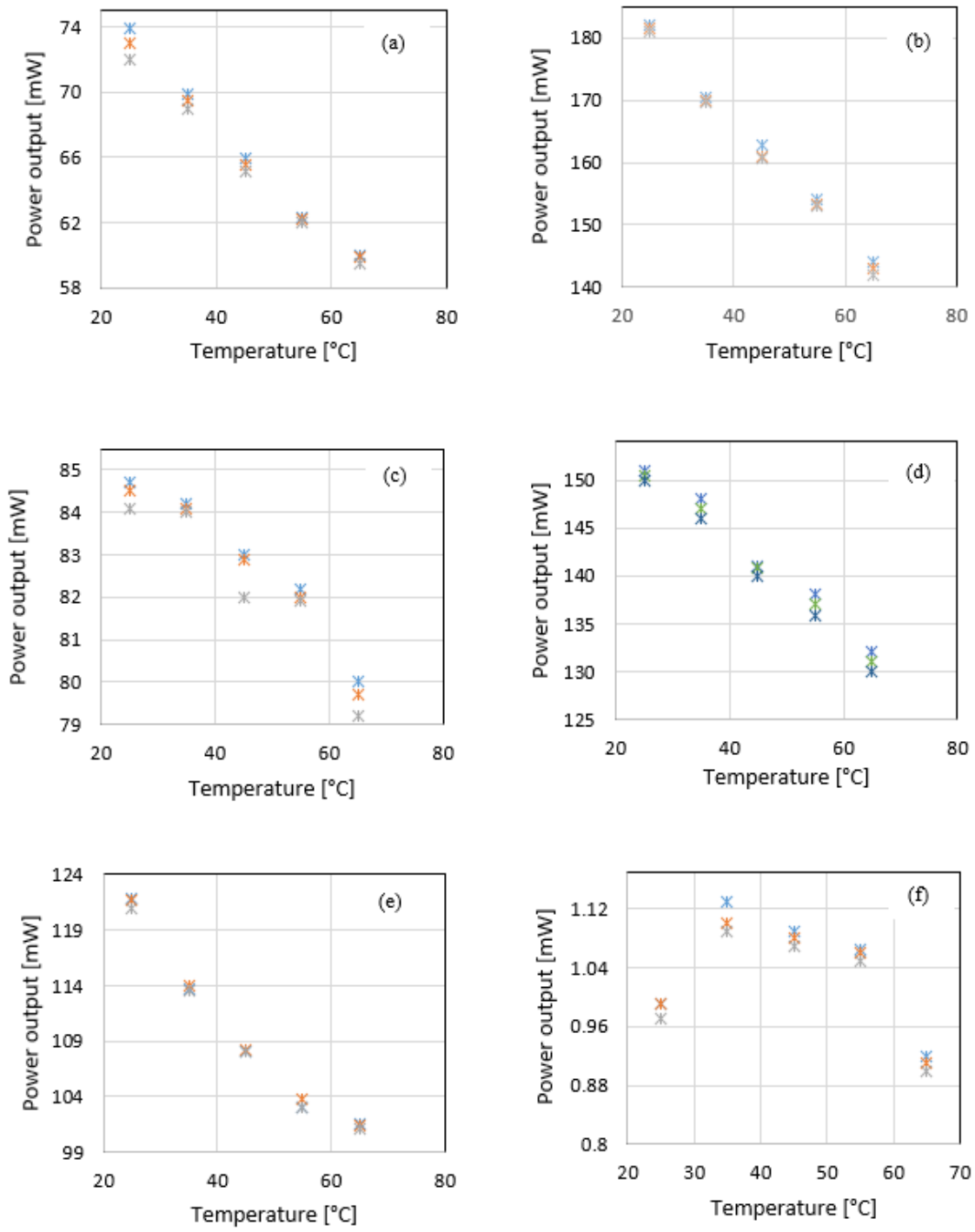

Figure 3. 14 The maximum power output as a function of temperature for (a) m-Si (b) p-Si (c) a-Si (d) CIS c) CdTe and (f) DSC, with each type of cells were measured three times.

It can be seen that the maximum power output of all types of PV cells except for DSC decreases with decreasing temperature almost linearly. The average rate of decrease in P_{max} was calculated over three ranges of temperatures as presented in Table 3.4. The first

range was (25 ^{o}C- 45 ^{o}C), where p-Si presented the quickest drop in P_{max}. This indicates that p-Si is the worst type of solar cells for use in a PV/TEG hybrid system because of significant power loss at higher temperatures required by efficient operation by TEG.

The DSC samples showed an interesting increase in P_{max} by 9.8 % when the temperature was close to 45 ^{o}C. This increase in the P_{max} of DSC makes it a suitable candidate for integration with TEG, which indicates that the hybrid system would gain the power from both the PV cell and the TEG over this range. The second range is 45 ^{o}C- 65 ^{o}C and DSC showed significant drop in P_{max} of -16.3 % after the P_{max} reached the maximum at 45 °C. The slope of the DSC was found to be close to the slop in reference [99]. The overall reductions in the investigated temperature range (25 ^{o}C- 65 ^{o}C) were also calculated. It can be seen that the P_{max} of the m-Si cells dropped significantly by 18 %. The p-Si device exhibited a higher drop in P_{max} of 21.2 %. The a-Si sample demonstrated the least temperature sensitivity of the samples tested (84.5– 9.70 mW, 5.7 %). For CIS cells P_{max} dropped by 13.3 % and the CdTe sample reduced by 16.7 %. Finally, the overall drop of P_{max} in DSCs over 25 ^{o}C- 65 ^{o}C is 8.1% due to a significant decrease (-16.3%) over the temperature range 45 ^{o}C- 65 ^{o}C, despite it increased by 9.8% over the temperature range 25^{o}C-45^{o}C

Table 3. 4 The drop in Pmax for the six solar cells in three regions

Temperature range [°C]	m-Si	p-Si	a-S	CIS	CdTe	DSC
25-45	-10.2%	-11.0%	-2.1%	-6.7%	-10.5%	**+9.8%**
45-65	-8.7%	-11.5%	-3.6%	-7.1%	-6.3%	-16.3%
25-65	-18.0%	-21.2%	-5.7%	-13.3%	-16.7%	-8.1%

The mean values of P_{max} were used to calculate the normalised P_{max} (or the power density) in Figure 3.15, the FF in Figure 3.16 and the η_{PV} in Figure 3.17. The normalised P_{max} was calculated by dividing the mean value of P_{max} (mW) of the cells by the active area of the PV cell (cm^2). Due to the size difference in the PV cells employed for this study, the normalised P_{max} provides a fair comparison among all types of the PV cells investigated. It can be seen from Figure 3.15 that all types of PV cells exhibited a linear decreases in the normalised P_{max} except for DSC, which reaches a maximum around temperatures of 40 ^oC.

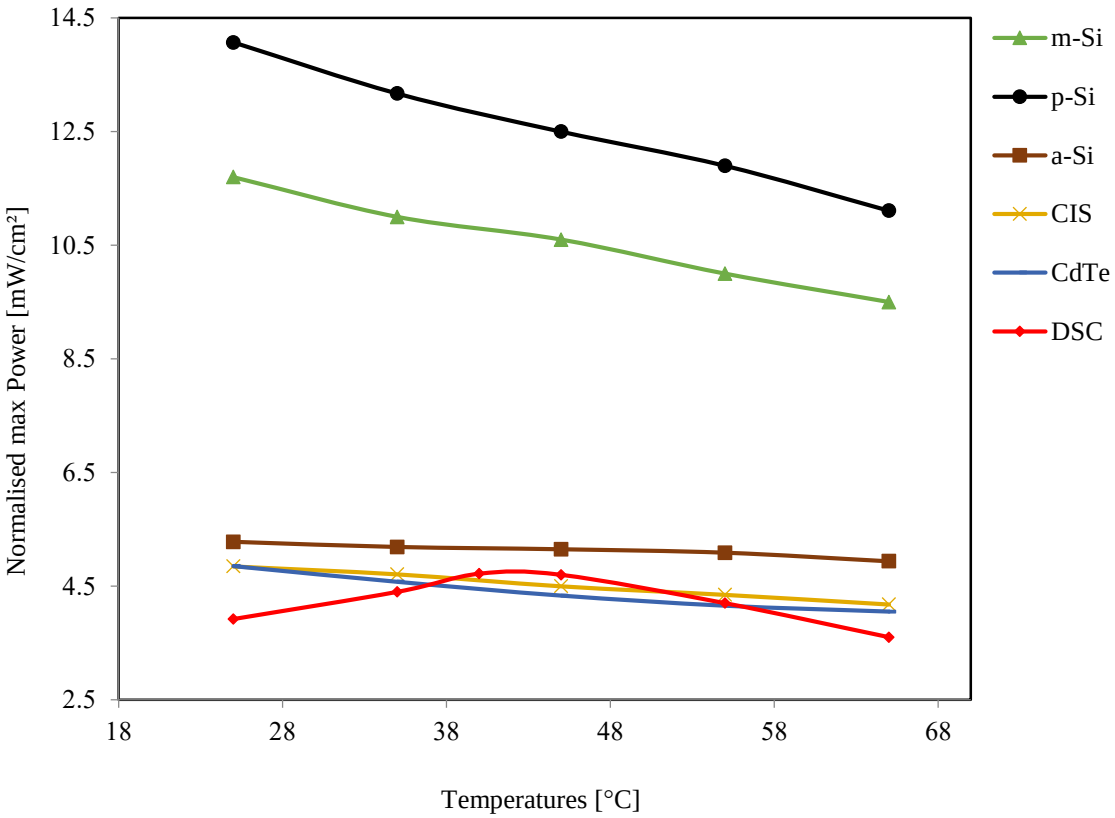

Figure 3. 15 Normalised maximum power as a function of temperature for 6 different types of PV cells

Similarly, the variation in FF and η_{PV} as a function of temperature are almost linear except for DSC, as shown in Figures 3.16 and 3.17, respectively.

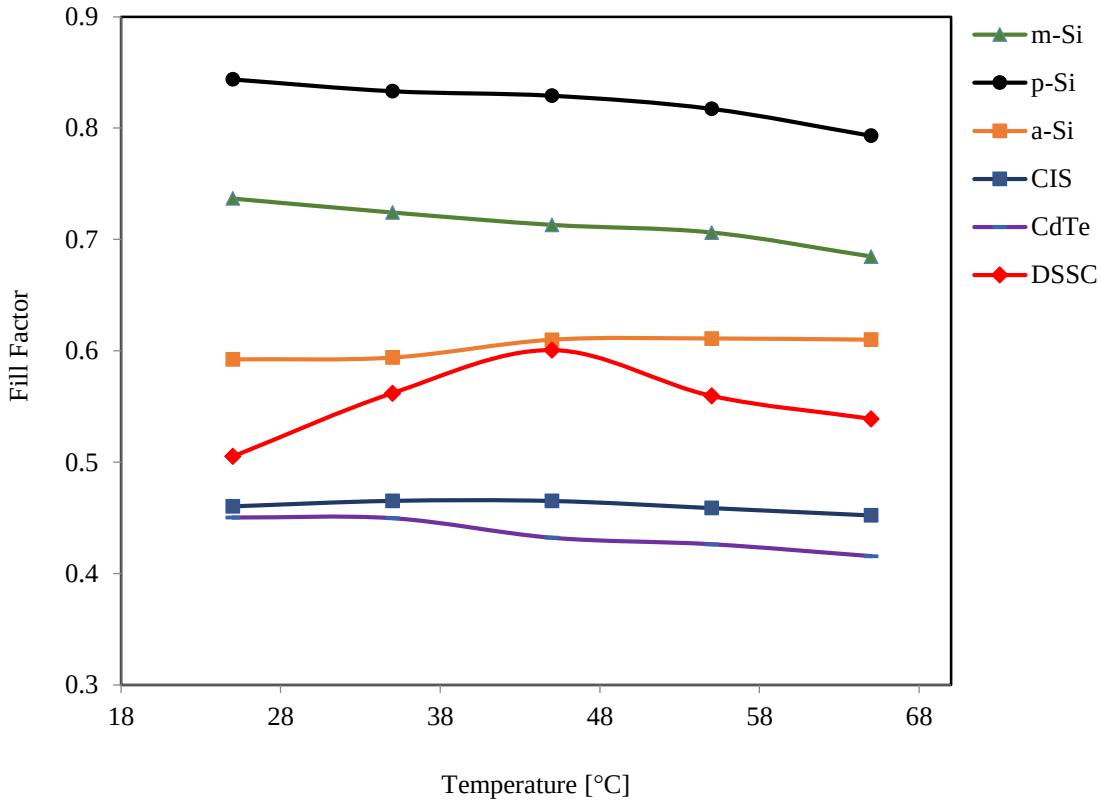

Figure 3. 16 Fill Factor as a function of temperature for m-Si, p-Si, a-Si, CIS, CdTe and DSC

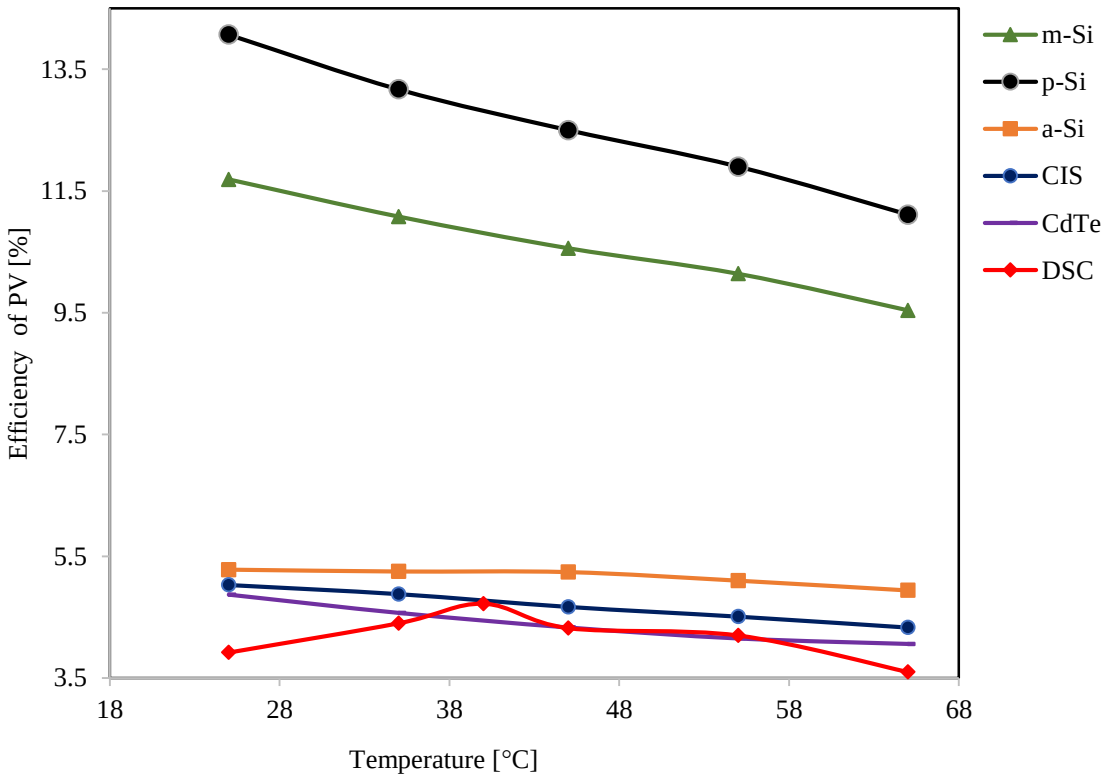

Figure 3. 17 Efficiency as a function of temperature for m-Si, p-Si, a-Si, CIS, CdTe and DSC

The FF of DSC increases with increasing temperature until reaching a maximum value at around 40 ^{o}C, and then decreases with further temperature increase. Based on this result, together with the data presented in Figure 3.13, it can be concluded that the unique temperature coefficient of DSC observed can be attributed to its temperature dependence on FF.

For each type of the PV cells, the η_{PV} decreases with increasing temperature (except for DSC). In general, this observation can be explained in terms of the kinetics of carrier recombination which increases under illumination at higher temperatures, resulting in a reduction in η_{PV} [33].

This different trend of DSC makes it a good candidate for integration with TEG because this type of solar cell will not lose too much power when the operating temperature increases due to the thermal resistance created by adding the TEG [100]. Although a-Si cells exhibit a decrease in the power output and the efficiency with increasing temperature, the rate of decrease is much lower than these of crystalline silicon solar cells. Therefore, they might be employed for integration with TEGs to develop PV/TEG hybrid system.

On the othe hand, P-Si exhibits the highest drop in efficiency with an increase in temperature, making this type of solar cell the worst for integration with TEG. This is because, the PV cells would lose more power than that which could be generated from TEG. The decrease in the slope ($\frac{\Delta_{\eta PV}}{\Delta_T}$) for crystalline solar cells was 0.06 (%/K) and it was found to be in reasonably good agreement with the value reported in [30], which was 0.08 (%/K).

3.5 Conclusions

In this study, experimental investigation on the temperature dependence of P_{max} and η_{PV} were carried out in order to identify suitable PV cells for the development of PV/TEG hybrid system. A total of 6 types of PV cells were investigated. The results show that the power output and efficiency of DSCs increases with increasing operating temperature over the range 25 ^{o}C-45 ^{o}C. This unique behaviour makes DSCs a promising candidate for the proposed PV/TEG hybrid system. Crystalline silicon cells exhibit the most significant reduction in P_{max} and $\eta_{PV,}$ making them unsuitable for PV/TEG system. Similarly, the power output and efficiency of a-Si solar cells decrease with increasing temperature. However, the rate of decrease in a-Si cells is much slower than that of crystalline silicon solar cells. Consequently, a-Si cells may also be employed in a PV/TEG system to produce a net improvement. In conclusion, the experimental results obtained from this work indicate that it is feasible to integrate either DSC or a-Si with TEG in a hybrid PV/TEG system. This will enable thermoelectric power generation using the waste heat from PV cells and the heat associated with light energy in the infrared region of the solar spectrum without causing a power reduction in the PV cells due to operating at an elevated temperature. The next chapters will discuss the integration of a-Si and DSC solar cells with TEG in details.

CHAPTER FOUR – GEOMETRY OPTIMISATION OF TEG IN HYBRID PV/TEG SYSTEM

4.1 Introduction

The geometry of TEG in a PV/TEG system plays an important role in controlling the operating temperature of the PV cell and the temperature difference across the TEG, which has significant influence on the performance of both PV cell and TEG. In this chapter, a model is developed for optimising the geometry of TEG in a PV/TEG system. The model can be used to determine the optimal thermoelement length and cross-sectional area, at which the maximum power output (P_{max}) would be achieved. The effect of the thermoelement length and cross-sectional area on the P_{max} of TEG, the PV cells, and the total power was studied, and the influence of thermoelement length and cross-sectional area on the conversion efficiency of TEG, PV cell and overall efficiency was analysed. This chapter also includes an experimental study that was conducted to validate the model. A PV/TEG system with 6 different TEG geometries was constructed. The performance of this hybrid system was investigated and compared with the theoretical simulation.

4.2 Model Outline

A hybrid PV/TEG system is shown schematically in Figure 4.1. It consists of a PV cell connected to a TEG via a copper plate that serves as a thermal concentrator. The interfaces were filled with thermally conductive paste to ensure good heat transfer across these interfaces. The copper plate forms the hot side of the TEG, with the cold side of the TEG is attached to a heat exchanger with water circulating through it. The advantages of such

a hybrid system are that the operating temperature of the PV cell will be reduced due to the transfer of heat into the TEG, and the TEG will generate additional power due to the temperature difference (ΔT) established across it.

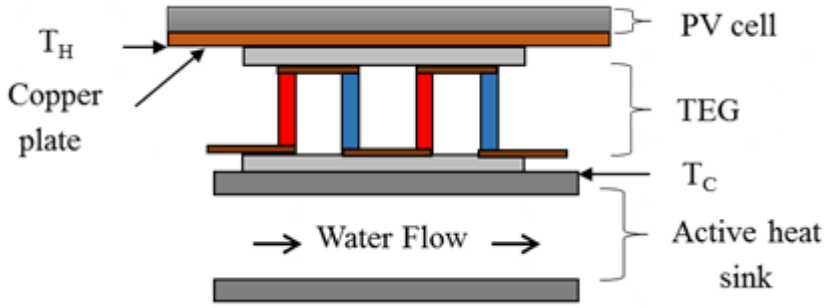

Figure 4.1 A schematic diagram of the hybrid PV and TEG system

In this hybrid system, the thermal energy generation and flow is considered as follows: The rate of solar energy available to the PV cell is equal to the heat losses from the PV and electrical power generation, thus:

$$\tau_g[\alpha_c\beta_c G + \alpha_T(1-\beta_c)G)]A_{PV} = Q_c + Q_r + Q_k + P_{PV}, \quad (4.1)$$

where, τ_g is the transmissivity of the glass, β_c is the packing factor, α_c is the absorptivity of the PV cell, α_T is the absorptivity of the tedlar (tedlar is a thin layer of polyvinyl fluoride is used for insulation and protection of the PV cell [101]), G is the solar radiation intensity and A_{PV} is the device area of the PV cell. On the right side of Equation 4.1, Q_c denotes the convective heat loss from the surface of the cell, Q_r is the radiative heat loss, Q_k is the heat conducted from the PV cell to the TEG, and P_{PV} is the electrical power generated by the PV cell [64][102]. The heat loss from the PV cell to the ambient air due to convection and conduction is given by:

$$Q_{c=}U_t A_{PV}(T_{cell}\text{-}T_{amb}), \quad (4.2)$$

where T_{cell} and T_{amb} represent the solar cell and ambient temperatures respectively. U_t is the heat transfer coefficient from the PV to the ambient air by convection and conduction [88]:

$$U_t = \left(\frac{L_g}{K_g} + \frac{1}{h_{cov}}\right)^{-1}, \tag{4.3}$$

where, L_g and k_g are the length and thermal conductivity of the glass respectively. h_{cov} is the convective heat transfer coefficient [103]. Radiative heat loss from the PV cell is described by:

$$Q_r = \varepsilon\sigma A_{PV}(T_{cell}^4 - T_{amb}^4), \tag{4.4}$$

where, ε is the surface emissivity of the cell and σ is the Stefan-Boltzmann constant. Heat conducted from the PV cell into the TEG is given by

$$Q_k = \frac{kA_{TE}N(T_{cell}-T_C)}{L_{TE}}, \tag{4.5}$$

where, k is the thermal conductivity of the thermoelectric material, A_{TE} is the cross-sectional area of thermoelements, N is the number of thermoelements and L_{TE} is the length of thermoelements. ΔT is the temperature difference across the TEG. It is assumed for simplicity that the effect of the solder and copper contacts has a negligible effect and consequently, ΔT can be approximated by ($T_{cell} - T_C$) if the TEG operates in open-circuit (where, T_C is the temperature at the cold side of the TEG).

An important distinction is required here, as ΔT makes no reference to whether or not the TE device is in the open-circuit condition or the closed-circuit condition. In all previous studies, the power output of the TEG was calculated using a ΔT that corresponds to open-circuit condition. This can introduce significant error because the ΔT across a TEG at

closed-circuit differs significantly from that at open-circuit. Figure 4.2 shows the drop in the ΔT and voltage due to the closed circuit which is shown in Figure 4.3.

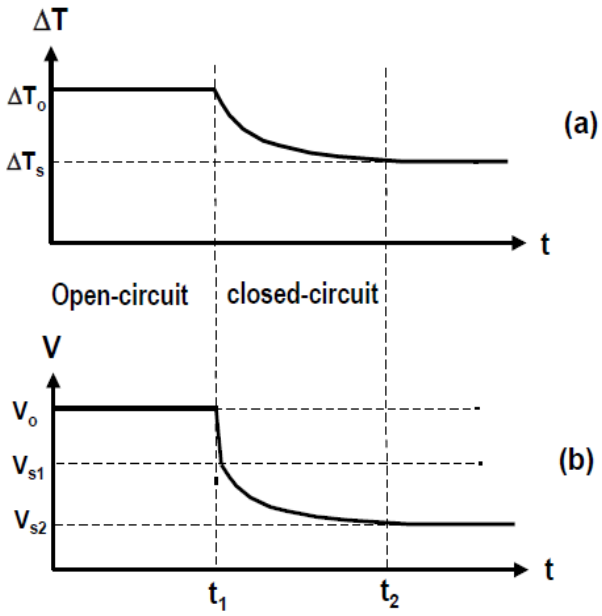

Figure 4.2 Schematic transient processes in thermoelectric materials with open circuit and short circuit: (a) Temperature difference; (b) Voltage across the specimen [104]

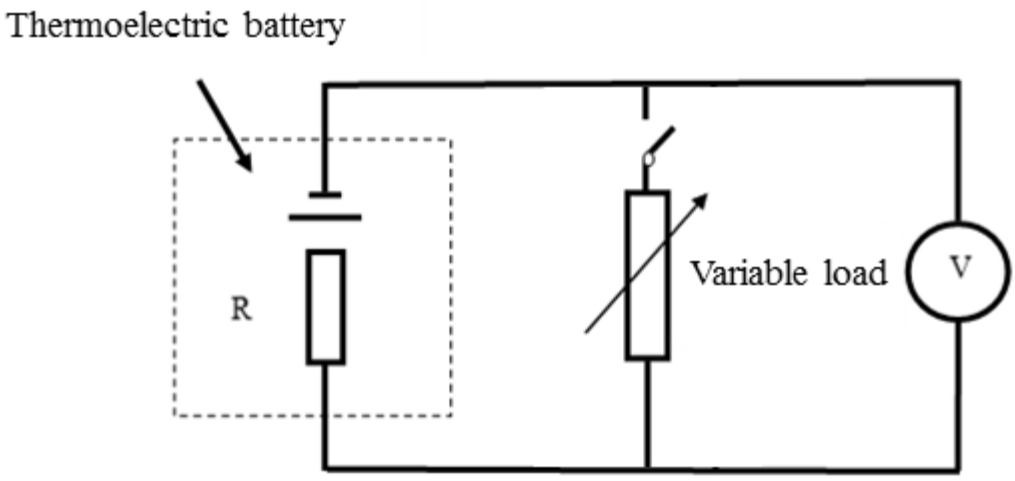

Figure 4.3 An equivalent electrical circuit for the thermoelectric generator

In a real system, TEG has to operate in the closed-circuit condition in order to deliver the power to external load.

Under such circumstances, the heat flow through the TEG consists of both heat conduction and the Peltier heat. As a result, the ΔT in Eq. (4.5) should be replaced by [44][104]

$$\Delta T = (1 + ZT_M)(T_{cell} - T_C) \tag{4.6}$$

where, Z $(= \alpha^2/\rho.k)$ is the thermoelectric figure of merit, α is the Seebeck coefficient, ρ is the electrical resistivity, T_M is given as

$$T_M = \frac{(1+2s)T_h+T_C}{2(1+s)^2}, \tag{4.7}$$

where, s is the ratio of the load resistance to the internal resistance of the TEG module.

Using Equation (4.6) to replace ($T_{cell} - T_C$) in Equation (4.5), with s=1 (i.e., operating under the matched-load condition) and assuming the hot side temperature of the TEG module is equal to the PV cell temperature, T_{cell}, Equation (4.5) can be written as:

$$Q_k = \frac{k \cdot A_{TE} \cdot N \cdot [1+\frac{Z(3T_{cell}+T_C)}{8}] \cdot (T_{cell}-T_C)}{L_{TE}}, \tag{4.8}$$

The power output of the TEG, with taking into account the electrical and thermal contact resistances, can be expressed as [105]

$$P_{TE} = \frac{\alpha^2.A_{TE}.N.(\Delta T_C)^2}{2.\rho.(n+L_{TE}).\left(1+\frac{2.r.L_C}{L_{TE}}\right)^2}\ , \tag{4.9}$$

Where, L_C is the thickness of the ceramic plates on the TEG. The variables n and r are the electrical and thermal contact parameters, which correspond to the ratio of the bulk material electrical resistance and thermal conductivity to that of the contacts, respectively [105].

Figure 4.4 shows visually the N, L_{TE} and L_C parameters of a TEG module.

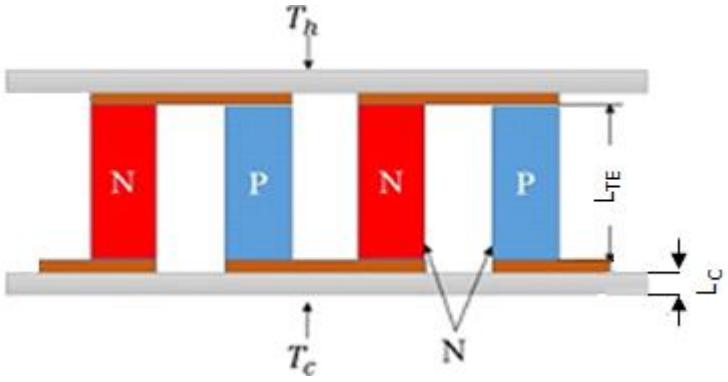

Figure 4.4 Schematic diagram showing two thermoelements

From Equation (4.8) and Equation (4.9), the conversion efficiency of the TEG, η_{TE},can be calculated by

$$\eta_{TE} = \frac{P_{TE}}{Q_k}. \tag{4.10}$$

The power output, P_{PV}, of the PV cell can be given as:

$$P_{PV} = \eta_{PV}\tau_g A_{PV} G\ , \tag{4.11}$$

Where, η_{PV} denotes the efficiency of the PV cell. It varies with temperature and can be expressed as [106]

$$\eta_{PV} = \eta_0[1 - \beta_0(T_{cell} - 298)] \tag{4.12}$$

where, η_0 is the efficiency of PV module at 25 °C, and β_0 is the temperature coefficient for silicon solar cells. As a result, the total power output, P_{tot}, from the PV/TEG hybrid system is calculated as;

$$P_{tot} = P_{PV} + P_{TE}\ , \tag{4.13}$$

Consequently, the overall efficiency of the hybrid system, $\eta_{tot,}$ can be obtained as:

$$\eta_{tot} = \frac{P_{PV}}{\eta_{PV}\tau_g A_{PV} G}, + \eta_{TE} \frac{1}{1+(\frac{Q_c+Q_r+P_{PV}}{Q_k})} \quad (4.14)$$

Employing appropriate operating parameters for the hybrid PV/TEG system shown in Figure 4.1, the temperature of the PV cell and the temperature difference across the TEG can be calculated using an iterative method based on Eqs. (4.1) – (4.8). The power output and conversion efficiency of the system can be determined using Eqs. (4.9) – (4.14). Consequently, the optimal geometry of the TEG can be achieved by investigating the dependence of the efficiency on the geometrical factors

4.3 Simulation procedure and input parameters

Simulation was performed to demonstrate the capability of the model for optimal design of hybrid PV/TEG system. A total of 8 types of TEG modules were chosen to study the dependence of the maximum power output on the geometry of TEG modules. Each type of the module has the same number of N and A_{TE}, but the length of the thermoelements was varied to obtain the maximum power output (P_{max}). The number of thermoelements (N) and the cross sectional areas (A_{TE}) employed in these modules are shown in table 4.1.

The simulation used a Matlab® programme (Appendix.5) to determine T_{cell} by solving equations (1) – (8) iteratively. Once T_{cell} is determined, the P_{TE} and η_{TE} in closed-circuit condition can be calculated using equations (4.9) and (4.10), respectively. The power output P_{PV} and η_{PV} of the solar cell are calculated using equations (4.11) and (4.12), respectively. Finally, the total power output P_{tot} and conversion efficiency η_{tot} of the hybrid system can be determined using equations (4.13) and (4.14), respectively. The parameters employed for the calculation were given in Table 4.2. The assumptions used are as follows:

1) The cold side of the TEG is maintained constant at room temperature (298K);

2) The intensity of solar radiation is maintained at 1000 $W.m^{-2}$, equivalent to 1 sun of radiation flux;

Table 4.1 Geometric parameters of the modules investigated

Module Type	**N**	**A_C [mm^2]**
I	62	0.64
II	62	1.44
III	62	1.96
IV	62	2.56
V	100	2.56
VI	150	2.56
VII	200	2.56
VIII	250	2.56

3) Heat transfer occurs in one dimension only, i.e., there is no heat transfer in lateral direction;

4) The η_{PV} of PV cell is 10 % at 25 ^oC and changes with temperature following equation (4.12) with the temperature coefficient listed in Table 4.2.

The simulations were carried out in two different atmospheres: the ambient and the vacuum. The calculation was carried out using type I module listed in Table 1 for an ideal operating condition where all heat losses are neglected. The results are identical for both procedures, indicating the validity of essential part of the model [44].

Table 4.2 Parameters used for simulation

Parameter	Value	Unit	Reference
τ_g	0.95	--	[88]
a_c	1	--	
β_c	1	--	
β_0	0.0011	K^{-1}	[107]
a_T	0.5	--	[88]
A_{PV}	40x40	mm^2	
h_{cov}	5	$Wm^{-2}K^{-1}$	[103]
T_{amb}	298.15	K	
ε	0.88	--	[88]
k	1.5	$W.m^{-1}K^{-1}$	[108]
k_g	1	$W.m^{-1}K^{-1}$	[64]
α	185	μVK^{-1}	[108]
ρ	1×10^{-5}	$\Omega.m$	[108]
n	0.0001	m	[34]
r	0.2	--	[34]
l_c	0.00009	m	
L_g	0.003	m	[64]

4.4 Results and discussion

Figure 4.5 shows the P_{TE} as a function of L_{TE} for modules with different sizes as described in Table 4.1. The results were obtained for operation in atmosphere (i.e., non-vacuum).

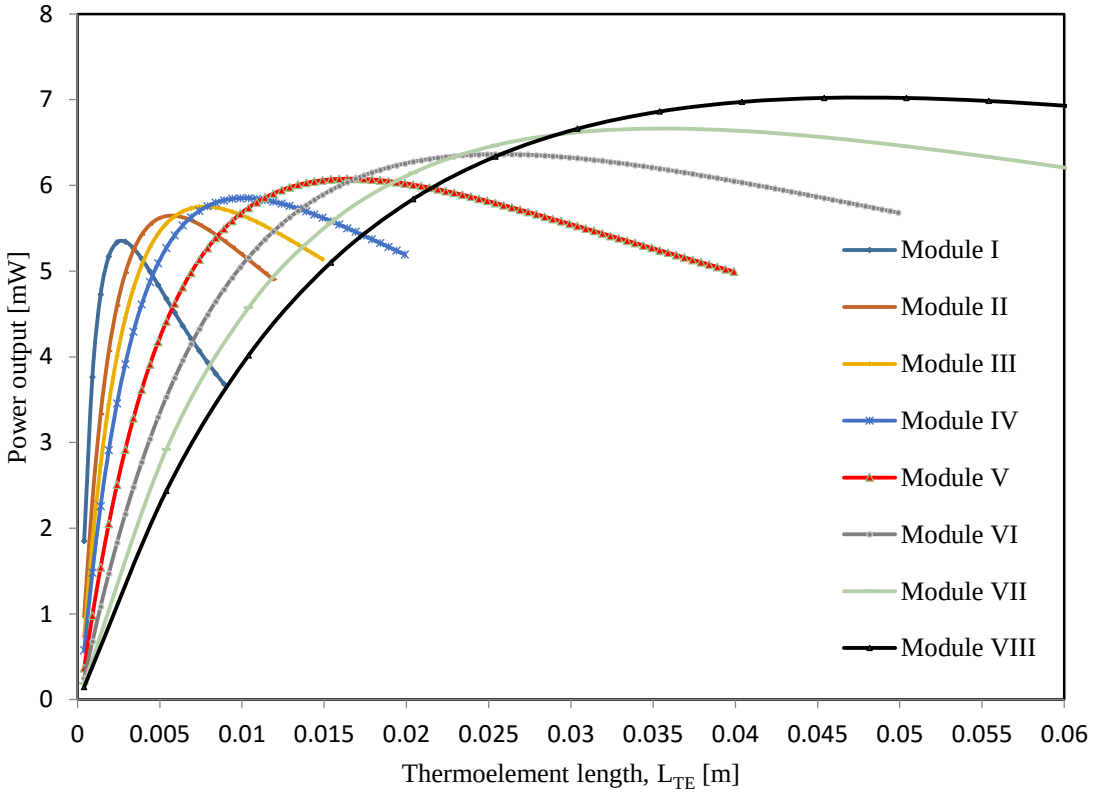

Figure 4.5 Power output vs thermoelement length for system operating within an ambient atmosphere

It can be seen that the P_{TE} for a given type of module increases initially with an increase in L_{TE} until reaching the P_{max} at an optimal length and then the P_{TE} starts to decrease with a further increase in L_{TE}. The results show clearly that it is necessary to design a TE module with the optimal length in order to obtain the P_{max}. It can also be seen that the P_{max} is higher for the modules that have larger N and A_{TE}. However, the optimal length required for the modules with larger N and A_{TE} is longer. This indicates that an increase in the power output is obtained at an expense of material consumption. For example, the optimal length for type VIII is 50 mm, compared with 3.4 mm for type I (i.e., a factor of

14), while the P_{max} is only increased from 5.2 mW to 7 mW. Clearly, the drawback of using longer length will overwhelm the benefit. An appropriate selection of thermoelectric module for a PV/TEG system requires a compromise between the power output and material consumption. In general, the modules with small area are more appropriate.

It is to be noted that type VIII modules exhibit an increase in the P_{max} due to two reasons: 1) the semiconductor area has increased (i.e., A_{TE} in eq.4.9) and 2) the area of TEG becomes close to the size of PV cell and this covers all back side area of PV cell. Consequently, the heat losses by convection and radiation from the bottom side of PV cell were eliminated. This analysis indicates that the operation of PV/TEG unit in vacuum can minimise the heat losses due to convection and consequently the power output is anticipated to be higher. Figure 4.6 shows the P_{TE} as a function of L_{TE}, when operating in vacuum and a sample of the calculations results for vacuum and non-vacuum is presented in (Appendix.6).

The operation in vacuum is beneficial due to elimination of the convective losses from both sides of the PV cell. It can be seen that the P_{max} of type I is almost doubled in vacuum compared with that in ambient. An increase in the power output of the smallest module (module I) when operating in vacuum is slightly significant than that of largest module (type VIII). This can be attributed to the fact that the increase in temperature difference across the module is more significant for type I than for type VIII.

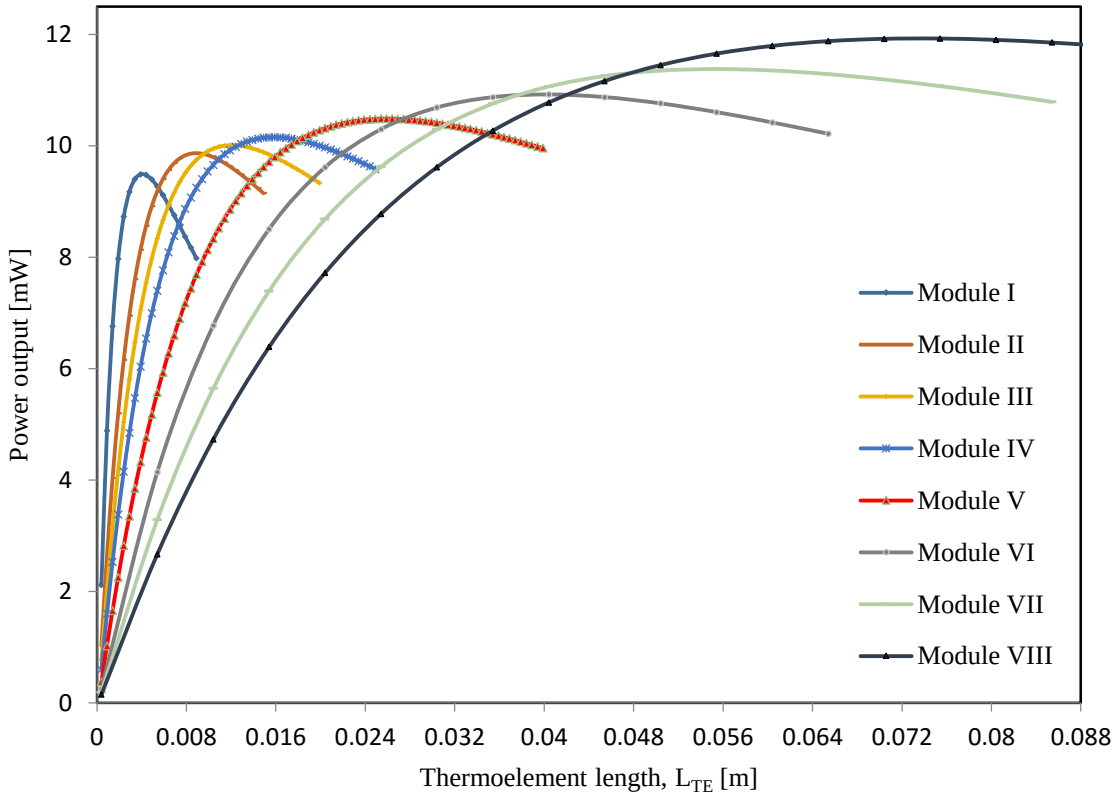

Figure 4.6 Power output vs thermoelement length for system operating in a vacuum

It can be seen that the data in Figures 4.5 and 4.6 are plotted as a function of L_{TE}, providing direct information on length optimisation. However, it is to be noted that the information about optimisation of other geometrical parameters such as the cross-sectional area (A_C), thermocouple number (N) and the volume of thermoelectric materials is also embedded in these figures.

The P_{max} for each type of module as a function of volume is shown in Figure 4.7 for operation in vacuum and at ambient pressure.

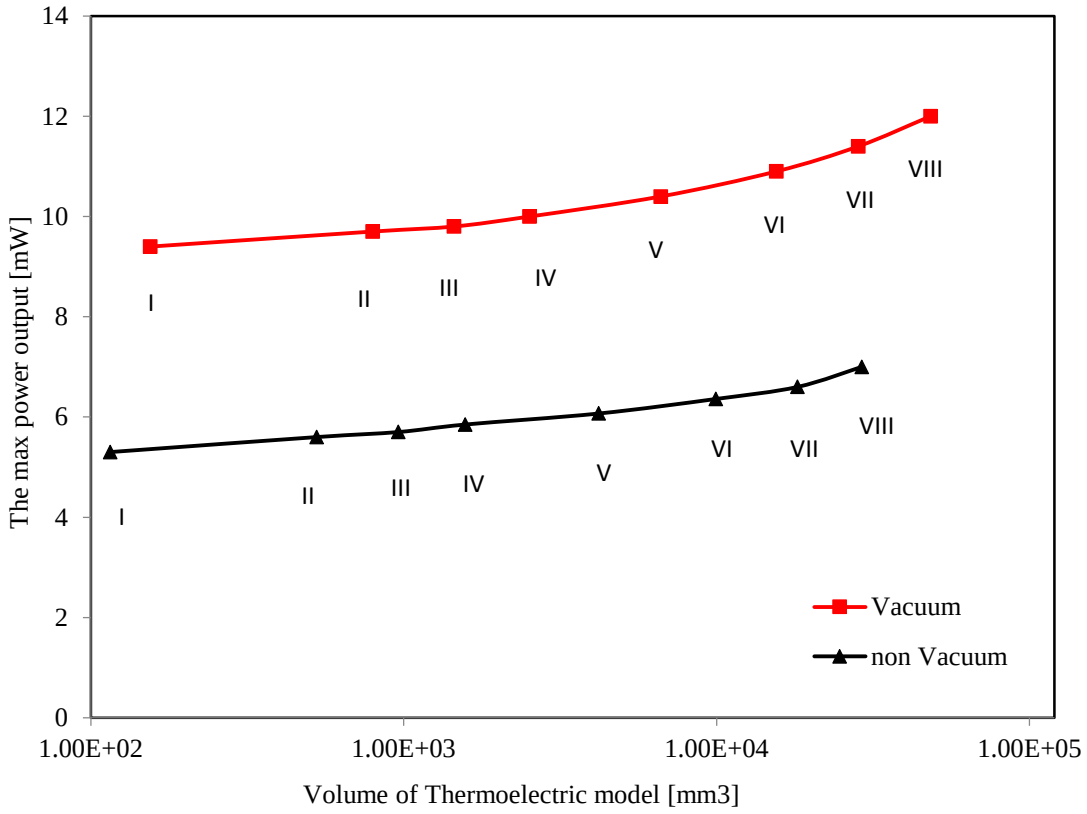

Figure 4.7 Maximum power output vs thermoelectric generator volume for vacuum and non-vacuum systems

It can be seen that the P_{max} of the TEG when operates in vacuum is higher than that in ambient. Increasing the volume of thermoelectric materials can improve the power output of the TEG, but the increase is relatively small (compared with the increase in the volume). For example, the P_{TE} for type I is 5.2 mW and it increases to 7.0 mW for type VIII (i.e., an increase by 35 %), compared with large increase in volume by more than 800%.

Figure 4.8 shows the temperature difference as a function of L_{TE} for type I (smallest module) and type VIII (largest module) in vacuum and at ambient atmosphere, respectively. It can be seen that the temperature difference across a module of type I is increased by 54.8 % when operating in vacuum due to elimination of the convection

losses from both side of PV cell. However, the increase for type VIII is marginal if the length of thermoelements is shorter than 20 mm. It is interesting to be noted that the increase in the L_{TE} caused further increasing in the ΔT for the large module (M-VIII), but the ΔT for the small module (M-A) was almost constant after 0.06 m. This is mainly because most of the heat will be wasted by convection and radiation losses.

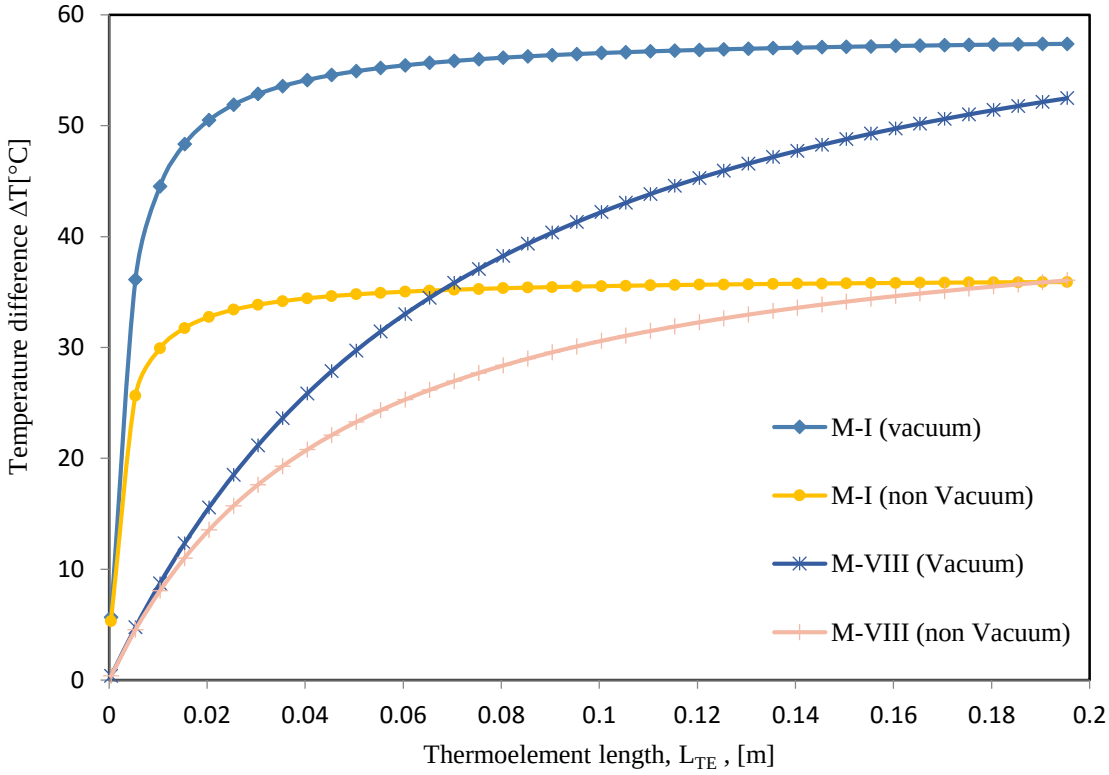

Figure 4.8 Temperature difference for Module I and Module VIII under vacuum and atmospheric conditions

Figure 4.9 shows the power output per unit area as a function of L_{TE} for type I and type VIII in vacuum and at ambient atmosphere, respectively. It is apparent that the small module (type I) exhibits a significantly higher power output per unit area than that of the large module (type VIII). It is to be noted that the optimal length for achieving high power output per unit area when operated in vacuum is longer than that when operated at ambient atmosphere. Figure 4.10 shows the P_{TE}, P_{PV} and P_{tot} of type I when operating in ambient atmosphere.

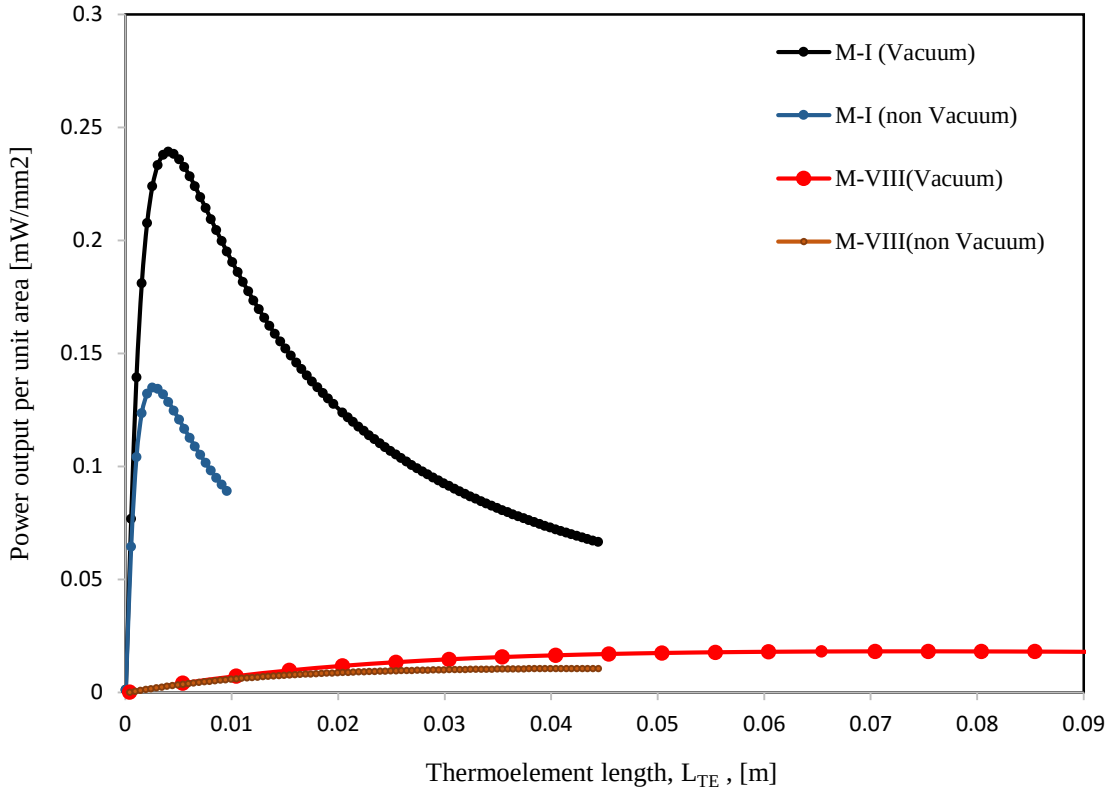

Figure 4.9 Power output per unit area vs thermoelement length in a vacuum and at ambient atmosphere, respectively

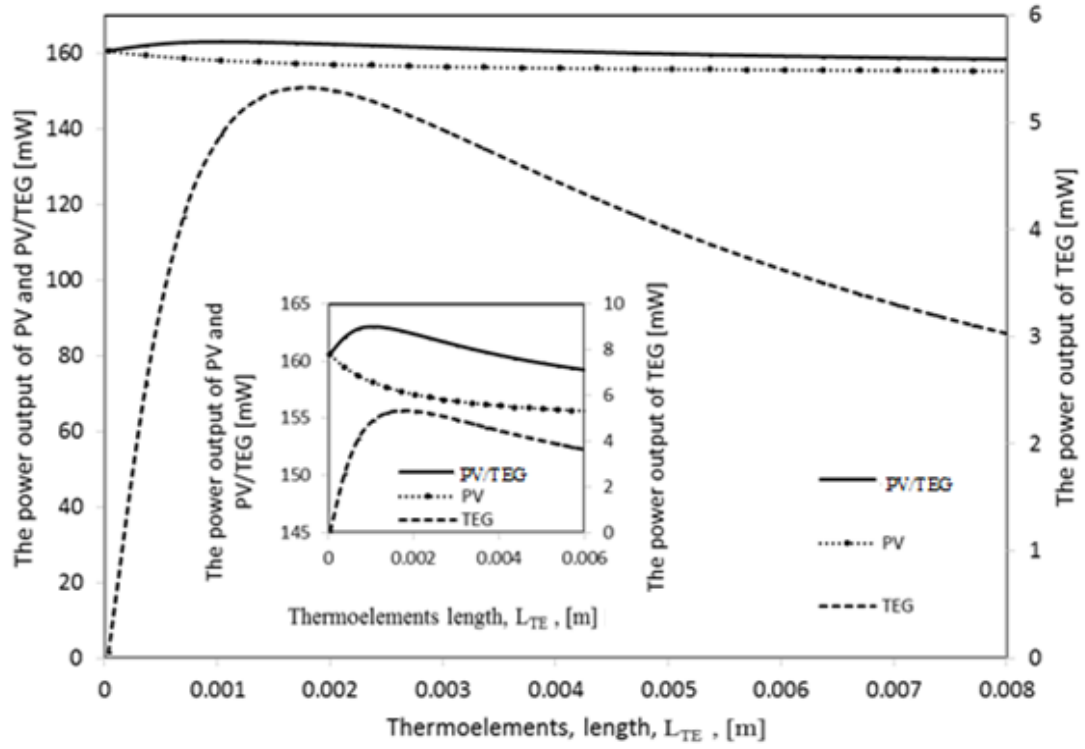

Figure 4.10 The power output of TEG, PV and PV/TEG type I vs thermoelement length in ambient atmosphere for amorphous silicon solar cells

It can be seen that the power output of the solar cell will decrease when integrated with a TEG because the operating temperature of the solar cell is increased duo to a large thermal resistance across the TEG. However, the power reduction in the solar cell (2mW) will be compensated by the power generation by TEG (5.2mW). As a result, the P_{tot} of the hybrid system is increased to 162mW.

Similarly, Figure 4.11 shows the efficiencies η_{TE}, η_{PV} and η_{tot} of type I for operation in ambient atmosphere.

For a PV cell with a cross-sectional area of 40 mm^2, the η_{tot} will increase from 10% to 10.2 % for a TEG with the optimal length L_{TE} of 2 mm. A further increase in η_{tot} is possible if the system is operated in vacuum or using TE module with high Seebeck coefficient.

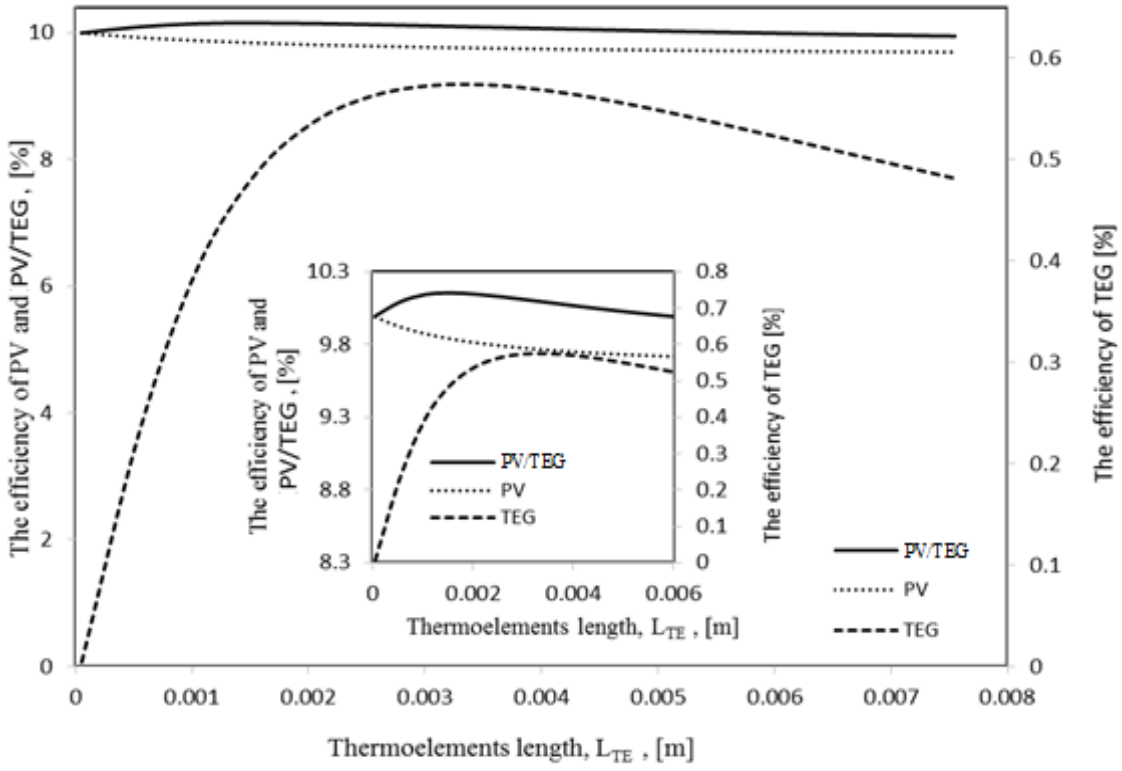

Figure 4.11 The conversion efficiency of TEG, PV and PV/TEG type I vs thermoelement length in ambient atmosphere for amorphous silicon solar cells

Figure 4.12 shows that total power output as a function of L_{TE} for the hybrid systems described above. In view of economic viability, a practical hybrid system should select small-size TEG. Considering the L_{TE} for majority of commercial available modules is around 1.5 mm, it appears that module "M-I" provides a suitable geometry for a practical PV/TEG hybrid system because it produces more total power output than other modules as shown in the Figure. However, if the TEG module with longer L_{TE} is available, the other modules might provide larger power output.

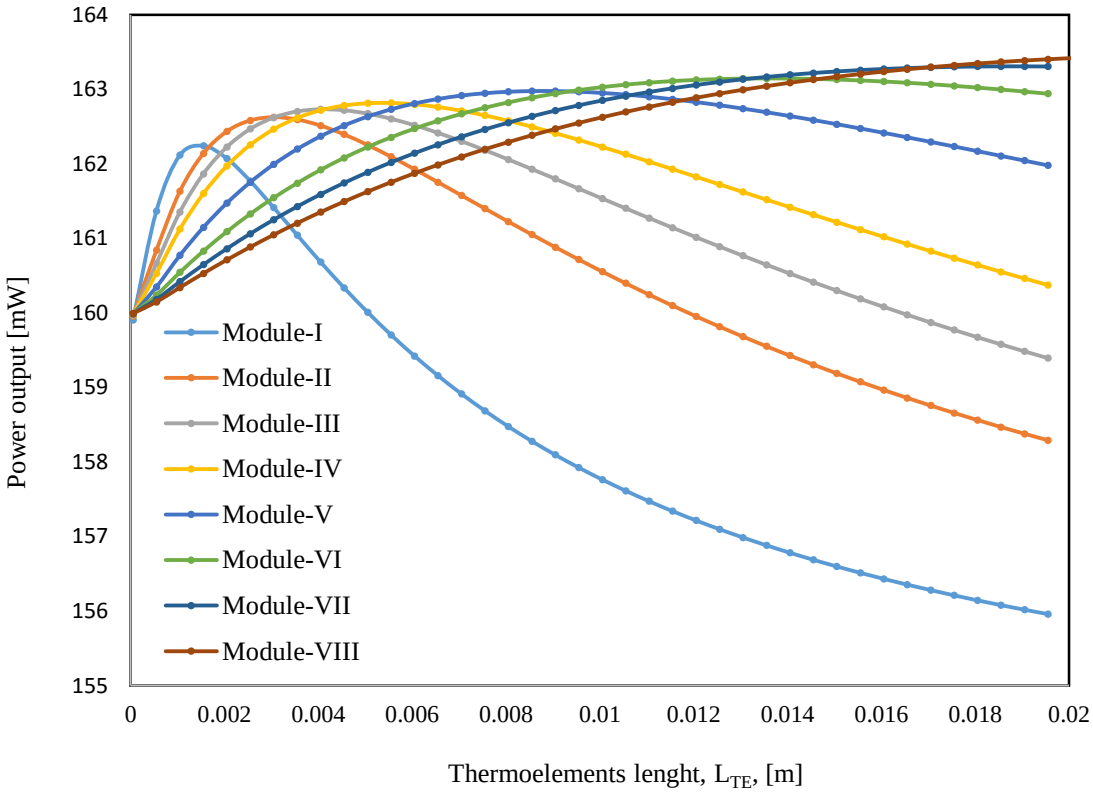

Figure 4.12 The Power output of a hybrid TEG/PV system vs thermoelement length

Figure 4.13 shows the overall system efficiency η_{tot} of the PV/TEG systems as a function of L_{TE} for the eight different module geometries. Similarly, higher overall efficiency is obtained using module type "M-I" if the available L_{TE} is less than 1.5 mm.

The selection of the type of PV cells for integration with TEG is another crucial step in the optimisation of a PV/TEG hybrid system, which must be considered carefully. In this

study, two cases were presented to demonstrate the importance of this aspect by using p-Si and a-Si cells, respectively, which have significantly different temperature coefficient, β_0, as shown in Table 4.3.

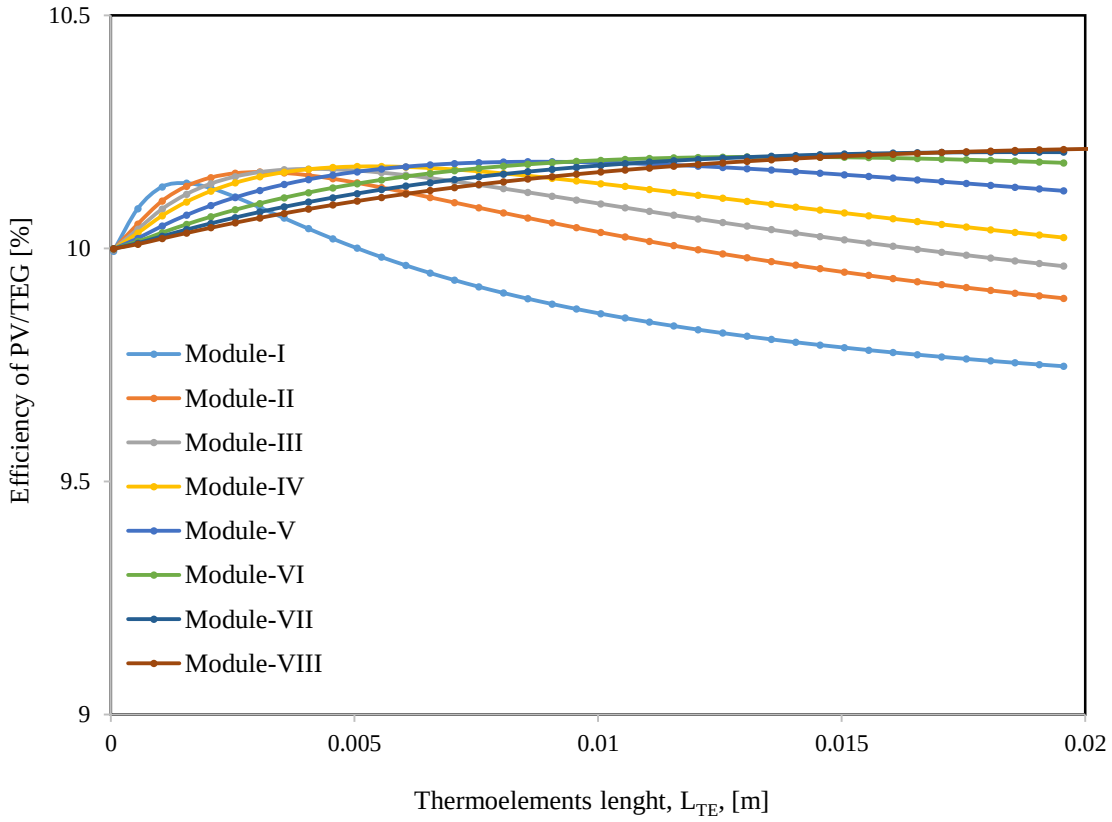

Figure 4.13 The efficiency of eight PV/TEG hybrid systems as a function of the thermoelement length for eight TEG modules

Table 4. 3 The values of β_0 for two silicon PV technologies

PV- technology	Temperature coefficient, β_0, [K^{-1}]	Reference
p-Si	0.004	[107]
a-Si	0.0011	[107]

The power outputs and conversion efficiencies of an a-Si based system (M-I) were calculated using $\beta_0 = 0.0011\ K^{-1}$ (see Table 4.2) and presented in Figures 4.10 and 4.11.

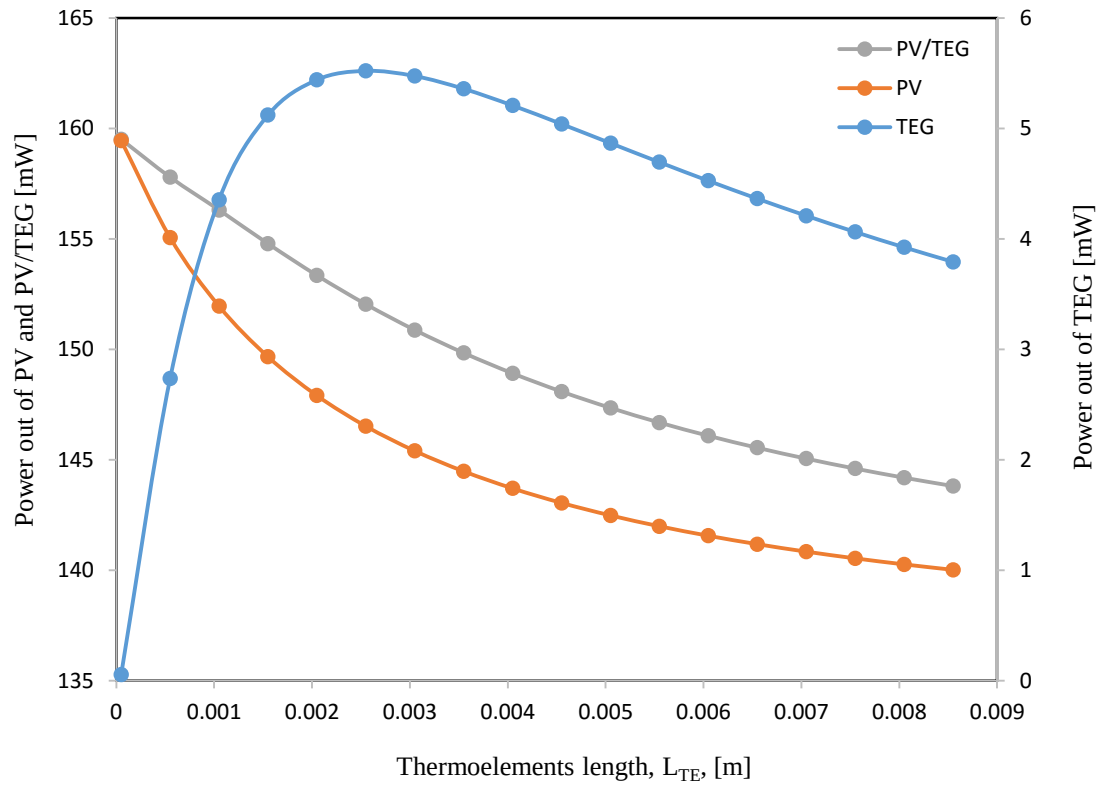

Figure 4.14 The power output of TE, PV and TEG/PV vs thermoelement length for p-Si integrated with M-I

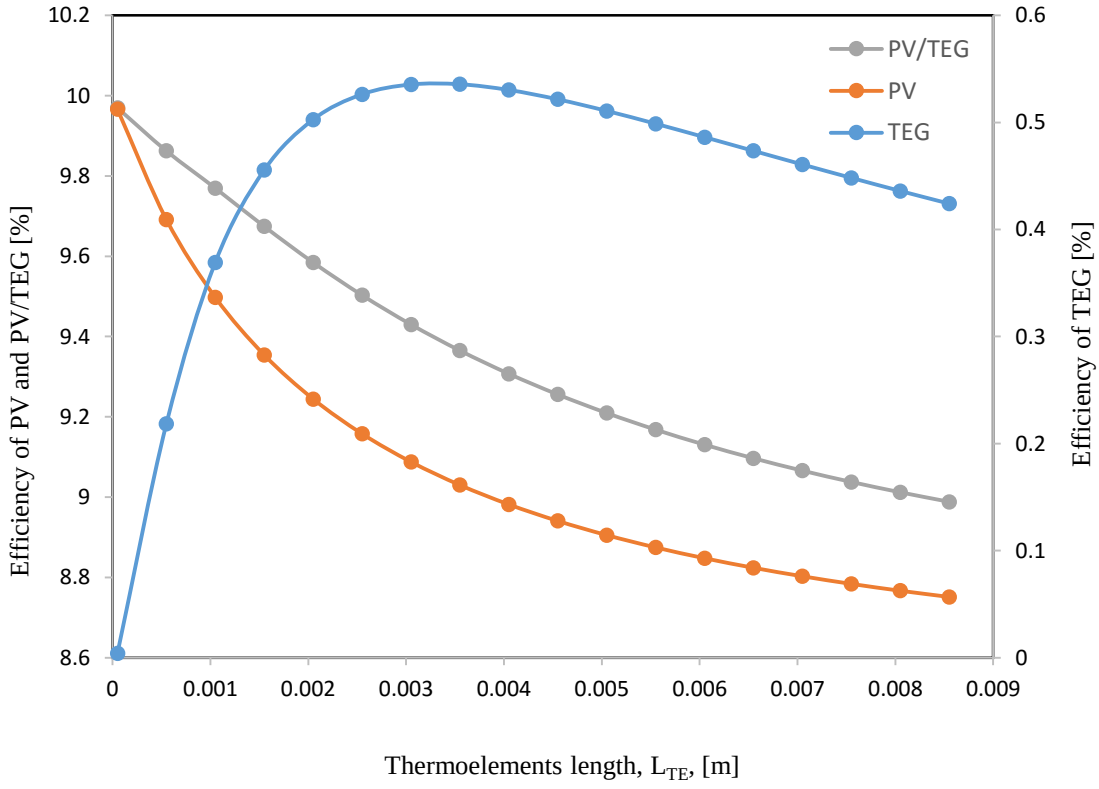

Figure 4.15 The efficiency of TE, PV and TEG/PV vs thermoelement length for p-Si integrated with M-I

Similarly, the calculations were carried out using a p-Si integrated with a M-I type TEG. The power outputs, P_{TE}, P_{PV} and P_{tot} as a function of thermoelement length are shown in Figure 4.14 while the η_{TEG}, η_{PV} and η_{tot} are shown in Figure 4.15. It can be seen that there is no increase in the overall power output of a p-Si based PV/TEG system. This is because the reduction in the power output of the p-Si cell with increasing T_{cell} is larger than the power gain from the TEG. As a result, adding TEG made no contribution to improve the P_{tot} and η_{tot}. On the contrary, it is likely to reduce the power output and efficiency and is clearly not suitable for integration with TEG.

It is to be noted that these two types of the PV cells used here are assumed to have the same η_{PV} of 10 %, but with different values for β_0. In reality, the efficiency of the a-Si cells is usually smaller than that of crystalline Si cells. However, this fact does not affect the conclusion obtained above regarding the criteria for determining the suitability of the PV cells for integration with TEG. The a-Si PV/TEG system displayed an increase in the power output and efficiency over the single PV system because the reduction in its power output is much smaller than that observed in as the p-Si system, making a-Si cell a good candidate for integrating with TEG.

In summary, the geometry of the TEG is crucial in the design of a PV/TEG hybrid system, since it presents a trade-off between expensive material and power generation. This is because the geometry of TEG affects directly the P_{tot} and η_{tot} of the PV/TEG hybrid system. In general, a TEG module that has a smaller A_{TE} than that of the PV cell, can generate more electrical power than those having a larger A_{TE}. Furthermore, a significant increase in the power output can be obtained if the system operates in vacuum. In an ideal case, where the convective heat losses are completely eliminated, the power output can be almost doubled. The PV cells suitable for constructing PV/TEG hybrid systems should

be the type of cells, such a-Si cells, which have a smaller temperature coefficient. This is because the power gain obtained from TEG (5.2 mW) can over-compensate the power loss in the PV cell (2 mW), leading to a net improvement. The section below will discuss the integration of TEG with a-Si experimentally, and compare the theoretical and experimental results.

4.5 Validation

Six commercially available TEG modules were used for validation of the theoretical results as shown in Figure 4.16. The specifications of the models used for this experiment are listed in Table 4.4. They were integrated with a-Si solar cells, which are one of the suitable types of the PV cells for integration with TEG. In this section, six PV/TEG hybrid systems were built and the performances were investigated in an attempt to validate the theoretical model presented in the previous sections and to determine experimentally the optimum geometry of the TEG.

Two methods are generally used to characterise TEG under operating conditions. The first is called ‘constant heat flux’, when the heat input to the module is constant. The second method is known as ‘constant ΔT’, where the ΔT across the TEG module is kept constant by the continuous addition of heat to the system. In this research, the first method is used because the system operates approximately in a “constant heat flux” condition. The TEG modules were characterised by varying the resistance of the load connected to them and measuring their output voltage. The PV cells are characterised by using the same procedure that was mentioned earlier in Chapter 3. It is to be noted that the PV cell and TEG were characterised separately, without series or parallel connections.

4.5.1 Experimental Setup

The six TEG modules employed for this investigation are shown in Figure 4.16. The PV/TEG hybrid systems were constructed based on Figure 4.1 using an a-Si solar cell to integrate with one of the six TEG modules, respectively. The temperature of the hot side of TEG was determined by two factors: the temperature at the cold side of TEG and the thermal resistance between the PV cell and the heat exchanger of each module.

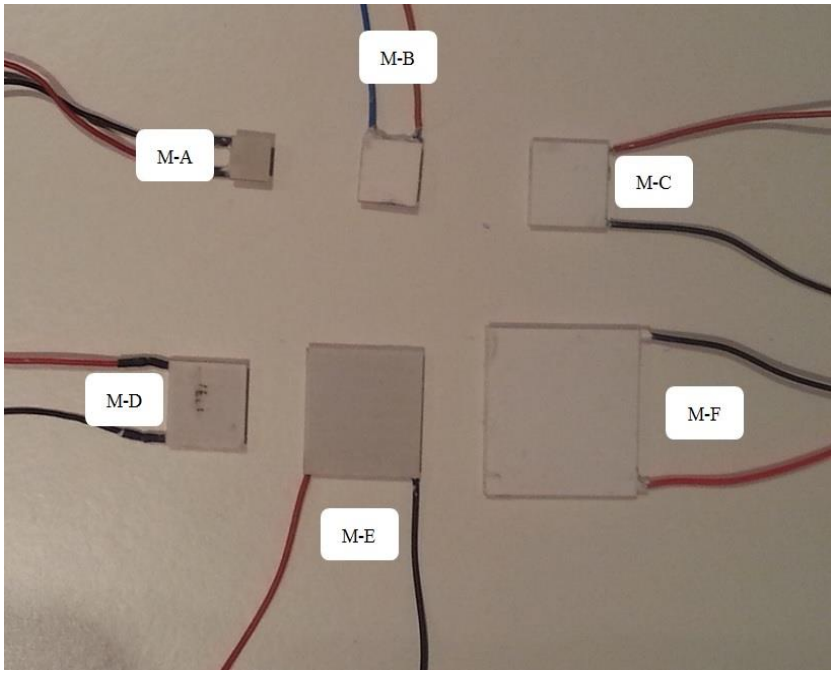

Figure 4.16 Photograph of the six thermoelectric generator modules, M-A, M-B, M-C, M-D, M-E and M-F

The cold side of TEG was maintained at 25 ^{0}C with an error of ± 1.5 ^{0}C. A key parameter that determines the thermal resistance of the TEG is $A_C N / L_{TE}$, the values of which are listed in Table 4.4. The dimensions of the TEGs in Table 4.4 were measured by using the microscope in Appendix.7.a. An example of the measurements is appeared in Appendix.7.b. Six different temperatures were therefore generated on the hot side of TEG by changing the geometry of the TEG. It is to be noted that the temperature of the hot side of TEG was measured by inserting the sensor inside copper plate (1mm thickness) between the TEG and PV cells. A heat sink compound used to fill the gap between PV

cells and TEG. This measured temperature assumed to be the same as the operating temperature of the PV cells.

The TEG modules were characterised by measuring the voltage across an external load with variable resistance, which was connected to the TEG during the test as shown in circuit in Figure 4.3. The light intensity (1000 W/m^2) of solar irradiation was maintained constant throughout the experiment.

Table 4.4 Characteristics of the thermoelectric modules

Modules	Total area (mm^2)	N	A_C (mm^2)	L_{TE} (mm)	A_CN/ L_{TE} (mm)
A	10 x 10	14	0.8 x 0.8	3	3
B	15 x 15	62	0.8 x 0.8	2	20
C	20 x 20	98	0.5 x 0.5	1	25
D	20 x 20	142	0.7 x 0.7	2	35
E	30 x 30	62	2.1 x 2.1	2.5	109
F	40 x 40	256	0.9 x 0.9	1.7	122

The P_{max} was extracted when the external load matched the internal resistance of the TEG module. A multi-meter (Agilent U1241A) was used for measuring the voltage, current and resistance in the circuit presented in Figure 4.3.

4.5.2 Results and Discussions

Figure 4.17 show the measured voltage as a function of load resistance for the hybrid systems which were constructed using modules M-A, M-B, M-C, M-D, M-E and M-F, respectively.

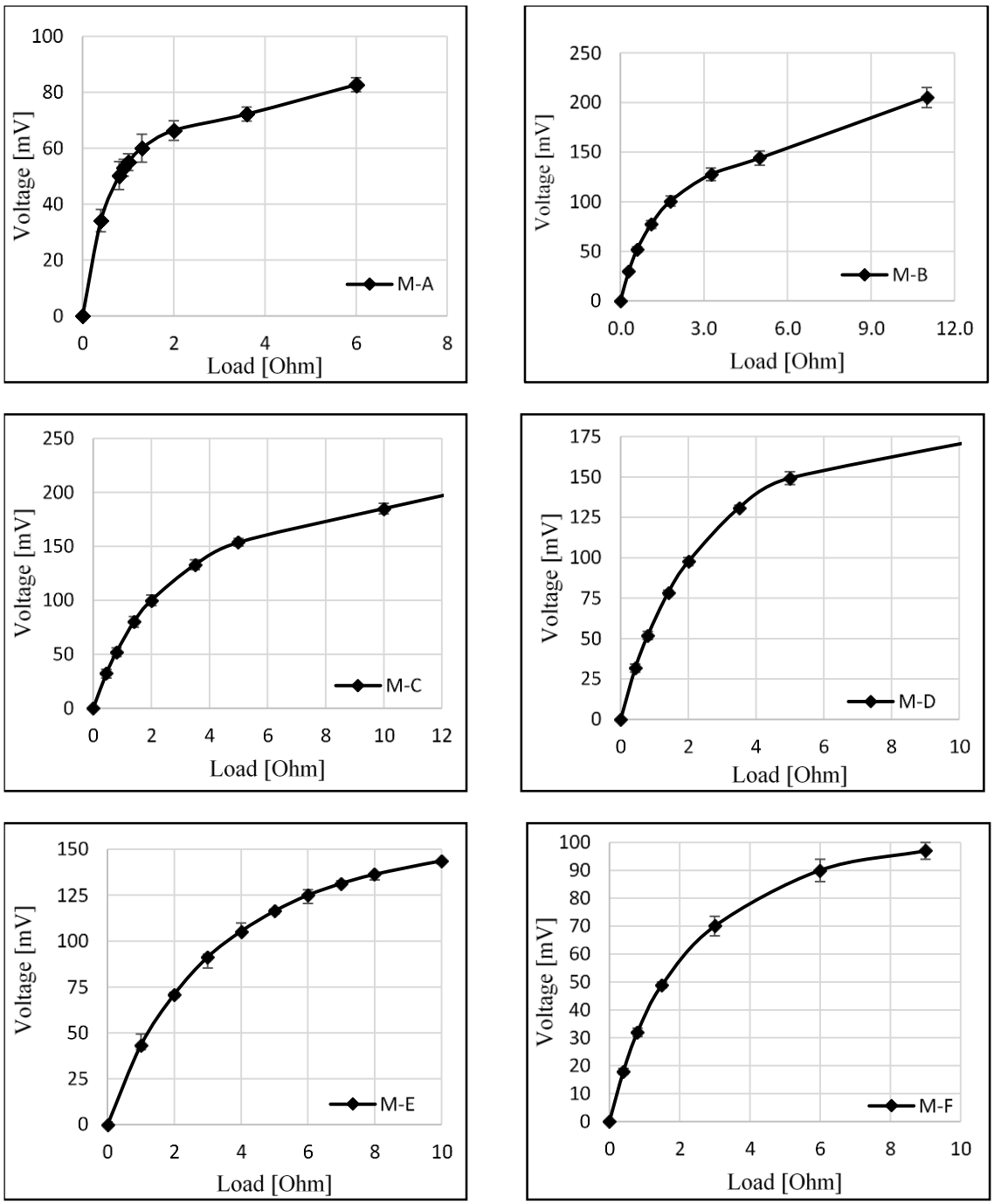

Figure 4.17 The voltage vs load resistance for six TEG modules, respectively

The TEG produced voltage because of the temperature difference (ΔT) established across it. It is clear that each TEG module generated different values of voltage because the N and ΔT for each module are different. It is interesting to note that the ΔT across TEG is depended on $A_C N / L_{TE}$ (see Table 4.5).

The value of electric current flowing through the TEG module can be calculated by dividing the measured voltage by the applied load. The I-V curves for the six TEG modules presented in Figure 4.18. It can be seen that an increase in ΔT across the TEG module led to an increase in the I_{SC}. For instance, M-A shows a highest electric current because ΔT established across it is the largest. However, this module produced the lowest V_{OC} because the N is very small (only 14 elements).

Table 4.5 The hot side temperature and the ΔT across each of the TEGs

Modules	T_H [^{0}C]	$\Delta T = T_H - T_C$ [^{0}C]	$A_C N / L_{TE}$ (mm)
M-A	51.0	26	3
M-B	39.0	14	20
M-C	38.0	13	25
M-D	33.0	8	35
M-E	27.0	2	109
M-F	26.0	1	122

The ΔT in M-B and M-C is also reasonably high, together with reasonably large *N*, leads to highest value of V_{OC} in these two modules. In M-D, a very large *N* (142 elements) is mainly responsible for the large V_{OC}. The worst module for integration with PV cell is M-F, because the I_{SC} and V_{OC} were the minimum values, because this module contains the largest *N* (256 elements) which resulted in the lowest ΔT established across the module. It is to be noted that the size of M-F is exactly the same size as the PV cells (4cm x 4cm).

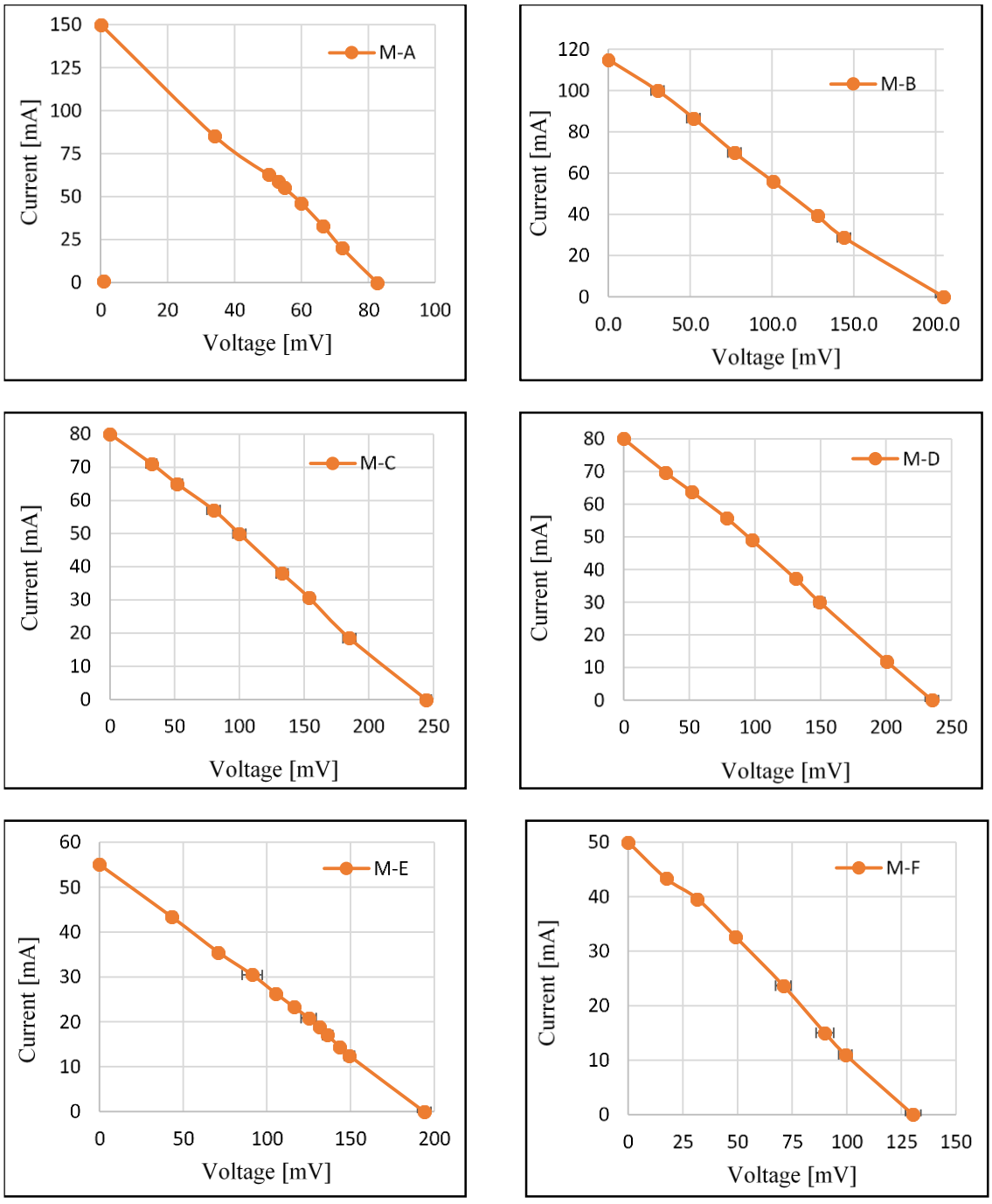

Figure 4.18 The I-V curves of six TEG modules; M-A, M-B, M-C, M-D, M-E and M-F

The experimental results demonstrated that M-B and M-C are preferable to the larger sizes because it generates more power and uses less material. The power output as a function of the voltage for all 6 modules investigated are presented in Figure 4.19.

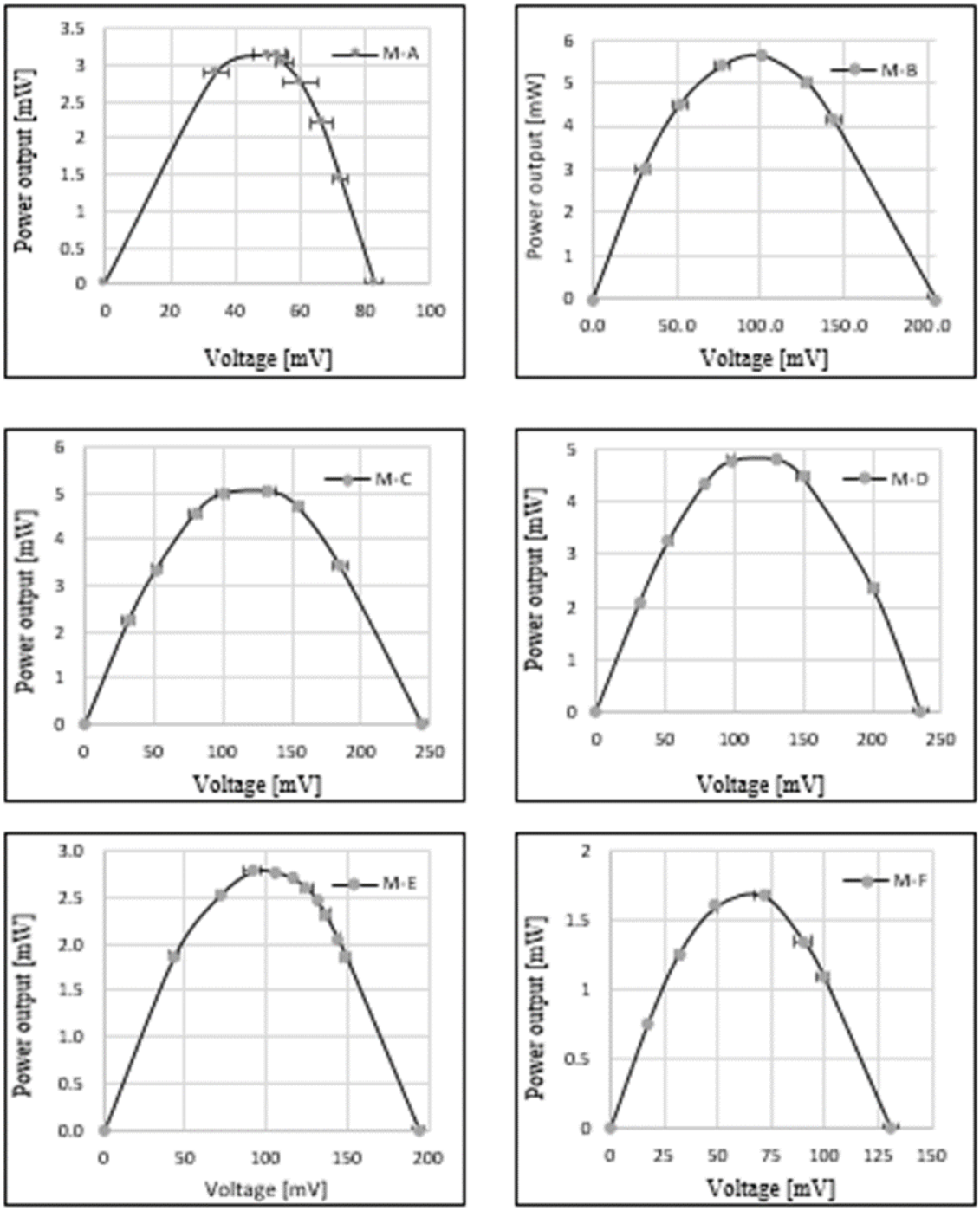

Figure 4.19 The P-V curves of six TEG modules M-A, M-B, M-C, M-D, M-E and M-F

M-B showed the highest performance among the six TEG modules, which is associated with a high thermal resistance. In this study, the T_H of the TEG modules is proportional to the thermal resistance of the module as the cold side of TEG was kept constant at 25 ^{0}C.

It can be seen that modules A and B showed the highest T_H, 51 ^{0}C and 39 ^{0}C respectively. Figure 4.20 shows experimental data of the T_H of the six TEG modules as a function of L_{TE}, compared with those obtained from theoretical calculation (the parameters of the modules are presented in Appendix.8.

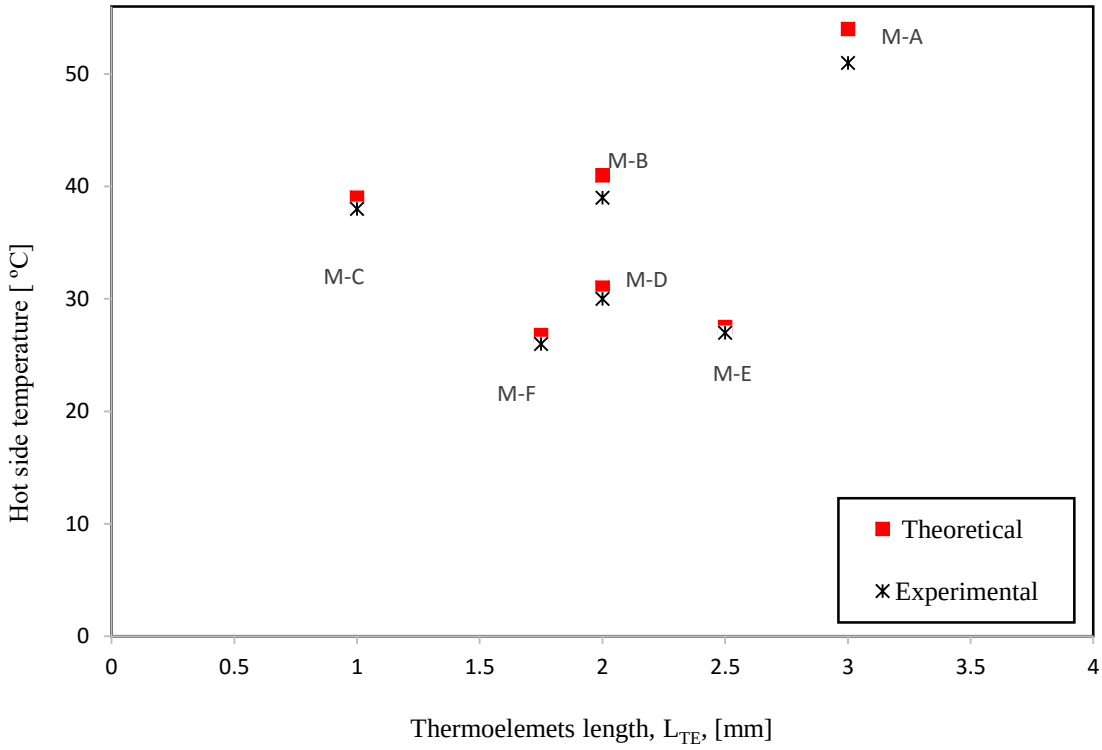

Figure 4.20 The hot side temperature of the thermoelectric vs Thermoelement length for six modules; M-A, M-B, M-C, M-D, M-E and M-F

Some modules, such as M-C, M-D, M-E and M-F, show very good agreement between the theoretical and experimental results. However, the smaller modules such as M-A and M-B show slightly higher deviation with the errors of 8% and 7%, respectively. In general, an increase in the L_{TE} causes an increased in the T_H of TEG because the thermal resistance increased for a given total cross-sectional area.

Figure 4.21 shows the calculated P_{max} as a function of L_{TE} using the parameters of the six modules investigated except for the length of the modules being varied. In Figure 4.21

the values of P_{max} measured from experiments on the six modules (which have fixed L_{TE}) are also presented for comparison. It is clear that, except for M-B and M-C, all commercial modules employed in this study are not optimised for such application. In order to obtain those maximum attainable values, a shorter length is needed for M-A while longer lengths are needed for M-D, M-E and M-F.

Figure 4.22 shows the efficiency of TEG modules as a function of L_{TE} for six modules. It was calculated by dividing the P_{max} of TEG by the total input power on the PV device of the PV/TEG hybrid system, which functioned as a heat collector for the TEG.

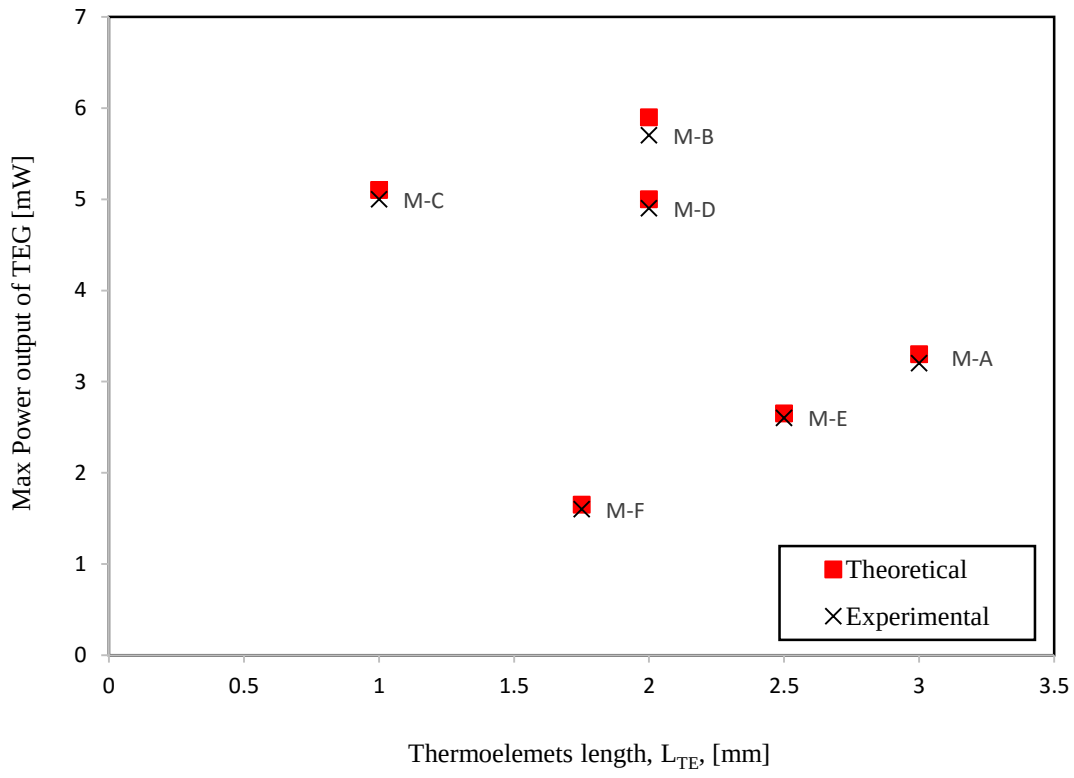

Figure 4.21 The maximum power output of thermoelectric against Thermoelement length for modules: M-A, M-B, M-C, M-D, M-E and M-F

It interesting to mention here, this efficiency represent the efficiency of TEG in the system not at the hot junction of TEG. Among the six TEG modules, M-B showed the highest efficiency (0.32 %), while M-F showed the worst (0.1 %).

The operating temperature of the PV in the hybrid system is affected by the TEG employed in the system. Figure 4.23 shows the calculated power output of the PV cell as a function of L_{TE} for the six TEG modules, respectively, compared with the P_{max} obtained from experiments. Figure 4.24 shows the corresponding η_{PV} of the PV cell operating on the top of the six TEG modules, respectively.

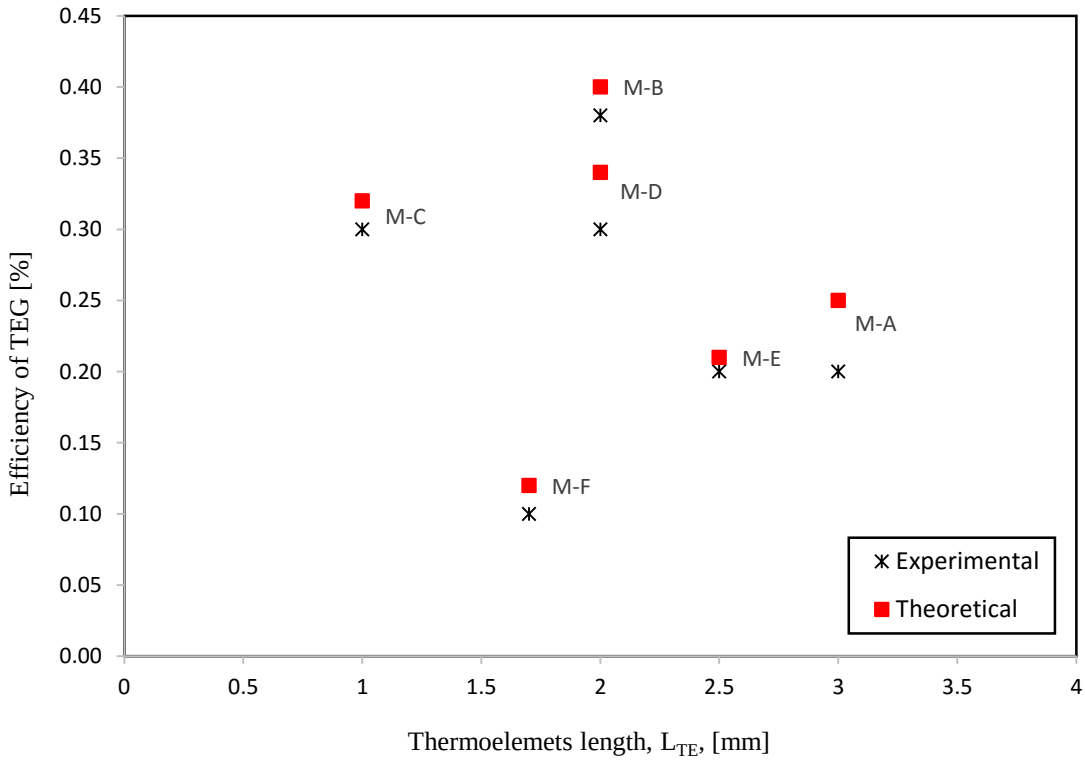

Figure 4.22 The efficiency of thermoelectric generators in the system vs Thermoelement length for six modules: M-A, M-B, M-C, M-D,, M-E and M-F

It can be seen that P_{PV} and η_{PV} decreased by increasing the L_{TE} of TEG modules, because increasing the L_{TE} increases the thermal resistance between the PV cells and the cold side of the TEG.

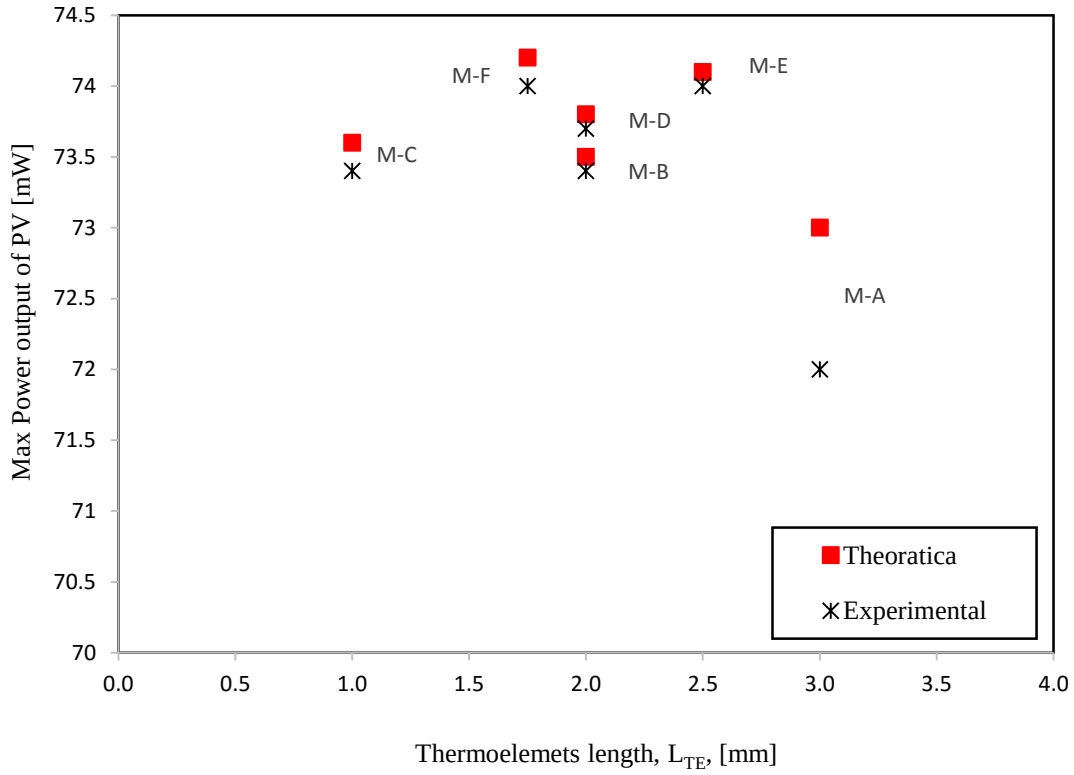

Figure 4.23 The maximum power output of the photovoltaics vs Thermoelement length for the six modules: M-A, M-B, M-C, M-D, M-E and M-F

It is clear that integrating PV with TEG to form a hybrid PV/TEG system results in a decrease in P_{PV} and η_{PV} because of increasing T_{cell}. However, the decrease of P_{PV} and η_{PV} in the PV cell may be compensated by the increase of P_{TE} and η_{TE} in the TEG, leading to an overall increase of the hybrid system.

Figures 4.25 and 4.26 show P_{tot} and the η_{tot} respectively. It can be seen that, among the six TEG modules that were integrated with PV cell, M-B presented the highest P_{tot} and highest η_{tot}.

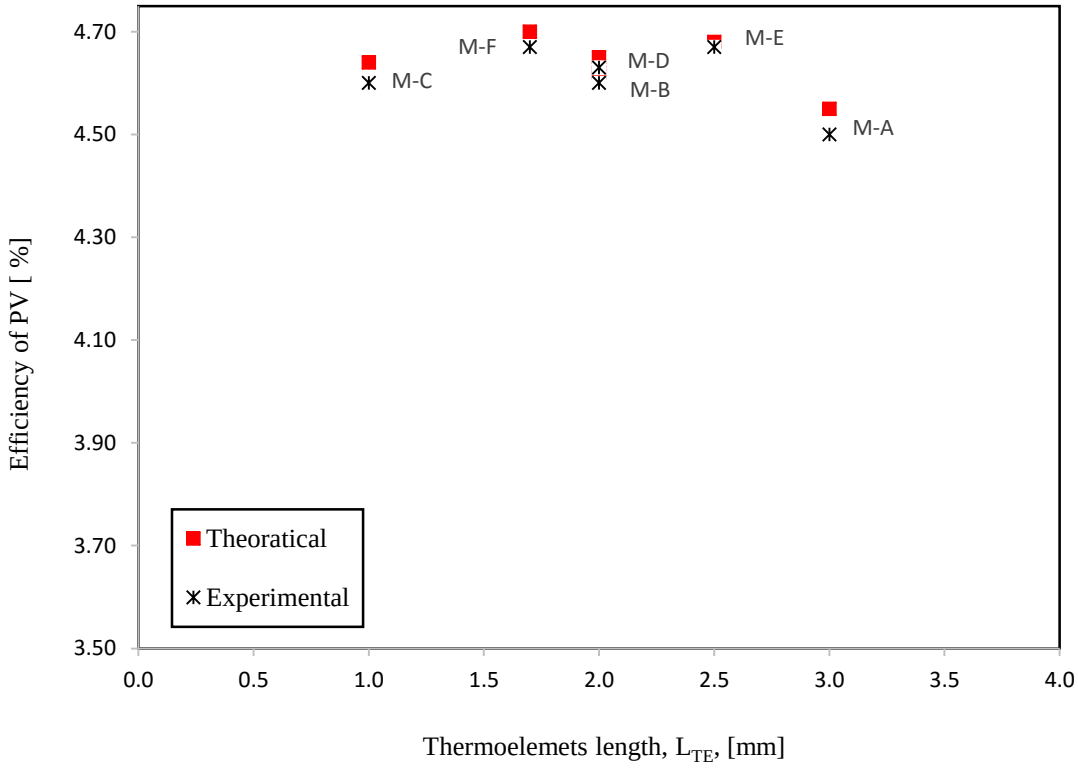

Figure 4.24 The efficiency of photovoltaic cells vs Thermoelement length for six modules: M-A, M-B, M-C, M-D,, M-E and M-F

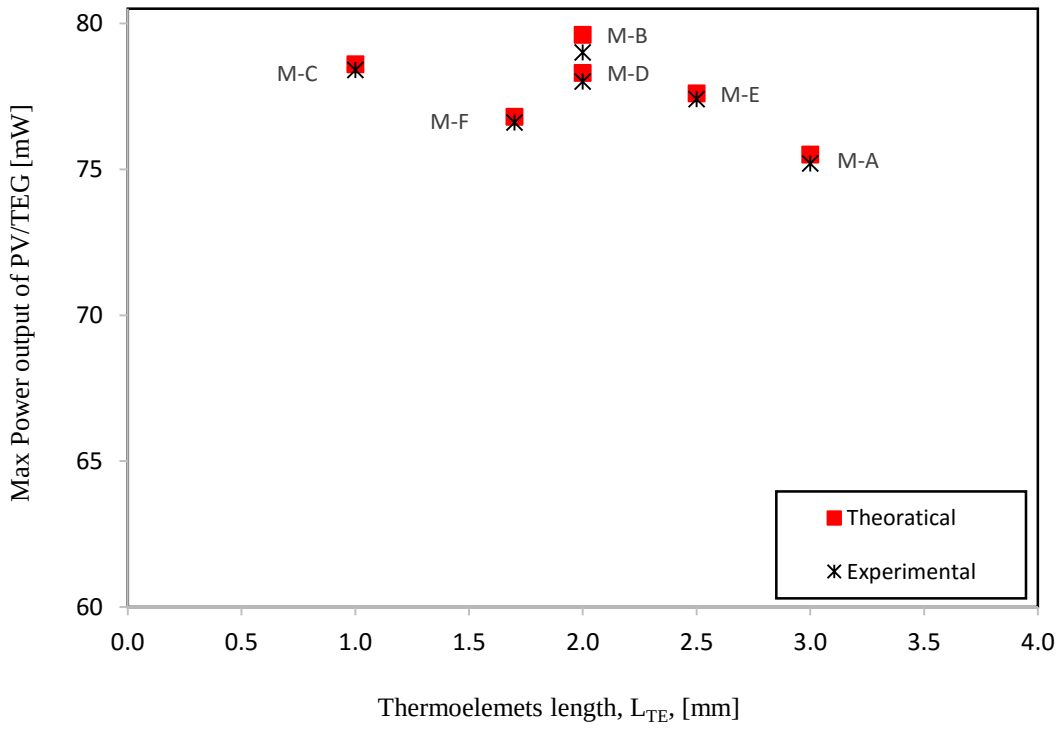

Figure 4.25 The power output of (PV/TEG) vs Thermoelements length for six modules; M-A, M-B, M-C, M-D, M-E and M-F

This is partly due to that fact the M-B provide "geometry match" with the PV cell employed, which has an area of (40mm x 40mm) and a smaller temperature coefficient.

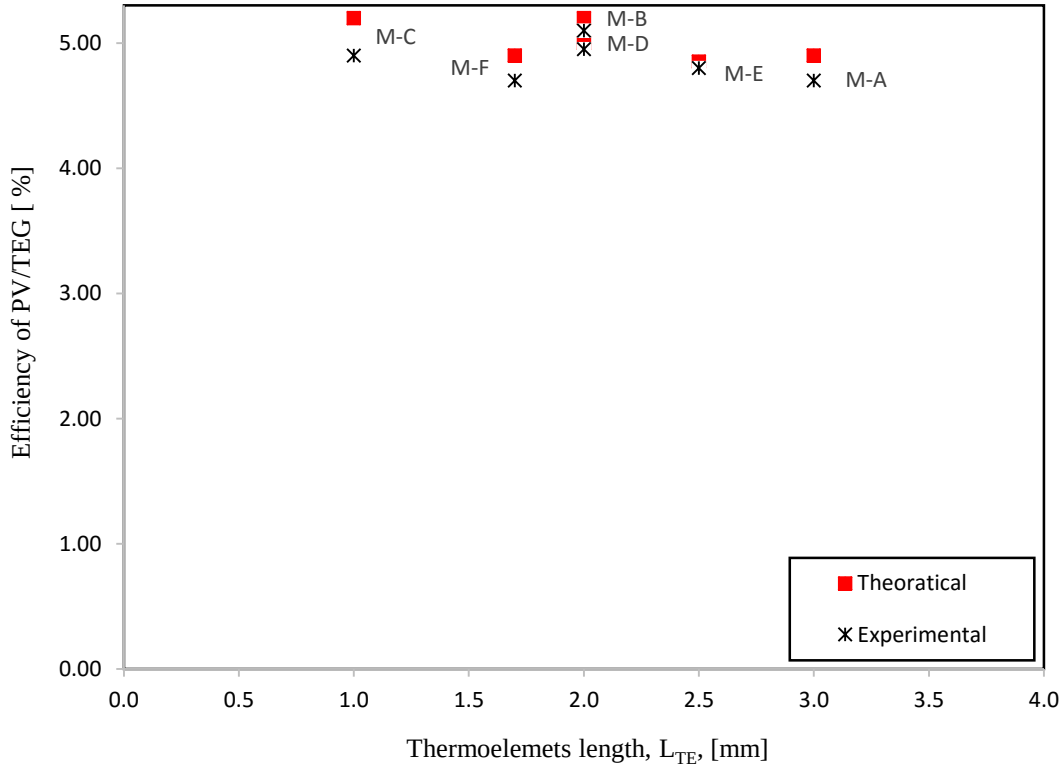

Figure 4.26 The efficiency of (PV/TEG) vs Thermoelement length for the six modules: M-A, M-B, M-C, M-D, M-E and M-F

In summary, the results of this investigation show that the integration of PV cell with TEG module requires a trade-off between P_{TE} and that P_{PV}. It is necessary and vital to determine the optimal geometry of TEG module in order to obtain the improvement in a hybrid PV/TEG system. If this is not carefully done, the PV may lose more power than that are generated from the TEG. The experimental results demonstrated that M-B is the optimum configuration for integration with the PV cell employed in this study because it produced the highest P_{tot} and η_{tot}. Also, the experimental results are in an agreement with theoretical calculation that predicted that the optimum geometry can be achieved using 62 elements with A_C of (0.8mm x 0.8mm) and L_{TE} of 2 mm. Geometrical factors have a significant effect on the power output and efficiency of both the PV cell and TEG module.

Because the integration of TEG created a thermal resistance between PV cells and the heat sink, it will contribute to an increase in the operating temperature of PV cell. Using the wrong geometry will result in losing power from the PV cell and possibly wasting thermoelectric materials. The results demonstrate that a small-size module is preferred, rather than a larger size (i.e. in a similar size to PV cell), due to facilitating a higher power density with the added benefit of lower material consumption.

4.6 Conclusions

The optimal geometry for obtaining maximum power output and conversion efficiency of a TEG in a hybrid PV/TEG system was investigated using a model developed in this study. Together with the knowledge of temperature dependence of PV cells, the overall power output P_{tot} and conversion efficiency η_{tot} of a hybrid PV/TEG system can be estimated. The results of simulation using this model shows that an increase in both the overall power output and conversion efficiency may be achieved by incorporating TEG to harvest waste heat from PV cell. In addition, the results demonstrate that in practice an optimised geometry has to be a "trade-off" between achieving a large power output and using minimal thermoelectric material. In general, a thermoelectric module that has a smaller cross-sectional area than that of the PV cell can generate more electrical power than these of having a larger area. Furthermore, a significant increase in the power output can be obtained if the system operates in vacuum. In an ideal case where the convective heat losses are completely eliminated, the power output can be almost doubled. The validation of the theoretical work by experimental study showed good agreement between the theoretical and experimental results with an average error of about 9 %.

CHAPTER FIVE - STRATEGIES FOR ENHANCING THE OPTIMISED PV/TEG HYBRID SYSTEM

5.1 Introduction

Two strategies are applied in this chapter in order to build an efficient PV/TEG hybrid system. The first strategy was achieved by increasing the light intensity on the PV/TEG, which increases the ΔT across the TEG. Two techniques were utilised to increase the light intensity. The first technique involved a solar parabolic dish with the inside surface coated with mirrors. This system has the ability to increase the light intensity to up to 5 suns using indoor light. The second concentrator technique was to reduce the distance between the solar simulator and the PV/TEG hybrid system, from (18cm) to (10.5cm), causing an increase in light intensity of up to two suns.

The second strategy was to reduce the cold side temperature of the system. The effect of the mass flowrate on the electrical power output was investigated.

5.2 The first strategy

This section explains the strategy of increasing the light intensity by employing solar concentrators. The solar concentrator receives the light from the sun and concentrates it on to the PV/TEG system in order to increase the intensity of light.

5.2.1 Parabolic concentrator system

5.2.1.1 Experimental set up

The experimental setup is shown photographically in Figure 5.1 and schematically in Figure 5.2.

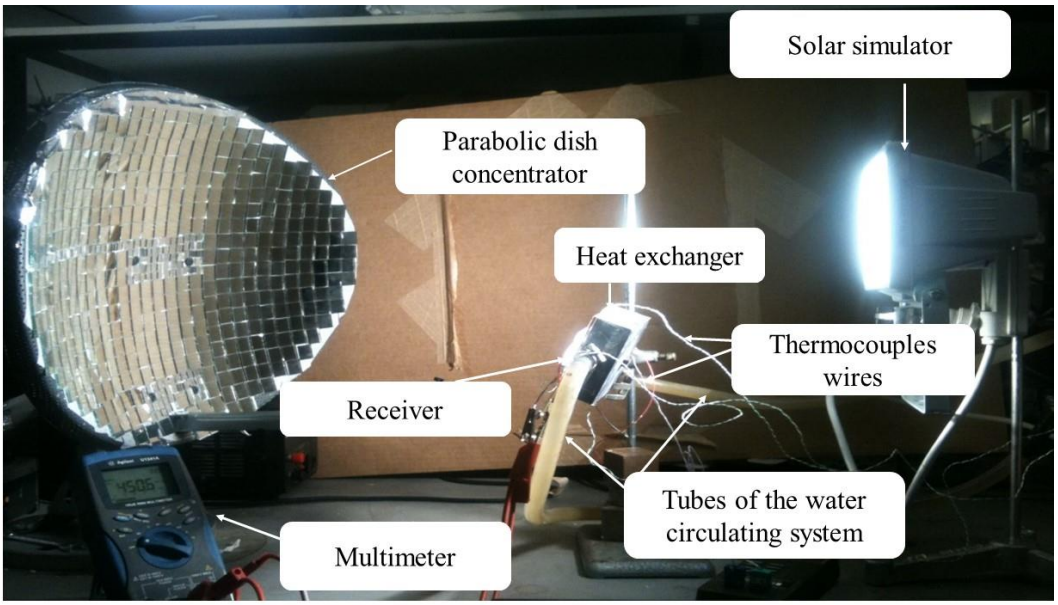

Figure 5.1 Photograph of the experimental setup of concentrated PV/TEG hybrid system

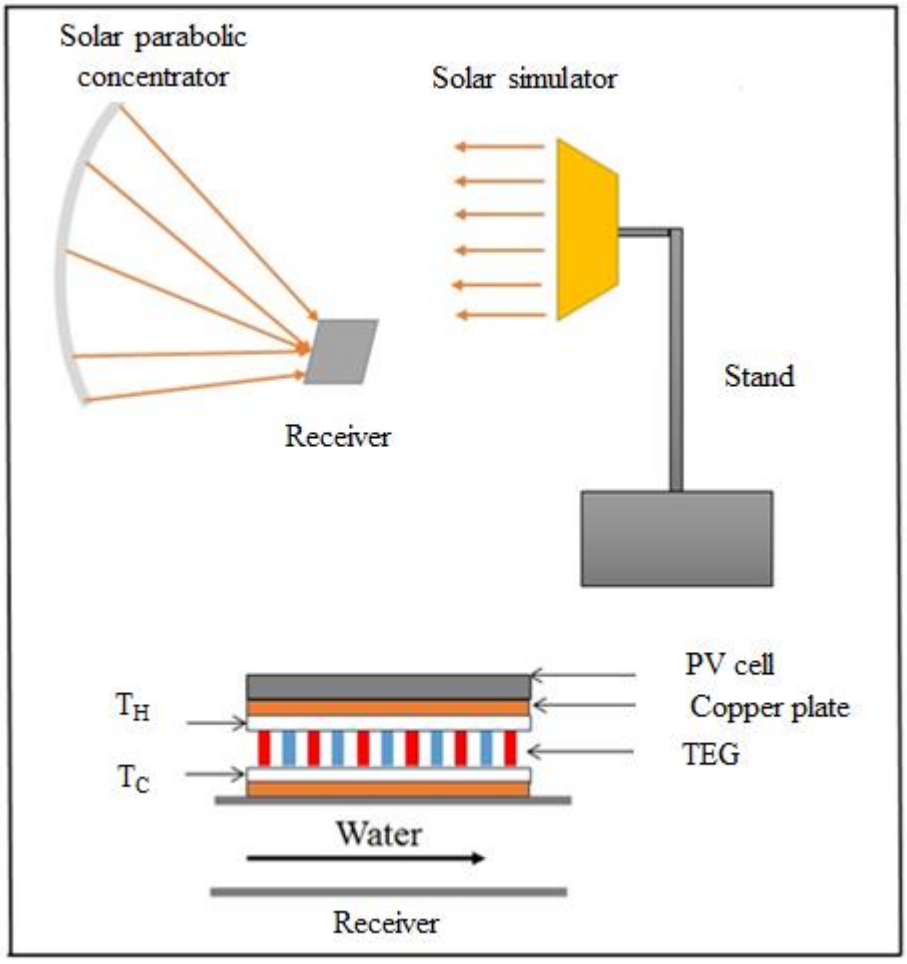

Figure 5.2 Schematic diagram of the concentrated PV/TEG hybrid system

The following equipment was used in the setup: the solar parabolic dish, solar simulator, receiver (PV/TEG system), water circulating system, rheostat and multimeter. The solar parabolic dish was built in the laboratory by coating a recycled satellite dish with commercial mirrors. Two sizes of mirrors were used to cover the entire inside area of the dish. They were 2cm x 2cm and 1cm x 1cm, with the latter used to cover only the centre of the dish where it was difficult to fit the larger mirrors due to the higher curvature. A photograph of the solar parabolic dish is shown in Figure 5.3.

Figure 5.3 A photograph for the constructed solar parabolic dish

The solar simulator used in this experiment was a commercial Xenon strip light. The Xenon light was used, as it is white and to mimic the sunlight. The receiver included the PV/TEG hybrid system. Two K-type thermocouples were employed for temperature measurement and one Agilent (U1241A) multi-meters used for measuring the voltage, current and electrical resistance. A heat sink compound was used to fill in any gaps between the PV cells and TEG or TEG and the heat sink, and a copper plate was used

with a groove machined into it to accommodate the thermocouple in order to avoid possible damage to the solar cells. The cold side of TEG was kept constant at 20 °C. A rheostat was used as the external load to the PV cells and to the TEG, as explained in Chapter 3 and Chapter 4 respectively.

5.2.1.2 Results and Discussions

An experimental study was conducted to find the optimum geometry of a TEG to integrate with PV cells. Four commercially available TEG modules were integrated with PV cells of type m-Si. The specifications of the PV cells are given in Table 5.1 and the characterisations of the four TEGs appear in Table 5.2.

Table 5. 1 The PV cell specifications under one sun

Technology	Total area (mm^2)	Active area (mm^2)	I_{SC} (mA)	V_{OC} (mV)	FF (%)	η_{PV} (%)
m-Si	40x40	35 x 35	220	576	65.6	6.8

Table 5. 2 The specifications of the TEG modules

Module	External area (mm^2)	N	L_{TE} (mm)
M-A	40x40	256	1.1
M-B	30x30	62	1.5
M-C	20x20	144	1.1
M-D	15x15	62	1.3

As mentioned previously, the integration of TEG leads power generation from the TEG in a supplementary stage. However, the PV cells will lose power due to an increase in the operating temperature of the PV cells. Therefore, the process of integration is a

compromise between the power generation from the TEG and the loss in power from the PV cells.

An experimental work has been already done by integrated the PV cell in Table 5.1 with the four TEG modules in Table 5.2 to identify the best PV/TEG hybrid system that could be used under increasing the light intensity. The solar simulator in Figure 5.1 was used as a solar simulator and the distance between the solar simulator and the sensor of the pyronometer was calibrated to measure one sun (1000 W/m^2) from the output light. The I–V characteristics of the PV cell and TEG are determined by measuring the voltage drops on a variable load resistor which is connected to the device under the test. The temperature of the T_H and T_C measured by using two K-type thermocouples.

Table 5.3 presented the power output of PV, TEG and PV/TEG, as it can be seen that the highest total power generation from the combined PV/TEG system was obtained from the integration with M-A, because the loss in power output from the PV cell was lower than the other modules.

Table 5. 3 The power output of PV, TEG and PV/TEG ($P_{PV/20}$ and $P_{PV/Th}$ represent the power output of the PV at 20 ºC and T_H, respectively)

Module	T_H (ºC)	ΔT (ºC)	$P_{PV/20}$ (mW)	$P_{PV/Th}$ (mW)	P_{TE} (mW)	P_{tot} (mW)
M- A	24	4	83.2	81.8	3.2	85
M- B	32.5	12.5	83.2	75	9	84
M- C	30	10	83.2	79.1	4.5	83.6
M- D	38	18	83.2	75.5	8.2	83.7

In this experiment, the same PV cell was used for integration with the TEGs, the purpose of which is mainly to remove the heat generated in the PV cell and transport it to the cold side of the TEG, rather than keeping it in the PV cells. The results in this section confirm the findings of Chapter 3, which showed that mono-crystalline silicon PV cells (Type m-Si) are not suitable for integration with TEG in a hybrid system.

However, the integration of TEG can ensure the operating temperature of the PV cells close to room temperature, which increases the lifetime of the PV cells and maintain the efficiency at certain level. It is to be noted that the size of TEG selected to integrate with PV cells was the same size as the PV cells because the smaller sized TEGs led to a decrease in the total power output P_{tot} of the PV/TEG system.

It is clear that the increase in power output due to integrating TEG (M-A) with the PV cell (m-Si) was not significant because the ΔT was low under one sun illumination. The following work investigated further the same hybrid PV/TEG system under 5 suns illumination to study the effect of higher light intensity on the PV cell and the ΔT across the TEG. Figure 5.4 shows the I-V curves of the PV cell in the PV/TEG system when one sun and five suns were applied respectively. Detailed measurement results are presented in Appendix.9.

The light intensity under both one sun and five suns were measured using the pyranometer described in section 3.2 by placing the pyranometer on the position of the receiver, exposing to the reflected light from the concentrating solar parabolic dish. It is clear from Figure 5.4 that increasing the light intensity caused an increase in the I_{SC} of the PV cell.

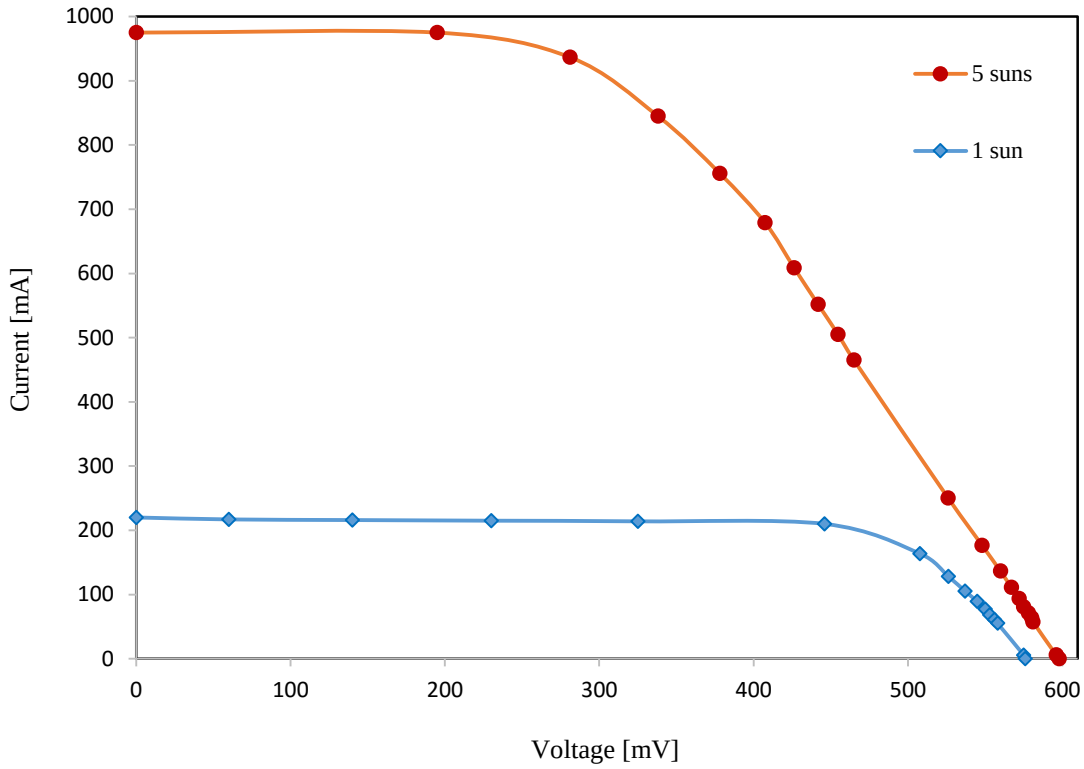

Figure 5. 4 The I-V curves of PV in a PV/TEG hybrid system under 1 sun and 5 suns

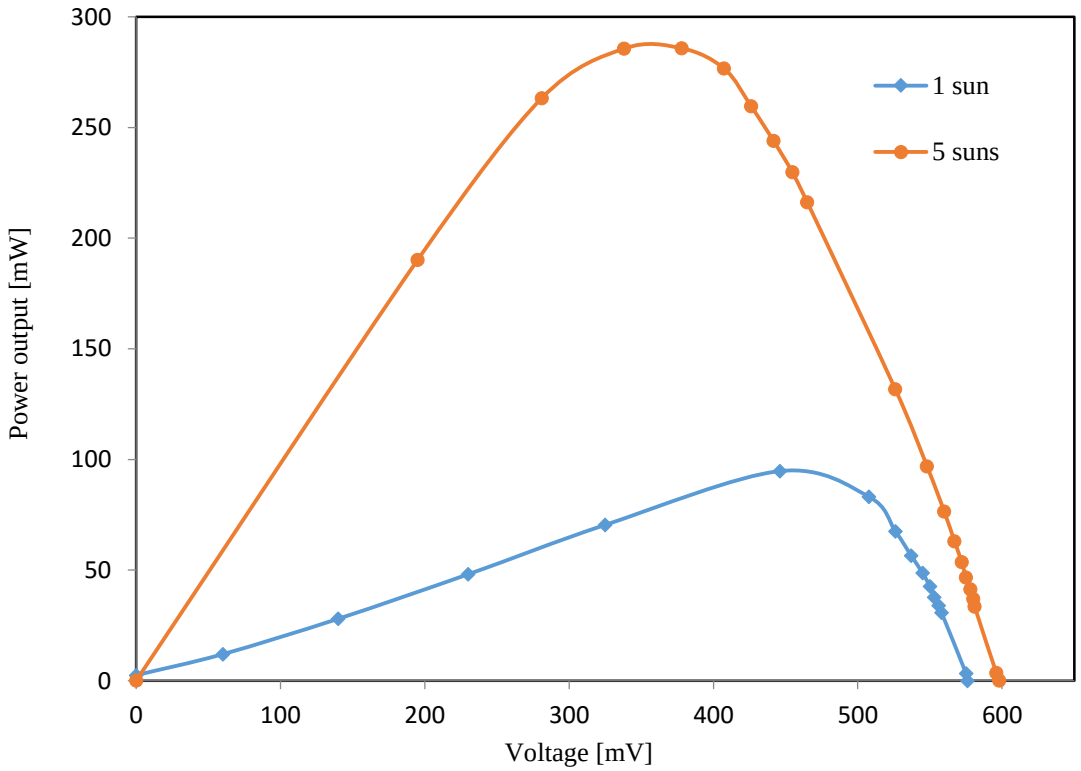

Figure 5. 5 The P-V curves of a PV cell in a PV/TEG hybrid system under 1 sun and 5 suns

The I_{SC} increased linearly with light intensity from 200 mA to 975 mA (i.e. almost a factor five), while the V_{OC} increased slightly. As a result, the P_{PV} increased from 84 mW to 285.7 mW, as can be seen in Figure 5.5. A more detailed of the measured results are presented in Appendix.10.

The I-V curves of a TEG in a PV/TEG system are presented in Figure 5.6.

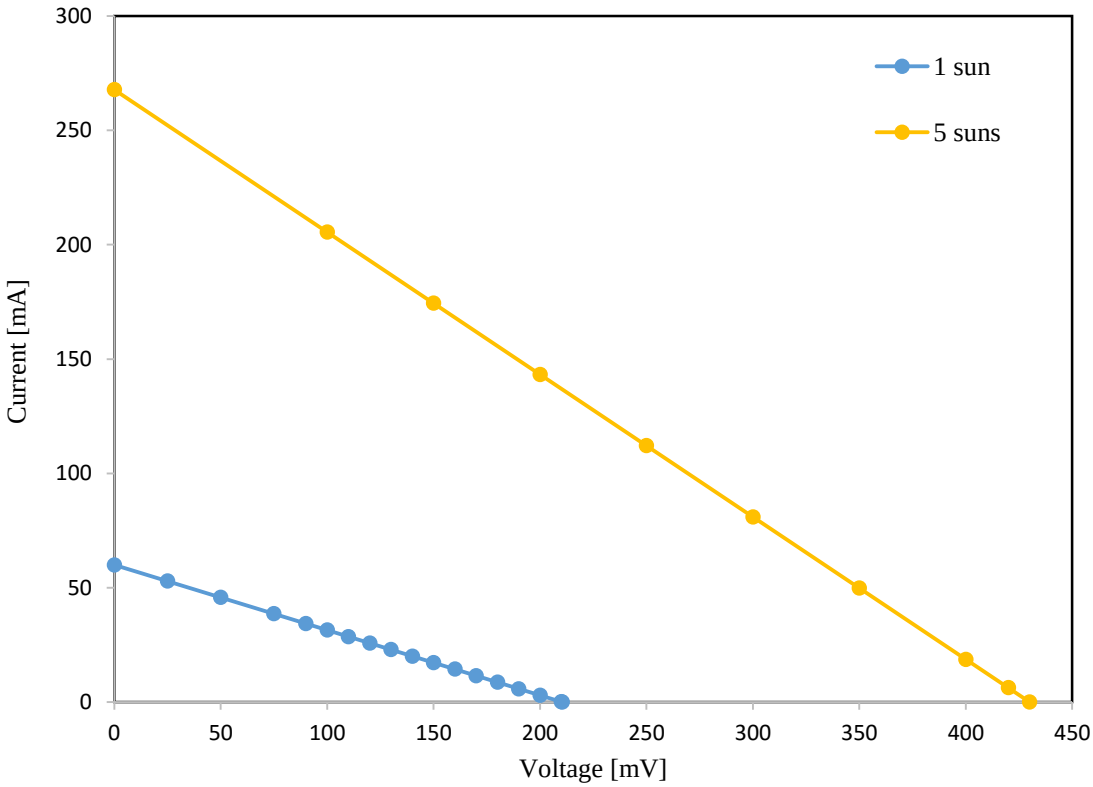

Figure 5. 6 The I-V curves of a TEG in a PV/TEG hybrid system under 1 sun and 5 suns

It can be seen that the V_{OC} and I_{SC} of the TEG were also increased since they both depend on ΔT, and the increased light intensity of five suns increased the ΔT from 4 °C to 13 °C, as shown in Table 5.4. As a result, the P_{max} of the TEG in the PV/TEG system increased from 3.2 mW to 28 mW as shown in Figure 5.7 because the power output of the TEG is a function of ΔT. Consequently, the η_{TE} increased from 0.2% to 0.35%, as can be seen in Table 5.4. The overall power output P_{tot} and efficiency η_{tot} of the PV/TEG hybrid system are also shown in Table 5.4.

Table 5. 4 The characterisation of the PV/TEG hybrid system

No.	T_H (°C)	ΔT (°C)	P_{TE} (mW)	P_{PV} (mW)	P_{tot} (mW)	η_{TE} (%)	η_{PV} (%)	η_{tot} (%)
1 sun	24	4	3.2	83.1	86.3	0.2	6.8	7
5 suns	33	13	28	285.7	313.7	0.35	4.7	5.1

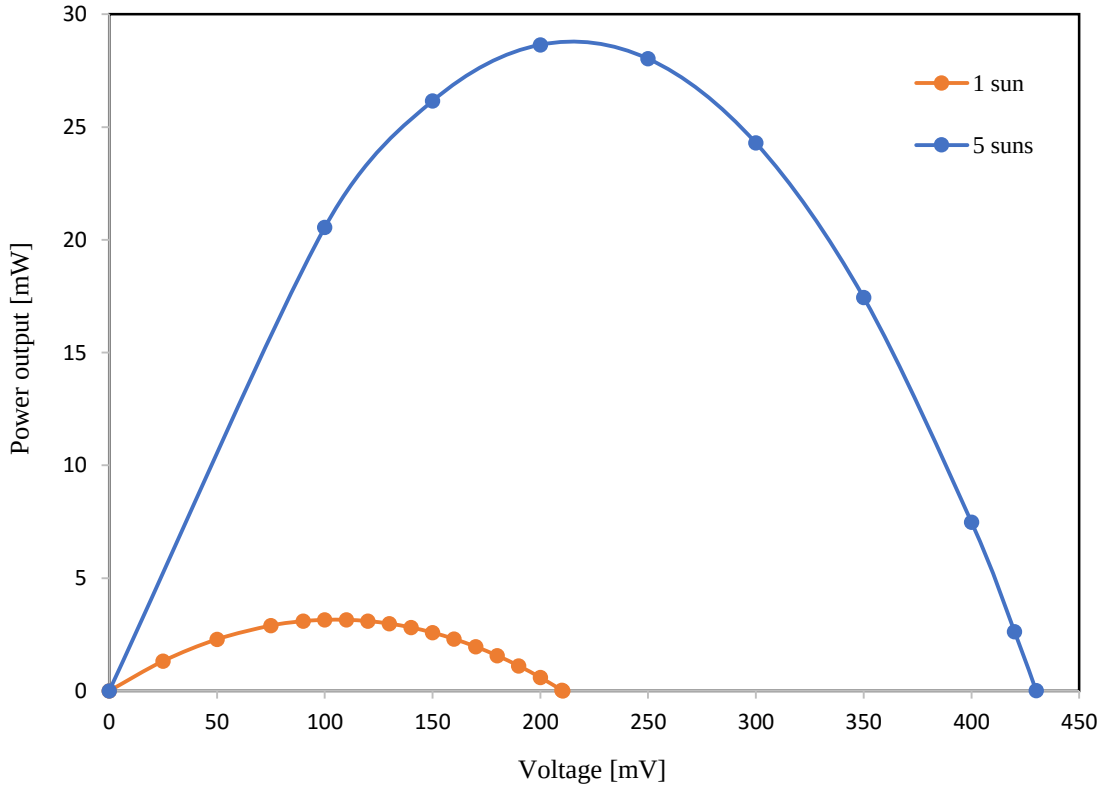

Figure 5. 7 The P-V curves of a TEG in a PV/TE hybrid system under 1 sun and 5 suns

5.2.2 Obtaining higher intensity using solar simulator

5.2.2.1 Experimental Set up

Figure 5.8 shows a photograph of the experimental setup established for this study and a schematic diagram of the system is shown in Figure 5.9. The experimental setup in section 4.5.1 was adopted and improved by including: a flow meter, a DC Pump, a heat exchanger, a DC power supply and type K thermocouples.

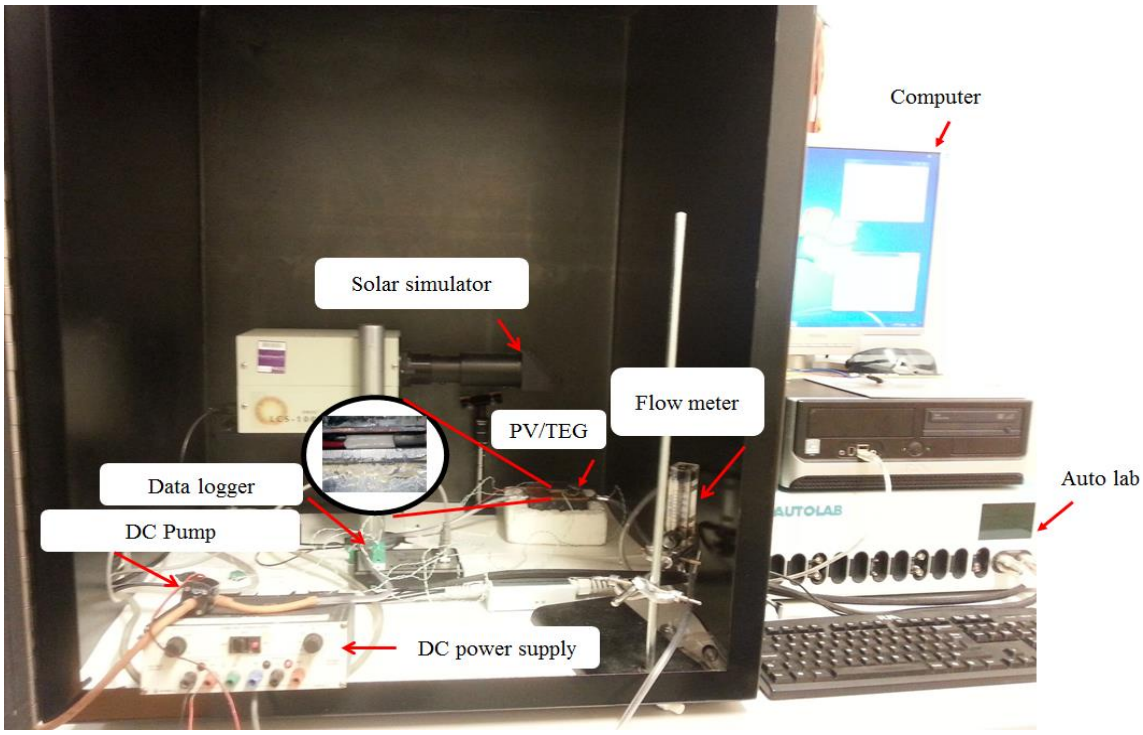

Figure 5. 8 A photograph of the experimental setup

- Flow meter

The water flow meter was purchased from RS (UK-RS/198-3029. http://uk.rs-online.com/web/p/flow-sensors-switches-indicators) and was used to measure the mass flow rate of the cooling fluid. This would allow the heat removed from the cold side of the TEG to be calculated. The specifications and details of the flowmeter are given in Appendix.11.

-DC Pump

A DC pump (model DC30A-1230) was used to circulate the cooling fluid to the heat exchanger. The voltage applied was constant at 3 V, and a photograph of the DC pump is shown in Figure 5.10.

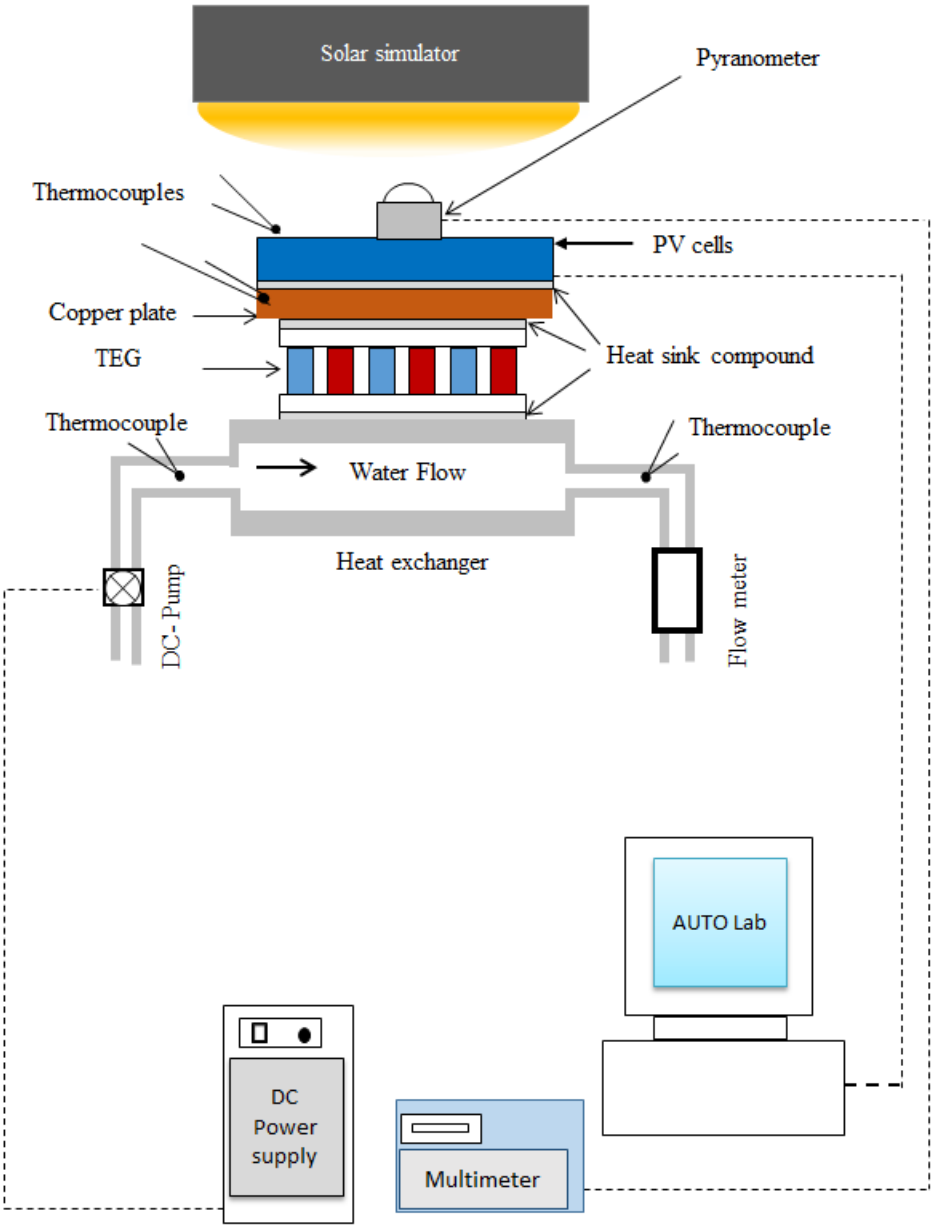

Figure 5. 9 A schematic diagram of the experimental setup

Figure 5. 10 Photograph of the DC pump

- Heat exchanger

A heat exchanger (9 cm X 9 cm X 2.2 cm) was used to transfer the heat effectively from the cold side of the TEG. It consists of a copper plate (9 cm x 9 cm x 0.2 cm) with seven fins (0.7 cm x 0.6 cm x 6 cm), which can remove the heat efficiently from the cold side of the TEG. Figure 5.11 shows a photograph of the heat exchanger.

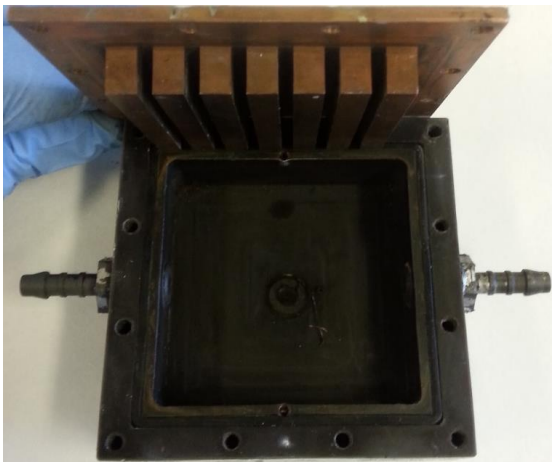

Figure 5. 11 Photograph of the heat exchanger

- DC power supply

A DC power supply (Type UK-FARNEKK) was used to supply the voltage to the DC pump in order to circulate the fluid and take the heat away from the cold side of the TEG.

- Type K thermocouples

Four type K thermocouples were used to measure the temperature in four places. They were positioned to measure: T_H, T_C, the inlet fluid temperature (T_{in}) and the outlet fluid temperature (T_{out}).

5.2.2.2 Results and Discussions

By changing the distance between the solar lamp and the PV surface, the maximum light intensity of 2 suns can be obtained in this system. An increase of light intensity from one sun to two suns was achieved by reducing the distance between the PV and the solar simulator from 18 cm to 10.5 cm. The optimised PV/TEG hybrid system in Chapter four

was selected to apply 2 suns and investigate the P_{tot} and the thermal power (P_{ther}). The PV cell was characterised initially without the TEG by attaching it directly to the cold side of the cooling system. One sun and two suns of light illumination were applied respectively.

Figure 5.12 shows the I-V curves of the PV cell under one sun and two suns. It can be seen that an increase in the light intensity from one sun to two suns resulted in an increase in the I_{SC} from 50 mA to 103 mA (i.e., more than doubled), while the V_{OC} remained almost constant. It can also be seen that the temperature of the PV cell only increased from 25 ^{0}C to 26.5 ^{0}C when the light intensity was increased from one sun to two suns because all the heat was transferred quickly from the PV cell to the heat exchanger.

Subsequently, the TEG was inserted between the PV cell and the cold side of the heat exchanger, which introduce an additional thermal resistance between the PV cells and the cold side of the heat exchanger, depending on the geometry of the TEG. Figure 5.12 also shows the I-V curves of a photovoltaic cell on top of a thermoelectric generator in the hybrid system under 1 sun and 2 suns.

Figures 5.13 shows the P-V curves of the PV cell under one sun and two suns while attached directly to the cold side of the heat exchanger, without the TEG. It can be seen that the P_{max} was also improved by increasing the light intensity.

Figure 5.14 shows the P-V curves for the PV cell on top of a TEG in a hybrid PV/TEG system. An increase in the temperature of the PV cell was observed due to an increase in the thermal resistance between the PV cells and the cold side of the heat exchanger. The temperature of the PV under one sun was 42 ^{0}C in this case and increased to 51 ^{0}C under two suns.

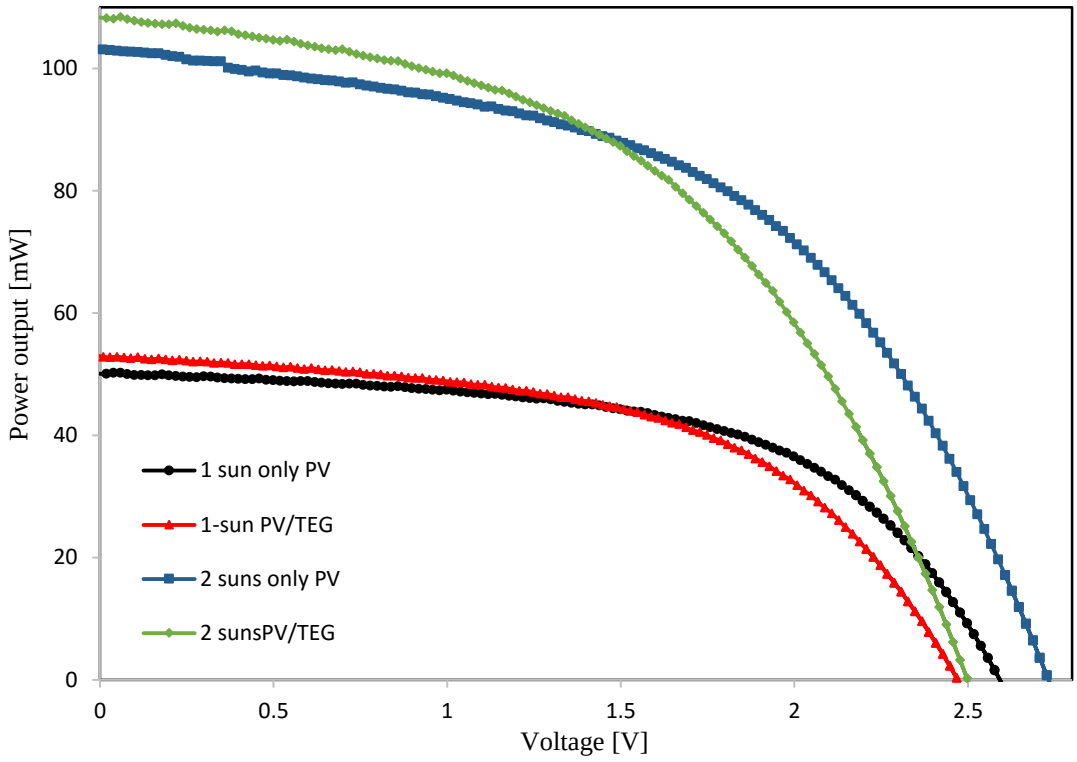

Figure 5. 12 The I-V curves of photovoltaic cell alone under 1 sun and 2 suns, and a photovoltaic cell on top of a thermoelectric generator in the hybrid system under 1 sun and 2 suns

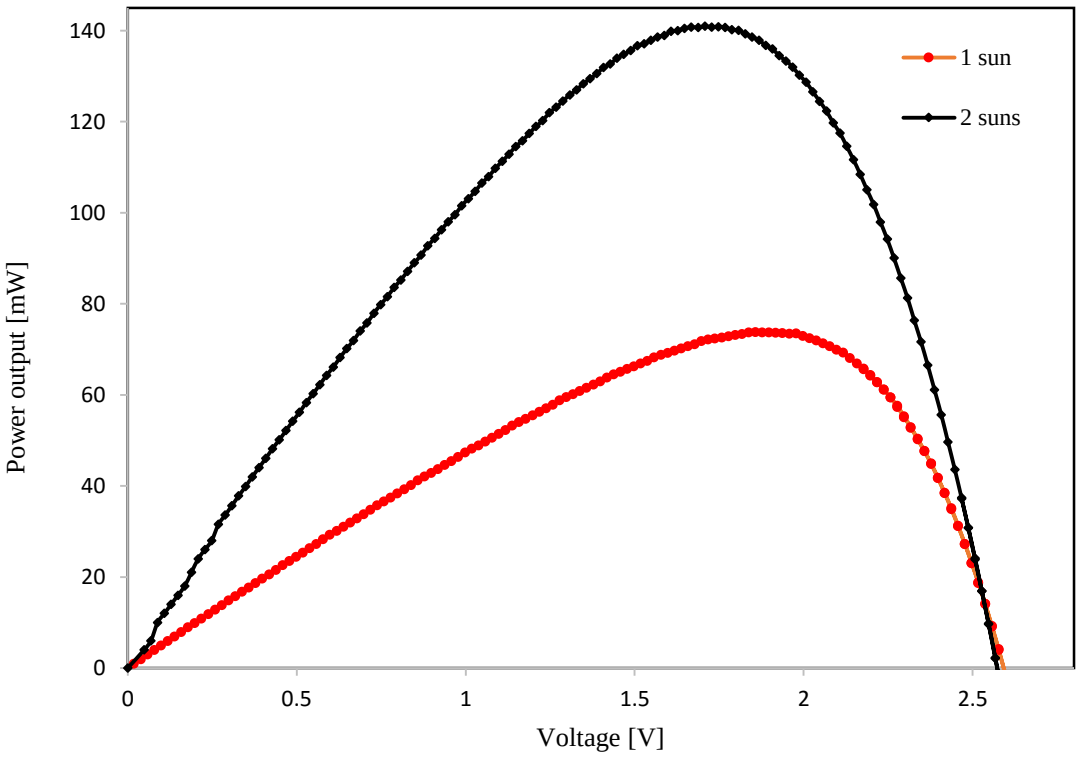

Figure 5. 13 The P-V curves of the photovoltaic cell alone under 1 sun and 2 suns

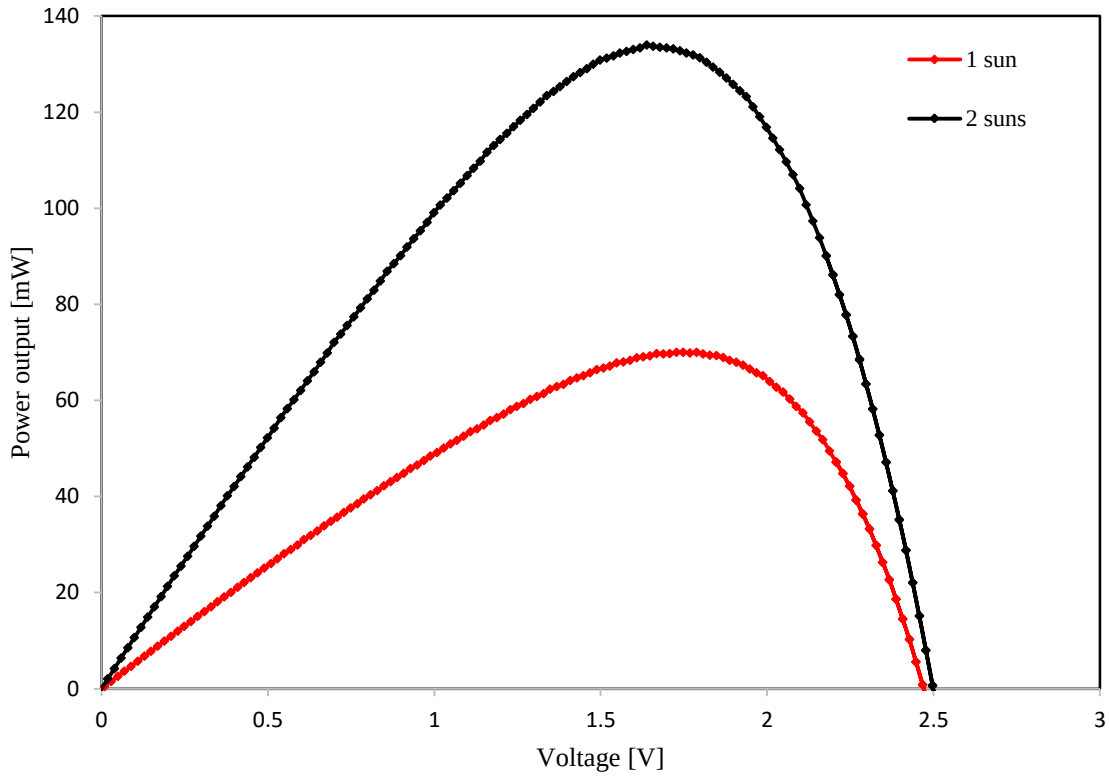

Figure 5. 14 The P-V curves of a photovoltaic cell on top of a thermoelectric generator in the hybrid system under 1 sun and 2 suns

The increase in the temperature of the PV cell caused a drop in P_{max} from 74 (mW) to 71.4 (mW) under the one sun illumination. This represents a decrease of the power output by 3.5 %. A decrease by 4.5 % was observed for the case of two suns illumination.

The power output of the TEG in the PV/TEG hybrid system was measured under the same test conditions. The I-V and P-V curves for the TEG are presented in Figures 5.15 and 5.16 respectively. Unlike in the PV cell, both I_{SC} and V_{OC} of the TEG were increased with increasing ΔT as shown in Figure 5.15. The increase in the V_{OC} of the TEG was significant, from 0.21 V to 0.38 V, representing an increase by 81 %.

There was a power gain from TEG when moving from one sun and two suns as shown in Figure 5.16. The power generated from the TEG in the hybrid PV/TEG system was 5.6 mW under one sun, and 18 mW under two suns because the ΔT across the TEG was increased from 17 ^{0}C under one sun to 26 ^{0}C for two suns.

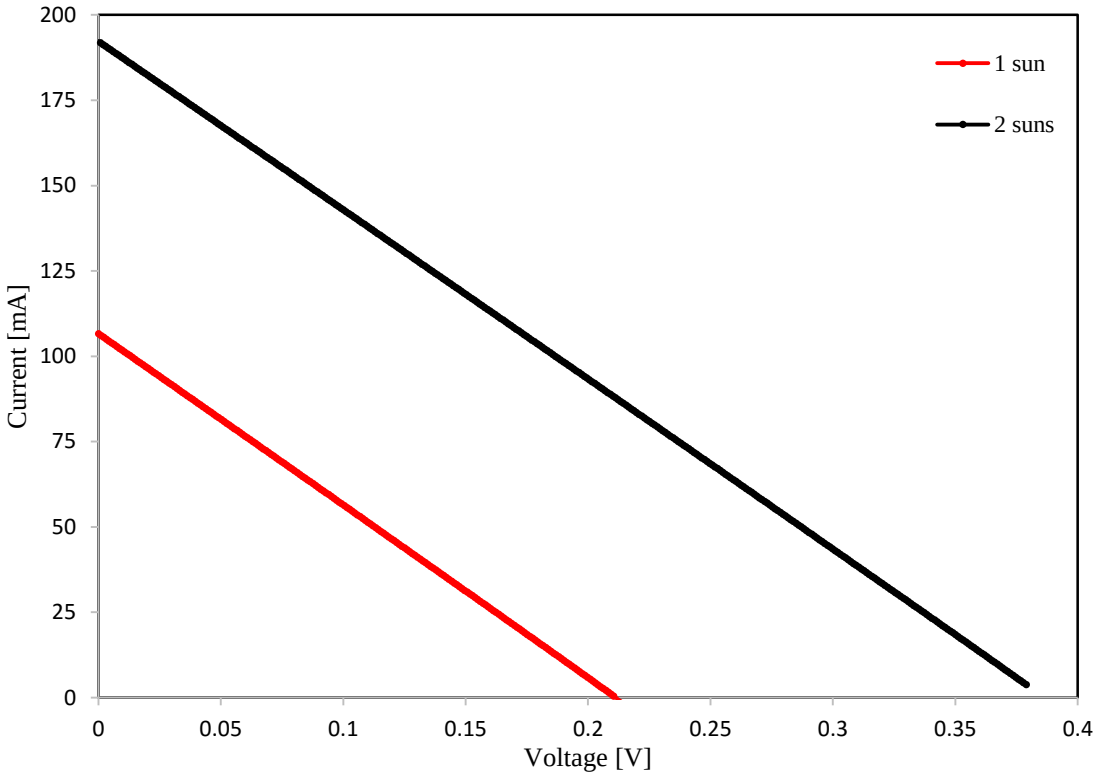

Figure 5. 15 The I-V curves of a thermoelectric generator in the hybrid system under 1 sun and 2 suns

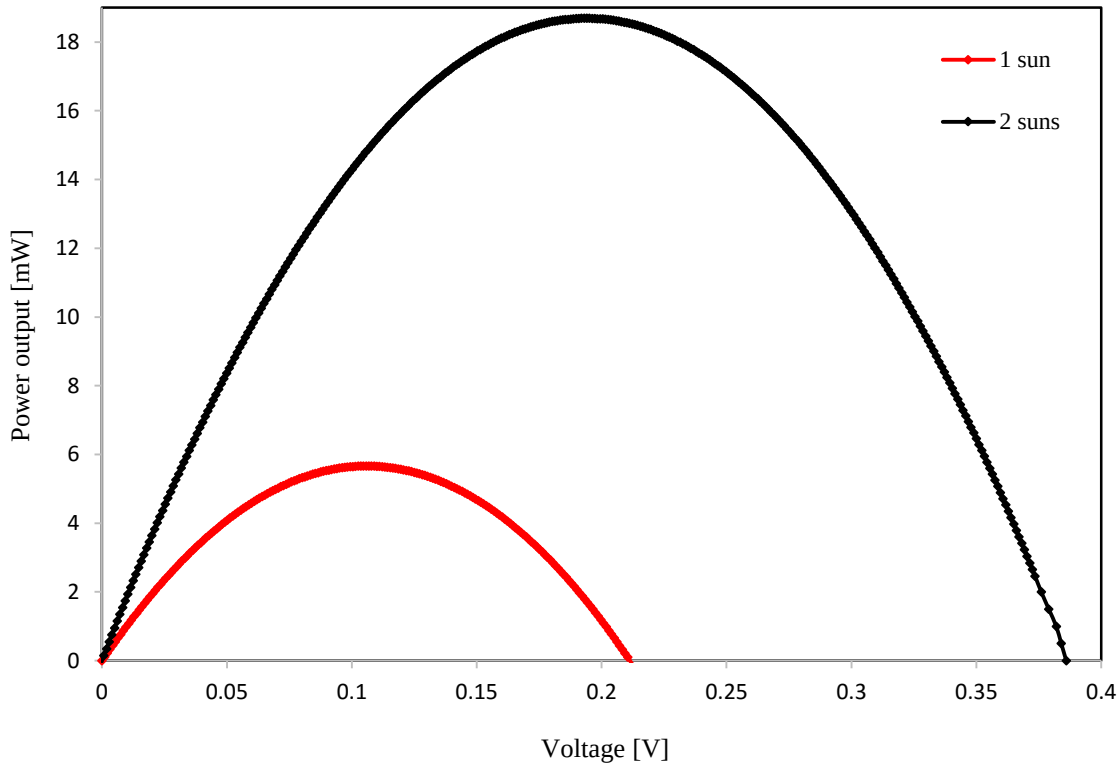

Figure 5. 16 The P-V curves of a thermoelectric generator in the hybrid system under 1 sun and 2 suns

As a result, an increase in the overall power output of the hybrid system (P_{tot}) due to integrating the TEG is achieved, which is of about 4 % under one sun and 8.9 % under two suns, respectively as shown in Table 5.5.

The η_{PV}, η_{TE} and η_{tot} are presented in Table 5.5. It can be seen that there is an increase of 6.5 % under one sun and 8.9 % under two suns due to the top-up power from the TEG. It is interesting to mention here, the η_{TE} was calculated using the total power input to the system.

Table 5. 5 The maximum power output and conversion efficiency of TEG, PV and PV/TEG under one sun and two suns

No	P_{PV} (mW) single	η_{PV} (%) Single	$P_{TE\text{-}max}$ (mW) in PV/TEG	$P_{PV\text{-}max}$ (mW) in PV/TEG	η_{TE} (%) in PV/TEG	η_{PV} (%) in PV/TEG	P_{tot} (mW)	η_{tot} (%)
1	74	4.6	5.6	71.4	0.4	4.5	77	4.9
2	140	4.4	18.8	133.9	0.6	4.2	152.7	4.8

Clearly, integrating TEG with PV can improve the power output from the system and has little effect on removing heat from the PV cell to the heat exchanger, which will help to increase the lifetime of PV, in particular if the operating temperature of the PV is close to room temperature.

5.3 The second strategy

The second strategy involved study the effect of changing mass flow rate on the performance of PV/TEG hybrid system by using the same experimental setup in Figures 5.8 and 5.9.

5.3.1 Results and discussion

The value of the mass flowrate (m) was changed five times; m1, m2, m3, m4 and m5) between 0.00008 kg/s and 0.0015 kg/s to see the effect on the power output of TEG and PV cell.

Figure 5.17 and 5.18 show the I-V and P-V curves of PV cells respectively in hybrid PV/TEG for different mass flow.

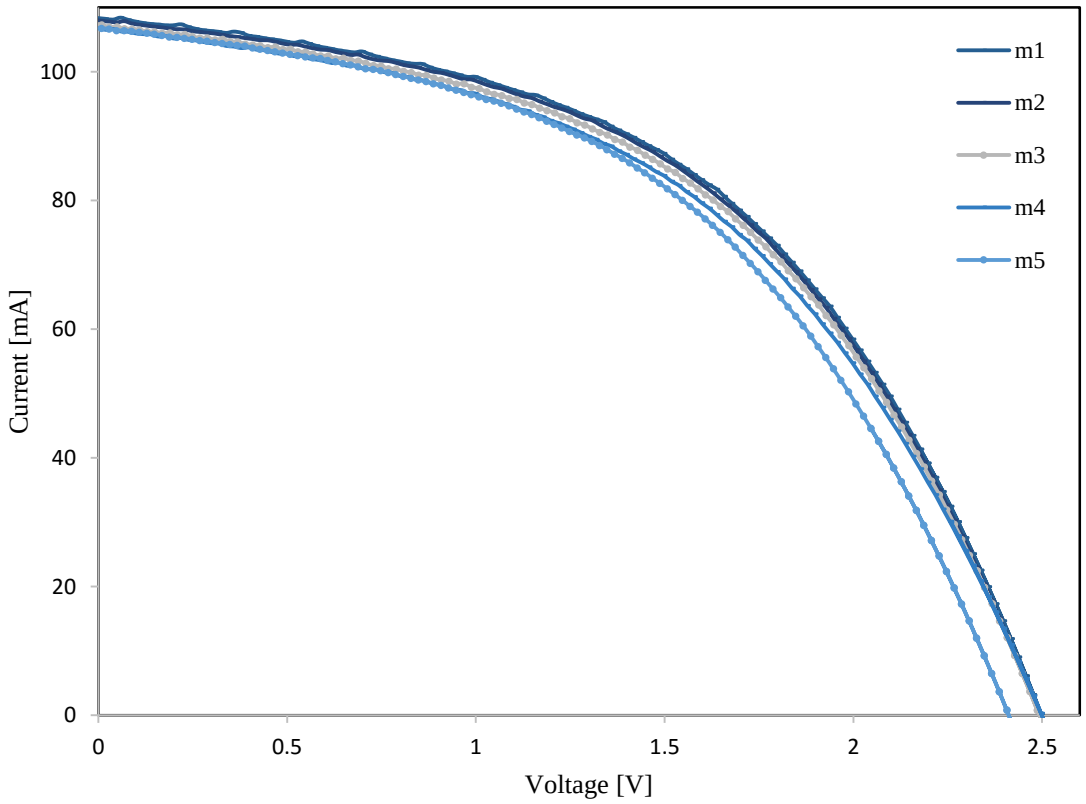

Figure 5. 17 The I-V curves of photovoltaic cells at different mass flow rates

It can be seen that the increase in the mass flowrate increased both the V_{OC} and P_{max} of PV cells because an increase in the mass flow rate increases the cooling rate. The change in the V_{OC} was very small because the PV cells were a-Si which are not highly affected by temperature. As a result, the T_C and T_H decreased, meaning that the operating temperature of the PV cells was decreased.

Furthermore, increasing the mass flow rate caused an increase in the V_{OC} and I_{SC} of TEG in the PV/TEG hybrid system as shown in Figure 5.19. This is because an increase in the mass flowrate caused an increase in the ΔT cross the TEG (see Appendix.12). The P_{max} of TEG also increased as a result of increasing the V_{OC} and $I_{SC,}$ as shown in Figure 5.20.

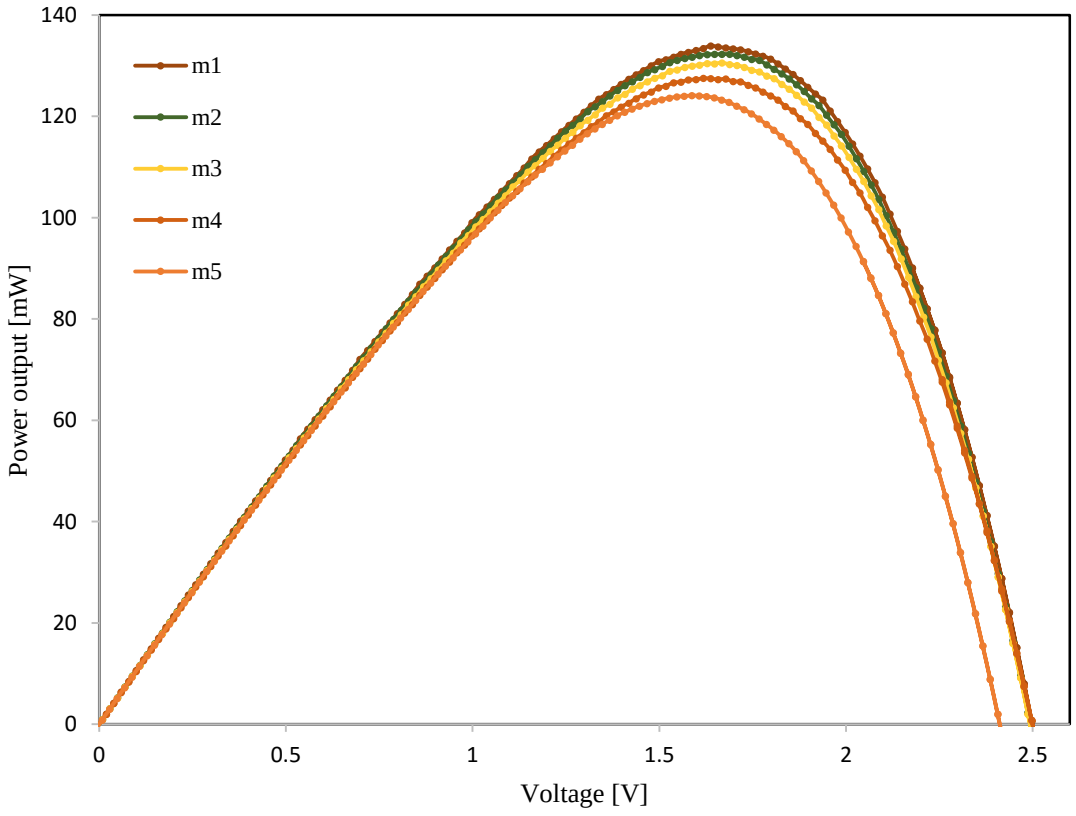

Figure 5. 18 The P-V curves of photovoltaic cells at different mass flow rates

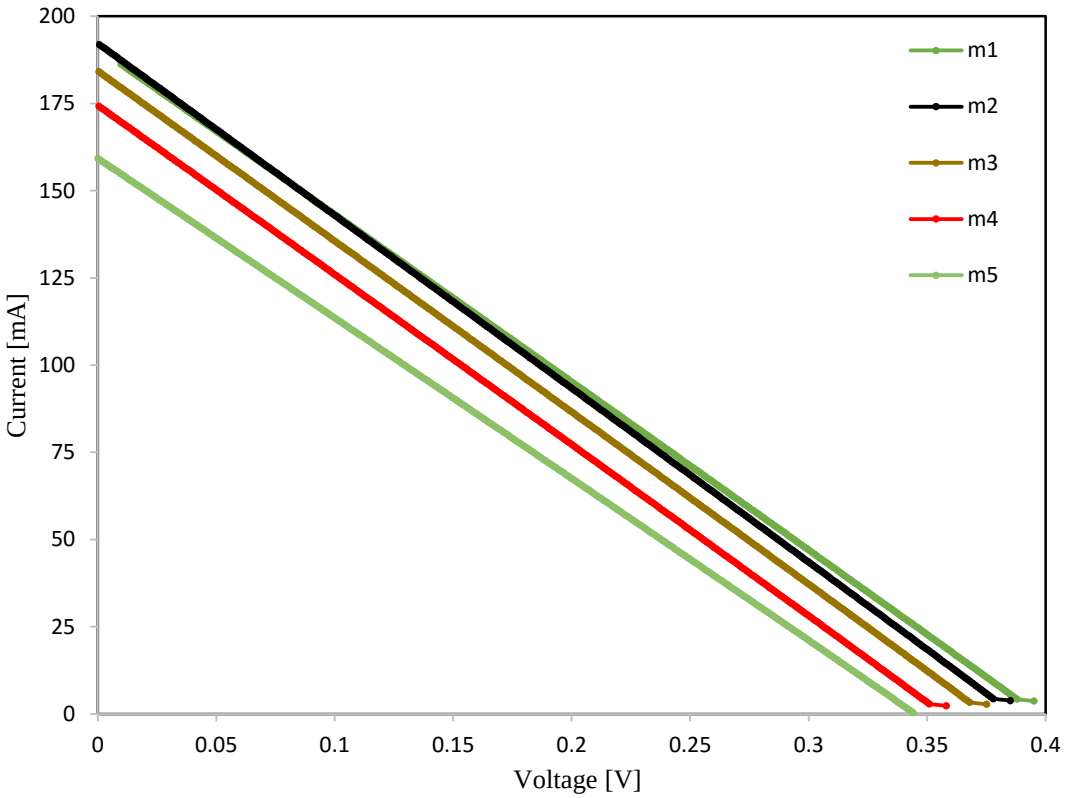

Figure 5. 19 The I-V curves of the thermoelectric generator, at different mass flowrates

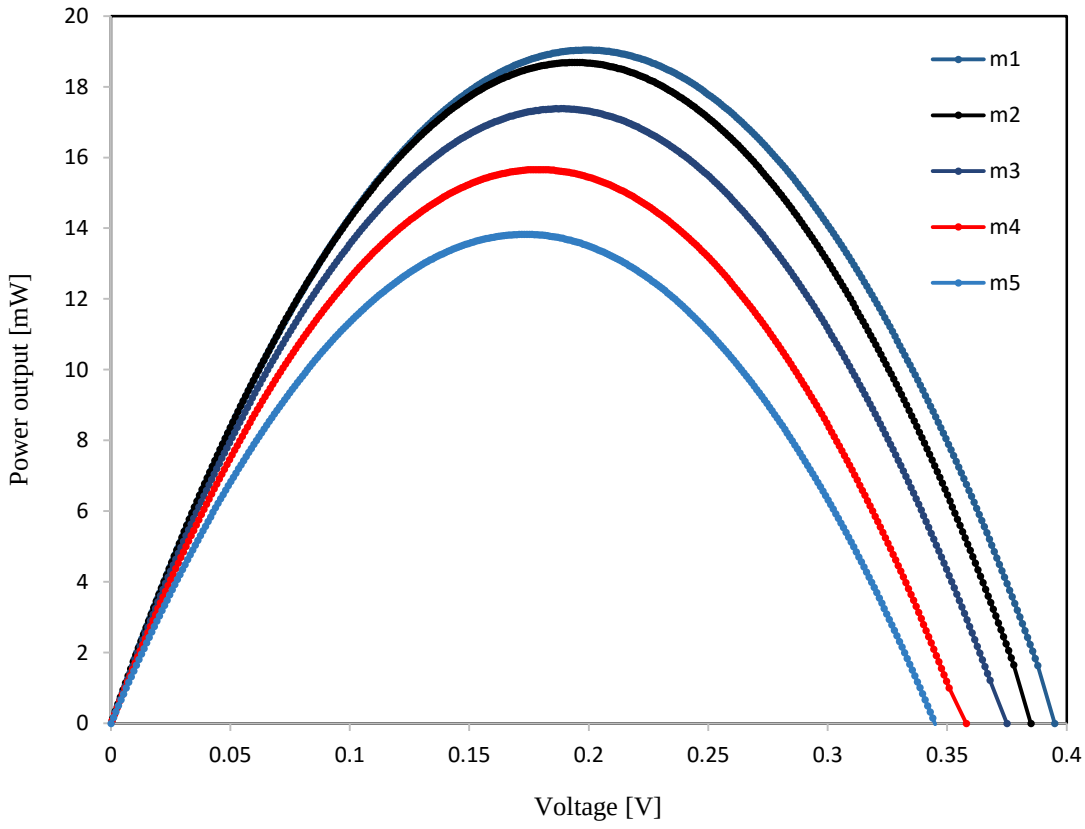

Figure 5. 20 The P-V curves of a thermoelectric generator at different mass flow rates

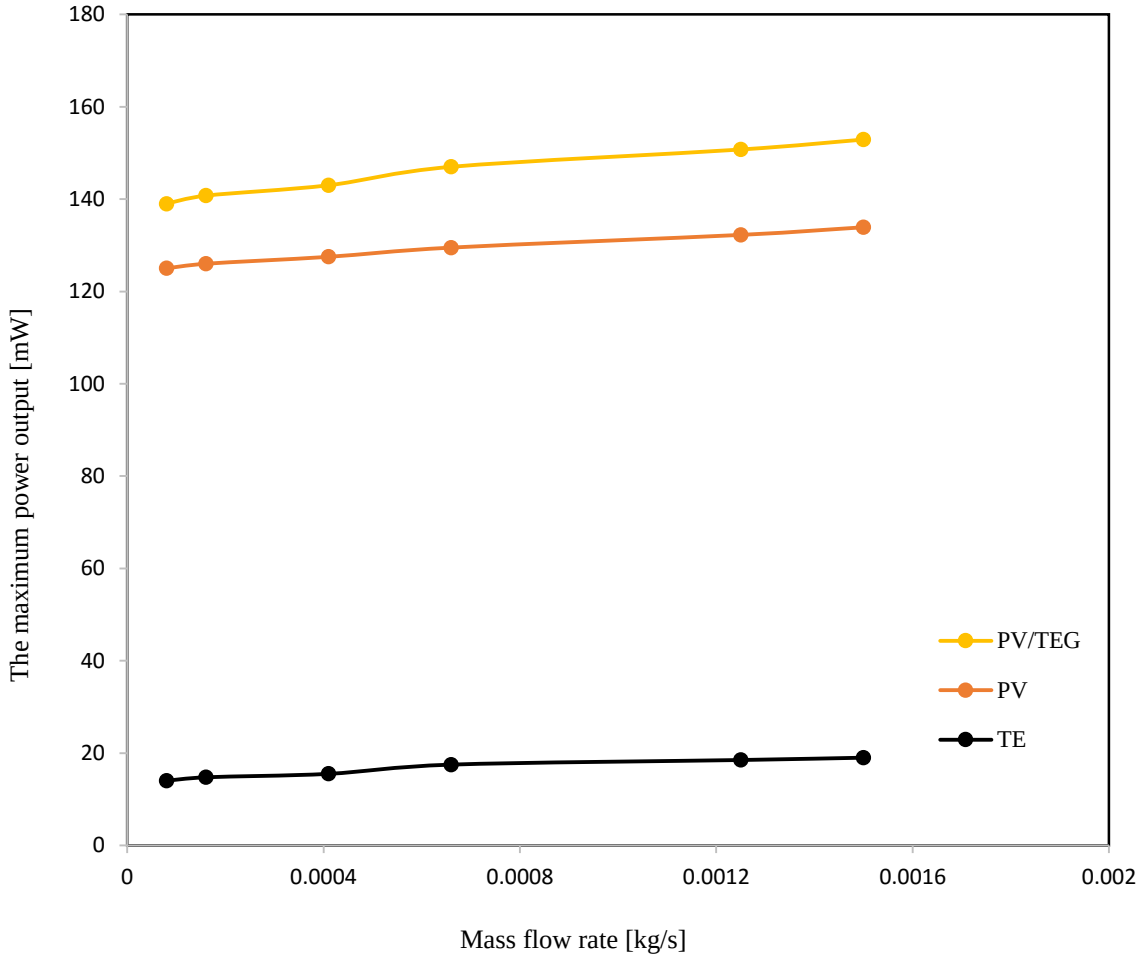

Figure 5. 21 The maximum power output power vs mass flowrate for PV, TEG and PV/TEG

Figure 5.21 shows the P_{max} of PV cell, TEG and P_{tot} as a function of mass flowrate. It can be seen that the P_{max} was increased by increasing the mass flowrate because increasing the mass flowrate resulted in an decrease in the temerapture of the PV cell, T_{cell}, and an increase in the temperature difference across the TEG, ΔT.

Consquently, the η_{TE}, η_{PV} and η_{tot} were increased with increasing mass flowrate, as shown in Figure 5.22.

The rate of thermal energy ($\dot{Q}_{ther}$), or the heat removed from the cold side of TEG, can be calculated using the following equation:

$$\dot{Q}ther = \dot{m}c_p\Delta T_f \quad 5.1$$

where $\dot{m}$ is the mass flowrate, c_p is the specific heat, and ΔT_f is the temperature difference between the inlet and outlet fluid.

The $\dot{Q}_{ther}$ was calculated at $\dot{m}$ = 0.00041 kg/s (measured using the flow meter in Figure 5.8), c_p = 4200 J/kg.K (for water) and ΔT_f = 1.1 ^{0}C, which represent the difference between the temperatures of outlet and inlet fluid that are measured using K-type thermocouples (see Appendix.13). It was found to be equal to 1.89 W.

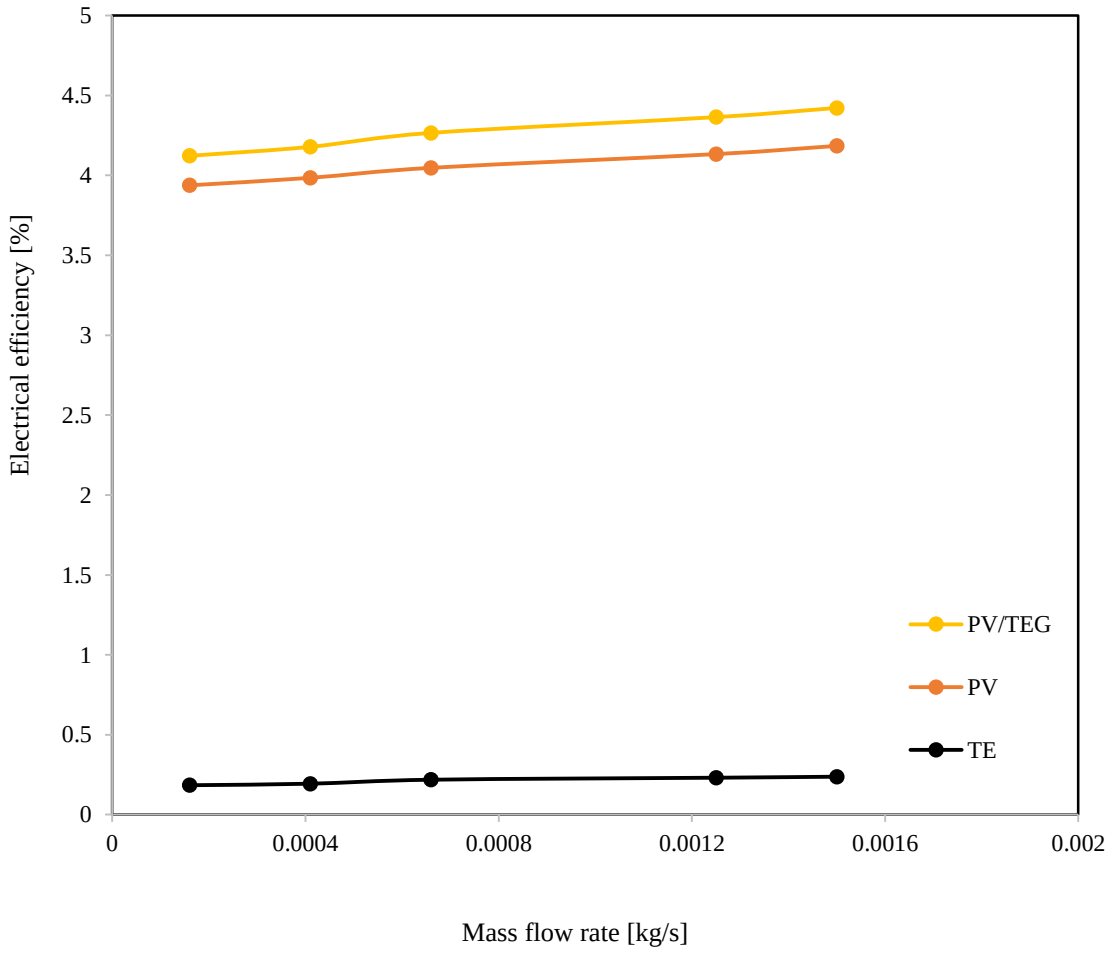

Figure 5. 22 The electric efficiency of PV, TEG and PV/TEG vs mass flowrate

Consequenly, the thermal efficiency (η_{ther}) was calculated by using the following equation:

$$\eta_{ther} = \frac{\dot{Q}_{ther}}{Q_{in}} \quad 5.2$$

where, the Q_{in} is the total power input to the system and it was calculated as:

$$Q_{in} = G * A_{PV} \quad 5.3$$

The $\boldsymbol{\eta}_{ther}$ was calculated at G= 2000 W/m^2 and A_{PV} = 4cm x 4cm, and it was found to be equal to 59.1 %.

In summary, the increase of light intensity increased the I_{SC} and P_{max} for PV cells. For TEG, the light intensity contributed to an increase in the V_{OC}, I_{SC} and P_{max} due to an increase in ΔT. Similarly, the increase in the mass flow rate can also improve P_{TE}, P_{PV},P_{tot},η_{TE}, η_{PV} and η_{tot}.

Adding nanoparticles to a base fluid such as pure water can change the physical properties of the base fluid [109][110]. Nonofluid was prepered and used as a coolant in the cooling system of the PV/TEG hybrid system. The results were compared with the pure water which was the reference fluid (see Appendix.14).

5.4 Conclusions

Integrating TEG with PV cells caused an increase in the operating temperature of the PV cells due to an additional thermal resistance introduced by the TEG. The temperature difference across TEG was higher under the solar concentrating system, which generate more power from TEG.

On the other hand, an increase in the light intensity reaching the PV cells caused a significant increase in the I_{SC} and the P_{max} for PV. However, the I_{SC} and the V_{OC} of the TEG were increased with increased light intensity, and as a result the P_{max} of TEG was increased from 5.6 mW to 18 mW. This is an increase of more than 200 %.

An increase in the mass flowrate of the fluid in the heat exchanger can increase the P_{max} from both the PV cells and the TEG by 6.8 % and 38.28 % respectively, and the η_{tot} also increases with increasing mass flowrate.

Since a-Si showed a lower drop in P_{max} with increasing temperature, the DSC presents an interesting increase in P_{max} with increasing temperature, which makes DSC a better candidate for integrating with TEG. Also, a-Si is fabricated on conductive glass, which is not a good conductor of heat to the TEG. The next chapter will discuss the fabrication of metallic DSC and the integration with TEG modules.

CHAPTER SIX - FABRICATION, CHARACTERISATION AND OPTIMISATION OF DSC FOR HYBRID SYSTEM

6.1 Introduction

In this chapter, the fabrication of DSC with fluorine-doped tin oxide (FTO) glass and metallic counter electrode is presented. The difficulties, obstacles and challenges associated with the procedure of fabrication are addressed, with an emphasis on developing efficient DSC using metallic counter electrode. The objective is to enhance the heat transfer between the PV cell and the TEG by optimising the thermal coupling between the DSC and the TEG. The procedure of fabrication is explained and two types of DSCs are fabricated. The first contains an FTO-glass counter electrode (G-SC) and the second uses titanium as the counter electrode (Ti-SC). The thermal coupling of these two types of DSCs was investigated by integrating with TEG to fabricate a hybrid tandem cell (HTC). TEGs with three different numbers of elements (N), cross sectional areas (A_C) and thermoelements length (L_{TE}) values were employed and optimisation study was conducted to find the optimum geometry of TEG for HTC.

6.2 Fabrication of Dye Sensitised Solar Cells

The flowchart in Figure 6.1 explains the procedure of DSC fabrication which includes the manufacture of the working electrode, dye, electrolyte and counter electrode, and DSC assembly.

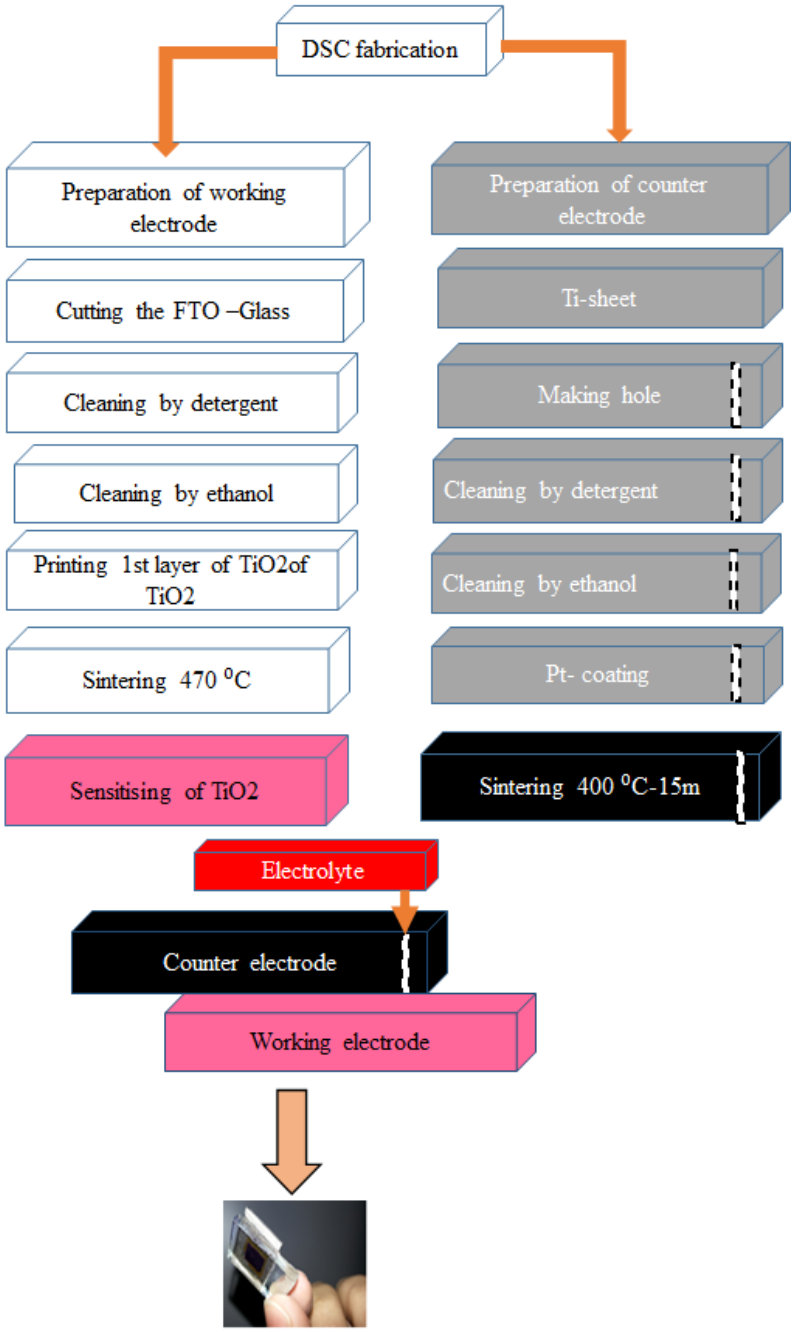

Figure 6.1 Flowchart of the DSC fabrication procedure

To date, most of DSCs are prepared using a common material, FTO – glass, for the working electrode and counter electrode. Few researchers have used different materials for both electrodes, such as flexible stainless steel [23]. This research concentrates on using FTO-glass for the working electrode, while using FTO-glass or metals for the counter electrode for comparative study of their thermal coupling with TEG.

6.2.1 Preparation of the working electrode

6.2.1.1 Cutting the FTO glass (15Ω/□).

The FTO-glass sheet (NSG, 3 mm thickness, 15Ω/□) was divided by ruler into small rectangular pieces (2 cm x 1.5 cm), and a glass cutter was used to make groove around the rectangular pieces as shown in Figure 6.2a. Breaking pliers were then used to snap off the FTO-glass segments as shown in Figure 6.2b.

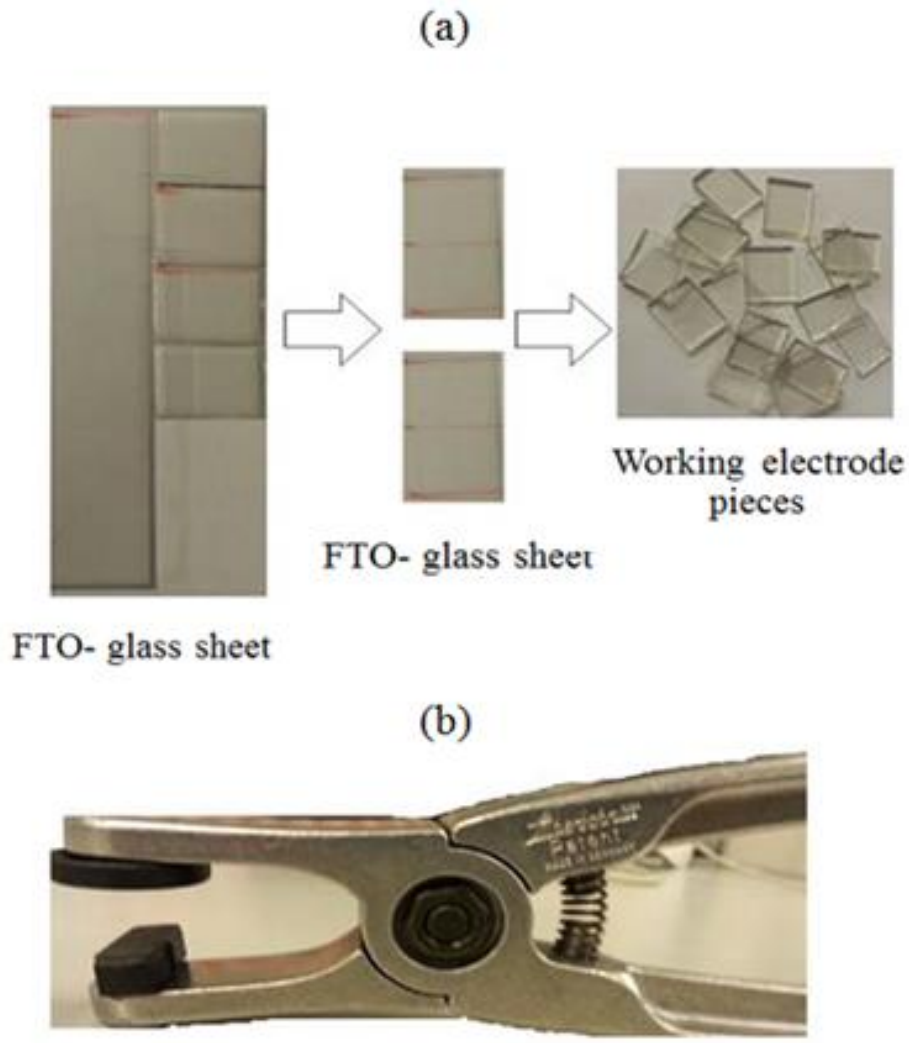

Figure 6.2 The cutting of FTO-glass: (a) process of cutting FTO-glass; (b) a photograph for the breaking pliers

6.2.1.2 Cleaning the FTO-glass.

The FTO-glass pieces were cleaned with detergent using a sonicator bath for 15 minutes, and then with ethanol for an additional 15 minutes sonication in order to remove all the organic substances that may be present on the surface.

6.2.1.3 Deposition of nanocrystalline titanium dioxide (TiO_2) layers.

Scotch tape was gently placed on the FTO-glass to form a square template with an area of 6 mm x 6 mm. The TiO_2 transparent layer, which was a paste of crystalline nanoparticles (18NR-T / Dyesol) was placed near the template and spread gently using a glass rode by the Doctor Blade method [23][111] in one direction, as shown in Figure 6.3.

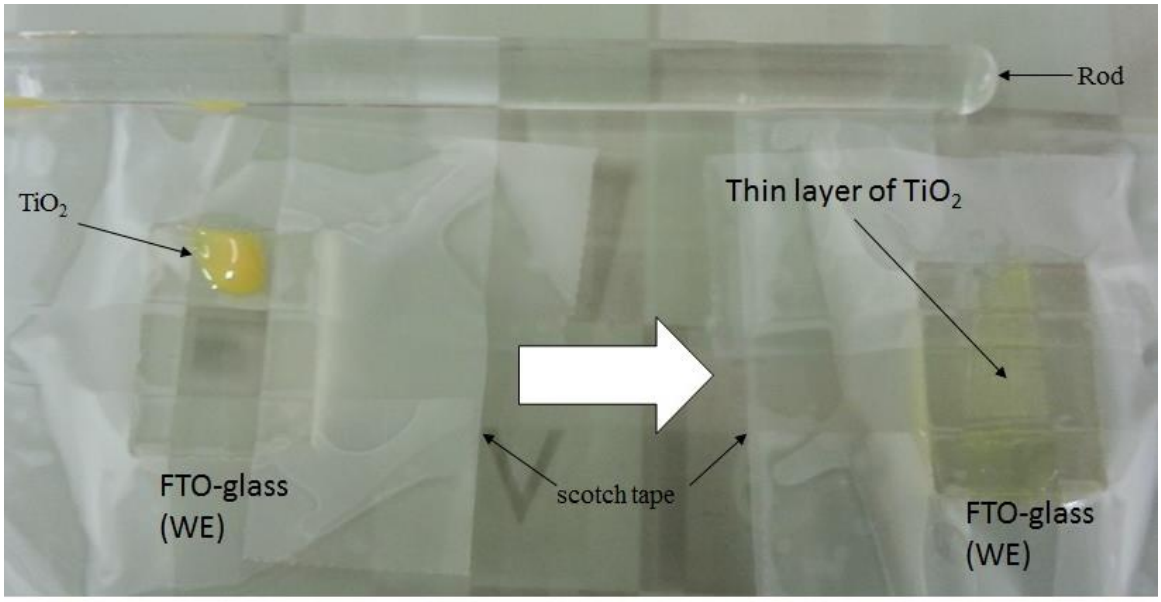

Figure 6. 3 Doctor Blade method for printing TiO2

The procedure was repeated twice to obtain the optimum thickness of TiO_2. A hot plate was used to heat the sample to 150 ^oC for 10 minutes between the two procedures to dry the TiO_2 paste at room atmosphere. Figure 6.4 shows two samples placed on the hot plate.

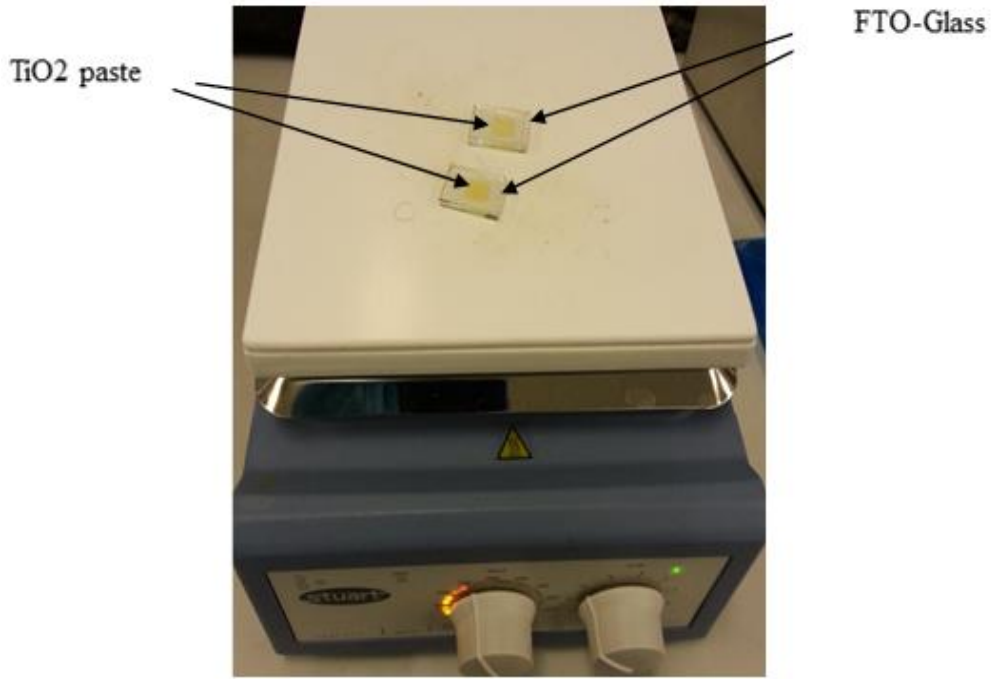

Figure 6. 4 A photograph for the hot plate

6.2.1.4 Sintering in the furnace.

The TiO_2 thin layer prepared on the FTO-glass was sintered at 470 ^oC for 30 minutes in a furnace shown in Figure 6.5. A programme was fixed to increase the temperature of the furnace gradually (3 degree/minute) in order to avoid the cracking that might be occurred in the TiO_2 layer during the sintering and the overall process is required about 6 hours to complete. The samples were left in the furnace overnight to cool down to room temperature. By this time the TiO_2 layer had converted to transparent nanocrystalline TiO_2. Figure 6.6 shows the scanning electronic microscopy (SEM) image of the sintered TiO_2.

6.2.1.5 Sensitising of TiO_2 in dye

N-719 dye from Dyesol was dissolved in ethanol and the TiO_2 film was immersed in a jar of this solution for 24 hours in order to sensitise the TiO_2. Figure 6.7 shows the process of sensitisation.

Figure 6. 5 Furnace used for the working electrode

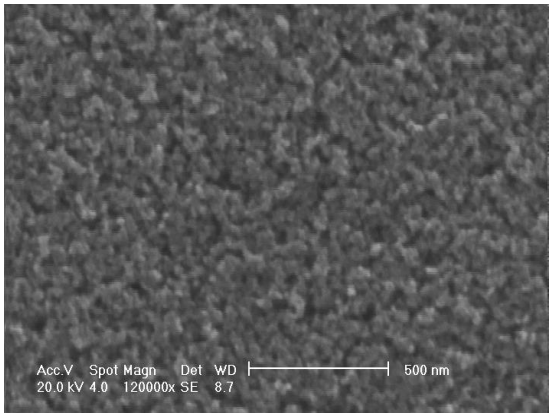

Figure 6. 6 SEM image of the TiO2 nanoparticle

Figure 6. 7 The samples inside the dye solution

6.2.2 Preparation of the counter electrode

In this research, two types of counter electrode were investigated. The first was FTO-glass, while the second was metallic plate. For the metallic counter electrode, different metals were investigated, including copper, aluminium, nickel, silver, stainless-steel and titanium. Copper, aluminium, nickel, silver, and stainless-steel showed poor performance and the η_{PV} was lower than 1 %. Some reasons behind the low performance include the platinum layer deposited on the surface of these metal not being very well attached and therefore being very easy to remove by hand. All the metals used in the experiment presented the problem of corrosion between the electrolyte and the metal, which was observed by a changing in the colour of the metal a few hours after the electrolyte being deposit onto the surface.

However, there was no corrosion observed in titanium over the course of three months. In addition, titanium has a low electrical resistance [112], below 1 ohm. The DSC made with a titanium counter electrode (Ti-SC) showed the best performance among all other metals investigated in this study, even better the G-SC.

6.2.2.1 Cutting the FTO-glass

The same procedure mentioned in section 6.2.1.1 is used here to prepare the FTO-glass (8Ω/□) counter electrode. It is to be noted that the FTO-glass was cut into the same size of the working electrode.

6.2.2.2 Cutting the titanium sheet

A titanium (Ti) sheet (1 mm thickness) with (99.99 % purity**,** from GoodFellow) was cut into small pieces of the same size as the working electrode. A cutter machine was used to

cut the titanium sheet. A photograph of the titanium sheet is presented in Figure 6.8a and the Ti pieces are shown in in Figure 6.8b.

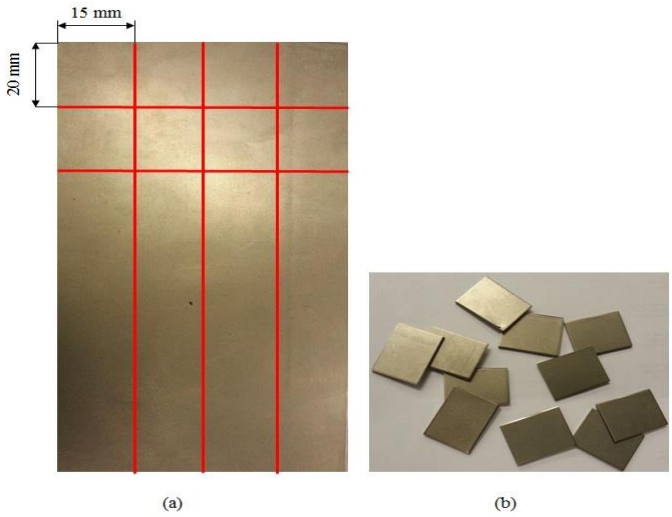

Figure 6. 8 Titanium (a) sheet and (b) pieces

After cutting, edges of the surface were rough. These rough edges were removed by sand paper to avoid them causing a short circuit that would damage the DSC cell at an early stage.

6.2.2.3 Preparation of the opening for electrolyte injection

A hole of 1 mm in diameter is required for injecting the electrolyte into the assembled cell. In principle, this can be achieved easily by any drilling device. However, a special care is needed to drill the FTO-glass to avoid possible damage, crack and dust. Figure 6.9 shows a photograph of the drilling setup. A diamond drill bit purchased from UK-Eternal-tools was used to make the hole. During drilling, the counter electrode (particularly FTO-glass) was placed on a sample holder which was immersed in water. It was drilled from the conductive side of the FTO-glass because the drill bit can damage the conductive layer during exit if the drilling process started from the nonconductive side. Meanwhile, a different drill bit was used for the Ti pieces. This was a high speed steel drill bit purchased from UK-Machine Mart.

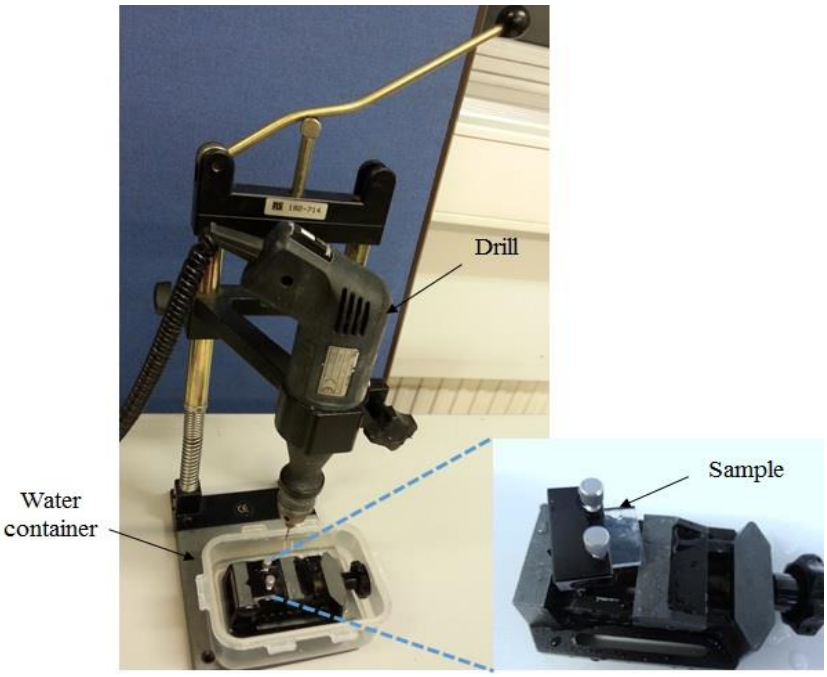

Figure 6. 9 A photograph of the drilling process

6.2.2.4 Deposition of platinum

Platinum nanoparticles were attached to the surface of the FTO-glass and to the Ti plate by spreading a few drops of a platinum solution (CELS Counter-Electrode Solution, from Dyesol). A glass rod was used to spread the solution by the doctor blade method.

6.2.2.5 Sintering in the furnace

A photograph of the furnace used in this work is shown in Figure 6.10. The FTO-glass and titanium pieces were sintered in air in this furnace. The temperature was maintained at 400 ^{0}C for 15 minutes. It is important to note that the furnace used was a different one to that used for the working electrode, in order to avoid possible cross contamination problems that might occur. The samples of both the FTO-glass and Ti were left in the furnace overnight to cool down. Figure 6.11 shows the counter electrode before and after the deposition of the platinum and sintering in the furnace.

Figure 6. 10 Furnace used for the counter electrode

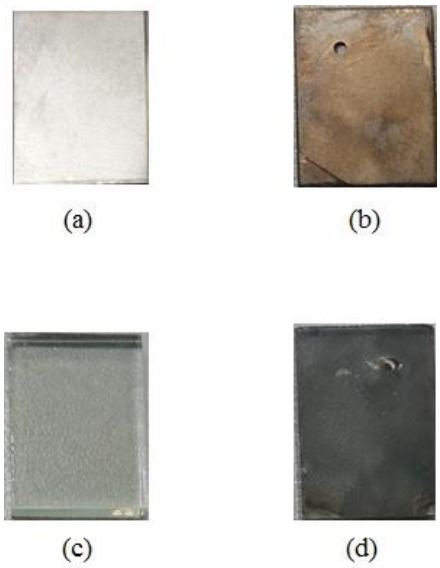

Figure 6. 11 A photograph for the counter electrode: (a) titanium before platinum coating, (b) titanium after platinum coating, (c) FTO-glass before platinum coating, and (d) FTO-glass after platinum coating

Both FTO glass and Ti samples were inspected by SEM (see Figures 6.12 and 6.13). It is clear that the platinum nanoparticles were attached to the substrate from the solution. The average size of the particles was 250 nm.

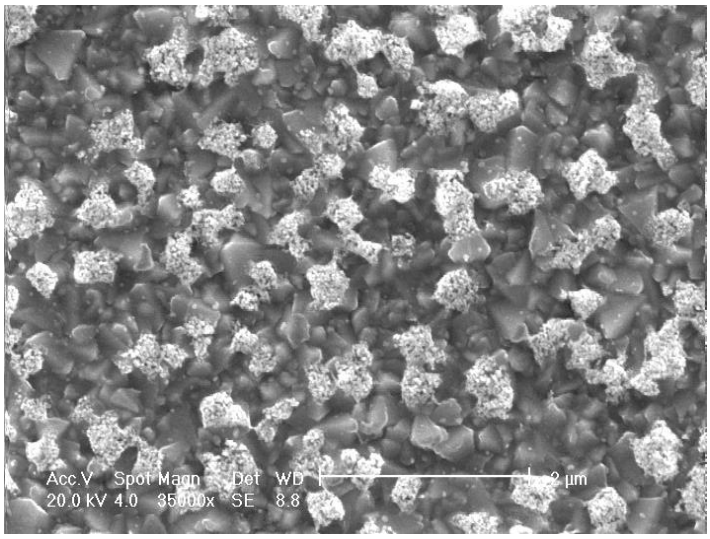

Figure 6. 12 SEM image of an FTO-glass counter electrode after sintering in the furnace at 400 ºC for 15 minutes

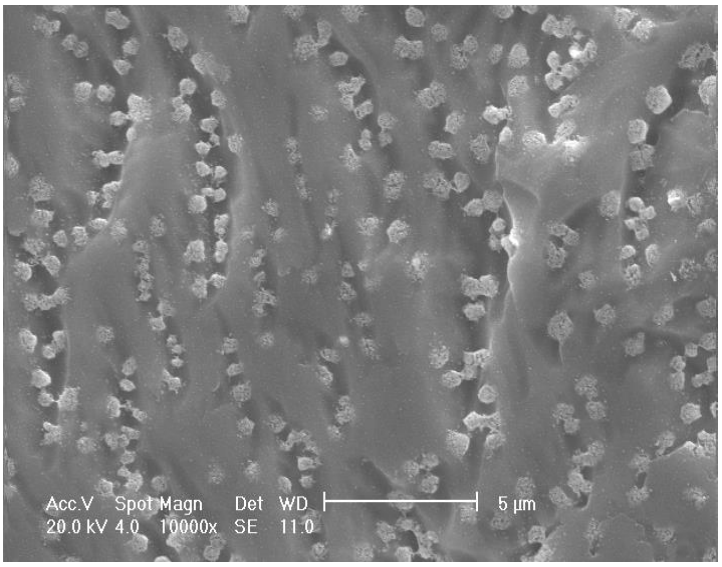

Figure 6. 13 SEM image of a Ti counter electrode after sintering in the furnace at 400 ºC for 15 minutes

6.2.3 The cell assembly

The two electrodes of the DSC cell were assembled together using Surlyn sealant (50 µm – Dyesol). For the sealing process a heat press was set up by integrating an AC heater, an aluminium block and a cold press. The temperature applied by the heater was measured

by a thermocouple (type-K) inserted into a 1 mm slot in the copper plate to estimate the temperature of the cell. The heat press was calibrated and it was found that the temperature required to melt Surlyn film and assemble a glass counter electrode solar cell (G-SC) was 120 ^{0}C. The temperature required to assemble a Ti counter electrode solar cell (Ti-SC) was 110 ^{0}C due to the heat was transferred and absorbed by titanium faster than by the glass, which causes the Surlyn to melt quickly. Figure 6.14 show photographs of a home-made heat press for this study and a cell was being assembled. To determine appropriate pressure for cell assembly is important because high pressure can break FTO-glass and damage the cell while applying a lower pressure can result in poor sealing which allows the electrolyte to escape and lower the performance of the DSC.

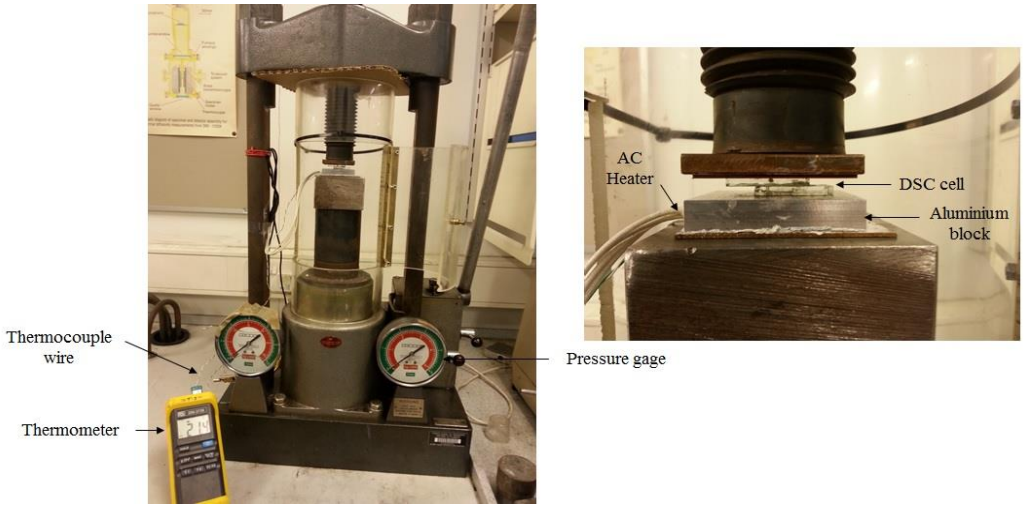

Figure 6. 14 Photographs of the heat press

6.2.4 Electrolyte injection

The cell was placed inside a sealed desiccator connected to a vacuum pump which was used to remove the air from the chamber. A drop of electrolyte was placed on the hole that was already made in the counter electrode. The cell was then exposed to the ambient

atmosphere by gradually opening a valve so that the electrolyte began to be injected inside the cell. The ionic-liquid electrolyte used in all the cells was composed of:

0.05 M iodine

0.5 M lithium iodide

0.1 M gaunidinium thiocyanate

0.5 M 4 tert butylpyridine and 7 ml of 3 Methoxypropionitrile as solvent.

Figure 6.15 shows a photograph of the equipment for electrolyte injection using a desiccator and vacuum pump.

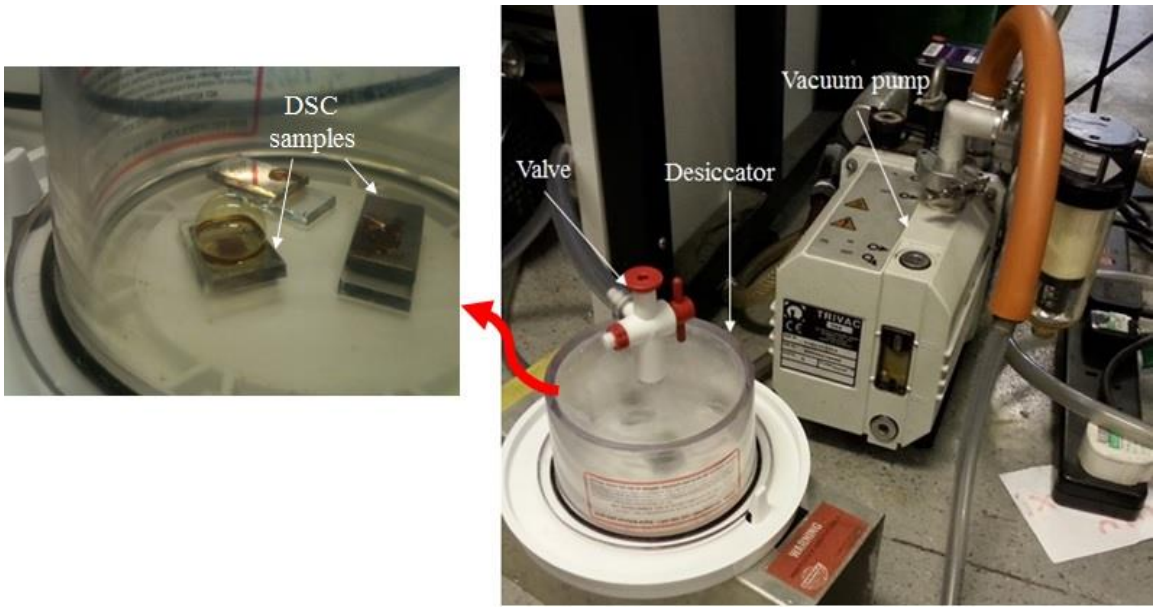

Figure 6. 15 A photograph of the desiccator and vacuum pump

6.2.5 Cell sealing

The hole in the counter electrode of the DSC was sealed after the electrolyte was injected into the cell in order to avoid the evaporation of the electrolyte. In this study, a small piece of aluminium sticky tape was used to seal the hole, which provide reasonable lifetime of investigation of DSC.

6.2.6 Electrical contacts

A silver conductive paint purchased from RS components was used to paint the edge of the conductive side of the working electrode and counter electrode as shown in Figure 6.16. This process must be done very carefully, because any mistake could cause a short circuit between the cathode and anode, killing the cell. The cell after it was coated with the silver paint was left in air to dry for several hours. After the painting process was completed, the cell was ready for characterisation.

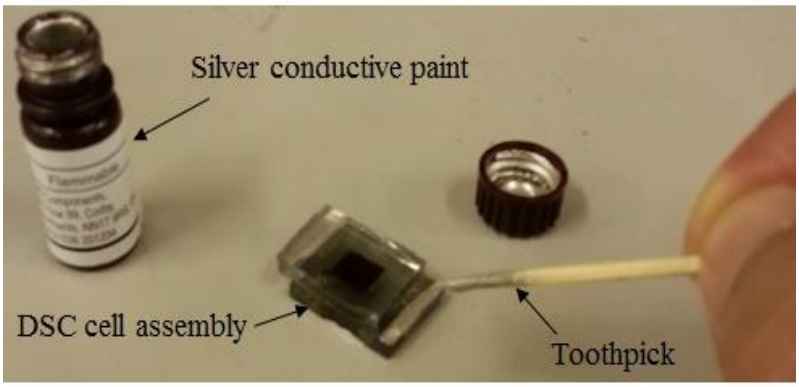

Figure 6. 16 A cell painted with silver conductive paint

Two types of DSCs, G-SC and Ti-SC, were prepared and tested in the laboratory. Both devices were prepared in a similar way and some of the samples are shown in Figure 6.17.

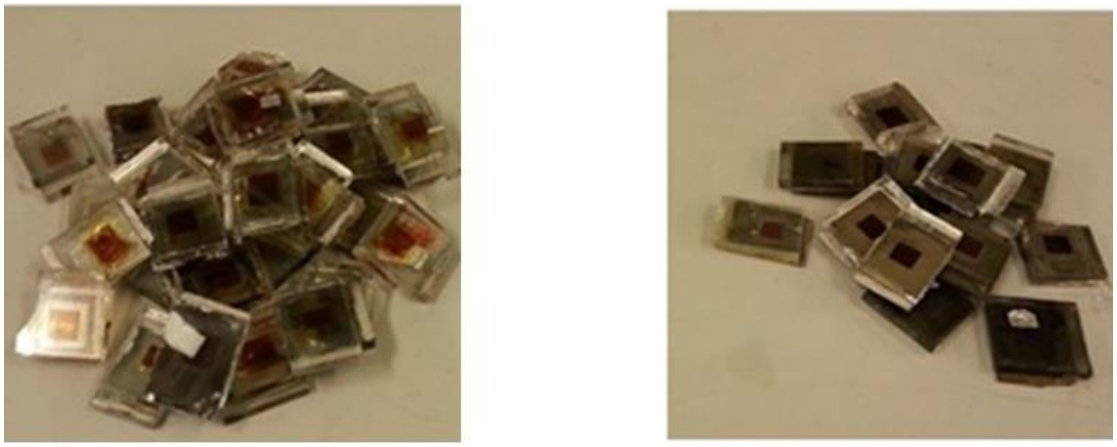

Figure 6. 17 Photographs of the dye sensitised solar cells: (a) cells with an FTO-glass counter electrode and (b) cells with a Ti counter electrode

6.3 Experimental Setup

A schematic diagram of the experimental setup is shown in Figure 6.18 and a photograph in Figure 6.19.

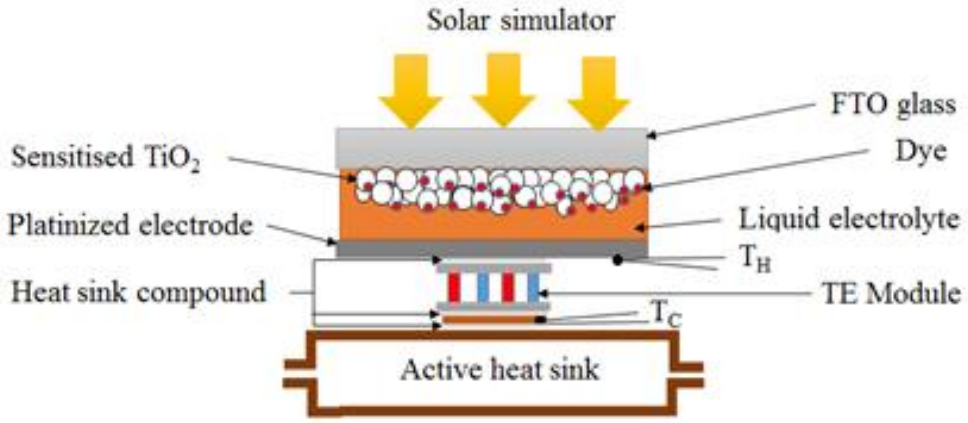

Figure 6. 18 Schematic diagram for the experimental setup of a DSC-TEG hybrid tandem cell

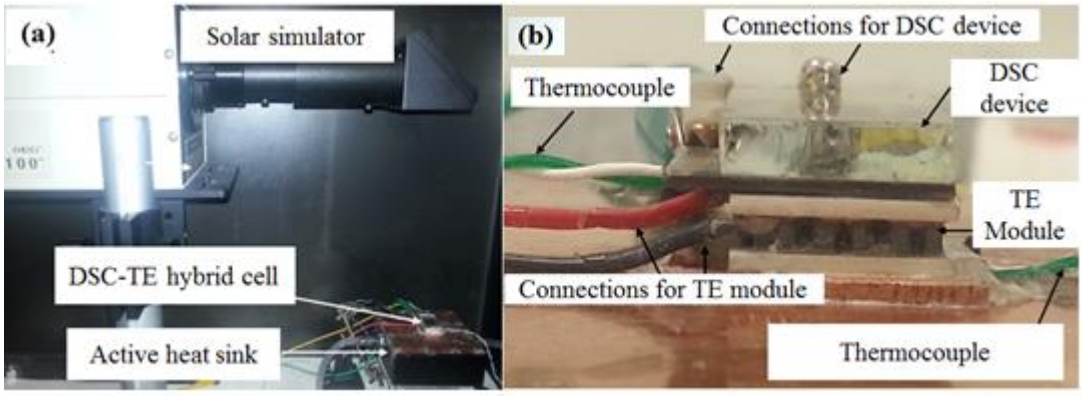

Figure 6. 19 Photograph of the experimental setup (a) and DSC-TE hybrid tandem cell (b)

The heat is extracted from the cold side of TEG and transferred to a heat exchanger which is maintained at 20 ^{0}C by manipulating the mass flowrate. Two thermocouples (type K) were positioned at T_H and T_C to measure the temperatures of hot side and cold side of the TEG, respectively. The thermocouple in the hot side was attached directly to the counter electrode of the DSC, whether the FTO-glass or Ti, with small amount of heat sink compound to provide good thermal contact.

The other thermocouple was inserted inside small hole in a copper plate of 1 mm thickness, which was placed on the heat exchanger with a heat sink compound in between. The DSC/TEG system was placed inside a Faraday cage as shown in Figure 3.7, and the same solar simulator as shown in Figure 3.1 is used as a source of light. The level of the light intensity was fixed at 1000 W/m^2 and it was measured via pyranometer as appeared in Figure 3.2. The temperature were recorded by a data logger which recorded the measurements every second and displayed them on the computer as shown in Figure 3.5. In this experiment 36 samples of DSCs were fabricated using the same procedure. The samples included 18 DSC of Ti- SC and others 18 samples were G-SC. The best two cells were characterised using standard test condition (STC), and the results are presented in Table 6.1 (see Appendix.15 for the I-V curves).

Table 6. 1 Experimental data from two best cells: Ti-SC and G-SC.

DSC - Modules	A_{PV} ((mm^2)	Active Area (mm^2)	V_{OC} (mV)	I_{SC} (mA)	Fill Factor (%)	P_{max} (mW)	η_{PV} (%)
Ti - SC	20x15	6.25x6.25	750	5.4	51.8	2.1	5.3
G - SC	20x15	5x5	720	3.2	43.4	1	4

These cells were integrated with three commercial TEG modules (M-A, M-B and M-C) with different L_{TE}, N and A_C as shown in Table 6.2. As a result, six HTC fabricated: three of them with Ti-SC and the other three with G-S as shown in Table 6.3. It is to be noted that the M-C in Table 6.2 was used twice in this experiment. Firstly, it was used as a heater and/or cooler (the Peltier effect) to study the influence of temperature on the DSC. Secondly, it was used as a generator (the Seebeck effect) to generate electricity due to the ΔT established across it.

Table 6. 2 Device parameters of the three thermoelectric generators

Modules	Total area (mm^2)	N	A_{TE} (mm^2)	L_{TE} (mm)	A_CN/L_{TE} (mm)
M-A	4x4	14	0.6x0.6	0.8	6.3
M-B	15x15	34	0.9x0.9	1.2	23
M-C	15x15	62	0.8x0.8	2.2	18

Table 6. 3 The six hybrid tandem cells (HTC)

Modules	M-A	M-B	M-C
Ti-SC	Ti-SC/M-A	Ti-SC/M-B	Ti-SC/M-C
G-SC	G-SC/M-A	G-SC/M-B	G-SC/M-C

6.4 Results and Discussion

This section focuses on three tasks: 1) studying the effect of temperature on the Ti – SC performance; 2) evaluating the performance of HTC with G–SC and Ti–SC and 3) identifying the optimum geometry (A_CN/L_{TE}) of the TEG for the HTC.

6.4.1 The Effect of Temperature on a Titanium Dye Sensitised Solar Cell (Ti – SC)

It is interesting to note that previous methods of measuring the operating temperature of a DSC involved attaching a temperature sensor to the FTO-glass. However, in this research the procedure was developed and the sensor was attached directly to the metallic counter electrode. This means that the measured temperature is close to reality because the metal transfers heat better than glass. Figures 6.20 and 6.21 show the Current density – Voltage (J-V) and the Power density – Voltage curves of Ti-SC, respectively. It is clear that the increase in temperature causes a significant decrease in V_{OC}.

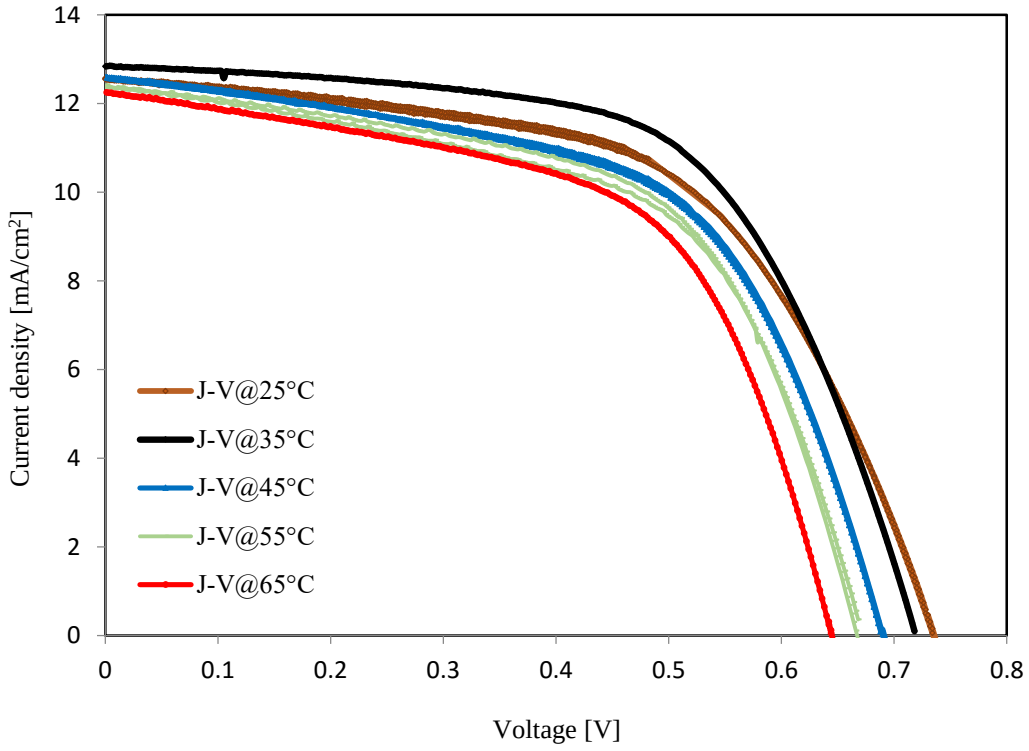

Figure 6. 20 J-V curves of a Ti-CE dye sensitised solar cell at different temperatures

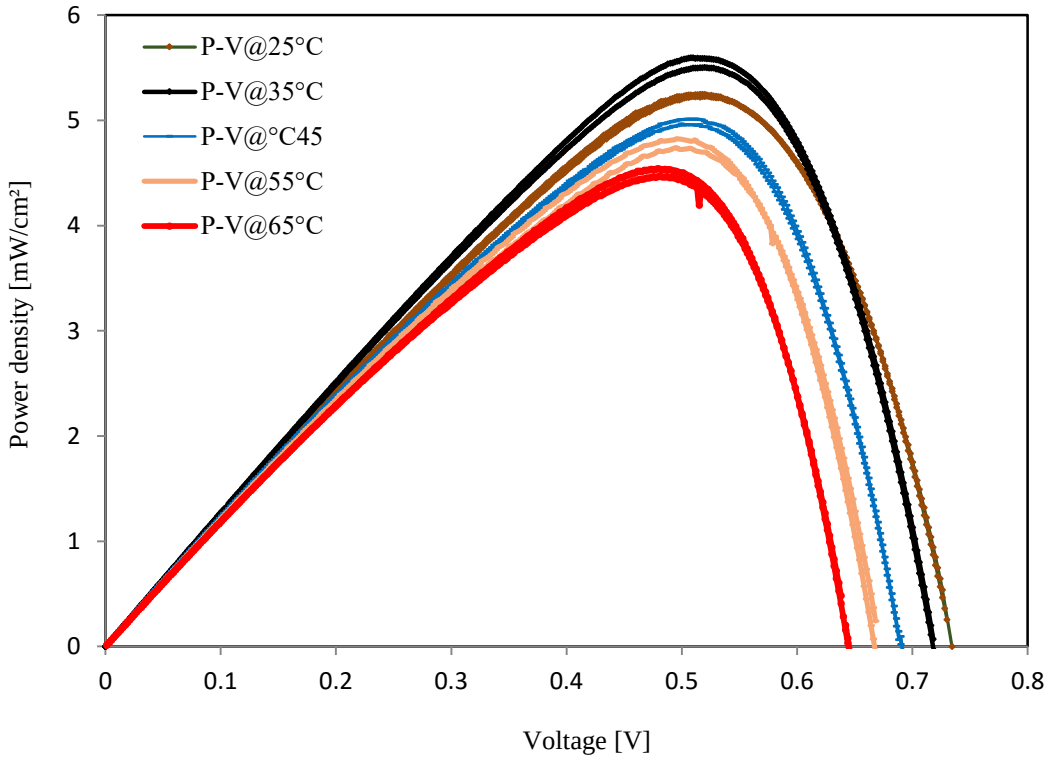

Figure 6. 21 P-V curves of Ti-CE dye sensitised solar cells at different temperatures

However, the P_{max} shows an increase with increasing temperature until it reaches an optimum value at 35 ºC. It is to be noted that the G-SC tested in chapter three showed an optimum temperature between 35 ºC and 45 ºC, as the P_{max} started to increase after 25 ºC until it reached a maximum value at 45 ºC.

Figure 6.22 shows the η_{PV} and P_{max} of the Ti-SC as a function of temperature. It can be seen that both variables show a similar trend with increasing temperature.

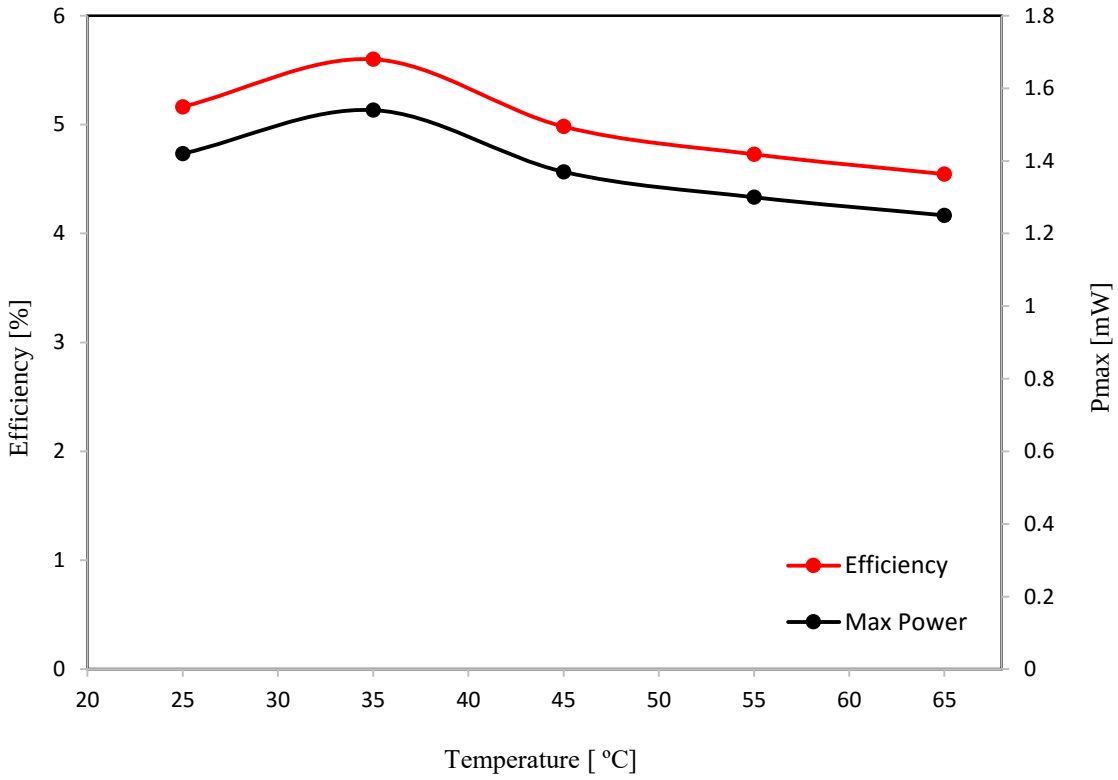

Figure 6. 22 The maximum power and efficiency of Ti-CE dye sensitised solar cells vs temperature

The Fill Factor and I_{SC} also increased with increasing the temperature, displaying similar trend of the P_{max} and η_{PV} for Ti-SC. This trend is an interesting phenomenon which was not observed in the other types of solar cell. Meanwhile, the V_{OC} presented a normal decrease with increasing temperature, as can be seen in Figure 6.23.

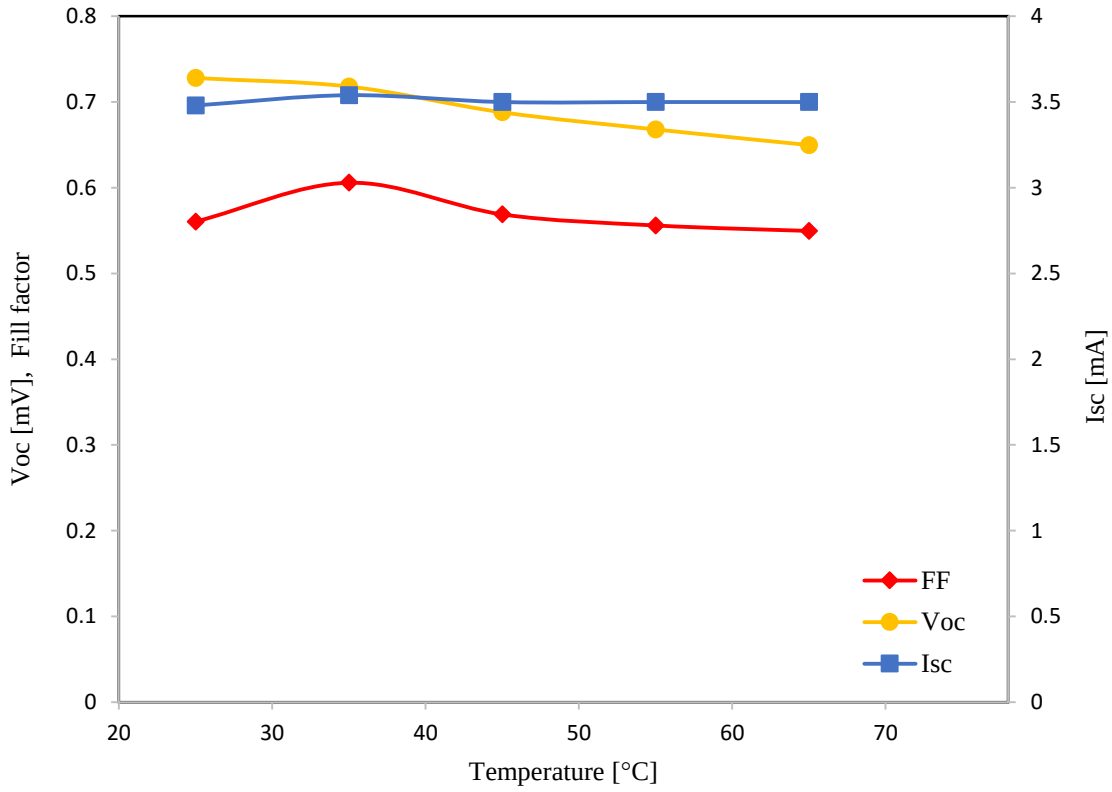

Figure 6. 23 The Voc, Isc and fill factor of Ti-CE dye sensitised solar cells vs temperature

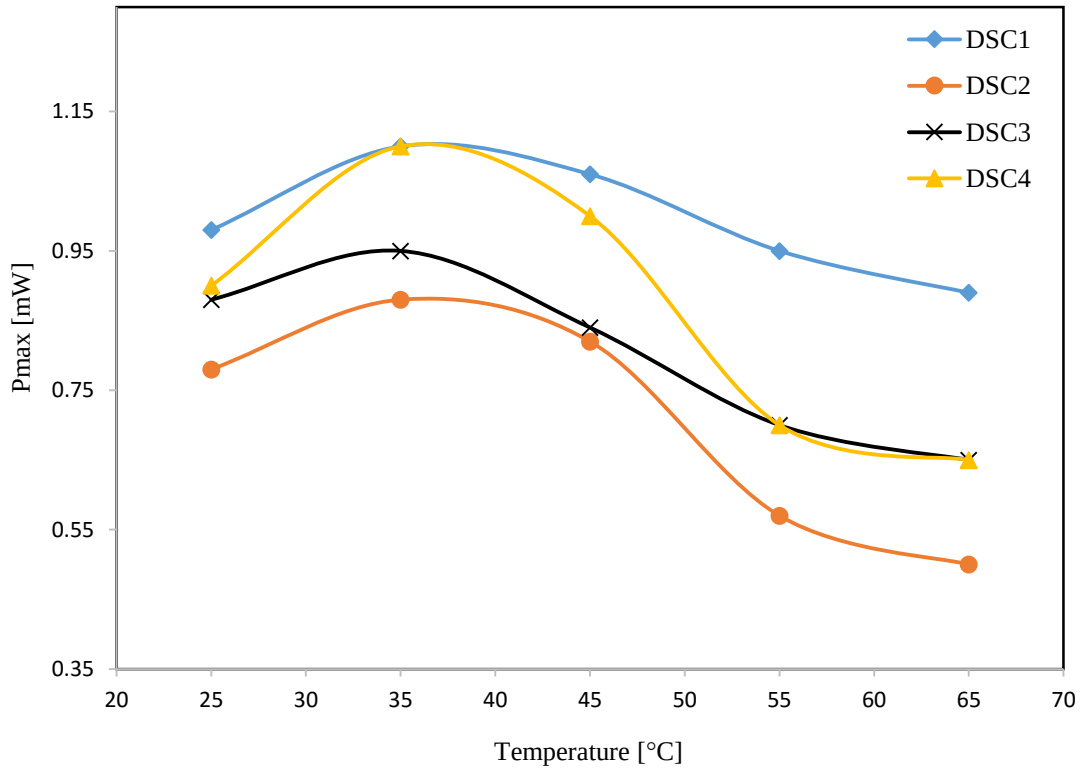

Figure 6. 24 The maximum power output vs temperature for four different Ti-CE dye sensitised solar cells

A further 4 samples of Ti-SC were fabricated and characterised to examine the reproducibility of the Ti-SC cells. Figure 6.24 shows the P_{max} of four Ti-SC cells fabricated using the same procedure described in section 6.2 and using the same compounds. They were tested using the same materials and the same equipment, and they exhibit similar trend with temperature.

Figure 6.25 shows the η_{PV} of four Ti-SCs, and the trend was the same as that of the P_{max}. These experimental results indicated that the DSC is the best type of solar cells to integrate with TEG because it is the only type that showed an increase in the power output with increasing temperature until reaching around 40 ^{o}C.

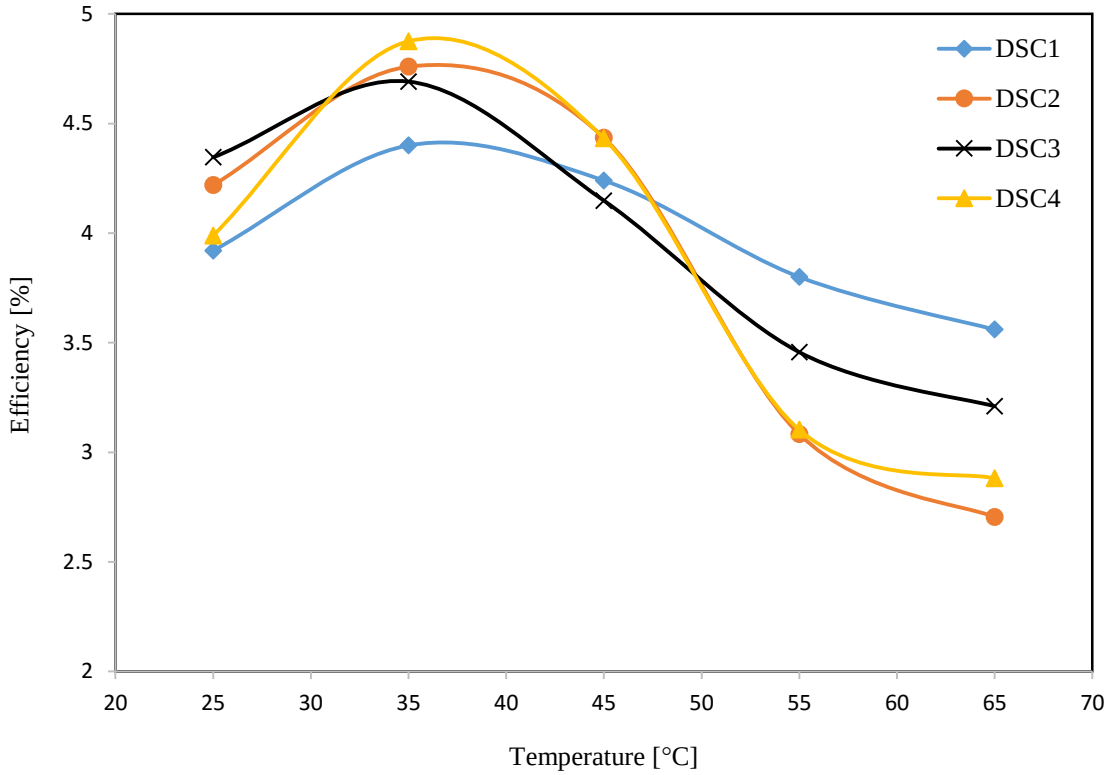

Figure 6. 25 Efficiency vs temperature for different Ti-CE dye sensitised solar cells

6.4.2 Integrating Dye Sensitised Solar Cells with TEG Modules

The work above demonstrated that DSCs can be fabricated by replacing the FTO-glass counter electrode with a Ti counter electrode, which have slightly better performance. Since the thermal conductivity of Ti is higher than the FTO-glass, this can improve the heat transfer from the DSC to the hot side of the TEG. Experiments were performed to investigate the performance of HTCs prepared using Ti-SC with M-A, M-B and M-C, respectively.

The J-V curves for Ti-SC were firstly measured by placing directly on the cold side of a heat exchanger without TEG for the operating temperature of the DSCs maintained at 20 °C. After that, the J-V curves for Ti-SC were measured when the DSC was integrated with three TEGs: M-A, M-B and M-C, as shown in Figure 6.26. It is clear that the integration of a TEG improved the performance of the Ti-SC cells because the operating temperature was increased.

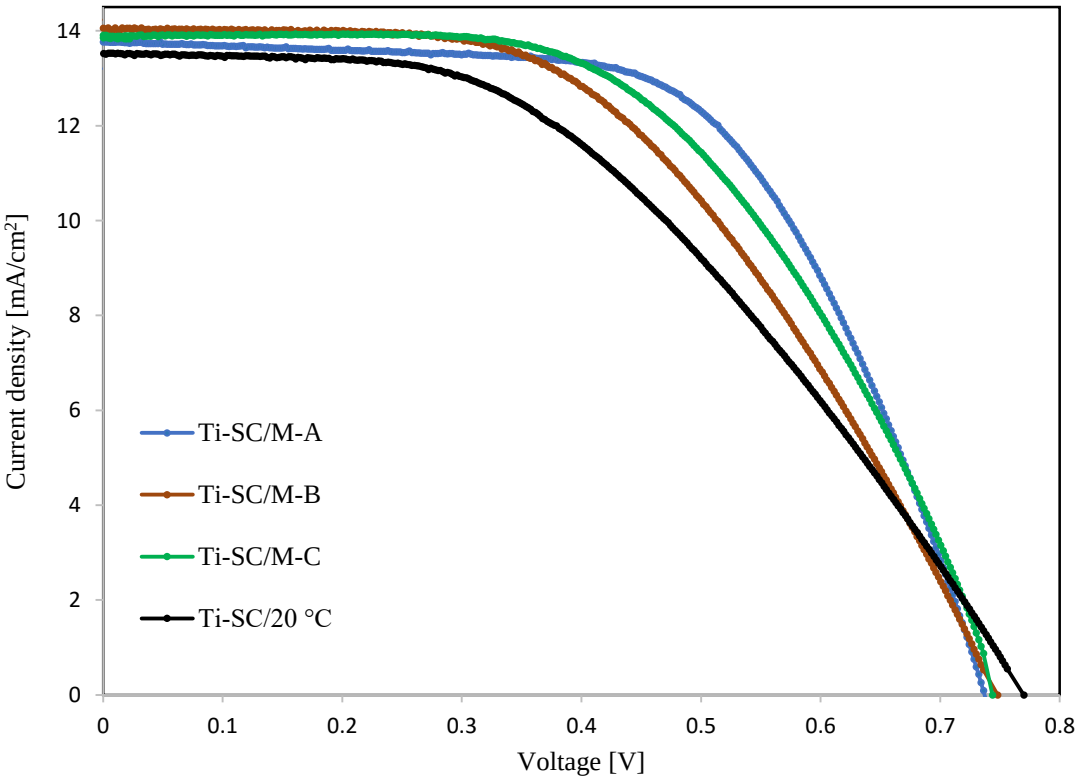

Figure 6. 26 The J-V curves of Ti-CE dye sensitised solar cells integrated with three TEGs

Figure 6.27 shows the corresponding power density vs voltage. It can be seen that the V_{OC} dropped slightly due to an increase in the operating temperature of the Ti-SC. However the P_{max} increased gradually by integrating different TEGs, reaching its highest value with the small TEG module (M-A) as the ($A_C N/L_{TE}$) was low for this module (see Table 6.2). Table 6.4 shows the characterization of TEG, DSC and HTC.

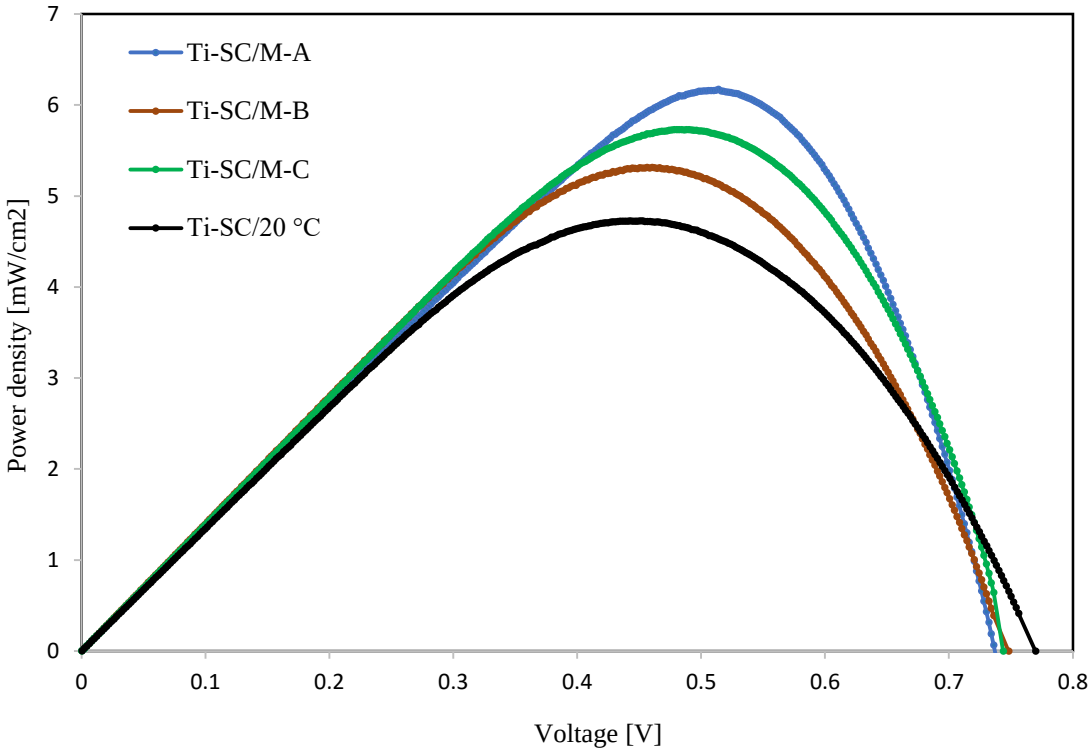

Figure 6. 27 Power density vs voltage for Ti-SC integrated with 3 TEGs

It is clear that the module with a smaller value of ($A_C N/L_{TE}$) makes the operating temperature of Ti-SC higher and vice versa.

Figure 6.28 shows the J-V curves for G-SC only (i.e., without a TEG) and the J-V curves when G-SC is mounted on the top of three TEGs, respectively. It can be seen that the J-V of the G-SC shows similar trends to those of Ti-SC.

Table 6. 4 The T_H and ΔT, and the characterization of TEG, DSC and HTC

Hybrid tandem cell	T_H °C	ΔT °C	P_{TE} mW	η_{TE} %	P_{PV} mW	FF %	η_{PV} %	P_{tot} mW	η_{tot} %
Ti-SC/20 °C	20	-----	-----	-----	1.9	46.5	4.8	1.9	4.8
Ti-SC/M-A	40	20	0.65	0.22	2.4	60.9	6.1	3.1	6.3
Ti-SC/M-B	27	7	0.48	0.16	2.1	51.6	5.3	2.6	5.5
Ti-SC/M-C	28.5	8.5	0.72	0.24	2.2	55	5.6	2.9	5.8

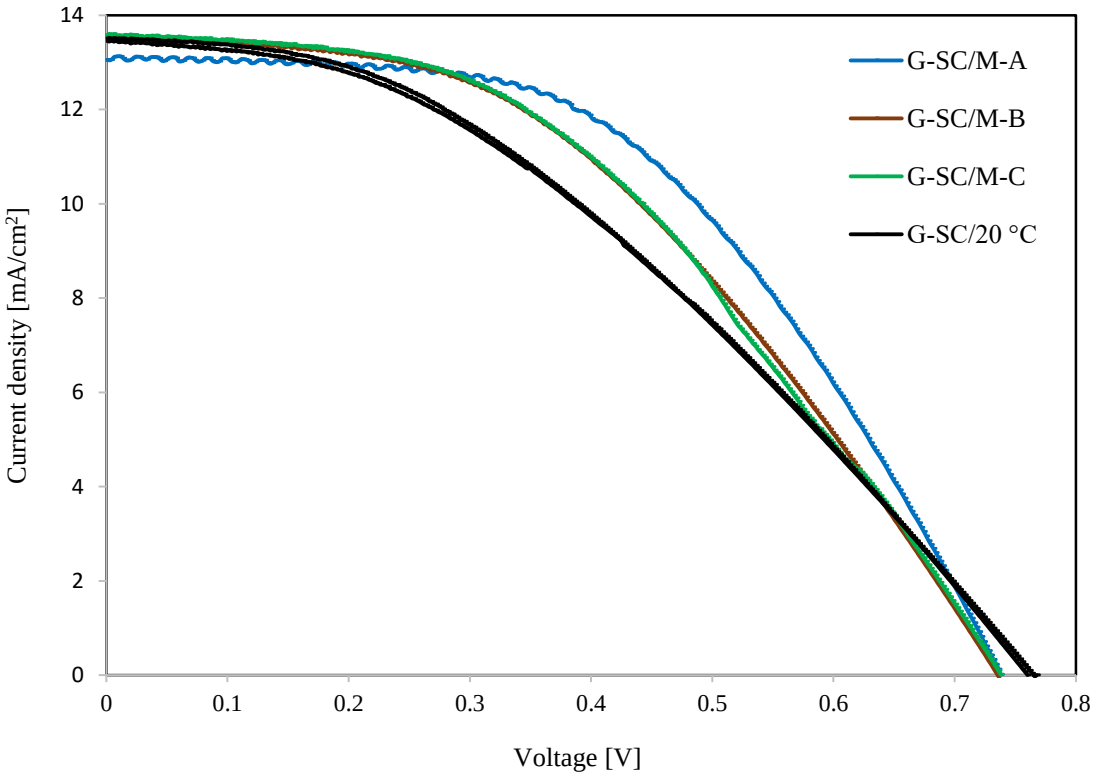

Figure 6. 28 The J-V curves of G-CE dye sensitised solar cells integrated with three TEGs

Figure 6.29 shows the power density vs voltage for G-SC. It is clear that the most significant increase in the P_{max} was observed for the smallest module (M-A) when integrated with G-SC, as the large thermal resistance of this module increased the operating temperature of the G-SC. The large TEGs, such as M-B and M-C, have a high

value of (A_CN/L_{TE}) that led to a low operating temperature of the G-SC and consequently a lower P_{PV}. Since ΔTs across TEG were also low, P_{TE} is also small. As a result, the P_{tot} and η_{tot} of the HTCs based on G-SC were low as seen in Table 6.5.

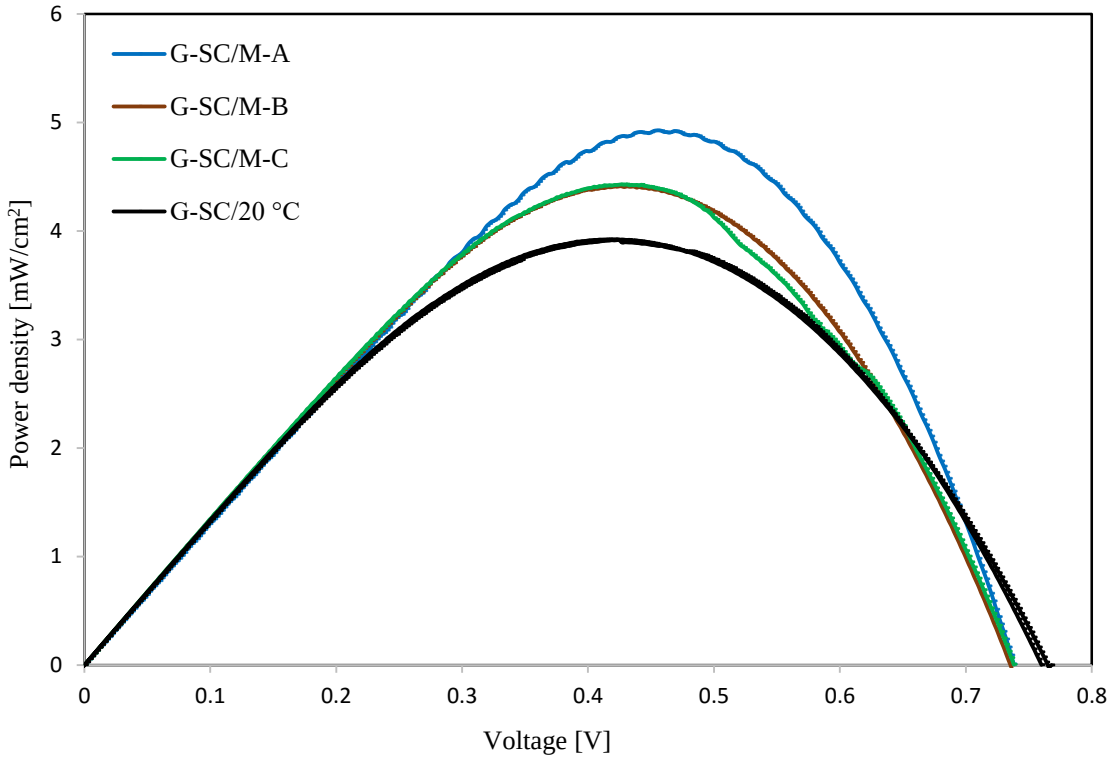

Figure 6. 29 Power density vs Voltage for G-SC integrated with 3 TEGs, respectively

Table 6. 5 The T_H and ΔT, and the characterization of TEG, DSC and HTC

Hybrid tandem cell	T_H °C	ΔT °C	P_{TE} mW	η_{TE} %	P_{PV} mW	FF	η_{PV} %	P_{tot} mW	η_{tot} %
G-SC/20 °C	20	------	------	------	1	38	4	1	4
G-SC/M-A	35	15	0.2	0.07	1.2	49	4.8	1.4	4.9
G-SC/M-B	26	6	0.4	0.1	1.1	44	4.4	1.5	4.5
G-SC/M-C	27	7	0.5	0.2	1.1	44	4.4	1.6	4.6

The Ti-SC and G-SC exhibited P_{max} at an operating temperature between 35 ^{o}C and 45 ^{o}C. Integrating these cells with the TEG modules with high values of A_CN/L_{TE} makes the cells matched the best temperature for the two cells. This unique temperature dependence of DSCs can be exploited for obtaining further improvements using TEG devices to harvest waste heat from the DSC.

The I-V curves and P-V curves of the TEG modules were measured in the same tests performed for determining the I-V curves of DSCs. Figure 6.30 shows the I-V curves of M-A when it was integrated with Ti-SC and G-SC. It is clear that the performance of M-A is improved when it is integrated with Ti-SC compared with the integration of the same module with G-SC. This is because the metallic counter electrode of the Ti-SC increased the heat transfer from the DSC to the TEG.

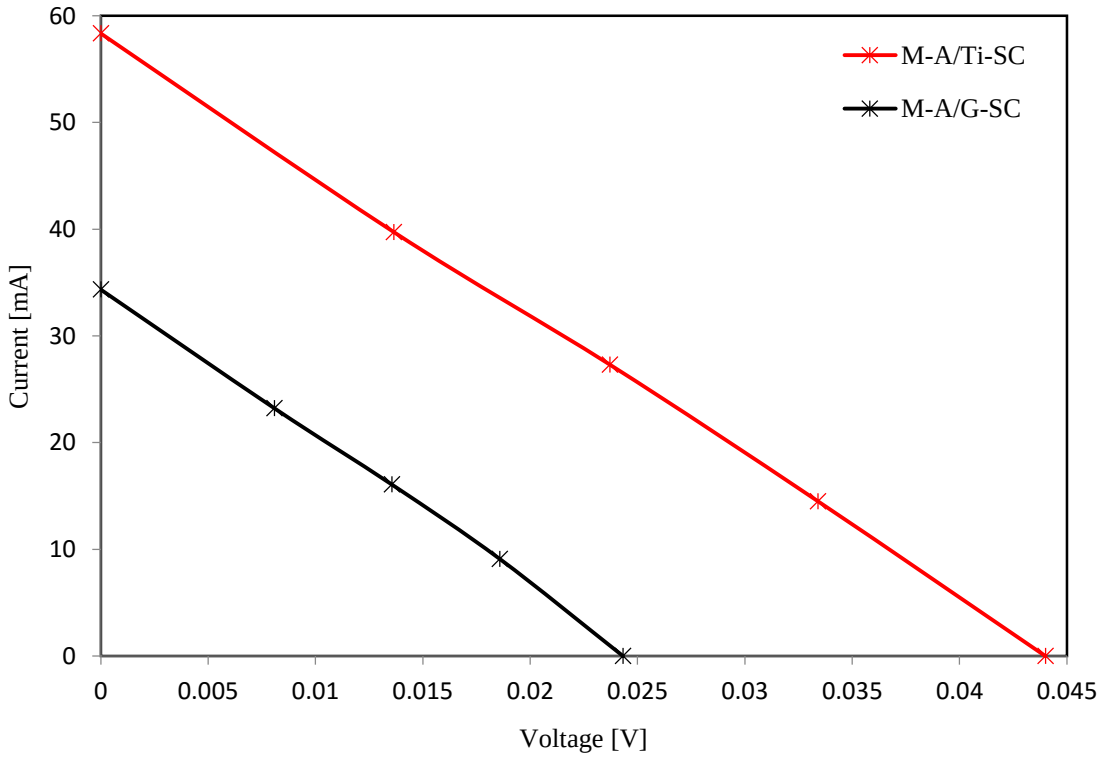

Figure 6. 30 The I-V curves of M-A integrated with Ti-SC (red line) and with G-SC (black line)

As a result, the T_H increased from 35 ºC (Table 6.5) to 40 ºC (Table 6.4). The increase in the ΔT established across TEG increased the I_{SC} of M-A from 34.3 mA to 58.3 mA, and the V_{OC} from 0.024 V to 0.044 V (i.e., almost doubled).

The P-V curves of M-A integrated with T-SC and G-SC are presented in Figure 6.31. The power output generated by M-A was significant in a HTC that is integrated with the Ti-SC rather than the G-SC and it was increased from 0.21 mW to 0.65 mW (three times). It is to be noted that the P_{max} of M-A was higher because the ΔT across M-A was higher as indicated by Equation 4.9 (in Chapter 4).

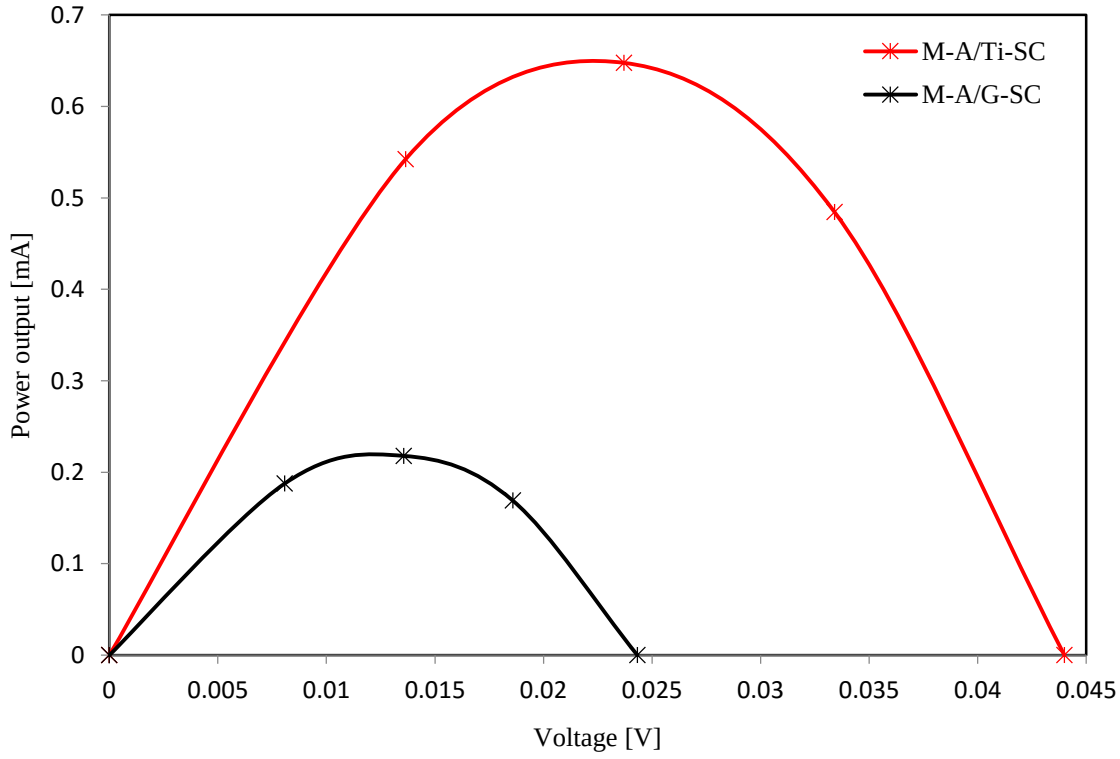

Figure 6. 31 The P-V curves of M-A integrated with Ti-SC (red line) and with G-SC (black line)

The I-V curves of M-B integrated with Ti-SC and G-SC are presented in Figure 6.32. It is clear that this module shows lower I_{SC} and V_{OC} than that of M-A since the ΔT across it was lower. The P-V curves of M-B incorporated with Ti-SC and G-SC are shown in

Figure 6.33. Compared with Figure 6.31, the P_{max} of M-B with Ti-SC was lower than that of M-A with the same cell because of the lower ΔT for this module.

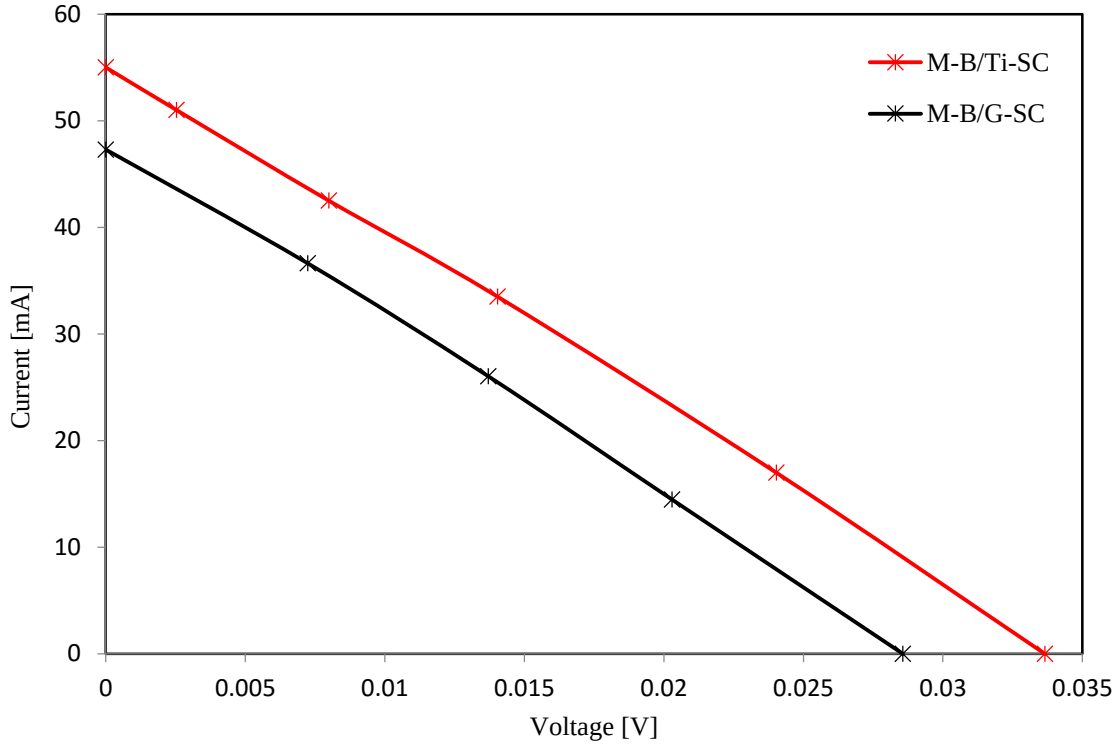

Figure 6. 32 The I-V curves of M-B integrated with Ti-SC (red line) and with G-SC (black line)

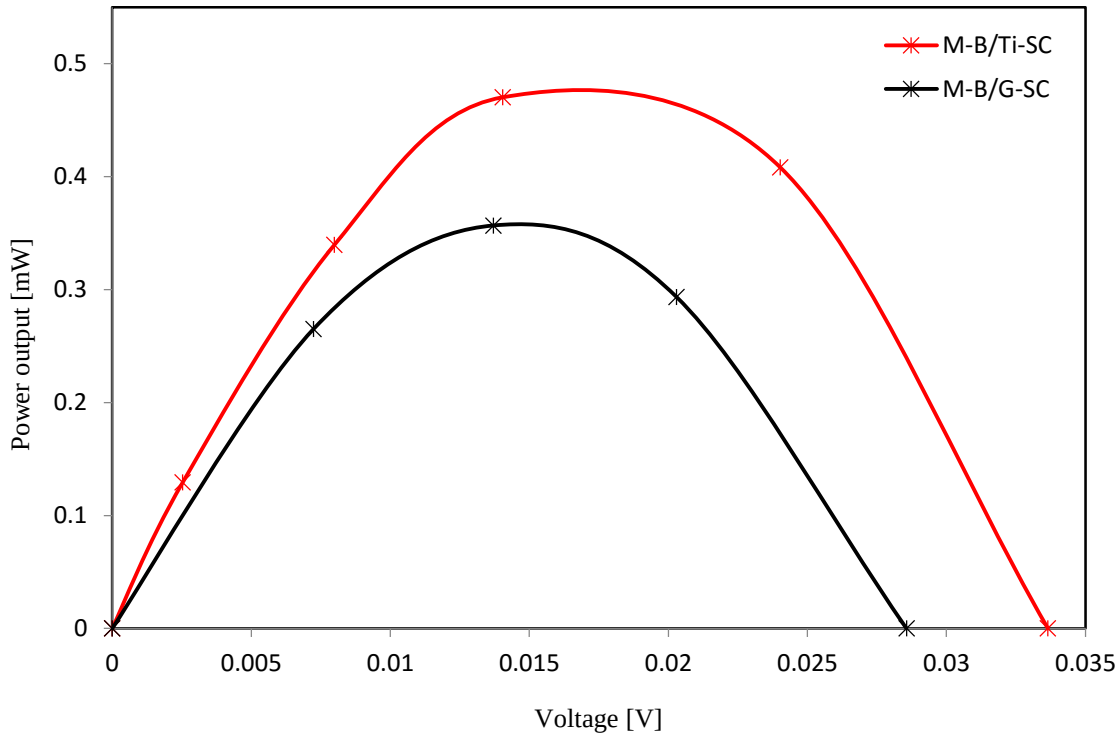

Figure 6. 33 The P-V curves of M-B integrated with Ti-SC (red line) and with G-SC (black line)

Figures 6.34 and 6.35 show the I-V curves and P-V curves of M-C integrated with Ti-SC and G-SC respectively.

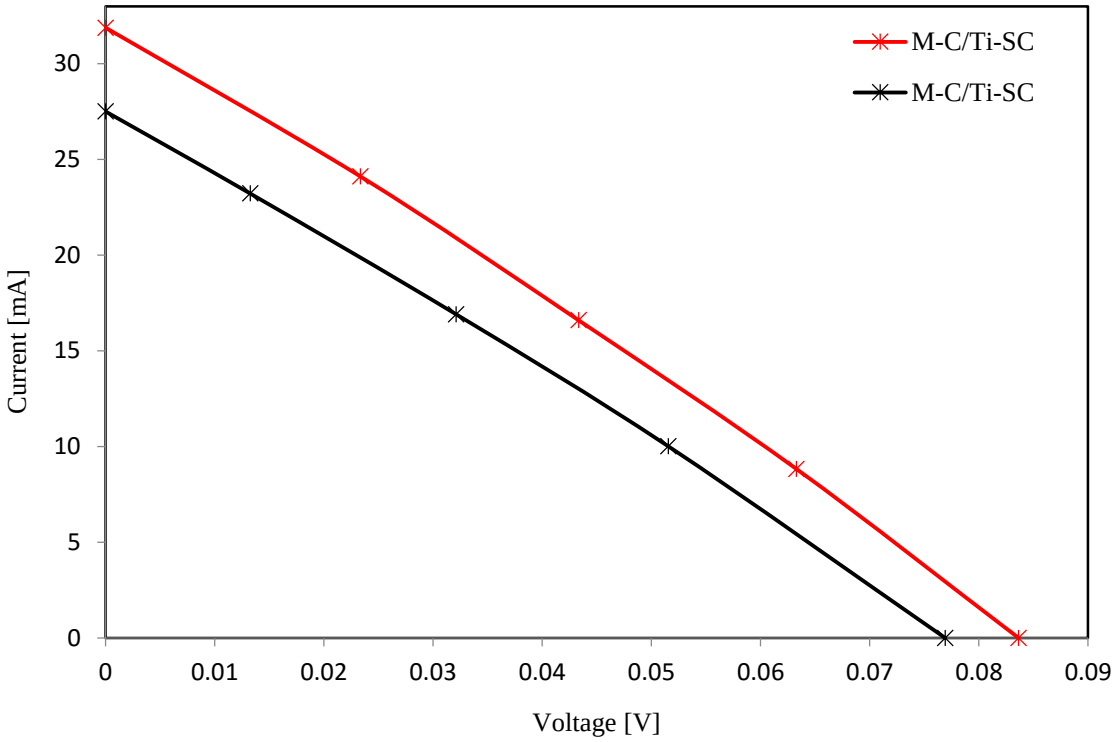

Figure 6. 34 The I-V curves of M-C integrated with Ti-SC (red line) and with G-SC (black line)

It can be seen that the P_{max} is increased by replacing the G-SC with Ti-SC, as the latter has a better ability to transfer the heat from the DSC to the TEG due to the use of the metal (Ti) rather than the glass. Furthermore, the P_{max} for M-C was the highest among the three modules because this module had the largest N (62 elements) and ΔT is higher than M-B, as the P_{max} increases by increasing N and ΔT (see Equation 4.9).

It is interesting to note here that the three TEG (M-A, M-B and M-C) modules showed better performance when integrated with Ti-SC than when integrated with G-SC. In fact, the Ti has physical properties, such as thermal conductivity k and specific heat c_p, which are superior to the glass.

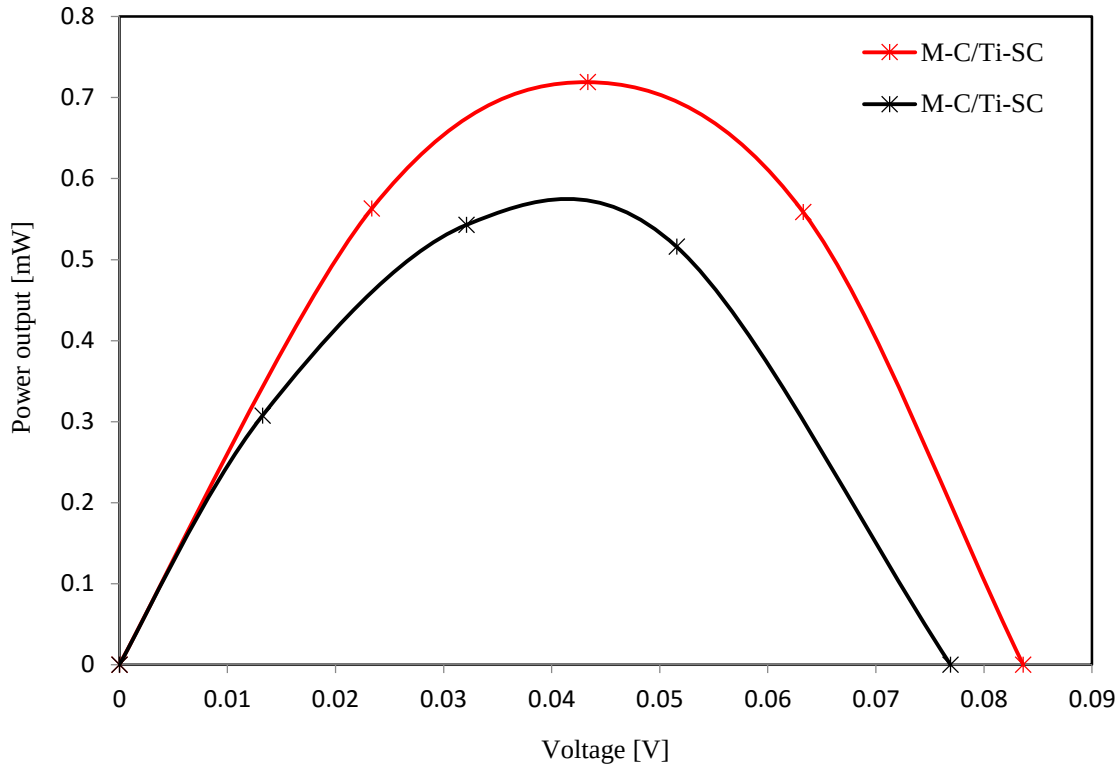

Figure 6. 35 The P-V curves of M-C integrated with Ti-SC (red line) and with G-SC (black line)

For example the k for titanium is 15.6 (W/m.ºC) while for glass this value is 0.8 (W/m.ºC), and the c_p for titanium is 5400 J/kg.K while for glass it is 670 J/kg.K. The increase in the P_{max} of the three TEGs in Ti-SC was due to improved thermal coupling between the Ti-SC and TEGs compared with G-SC. This result demonstrate for the first time that the thermal coupling is an important factor in improving the overall power output and efficiency of a DSC/TEG hybrid system.

In order to confirm the repeatability, the I-V and P-V curves for three TEGs characterised by constant temperature difference method and the results are presented in Appendix.16.

6.4.3 Optimisation of Hybrid Tandem Cells

The parameters obtained from the I-V and P-V curves in the previous section were analysed for the six HTCs and presented in Tables 6.4 and 6.5 to find the optimum geometry amongst all the modules used. It is clear that the integration of the TEGs with different geometries (i.e., different values of A_CN/L_{TE}) changed the operating temperature of the DSC, as shown in Tables 6.4 and 6.5. The experimental results show that the TEG with the smallest size (M-A) established the largest ΔT when it integrated with Ti-SC due to the smallest value of A_CN/L_{TE}. In contrast, the ΔTs for the other two modules (M-B and M-C) were 7 °C and 8.5 °C, respectively because of higher values of A_CN/L_{TE}.

Although the highest P_{max} of TEG was obtained from the module with the largest N (M-C) when it was integrated with Ti-SC, the overall maximum power output was obtained from the system using M-A. This is because the module M-A enables the Ti-SC operate at its optimal operating temperature to generate highest P_{PV} and, at the same time, provides a reasonably higher power output from the TEG due to the highest ΔT. In general, the hybrid systems using Ti counter electrode (Ti-SC) generate more overall power output than those using FTO-glass counter electrode (G-SC). This is because the waste heat in the DSC has been efficiently used by TEG in a Ti-SC, while most of the heat in a G-SC was lost through the glass by convection and conduction. The results indicate that the thermal coupling between the DSC and the TEG is crucial to achieving effective heat recovery from the DSC, and the best DSC for the tandem configuration should therefore have a metal counter electrode to ensure an optimal thermal coupling.

It is to be noted that the improvement was achieved using TEG materials and devices that are commercially available. It is anticipated that further improvement is possible if high

performance thermoelectric materials and module is employed. Also, development of DSCs with metallic counter electrode that has a higher operating temperature (e.g., up to 80 °C) would bring further improvement.

6.5 Conclusions

DSCs with conventional FTO-glass counter electrode (G-SC) and new type of Ti counter electrode (Ti-SC) were successfully fabricated for the first time in Cardiff Thermoelectric Laboratory. Both type of cells exhibit efficiencies of about 5% that are comparable to the data published internationally for this type of solar cells. It is interesting to note that although both types of DSCs were fabricated using identical processes except for using different counter electrodes, the efficiency of the DSCs with Ti counter electrode is slightly higher than that with conventional FTO-glass electrode.

The main purpose of developing Ti counter electrode DSCs is to improve the thermal coupling between the DSC and TEG in a PV/TEG hybrid system. Experimental investigation of this study demonstrate that the overall power output and efficiency of a DSC/TEG hybrid system that uses a Ti counter electrode is significantly higher than that with conventional FTO-glass counter electrode. This result confirms the rationale of developing DSCs with the Ti counter electrode, which improves thermal coupling between the DSC and TEG, so that the heat generated inside the DSC can be efficiently removed and transferred through the TEG. In addition, Ti counter electrode also improves light reflection and heat absorption over the FTO-glass, leading to further enhancement of both electrical and thermal efficiency.

Optimisation of the geometry of TEG plays important role in achieving maximum performance for a DSC/TEG hybrid systems because the TEG geometry determines the

operating temperature of DSC and the temperature difference across TEG. Both have significant influence on the overall power output and efficiency of the system. The results of this study demonstrates that a small-size TEG is preferable for integrating with Ti-SC because it creates a large ΔT across it and the power output was increased from 0.21 mW to 0.65 mW, (>200 %). On the other hand, the G-SC appears to require a TEG which has the same area as the DSC. This is probably because the large size reduces the heat loss by convection and radiation from the bottom side of the cell. The hybrid systems with Ti-SC also reduce the consumption of thermoelectric materials because they require small size TEGs.

Experimental results from this study demonstrate that a DSC/TEG hybrid system generates more power and has higher conversion efficiency than that can be obtained from an individual system. Further improvement may be achieved by developing more efficient TEG (rather than commercial type) and by making the DSCs having higher operating temperatures with metallic counter electrode.

CHAPTER SEVEN - CONCLUSIONS AND FURTHER WORK

7.1 CONCLUSION

The main objective of the work embodied in the thesis was to design, construct and investigate the feasibility and performance of a PV/TEG hybrid system. This objective has been achieved through systematic experimental investigation on the temperature coefficients of all available solar cells, development of theoretical model (and experimental validation) for design and optimisation of TEG geometry, and creation of an unique DSC/TEG hybrid system based on Ti counter electrode, which showed a significant improvement in the power output and efficiency due to enhanced thermal coupling between DSC and TEG. The major achievements are summarised as follows:

1) A systematic experimental work was conducted to investigate the suitability of solar cells for integration with TEG to develop PV/TEG hybrid system based on their temperature dependence. Six types of PV cells were examined under standard test conditions in the laboratory, which include monocrystalline silicon (m-Si), polycrystalline silicon (p-Si), amorphous silicon (a-Si), copper indium sulphide (CIS), cadmium telluride (CdTe) and dye sensitized solar cell (DSC). The experimental results show that a-Si and DSC are preferable for integration with TEG. The a-Si showed the lowest drop in P_{max} and η_{PV} with increasing temperature. The DSC exhibits an even more interesting feature that P_{max} and η_{PV} increases with increasing temperature over 25 ^{o}C to 45 ^{o}C. This makes the DSC an ideal solar cell for integration with TEG because it can lead to an increase in power outputs and efficiencies from both DSC and TEG over this temperature range. The experiment results

from this work also demonstrate that the p-Si and m-Si cells exhibit significant drop in P_{max} and η_{PV} when the temperature was increased from 25 ^{o}C to 65 ^{o}C, indicating that they are not suitable for integration with TEG because the power gain from the TEG would be offset by reduction in these PV cells.

2) The geometry of TEG has an important influence on the performance of a PV/TEG hybrid system. A theoretical model was developed in this research to provide an effective method to determine the optimal geometry for the hybrid systems and to guide experimental study. The simulation results using the model show that the value of A_CN/L_{TE} is crucial to building an efficient PV/TEG hybrid system. In this work, the optimum TEG geometry to obtain the P_{max} from the TEG and the maximum P_{tot} and η_{tot} from the hybrid PV/TEG system was investigated and the results show a small-size TEG is preferable because a larger ΔT can be established across the TEG. Consequently, the P_{max} is higher. Using a TEG that has the same size as the PV cell will result in much smaller ΔT across the TEG. In addition, it also consumes more materials. Furthermore, simulation results show that the power output of the TEG in the hybrid system can be improved by operating in a vacuum.

3) Theoretical calculations showed that not all types of PV cells are suitable for integration with TEG. A theoretical work was carried out to verify this result using two types of PV cells with different temperature coefficient, β_0. When integrated with a TEG using a p-Si that has large value of β_0, the PV cell loses significant amounts of power because of increased operating temperature. Although the TEG generated some power, the gain from the TEG is less than the loss in the PV, resulting an overall reduction in power output. However, when a-Si PV cell that has a small value of β_0 was integrated with a TEG, the

power gained from the TEG overcompensate the loss from the PV and consequently overall increases in the P_{tot} and η_{tot} are obtained.

4) A hybrid PV/TEG system was constructed using an amorphous silicon PV cell (a-Si) integrated with a TEG that can be replaced by one of the other 5 TEGs with different sizes (i.e., with different values of AcN/L_{TE}). This system facilitated in-depth experimental study of geometrical influence of the TEG on the performance of the hybrid system and provided experimental verification of the developed theoretical model. The results from this study show a good agreement between experiments and simulations with an average deviation of 9 %. In addition, a suitable TEG that has an optimal geometry for this experimental hybrid system was identified among these 6 commercial TEGs investigated in this study, which was then used in the following studies for developing improved PV/TEG hybrid systems.

5) The effect of light intensity on the performance of the hybrid PV/TEG system was investigated using a home-made concentrator. The experimental results from this study show that the P_{TE} and η_{TE}, P_{PV} and η_{PV}, and P_{tot} and η_{tot} were all further improved when the hybrid system was tested under 2 suns and 5 suns concentration, respectively. This work indicates that it is more beneficial to operate a hybrid PV/TEG system under concentrated solar illumination. The effect of mass flowrate of the heat exchanger was also studied and it was found that the P_{tot} and η_{tot} were increased with increasing the mass flowrate. This is because an increase mass flowrate resulted in a decrease in the cold side temperature of the TEG. As a result, the ΔT cross the TEG increased while T_{cell} of the PV cell decreased, leading to an increase in both the P_{TE} and P_{PV}.

6) Dye sensitized solar cells (DSC) were successfully fabricated and characterised for the first time at Cardiff Thermoelectric Laboratory. This involved developing fabrication procedures and facilities using the available equipment at Cardiff. Two types of DSCs were fabricated in this research: the first was a conventional type of DSC (G-SC), which uses FTO-glass as the counter electrode; and the second was an improved design (Ti-SC), which uses Ti as the counter electrode. The G-SC was chosen as a benchmark for a comparative study. The Ti-SC was specifically designed to improve the thermal coupling between DSC and TEG. The experimental results of this study demonstrated that while the efficiency of both G-SC and Ti-SC are similar, the thermal coupling between the DSC and TEG in Ti-SC was substantially improved compared with in G-SC. The successful fabrication of this special Ti-SC provided a crucial component for the following development of more efficient hybrid PV/TEG systems.

7) A unique DSC/TEG hybrid system was designed and constructed by integrating the specifically developed Ti-SC with an optimised TEG. Due to the use of Ti counter electrode, which also serves as the thermal interface between DSC and TEG, the thermal coupling between DSC and TEG were significantly improved. As a result, the waste heat produced in the solar cell can be removed and transferred effectively through the TEG for energy harvesting. The experimental results show that the power output from TEG in a Ti-SC based hybrid system increased by more than 200 % compared with the system based on G-SC. Consequently, the overall power output and conversion efficiency of the hybrid DSC/TEG system exhibit significant improvement when the Ti counter electrode is employed.

7.2 FUTURE WORK

The following potential improvements and recommendation have been identified in terms of the simulation, experiments and design:

1) The solar cells used in the experiment to study the influence of temperature had a low η_{PV}. This is mainly due to the fact that most of these solar cells (except CdTe and DSC) were commercial products. In order to evaluate their future prospects, the investigation should be performed using the solar cells with the highest efficiency. In this work, due to limited time and resources, only few samples from each type were investigated. If the time and resource are available, it is important to test more samples of the same type and also from different manufacturers to obtain more accurate evaluation of the parameter β_0. The study should be expanded to include a wide range of other new solar cells such as perovskite and polymer solar cells.
2) The current simulation assumed that the temperature of the cold side of thermoelectric generator is constant. The simulation will form a more comprehensive study if the hot side temperature of TEG is controlled by the inlet temperature and the mass flowrate of the cooling fluid. In order to do this the thermal resistance between the cold side and the mean temperature of the inlet and outlet fluid has to be considered. The effect of using different coolants (such as Al_2O_3 nanofluid, TiO_2 nanofluid) instead of water should be theoretically studied in terms of the thermal power that could be generated by recycling the waste heat from the PV/TEG hybrid system. Furthermore, the use of thermal power to generate electricity from the TEG during the night time should be investigated, perhaps by storing thermal energy.

3) It has been predicted theoretically that the vacuum system improved the P_{max} and η_{TE} of the TEG. This investigation could be extended to involve PV cell and the PV/TEG hybrid system. Also, expanding the validation study to verify the theoretical results of the vacuum system should be considered. A specifically designed TEG with optimised geometry should be fabricated and used for the validation, rather than the commercially available modules, to obtain more accurate data.
4) The maximum light intensity produced by the solar parabolic dish concentrator of this study was five suns. It is interesting to carry out further investigation on the hybrid PV/TEG systems under much higher solar illumination using high concentration systems. Another interesting route is to split the solar spectrum into two parts using hot mirrors and focus the visible light only on the PV cells and the infrared on the TEG. In addition, the energy storage system should be considered to store excess heat either for generating the electricity using the TEG during the night time or for domestic use as a hot water.
5) Improving the heat exchanger by using nanofluid as a coolant can be further investigated to evaluate its potential benefit by conducting experimental study.
6) The dye sensitised solar cells fabricated in this research had an efficiency of about 5 %. It is possible to increase the efficiency by conducting more work, which was not possible during this research because of time and equipment constraints. Some of potential approaches include:
    a) Adding the second layer of TiO_2 to improve light scattering and absorption.
    b) Treating the FTO-glass with HCL to enhance the bond of the TiO_2 with the wall.
    c) Optimising the thickness of the TiO_2 layers printed on the FTO-glass.

d) Using anti-reflective film to reduce reflection to the incident light.

e) Employing perovskite hole transport materials to replace conventional electrolyte.

7) The experimental results demonstrated that the optimum operating temperature for the dye sensitised solar cells is between 35 ºC and 45 ºC. It is recommended to increase the operating temperature of DSCs up to 80 ºC by investigating different electrolytes. A higher operating temperature enables a large ΔT across the TEG and consequently increases the power output of the TEG without causing power loss from the PV cells.

8) The current hybrid system was fabricated by attaching the TEG to the backside of the DSC. Heat sink compound was used to fill gaps between the DSC and the TEG, which introduces potential reliability problems and additional thermal interfaces. Fabrication of the TEG directly on to the backside of the PV using integrated technology will eliminate many thermal interfaces and consequently minimise thermal resistance and improve the reliability.

9) Potential benefit of improving the performance of a hybrid PV/TEG system by using vacuum to minimise convective heat loss would be investigated. The performance of the hybrid system under higher solar illumination (> 5x) should also be evaluated by using high intensity concentrators such as parabolic mirrors and Fresnel lenses.

APPENDIXES

Appendix.1 An example of measurement commands is illustrated by a screenshot.

Commands	Parameters	Links
Cyclic voltammetry potentiostatic		
Remarks	Cyclic voltammetry potentiostatic	
End status Autolab		
Signal sampler	Time, WE(1).Potential, WE(1).Current	
Options	1 Options	
Instrument	AUT40008	
Instrument description		
Autolab control		
Set potential	0.000	
Set cell	On	
Wait time (s)	5	
Optimize current range	5	
CV staircase	[0.000, 1.000, -1.000, 0.000, 2, 0.1000000]	
Start potential (V)	0.000	
Upper vertex potential (V)	1.000	
Lower vertex potential (V)	-1.000	
Stop potential (V)	0.000	
Number of stop crossings	2	
Step potential (V)	0.00244	
Scan rate (V/s)	0.1000000	
Estimated number of points	1650	
Interval time (s)	0.024400	
Signal sampler	Time, WE(1).Potential, WE(1).Current	
Options	1 Options	
Potential applied	<..array..> (V)	
Time	<..array..> (s)	
WE(1).Current	<..array..> (A)	
Scan	<..array..>	
WE(1).Potential	<..array..> (V)	
Index	<..array..>	
i vs E		
Set cell	Off	
<..>		

Appendix.2 Sample of a measured I-V curve of DSC.

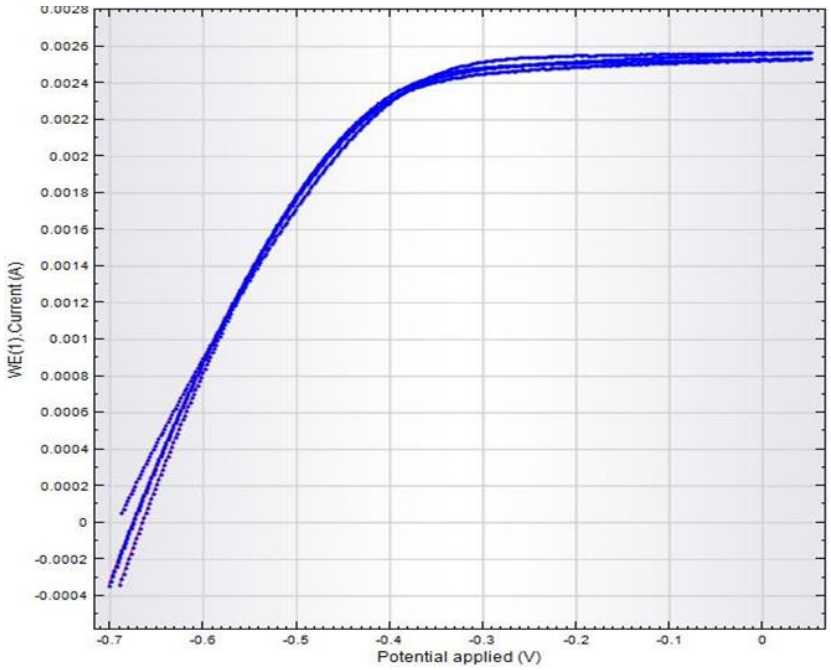

Appendix.3 A photograph of all 6 types of PV cells.

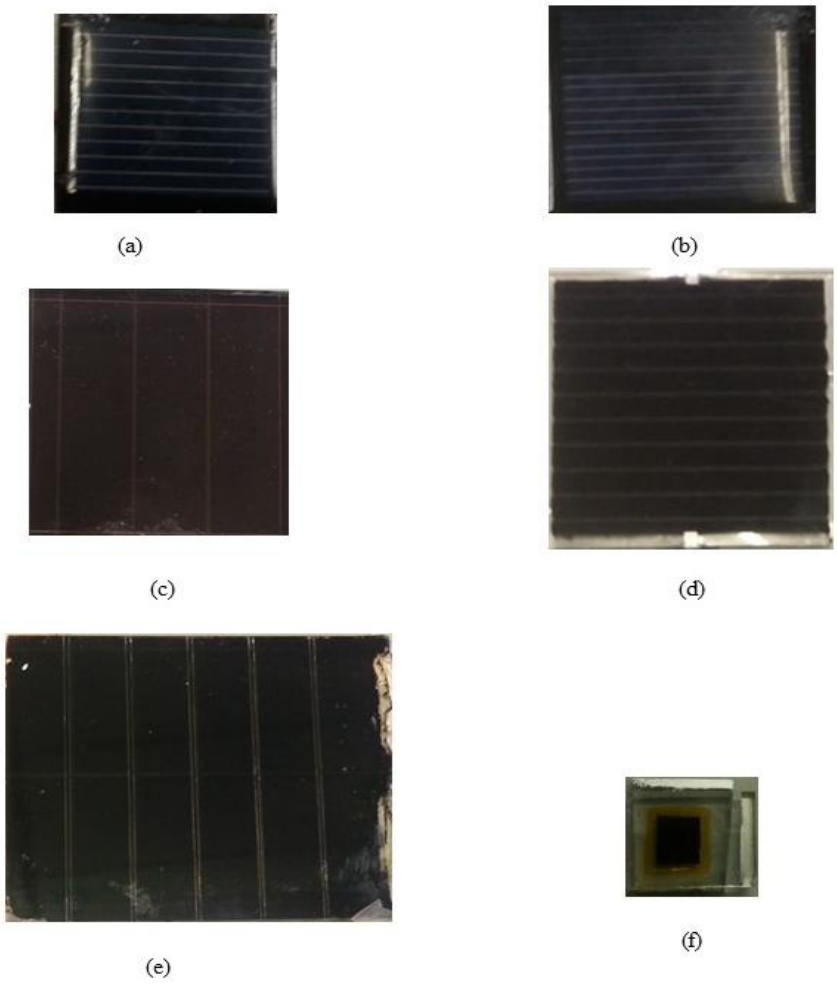

Appendix.4 Standard deviation

The standard deviation of six PV cells

T °C	m-Si		p-Si		a-Si		CIS		CdTe		DSC	
	P_{max} mW	σ mW	P_{max} mW	σ mW	P_{max} mW	σ mW	P_{max} mW	σ mW	P_{max} mW	σ mW	P_{max} mW	σ mW
25	73	1	181.5	0.5	84.4	0.3	150.5	0.5	121.5	0.5	1	0.01
35	69.5	0.5	170.1	0.4	84.1	0.1	147	1.1	113.7	0.3	1.1	0.02
45	65.5	0.4	161.5	1.1	82.6	0.6	140.6	0.5	108.1	0.1	1.1	0.01
55	62.2	0.2	153.4	0.7	82	0.2	137	1.1	103.2	0.4	1.1	0.01
65	59.8	0.3	143	1	79.6	0.4	131	1	101.3	0.3	0.9	0.01

Appendix.5 The Matlab Code.

System at atmosphere

```
clear;
clc;
Apv=(0.04)^2;% PV device area
G=1000;
effpv=0.1;% PV cell efficiency
Lg=0.003;% thickness of the glass of PV cell
Kg=1;% thermal conductivity of the glass
hcov=5;% convective heat transfer
Ut=((Lg/Kg)+(1/hcov))^-1;
Tamb=298.15;
Tc=298;% cold side temperature
Tg=0.95;% the transmissivity of the glass
ems=0.88;% the surface emissivity of the cell
S=5.67*10^-8; the Stefan-Boltzmann constant
k=1.5;% thermal conductivity of TEG
N=62;% number of thermoelements
ATE=(.8*10^-3)^2; TEG area
A=ATE*N;% area of TEG
alf=185*10^-6;% the Seebeck coefficient
row=1*10^-5;% the electrical resistivity
Z=alf^2/(row*k);%the thermoelectric figure of merit
n=0.0001;% electrical contact parameters
r=0.2;% thermal contact parameters
Lc=0.00009;% the thickness of the ceramic plates
Bref=0.0011;% the temperature coefficient for silicon solar
cells,%/K

Tref=298;%reference temperature
syms tempsym
count=0;
f=@(Ts,L) (-G*Tg*Apv+(ems*5.67)*10^(-8)*(2*Apv-A)*(Ts^4-
Tamb^4)+Ut*(2*Apv-A)*(Ts-
Tamb)+(k*(1+Z*((3*Ts+Tc)/8))*ATE*N)*(Ts-
Tc)/(L)+((G*Tg*Apv*(effpv*(1-Bref*(Ts-Tref))))));

for L=0.00005:0.0005:0.008
count=count+1;
roots=solve(f(tempsym,L));
posroot(count)=subs(roots(1),1);
delT(count)=posroot(count)-Tc;
B(count)=delT(count);
Pmax(count)=1000*(alf^2*ATE*N*(delT(count))^2/(4*row*(n+L)*(1+2*
r*Lc/L)^2));
Pmax1(count)=Pmax(count)/A;
L_plot(count)=L;
PA(count)=Pmax(count)*10^-6/(A);

QTE(count)=1000*(G*Tg*Apv-hcov*(2*Apv-A)*(posroot(count)-Tamb)-
(ems*5.67)*10^(-8)*(2*Apv-A)^2*((posroot(count))^4-Tamb^4)-
((G*Apv*Tg*(effpv*(1-Bref*(posroot(count)-Tref))))));

effTEG1(count)=100*Pmax(count)/QTE(count);
```

```
effTEG2(count)=Pmax(count)*.1/(1000*Apv)



effpv1(count)=((G*Apv*(effpv*(1-Bref*(posroot(count)-
Tref))))/(G*Apv));% efficiency of PV as a function of
temperature
effpv2(count)=100*effpv1(count);% (%)

Ppvmax(count)= 1000*effpv1(count)*G*Apv;% (mW)
PmaxT(count)=Ppvmax(count)+Pmax(count);% Ptot
effT(count)=(effpv2(count)+effTEG2(count))
end


figure;
plot(L_plot, Pmax);
xlabel('Thermoelectric length,(m)')
ylabel('Power output TEG, (mW)')
grid

figure;
plot(L_plot, Ppvmax);
xlabel('Thermoelectric length,(m)')
ylabel('Power output PV, (mW)')
grid

figure;
plot(L_plot, PmaxT);
xlabel('Thermoelectric length,(m)')
ylabel('Total Power output, PV+TEG, (mW)')
grid


figure;
plot(L_plot,delT);
grid
xlabel('Thermoelectric length,(m)')
ylabel('Temperature difference,(°C)')
figure;
plot(L_plot,PA);
grid
xlabel('Thermoelectric length,(m)')
ylabel('Power per unit area, (mW/mm2)')

figure;
plot(L_plot, effpv2);
grid
xlabel('Thermoelectric length,(m)')
ylabel('Efficiency PV, (%)')

figure;
plot(L_plot,effTEG1);
grid
xlabel('Thermoelectric length,(m)')
ylabel('Efficiency TEG, (%)')
```

```
figure;
plot(L_plot,effT);
xlabel('Thermoelectric length,(m)')
ylabel('Efficiency PV+TEG, (%)')
grid
```

System at Vacuum

```
clear;
clc;
Apv=(0.04)^2;% PV device area
G=1000;
effpv=0.1;% PV cell efficiency
Lg=0.003;% thickness of the glass of PV cell
Kg=1;% thermal conductivity of the glass
hcov=5;% convective heat transfer
Ut=((Lg/Kg)+(1/hcov))^-1;
Tamb=298.15;
Tc=298;% cold side temperature
Tg=0.95;% the transmissivity of the glass
ems=0.88;% the surface emissivity of the cell
S=5.67*10^-8; the Stefan-Boltzmann constant
k=1.5;% thermal conductivity of TEG
N=62;% number of thermoelements
ATE=(.8*10^-3)^2; TEG area
A=ATE*N;% area of TEG
alf=185*10^-6;% the Seebeck coefficient
row=1*10^-5;% the electrical resistivity
Z=alf^2/(row*k);%the thermoelectric figure of merit
n=0.0001;% electrical contact parameters
r=0.2;% thermal contact parameters
Lc=0.00009;% the thickness of the ceramic plates
Bref=0.0011;% the temperature coefficient for silicon solar
cells,%/K

Tref=298;%reference temperature
syms tempsym
count=0;
f=@(Ts,L) (-G*Tg*Apv+(ems*5.67)*10^(-8)*(2*Apv-A)*(Ts^4-
Tamb^4)+(k*(1+Z*((3*Ts+Tc)/8))*ATE*N)*(Ts-
Tc)/(L)+((G*Tg*Apv*(effpv*(1-Bref*(Ts-Tref))))));

for L=0.00005:0.0005:0.008
count=count+1;
roots=solve(f(tempsym,L));
posroot(count)=subs(roots(1),1);
delT(count)=posroot(count)-Tc;
B(count)=delT(count);
Pmax(count)=1000*(alf^2*ATE*N*(delT(count))^2/(4*row*(n+L)*(1+2*
r*Lc/L)^2));
Pmax1(count)=Pmax(count)/A;
L_plot(count)=L;
PA(count)=Pmax(count)*10^-6/(A);
```

```
QTE(count)=1000*(G*Tg*Apv-hcov*(2*Apv-A)*(posroot(count)-Tamb)-
(ems*5.67)*10^(-8)*(2*Apv-A)^2*((posroot(count))^4-Tamb^4)-
((G*Apv*Tg*(effpv*(1-Bref*(posroot(count)-Tref))))));

effTEG1(count)=100*Pmax(count)/QTE(count);
effTEG2(count)=Pmax(count)*.1/(1000*Apv)



effpv1(count)=((G*Apv*(effpv*(1-Bref*(posroot(count)-
Tref))))/(G*Apv));% efficiency of PV as a function of
temperature
effpv2(count)=100*effpv1(count);% (%)

Ppvmax(count)= 1000*effpv1(count)*G*Apv;% (mW)
PmaxT(count)=Ppvmax(count)+Pmax(count);% Ptot
effT(count)=(effpv2(count)+effTEG2(count))
end


figure;
plot(L_plot, Pmax);
xlabel('Thermoelectric length,(m)')
ylabel('Power output TEG, (mW)')
grid

figure;
plot(L_plot, Ppvmax);
xlabel('Thermoelectric length,(m)')
ylabel('Power output PV, (mW)')
grid

figure;
plot(L_plot, PmaxT);
xlabel('Thermoelectric length,(m)')
ylabel('Total Power output, PV+TEG, (mW)')
grid
figure;
plot(L_plot,delT);
grid
xlabel('Thermoelectric length,(m)')
ylabel('Temperature difference,(°C)')

figure;
plot(L_plot,PA);
grid
xlabel('Thermoelectric length,(m)')
ylabel('Power per unit area, (mW/mm2)')

figure;
plot(L_plot, effpv2);
grid
xlabel('Thermoelectric length,(m)')
ylabel('Efficiency PV, (%)')

figure;
```

```
plot(L_plot,effTEG1);
grid
xlabel('Thermoelectric length,(m)')
ylabel('Efficiency TEG, (%)')


figure;
plot(L_plot,effT);
xlabel('Thermoelectric length,(m)')
ylabel('Efficiency PV+TEG, (%)')
grid
```

Appendix.6 Sample of calculation results for M-I in Vacuum and non-vacuum.

The maximum power output Vs thermoelements length in vacuum and non-vacuum

Vacuum		Non Vacuum	
L (m)	P_{max} (mW)	L (m)	P_{max} (mW)
0.0005	0.441453	0.0005	0.398966
0.0055	5.489172	0.001	1.117635
0.0105	5.687715	0.0015	1.719409
0.0155	5.145873	0.002	2.166411
0.0205	4.567183	0.0025	2.485517
0.0255	4.065174	0.003	2.707594
0.0305	3.646595	0.0035	2.857724
0.0355	3.298748	0.004	2.95479
0.0405	3.007651	0.0045	3.0127
0.0455	2.761618	0.005	3.041665
0.0505	2.551517	0.0055	3.049203
0.0555	2.370324	0.006	3.040879
0.0605	2.212638	0.0065	3.020839

0.0655	2.074271	0.007	2.992192
0.0705	1.951948	0.0075	2.95728
0.0755	1.843074	0.008	2.917881
0.0805	1.745577	0.0085	2.875344
0.0855	1.657783	0.009	2.830701
0.0905	1.578326	0.0095	2.784742
0.0955	1.506083	0.01	2.738069
0.1005	1.440122	0.0105	2.691145
0.1055	1.379663	0.011	2.644322
0.1105	1.32405	0.0115	2.597867
0.1155	1.272725	0.012	2.551983
0.1205	1.225214	0.0125	2.506818
0.1255	1.181108	0.013	2.462484
0.1305	1.140055	0.0135	2.419059
0.1355	1.101751	0.014	2.376598
0.1405	1.06593	0.0145	2.335135
0.1455	1.032357	0.015	2.294689
0.1505	1.000829	0.0155	2.255271
0.1555	0.971165	0.016	2.216877
0.1605	0.943205	0.0165	2.179501
0.1655	0.916806	0.017	2.143129
0.1705	0.891841	0.0175	2.107743
0.1755	0.868198	0.018	2.073324

Appendix.7 Measuring the geometry of thermoelectric generator using Microscope; a) actual picture for the microscope, computer and modules. b) Module with the measurements.

(a)

(b)

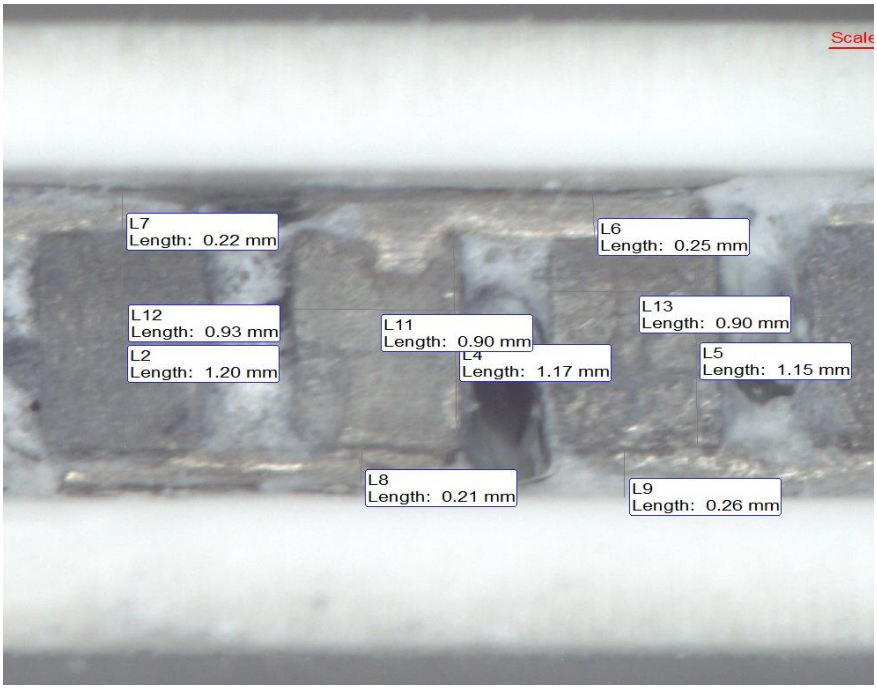

Appendix.8: The parameters of the six TEG (M-A, M-B, M-C, M-D, M-E and M-F) used for validation.

Module A			**Module B**		
Parameter	**Value**	**Unit**	**Parameter**	**Value**	**Unit**
A_{PV}	$(0.04)^2$	m^2	A_{PV}	40x40	m^2
A_{TE}	$(0.8x10^{-3})^2$	m^2	A_{TE}	$(0.8x10^{-3})^2$	m^2
N	14	--	N	62	--
G	1000	W/m^2	G	1000	W/m^2
η_{PV}	4.9	%	η_{PV}	4.9	%
τ_g	0.95	--	τ_g	0.95	--
β_c	1	--	β_c	1	--
β_0	0.0011	K^{-1}	β_0	0.0011	K^{-1}
h_{cov}	5	$W.m^{-2}K^{-1}$	h_{cov}	5	$Wm^{-2}K^{-1}$
T_{amb}	296	K	T_{amb}	298	K
ε	0.9	--	ε	0.9	--
k	1.5	$W.m^{-1}K^{-1}$	k	1.5	$W.m^{-1}K^{-1}$
kg	1	$W.m^{-1}K^{-1}$	kg	1	$W.m^{-1}K^{-1}$
α	182	μVK^{-1}	α	170	μVK^{-1}
ρ	1×10^{-5}	Ω.m	ρ	1 x 10-5	Ω.m
n	0.0001	m	n	0.0001	m
r	0.03	--	r	0.01	--
l_c	0.002	m	l_c	0.002	m
T_{ref}	298	K	T_{ref}	298	K

Module C			**Module D**		
Parameter	**Value**	**Unit**	**Parameter**	**Value**	**Unit**
A_{PV}	$(0.04)^2$	m^2	A_{PV}	40x40	m^2
A_{TE}	$(0.5x10^{-3})^2$	m^2	A_{TE}	$(0.7x10^{-3})^2$	m^2
N	98	--	N	142	--
G	1000	W/m^2	G	1000	W/m^2
η_{PV}	4.9	%	η_{PV}	4.9	%
τ_g	0.95	--	τ_g	0.95	--
β_c	1	--	β_c	1	--
β_0	0.0011	K^{-1}	β_0	0.0011	K^{-1}
h_{cov}	5	$W.m^{-2}K^{-1}$	h_{cov}	5	$Wm^{-2}K^{-1}$
T_{amb}	298	K	T_{amb}	296	K
ε	0.9	--	ε	0.9	--
k	1.5	$W.m^{-1}K^{-1}$	k	1.5	$W.m^{-1}K^{-1}$
kg	1	$W.m^{-1}K^{-1}$	kg	1	$W.m^{-1}K^{-1}$
α	162	μVK^{-1}	α	157	μVK^{-1}
ρ	1×10^{-5}	Ω.m	ρ	1 x 10-5	Ω.m
n	0.0001	m	n	0.0001	m
r	0.02	--	r	0.01	--
l_c	0.0009	m	l_c	0.002	m
T_{ref}	298	K	T_{ref}	298	K

Module E			**Module B**		
Parameter	**Value**	**Unit**	**Parameter**	**Value**	**Unit**
A_{PV}	$(0.04)^2$	m^2	A_{PV}	40x40	m^2
A_{TE}	$(2.1x10^{-3})^2$	m^2	A_{TE}	$(0.9x10^{-3})^2$	m^2
N	62	--	N	256	--
G	1000	W/m^2	G	1000	W/m^2
η_{PV}	4.9	%	η_{PV}	4.9	%
τ_g	0.95	--	τ_g	0.95	--
β_c	1	--	β_c	1	--
β_0	0.0011	K^{-1}	β_0	0.0011	K^{-1}
h_{cov}	5	$W.m^{-2}K^{-1}$	h_{cov}	5	$Wm^{-2}K^{-1}$
T_{amb}	298	K	T_{amb}	298	K
ε	0.9	--	ε	0.9	--
k	1.5	$W.m^{-1}K^{-1}$	k	1.5	$W.m^{-1}K^{-1}$
kg	1	$W.m^{-1}K^{-1}$	kg	1	$W.m^{-1}K^{-1}$
α	165	μVK^{-1}	α	155	μVK^{-1}
ρ	1×10^{-5}	Ω.m	ρ	1 x 10-5	Ω.m
n	0.0001	m	n	0.0001	m
r	0.04	--	r	0.04	--
l_c	0.002	m	l_c	0.002	m
T_{ref}	298	K	T_{ref}	298	K

Appendix.9 Sample of measurement results for PV cell under one sun and five suns.

Characterisation of PV cell under one sun

R (ohm)	V (mW)	I (mA)	P (mW)
0.1	0.0	220.0	2.5
0.3	60.0	217.0	13.0
0.7	140.0	216.0	30.2
1.1	230.0	215.0	49.5
1.5	325.0	214.0	69.6
2.1	446.0	210.0	93.7
3.1	507.7	163.8	83.1
4.1	526.1	128.3	67.5
5.1	537.0	105.3	56.5
6.1	544.9	89.3	48.7
7.1	550.0	77.5	42.6
8.1	553.0	68.3	37.8
9.1	556.1	61.1	34.0
10.1	558.0	55.2	30.8
100.0	575.0	5.8	3.3
0.0	576.0	0.0	0.0

Characterisation of PV cell under five suns

R	V (mW)	I (m Am)	P (mW)
0.1	0.0	975.0	0.0
0.2	195.0	975.0	190.1
0.3	281.0	936.7	263.2
0.4	338.0	845.0	285.6
0.5	**378.0**	**756.0**	**285.8**
0.6	407.4	679.0	276.6
0.7	426.2	608.9	259.5
0.8	441.7	552.1	243.9
0.9	454.7	505.2	229.7

1	465.0	465.0	216.2
2.1	526.0	250.5	131.8
3.1	548.0	176.8	96.9
4.1	559.9	136.6	76.5
5.1	567.0	111.2	63.0
6.1	572.0	93.8	53.6
7.1	575.0	81.0	46.6
8.1	578.0	71.4	41.2
9.1	580.0	63.7	37.0
10.1	581.0	57.5	33.4
100	596.0	6.0	3.6
0	598.0	0.0	0.0

Appendix.10 Characterisation of PV cell under one sun and five suns

No.	T_H (^oC)	ΔT (^oC)	V_{OC} (mV)	I_{SC} (mA)	FF (%)	η_{PV} (%)
1 sun	24	4	576	220	65.6	6.8
5 suns	33	13	598	975	49	4.7

Appendix.11 The specifications and details of the flowmeter.

NPT Female	Connection Type 1/8
Device Type	Flow Indicator
Material	Brass
Maximum Flow Rate	100 cm/m
Maximum Media Temperature	+ 65°C

Maximum Operating Temperature	+ 65°C
Maximum Pressure	6.89 bar
Media Monitored	Liquid
Minimum Flow Rate	10 ccm
Pipe Diameter Range	1/8 in
Accuracy	± 5 % full scale

Appendix.12 The effect of mass flowrate on temperature difference across TEG.

Mass flowrate (kg/s)	T_C [ºC]	T_H [ºC]	ΔT= [ºC]
m1= 0.0015	20.2	42	21.9
m2= 0.00125	23.1	46.8	23.6
m3= 0.00066	24.4	51.4	26.3
m4= 0.00041	26.6	54.14	27.5
m5= 0.00016	33	60	26.6

Appendix.13 The mass flowrate and the temperature difference between the inlet and outlet fluid.

Mass flowrate (kg/s)	T_{in} [ºC]	T_{out}[ºC]	ΔT_f= [ºC]
0.00041	22.1	23.2	1.1

Appendix.14 Improving Cooling Using Nanofluid

This section discusses the laboratory testing of a nanofluid for improving cooling performance in a concentrated PV/TEG system. The section is divided into two processes: 1) the procedure of preparing the nanofluid in the laboratory, and 2) using it as a cooling media. The result was compared with a base fluid (the pure water in this study).

Preparing nanofluid

There are two main methods to prepare nanofluid; the first method is called the Single Step Method and the second one is called the Two Step Method. In the Single Step method, the nanoparticle is made and dispersed simultaneously in one step whereas in the Two Step method the nanoparticles are fabricated first and then dispersed into the base fluid(s).

In this work copper oxide (CuO) purchased from Schema Aldrich was used to prepare the CuO nanofluid. The diameter of nanoparticles was 50 nm. Figure A.14.1 showed a SEM image of CuO under different magnifications.

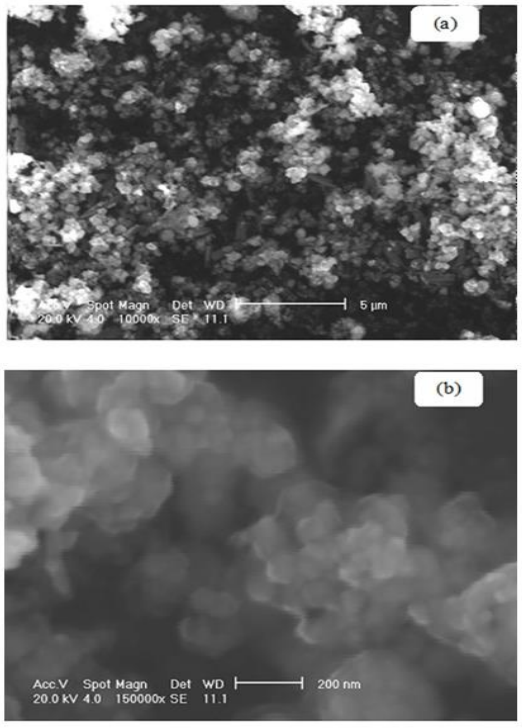

Figure A.14.1 SEM image of CuO nanoparticles; (a) 10000x and (b.)150000x magnification

A scale was used to weigh CuO nanoparticles and then the weighted amount was dispersed in pure water. A sonicator bath was used to disperse the CuO nanoparticles in the base fluid for 30 minutes. Figure A.14.2 shows a photograph of the pure water, the sonicator bath and the prepared nanofluid.

Figure A.14.2 A photograph of pure water and nanofluid

Experimental rig to test nanofluid:

Figures A.14.3 and A.14.4 show a schematic diagram and actual construction of the experimental setup, respectively. The same PV/TEG hybrid system presented in section 5.2.1.2 is used here, which includes crystalline solar cells of type (m-Si) with the TEG (M-A).

The TEG was mounted on an aluminium heat sink (12cm X 10 cm X 3.6 cm) with heat sink compound. The heat sink was then immersed in water inside an insulator box. The insulator box placed on magnetic stirrer to circulate the fluid inside the box. The same solar simulator used in Chapter 3 was used as the light source and the intensity of illumination was measured using the pyranometer. The experiment was conducted under a light intensity of two suns.

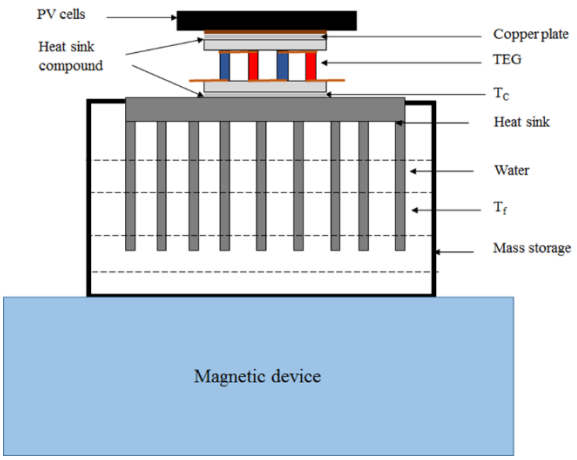

Figure A.14.3 A schematic diagram of the experimental setup

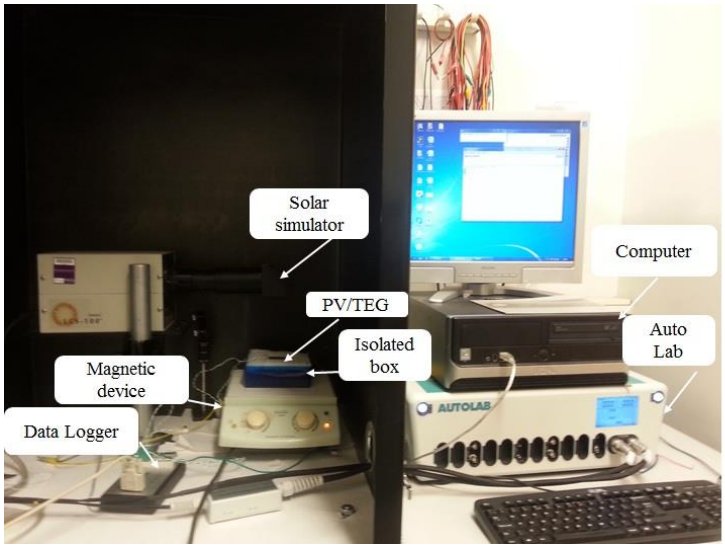

Figure A.14.4 A photograph of the experimental setup

A multi-channel data logger (explained in Chapter 3) was used for recording the temperature measurement. The I–V characteristics of the PV cells are determined by the same procedure mentioned in Chapter 3 and the TEG was characterised by using the procedure discussed in Chapter 4.

Results and Discussion

In the absence of facilities to measure the physical properties (e.g. density and specific heat) directly, they can be calculated based on the amount of nanoparticles dispersed in

the base fluid. These properties can then be used in the calculation of the total heat that can be removed from the cold side of TEG by the fluid.

The following equation is used to calculate the density of a nanofluid solution [110]:

$$\rho_{n,f} = (1 - \emptyset)\rho_{b,f} + \emptyset\rho_{n,p} \quad \text{A.1}$$

where $\rho_{n,f}$ is the density of nanofluid, $\rho_{b,f}$ is the density of base fluid, $\rho_{n,p}$ is the density of the nanoparticles and $\emptyset$ is the volume fraction. The volume fraction can be calculated as [109]:

$$\emptyset = \frac{V_n}{V_n + V_{b,f}} \quad \text{A.2}$$

where V_n is the volume of nanoparticles and $V_{b,f}$ is the volume of base fluid. Equation A.2 can also be expressed as:

$$\emptyset = \frac{(\frac{m}{\rho})_n}{(\frac{m}{\rho})_n + (\frac{m}{\rho})_{b,f}} \quad \text{A.3}$$

where $(\frac{m}{\rho})_n$ is the mass of nanoparticles divided by their density, and $(\frac{m}{\rho})_{b,f}$ is the mass of base fluid divided by its density. Consequently, the specific heat of a nanofluid can be calculated by using equations A.4 [109]:

$$cp_{n,f} = \frac{(1-\emptyset)\rho_{b,f}cp_{b,f} + \emptyset\rho_{n,p}cp_{n,p}}{\rho_{n,f}} \quad \text{A.4}$$

The weight of the CuO nanoparticles required for preparation of 400 ml of CuO nanofluid was calculated by using equation A.3. Table A.14.1 shows the physical properties of the nanoparticles and base fluid that were used to calculate the physical properties of CuO-nanofluid in Table A.14.1.

The benefit of using the nanofluid was examined by measuring the temperatures at three places: T_H, T_C and the fluid temperature (T_f) inside the mass storage. Figure A.14.5 shows the temperature results at T_H for the TEG when pure water was used as a cooling fluid, and when nanofluid was used.

Table A.14.1 Physical properties of pure water, CuO nanoparticles and CuO nanofluid

	Pure water	CuO - nanoparticle	CuO – Nanofluid
ρ (kg/m^3)	971	6510	2289.7
c_p $(J/kg.\ K)$	4197	540	1721.5

It can be seen that the nanofluid contributed to reduce the T_H of the TEG, which is beneficial for the PV cells as it assumed that the PV cells have the same temperature as the T_H of the TEG.

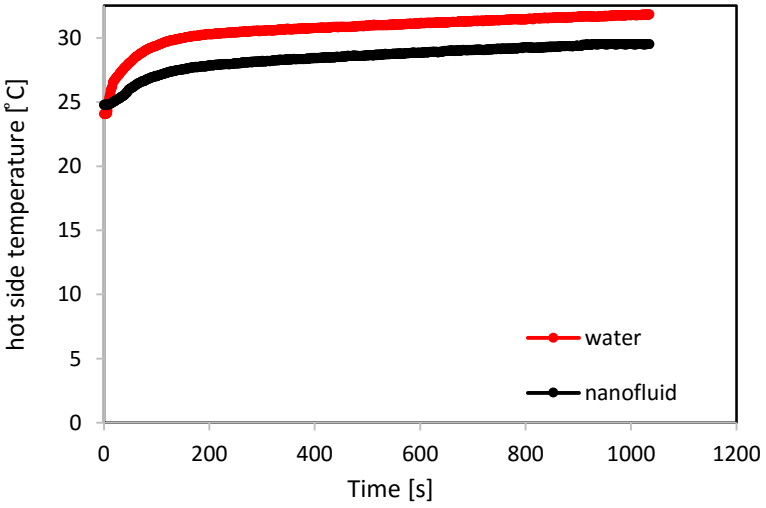

Figure A.14.5 The temperatures of the hot side of the TEG vs time for pure water and for nanofluid

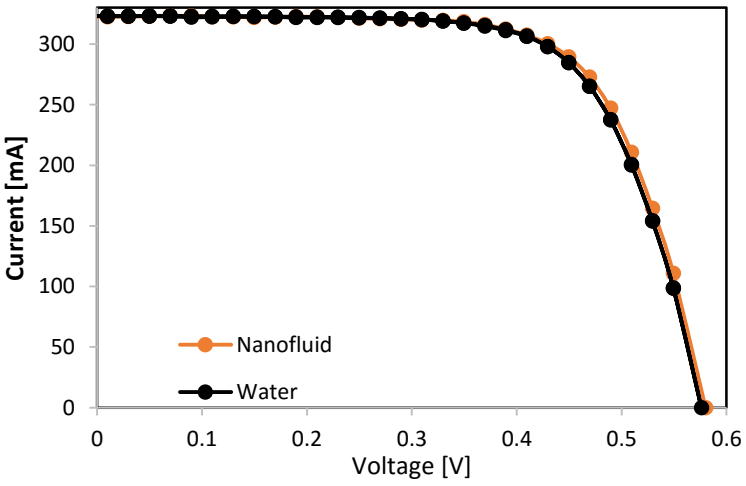

Figure A.14.6 The I-V curves of a PV cell when pure water and nanufluid are used as cooling fluids

As a result, the I-V curves are modified as shown in Figure A.14.6. Furthermore, the P_{PV} was improved as seen in Figure A.14.7 and the P_{max} of the PV increased from 127.9 mW to 130.1 mW. However, the ΔT established across the TEG device was affected because the T_H of the TEG with nanofluid was lower. This is because the heat was transferred to the fluid quickly when nanofluid was used.

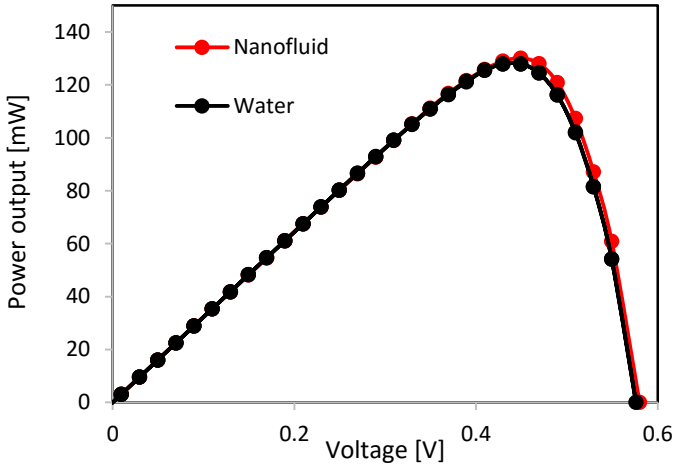

Figure A.14.7 The P-V curves of a PV cell when pure water and nanufluid are used as cooling fluids

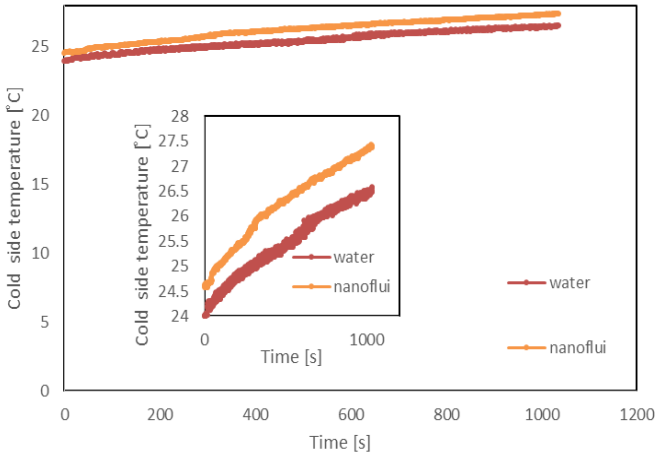

Figure A.14.8 The temperatures profile vs time when pure water and CuO nanofluid are used as cooling fluids

Consequently, Figure A.14.8 shows the T_C of the TEG with pure water and nanofluid. It is clear that the T_C with nanofluid presents a higher temperature because the T_f in the isolator box was higher as can be seen in Figure A.14.9.

As a result, the ΔT established across the TEG decreased and hence reduced the I_{SC}, and V_{OC} as can be seen in Figure A.14.10. Also, the P_{max} from the TEG dropped from 2 mW to 0.94 mW as shown in Figure A.14.11.

The rate of thermal energy ($\dot{Q}_{ther}$) removed from the cold side of the heat sink is calculated by using the following equation:

$$\dot{Q}_{ther} = mc_p \frac{\Delta T_f}{t} \qquad \text{A.5}$$

where, m is the mass of the fluid inside the box, t is the time and ΔT_f is the increase in the temperature during the time of measurement. The $\dot{Q}_{ther}$ calculated for time of 1000 second (s), and presented in Table A.14.2.

Table A.14.2 The time, mass, ΔT_f and Q_{ther}

	Time (s)	Mass of water (kg)	ΔT_f (^{0}C)	$\dot{Q}_{ther}$ (W)
Water	1000	0.1	2.33	0.98
Nanofluid	1000	0.1	2.6	0.45

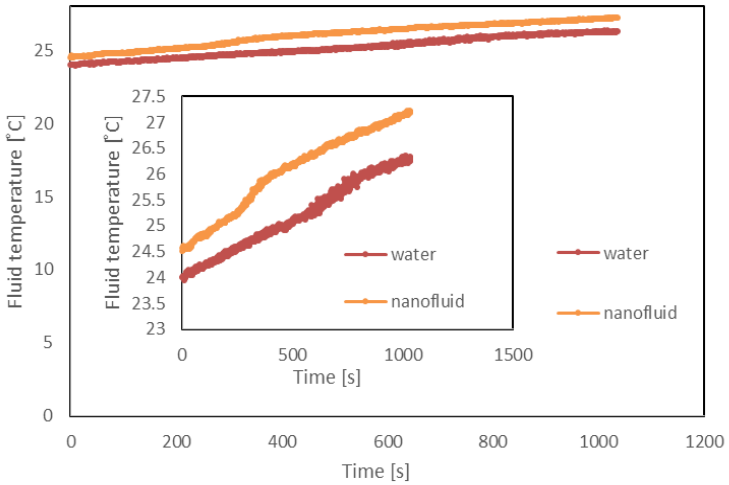

Figure A.14.9 The temperature of fluid inside the mass storage vs time when pure water and nanofluid are used as cooling fluids

Finally, the experimental results indicated that using nanofluid in the cooling system is recommended in order to reduce the operating temperature of PV cells.

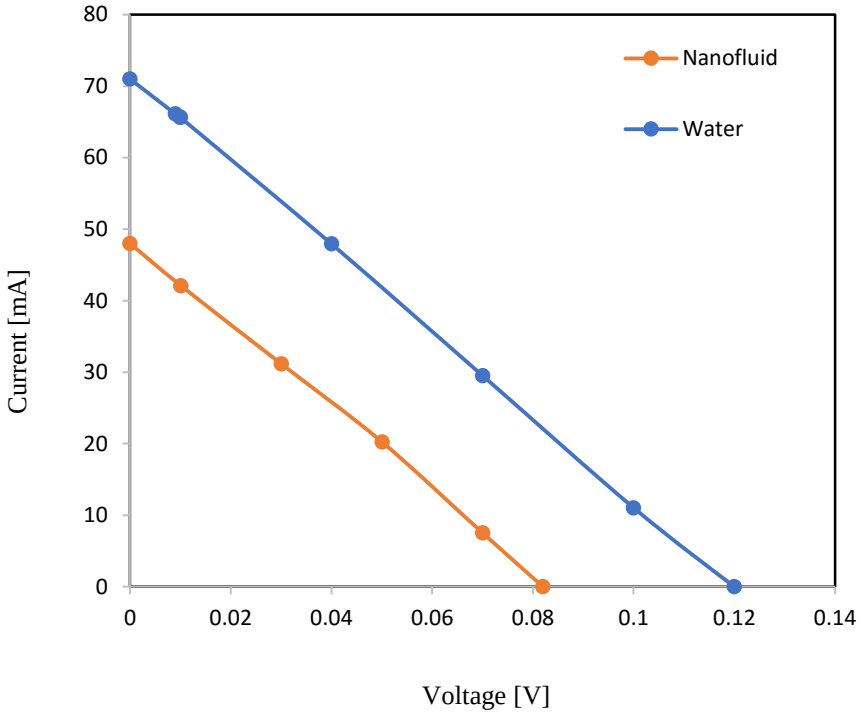

Figure A.14.10 The I-V curves of the TEG when pure water and nanufluid are used as cooling fluids

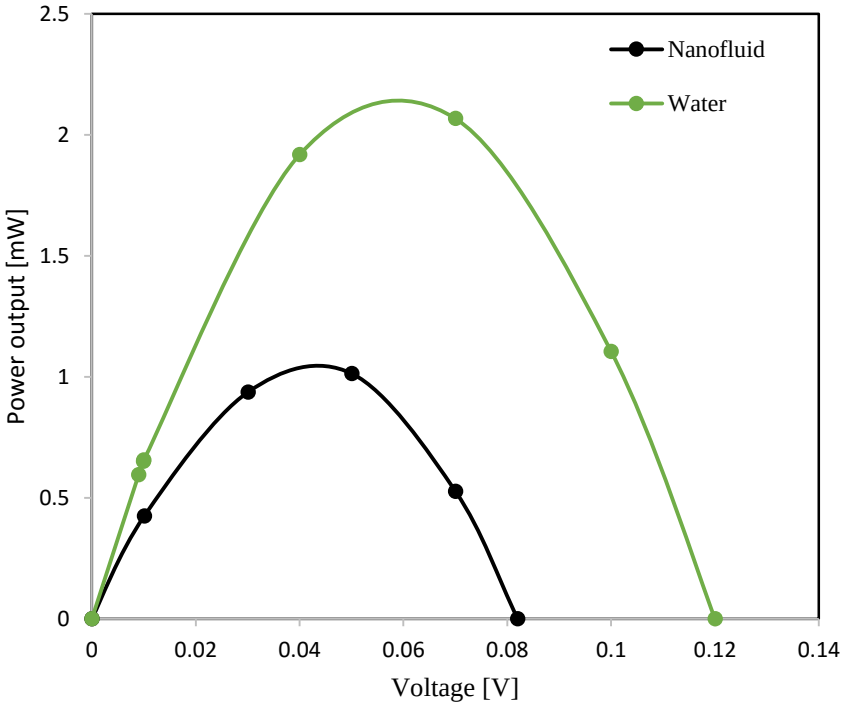

Figure A.14.11 The P-V curves of the TEG when pure water and nanufluid are used as cooling fluids

Appendix.15 The I-V curves of Ti-SC and G-SC.

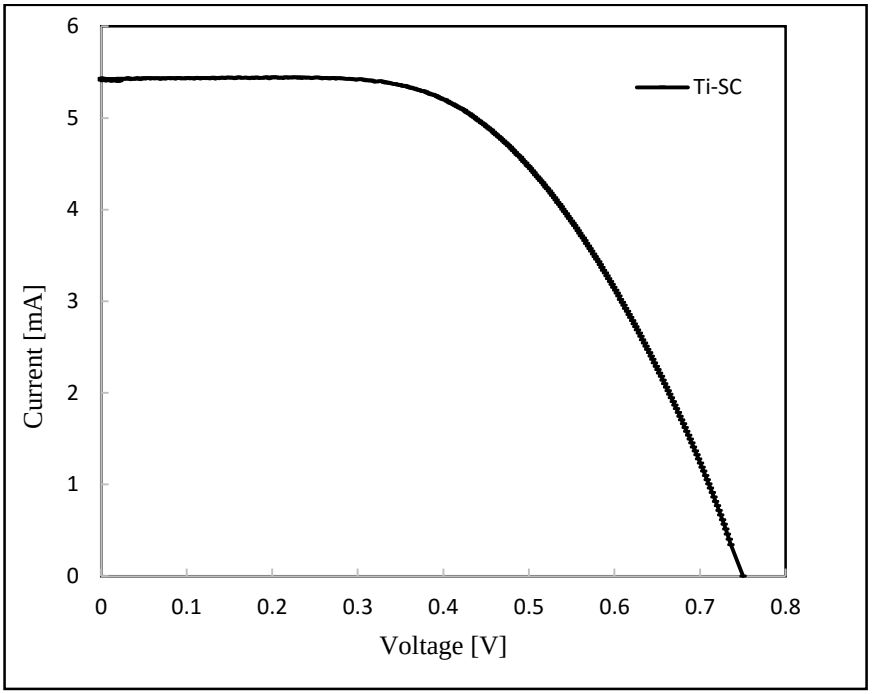

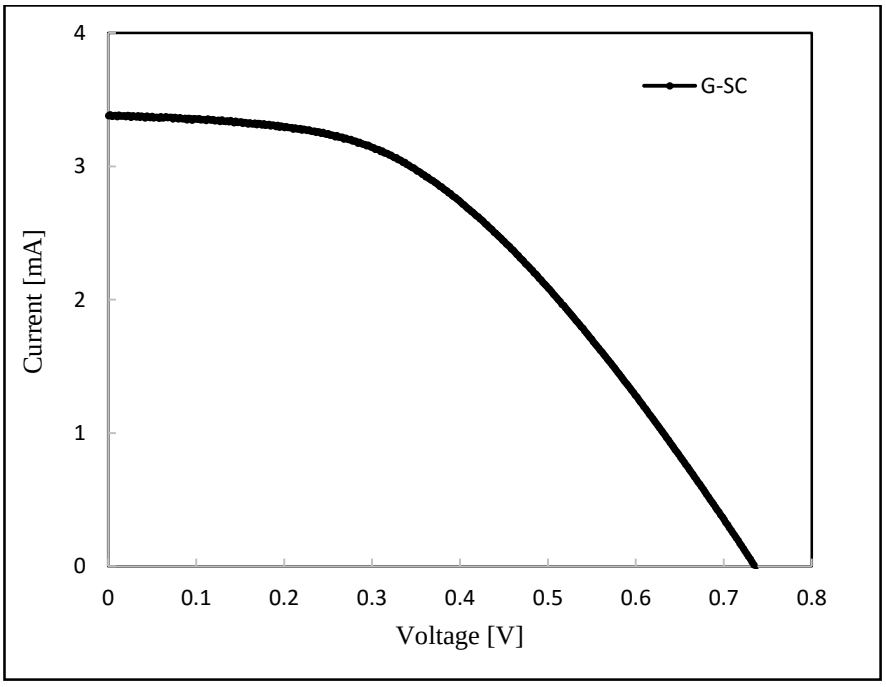

Appendix.16 The I-V and P-V curves for three TEGs method, a) M-A, b) M-B and c) M-C in HTC with titanium solar cells (Ti-SC) and glass solar cells (G-SC).

(a)

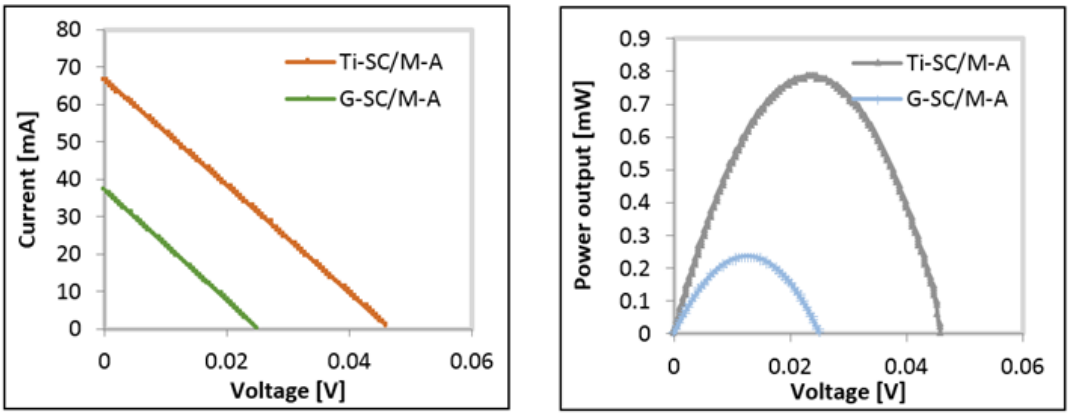

(b)

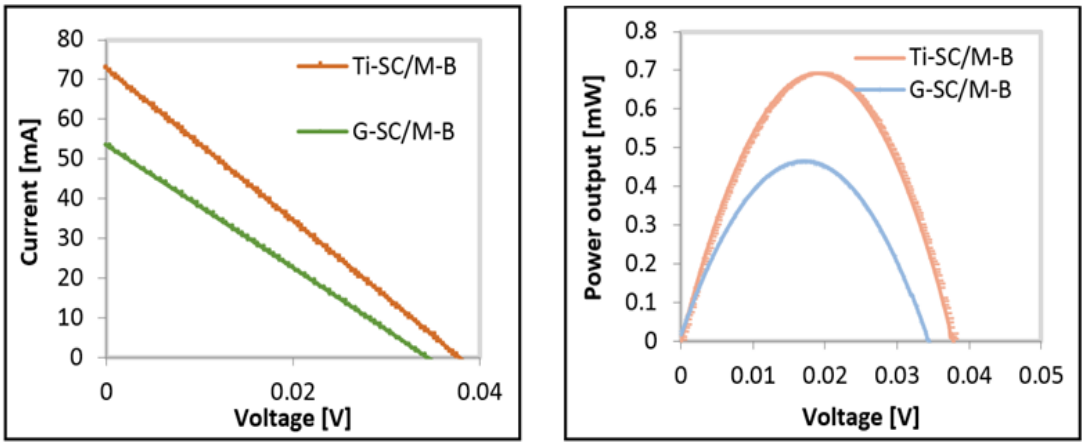

(a)

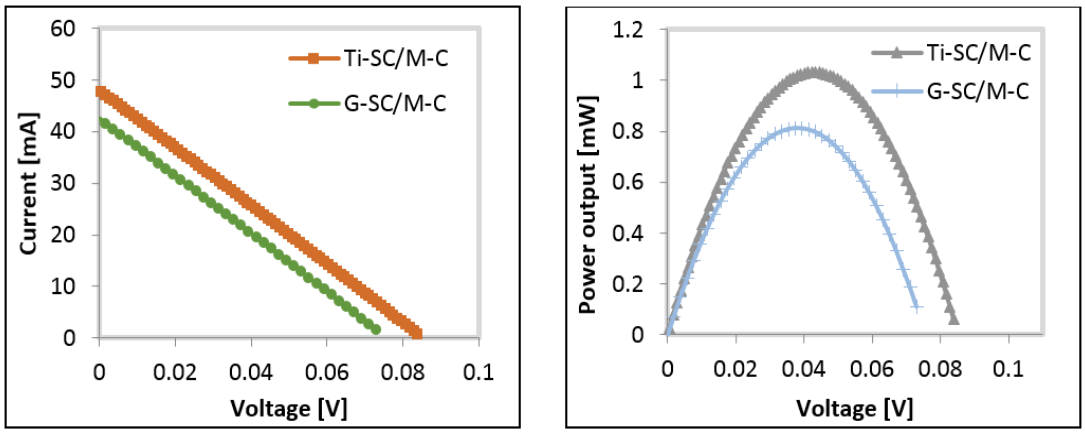

REFERENCES

REFERENCES

[1] E. Cuce, T. Bali, and S. A. Sekucoglu, "Effects of passive cooling on performance of silicon photovoltaic cells," *Int. J. Low-Carbon Technol.*, vol. 6, no. 4, pp. 299–308, Sep. 2011.

[2] Y. M. Irwan, W. Z. Leow, M. Irwanto, F. M, S. I. S. Hassan, I. Safwati, and A. R. Amelia, "Comparison of solar panel cooling system by using dc brushless fan and dc water," *J. Phys. Conf. Ser.*, vol. 622, p. 012001, Jun. 2015.

[3] H. Najafi and K. A. Woodbury, "Optimization of a cooling system based on Peltier effect for photovoltaic cells," *Sol. Energy*, vol. 91, pp. 152–160, May 2013.

[4] A. Kane and V. Verma, "Performance Enhancement of Building Integrated Photovoltaic Module using Thermoelectric Cooling," *Int. J. Renew. ENERGY Res.*, vol. 3, no. 2, 2013.

[5] G. Moore and W. Peterson, "Solar PV-thermoelectric generator hybrid system: case studies," in *Conf. Rec. IEEE 10th Int. Conf.Telecommunications Energy Conf, San Diego, CA*, 1988, pp. 308–311.

[6] Y. Vorobiev, J. González-Hernández, P. Vorobiev, and L. Bulat, "Thermal-photovoltaic solar hybrid system for efficient solar energy conversion," *Sol. Energy*, vol. 80, no. 2, pp. 170–176, Feb. 2006.

[7] X. Zhang, K. T. Chau, and C. C. Chan, "Design and Implementation of a Thermoelectric- Photovoltaic Hybrid Energy Source for Hybrid Electric Vehicles," *World Electr. J.*, vol. 3, pp. 1–11, 2009.

[8] H. Chang, M.-J. Kao, K. D. Huang, S.-L. Chen, and Z.-R. Yu, "A Novel Photo-Thermoelectric Generator Integrating Dye-sensitized Solar Cells with Thermoelectric Modules," *Jpn. J. Appl. Phys.*, vol. 49, no. 6, p. 06GG08, Jun. 2010.

[9] X.-Z. Guo, Y.-D. Zhang, D. Qin, Y.-H. Luo, D.-M. Li, Y.-T. Pang, and Q.-B. Meng, "Hybrid tandem solar cell for concurrently converting light and heat energy with utilization of full solar spectrum," *J. Power Sources*, vol. 195, no. 22, pp. 7684–7690, Nov. 2010.

[10] H. Chang, M.-J. Kao, K.-C. Cho, S.-L. Chen, K.-H. Chu, and C.-C. Chen, "Integration of CuO thin films and dye-sensitized solar cells for thermoelectric generators," *Curr. Appl. Phys.*, vol. 11, no. 4, pp. S19–S22, Jul. 2011.

[11] N. Wang, L. Han, H. He, N.-H. Park, and K. Koumoto, "A novel high-performance photovoltaic–thermoelectric hybrid device," *Energy Environ. Sci.*, vol. 4, no. 9, p. 3676, 2011.

[12] H. Chang and Z.-R. Yu, "Integration of Dye-Sensitized Solar Cells, Thermoelectric Modules and Electrical Storage Loop System to Constitute a Novel Photothermoelectric Generator," *J. Nanosci. Nanotechnol.*, vol. 12, no. 8, pp. 6811–6816, Aug. 2012.

[13] S. Su, T. Liu, Y. Wang, X. Chen, J. Wang, and J. Chen, "Performance optimization analyses and parametric design criteria of a dye-sensitized solar cell thermoelectric hybrid device," *Appl. Energy*, vol. 120, pp. 16–22, May 2014.

[14] P. M. Cuce and E. Cuce, "A novel model of photovoltaic modules for parameter estimation and thermodynamic assessment," *Int. J. Low-Carbon Technol.*, vol. 7, no. 2, pp. 159–165, Nov. 2011.

[15] T. Marnoto, K. Sopian, W. R. W. Daud, M. Algoul and A. Zaharim, "Mathematical Model for Determining the Performance Characteristics of Multi-Crystalline Photovoltaic Modules," in *Proc. of the 9th WSEAS Int. Conf. on Mathematical and Computational Methods in Science and Engineering, Trinidad and Tobago,November 5-7*, 2007, pp. 79–84.

[16] A. R. Jha, *Solar Cell Technology and Applications*. CRC Press, Boca Raton & Francis Group, LLC, 2010.

[17] H. Graßl, J. Kokott, M. Kulessa, J. Luther, F. Nuscheler, R. Sauerborn, H.-J. Schellnhuber, R. Schubert, and E.-D. Schulze, "World in Transition Towards Sustainable Energy Systems," Technical report, German Advisory Council on Global Change, 2003.

[18] V. V. Tyagi, S. C. Kaushik, and S. K. Tyagi, "Advancement in solar photovoltaic/thermal (PV/T) hybrid collector technology," *Renew. Sustain. Energy Rev.*, vol. 16, no. 3, pp. 1383–1398, 2012.

[19] B.O'Regan and M. Grätzel, "A low cost, high efficiency solar cell based on dye sensitized colloidal Tio2 films," *Nat. 353*, no. 6346, pp. 737–740, 1991.

[20] S.Guo, M.Sun,G.Gao, and L. Liu, "Scalable low-cost CdS nanospheres@graphene nanocomposites counter electrode for high efficiency dye-sensitized solar cells," *Electrochim. Acta*, vol. 176, pp. 1165–1170, 2015.

[21] S. Mathew, A. Yella, P. Gao, R. Humphry-Baker, B. F. E. Curchod, N. Ashari-Astani, I. Tavernelli, U. Rothlisberger, M. K. Nazeeruddin, and M. Grätzel, "Dye-sensitized solar cells with 13% efficiency achieved through the molecular engineering of porphyrin sensitizers," *Nat. Chem.*, vol. 6, no. 3, pp. 242–247, 2014.

[22] X. Yang, M. Yanagida, and L. Han, "Reliable evaluation of dye-sensitized solar cells," *Energy Environ. Sci.*, vol. 6, no. 1, pp. 54–66, 2013.

[23] M. G. Kang, N.-G. Park, K. S. Ryu, S. H. Chang, and K.-J. Kim, "A 4.2% efficient flexible dye-sensitized TiO2 solar cells using stainless steel substrate," *Sol. Energy Mater. Sol. Cells*, vol. 90, no. 5, pp. 574–581, Mar. 2006.

[24] T. Jiao, D. Wei, J. Liu, W. Sun, S. Jia, W. Zhang, Y. Feng, H. Shi, and C. Du, "Flexible solar cells based on graphene-ultrathin silicon Schottky junction," *RSC Adv.*, vol. 5, no. 89, pp. 73202–73206, 2015.

[25] C.-H. Lee, M.-D. Lu, Q.-Z. Guan, Y.-L. Tung, S.-Y. Tsai, and F.-M. Lin, "Thickness-controllable textured TiO 2 underlayer for a flexible dye-sensitized solar cell sub-module," *Mater. Res. Express*, vol. 1, no. 2, p. 025503, May 2014.

[26] V. B. Omubo-Pepple,C. Israel-Cookey, and G. I. Alaminokuma,, "Effects of Temperature , Solar Flux and Relative Humidity on the Efficient Conversion of Solar Energy to Electricity," *Eur. J. Sci. Res.*, vol. 35, no. 2, pp. 173–180, 2009.

[27] M. Berginc, U. Opara Krašovec, M. Jankovec, and M. Topič, "The effect of temperature on the performance of dye-sensitized solar cells based on a propyl-methyl-imidazolium iodide electrolyte," *Sol. Energy Mater. Sol. Cells*, vol. 91, no. 9, pp. 821–828, May 2007.

[28] E. Radziemska, "Thermal performance of Si and GaAs based solar cells and modules: a review," *Prog. Energy Combust. Sci.*, vol. 29, no. 5, pp. 407–424, Jan. 2003.

[29] E. Radziemska, "Performance Analysis of a Photovoltaic-Thermal Integrated System," *Int. J. Photoenergy*, pp. 1–6, 2009.

[30] E. Radziemska, "The effect of temperature on the power drop in crystalline silicon solar cells," *Renew. Energy*, vol. 28, no. 1, pp. 1–12, Jan. 2003.

[31] B. J. Brinkworth, B. M. Cross, R. H. Marshall, and H. Yang, "Thermal regulation of photovoltaic cladding," *Sol. Energy*, vol. 61, no. 3, pp. 169–178, 1997.

[32] X. Zhao, X. Zhang, S. B. Riffat, and Y. Su, "Theoretical study of the performance of a novel PV/e roof module for heat pump operation," *Energy Convers. Manag.*, vol. 52, no. 1, pp. 603–614, Jan. 2011.

[33] S. R. Raga and F. Fabregat-Santiago, "Temperature effects in dye-sensitized solar cells.," *Phys. Chem. Chem. Phys.*, vol. 15, no. 7, pp. 2328–36, Feb. 2013.

[34] D. M. Rowe and G. Min, "Evaluation of thermoelectric modules for power generation," *J. Power Sources*, vol. 73, pp. 193–198, 1998.

[35] G. Min and D. M. Rowe, "Optimisation of thermoelectric module geometry for 'waste heat' electric power generation," *Journal of Power Sources*, vol. 38, no. 3. pp. 253–259, 1992.

[36] D. M. Rowe, "Thermoelectrics, an environmentally-friendly source of electrical power," *Renew. Energy*, vol. 16, no. 1–4, pp. 1251–1256, 1999.

[37] D. M. Rowe and C. M. Bhandari, *Bhandari, Modern Thermoelectrics.* London: Holt Rinehart and Winston, 1989.

[38] C. Rowe, D. M., *Handbook of Thermoelectric, ,*. Boca Raton, FL, CRC Press, 1995.

[39] T. M. Tritt, "Thermoelectric Materials : Principles , Structure , Properties , and Applications," *Encycl. Mater. Sci. Technol.*, pp. 1–11, 2002.

[40] Yatim, Nadhrah. Md, "Development o f ' Open - Short Circuit ' Dimensionless Figure-of-Merit (ZT) Measurement Technique for Investigation of Thermoelements and Segmented Thermoelectric Structures," Ph.D, Cardiff University, 2012.

[41] G. Min, D. M. Rowe, and K. Kontostavlakis, "Thermoelectric figure-of-merit under large temperature differences," *J. Phys. D Appl. Phys*, vol. 37, pp. 1301–1304, 2004.

[42] C. Rowe. D. M., *Handbook of Thermoelectrics: Micro to Nano*. London: CRC Press., 2005.

[43] F. S. Moraes, L. C. Santos, R. N. Alencar, É. V. Sempels, J. C. Sandoval V, and F. J. Lesage, "Solar thermoelectric generator performance relative to air speed," *Energy Convers. Manag.*, vol. 99, pp. 326–333, 2015.

[44] G. Min, "Thermoelectric Module Design Under a Given Thermal Input: Theory and Example," *Electron. Mater.*, vol. 42, no. 7, pp. 2239–2242, 2013.

[45] E. A. Chávez Urbiola and Y. Vorobiev, "Investigation of Solar Hybrid Electric/Thermal System with Radiation Concentrator and Thermoelectric Generator," *Int. J. Photoenergy*, vol. 2013, no. 4, pp. 1–7, 2013.

[46] L. Miao, M. Zhang, S. Tanemura, T. Tanaka, Y. P. Kang, and G. Xu, "Feasibility Study on the Use of a Solar Thermoelectric Cogenerator Comprising a Thermoelectric Module and Evacuated Tubular Collector with Parabolic Trough Concentrator," *J. Electron. Mater.*, vol. 41, no. 6, pp. 1759–1765, Apr. 2012.

[47] N. Vatcharasathien, J. Hirunlabh, J. Khedari, and M. Daguenet, "Design and analysis of solar thermoelectric power generation system," *Int. J. Sustain. Energy*, vol. 24, no. 3, pp. 115–127, Sep. 2005.

[48] N. Miljkovic and E. N. Wang, "Modeling and optimization of hybrid solar thermoelectric systems with thermosyphons," *Sol. Energy*, vol. 85, no. 11, pp. 2843–2855, Nov. 2011.

[49] D. Kraemer, B. Poudel, H.-P. Feng, J. C. Caylor, B. Yu, X. Yan, Y. Ma, X. Wang, D. Wang, A. Muto, K. McEnaney, M. Chiesa, Z. Ren, and G. Chen, "High-performance flat-panel solar thermoelectric generators with high thermal concentration.," *Nat. Mater.*, vol. 10, no. 7, pp. 532–8, Jul. 2011.

[50] O. Zogou and H. Stapountzis, "Flow and heat transfer inside a PV/T collector for building application," *Appl. Energy*, vol. 91, no. 1, pp. 103–115, Mar. 2012.

[51] H. P. Garg and R. K. Agarwal, "Some aspects of a PV/T collector/forced circulation flat plate solar water heater with solar cells," *Energy Convers. Manag.*, vol. 36, no. 2, pp. 87–99, Feb. 1995.

[52] D. Kraemer, L. Hu, A. Muto, X. Chen, G. Chen, and M. Chiesa, "Photovoltaic-thermoelectric hybrid systems: A general optimization methodology," *Appl. Phys. Lett.*, vol. 92, no. 24, p. 243503, 2008.

[53] A. Royne, C. Dey, and D. Mills, "Cooling of photovoltaic cells under concentrated illumination: a critical review," *Sol. Energy Mater. Sol. Cells*, vol. 86, no. 4, pp. 451–483, Apr. 2005.

[54] S. Wu and C. Xiong, "Passive cooling technology for photovoltaic panels for domestic houses," *Int. J. Low-Carbon Technol. A*, vol. 9, no. 2, pp. 118–126, 2014.

[55] X. Zhang, X. Zhao, S. Smith, J. Xu, and X. Yu, "Review of R&D progress and practical application of the solar photovoltaic/thermal (PV/T) technologies," *Renew. Sustain. Energy Rev.*, vol. 16, no. 1, pp. 599–617, Jan. 2012.

[56] H. P GARG and R. S. ADHIKARI, "Conventional hybrid photovoltaic / thermal (PV/T) air heating collectors : steady-state simulation," *Renew. Energy*, vol. 11, no. 3, 1997.

[57] G. Fraisse, C. Ménézo, and K. Johannes, "Energy performance of water hybrid PV/T collectors applied to combisystems of Direct Solar Floor type," *Sol. Energy*, vol. 81, no. 11, pp. 1426–1438, Nov. 2007.

[58] H. Chen, X. Chen, S. Chu, L. Zhang, and Y. Xiong, "Numerical and Experimental Study on Energy Performance of Photovoltaic-Heat Pipe Solar Collector in Northern China," *Int. J. Photoenergy*, vol. 2015, pp. 1–8, 2015.

[59] C. J. Smith, P. M. Forster, and R. Crook, "Global analysis of photovoltaic energy output enhanced by phase change material cooling," *Appl. Energy*, vol. 126, pp. 21–28, 2014.

[60] J. K. Tonui and Y. Tripanagnostopoulos, "Improved PV/T solar collectors with heat extraction by forced or natural air circulation," *Int. J. Hydrogen Energy*, vol. 31, no. 15, pp. 2137–2146, 2006.

[61] A. Ndiho, K. N'wuitcha, H. A. Samah, and M. Banna, "Numerical Study Of Natural Convection Through A Photovoltaic-Thermal (PV / T) Building Solar Chimney Suitable For Natural Cooling," *Int. J. Sci. Technol. Res.*, vol. 3, no. 12, pp. 148–155, 2014.

[62] H. Chen, X. Chen, S. Li, and H. Ding, "Comparative study on the performance improvement of photovoltaic panel with passive cooling under natural ventilation," *Int. J. Smart Grid Clean Energy*, pp. 374–379, 2014.

[63] J. Sun and M. Shi, "Numerical study on optical and electric-thermal performance for solar concentrating PV/T air system," *Sci. China Ser. E Technol. Sci.*, vol. 52, no. 12, pp. 3514–3520, Dec. 2009.

[64] F. Sarhaddi, S. Farahat, H. Ajam, and A. Behzadmehr, "Exergetic performance assessment of a solar photovoltaic thermal (PV/T) air collector," *Energy Build.*, vol. 42, no. 11, pp. 2184–2199, Nov. 2010.

[65] S. M. Bambrook and A. B. Sproul, "Maximising the energy output of a PVT air system," *Sol. Energy*, vol. 86, no. 6, pp. 1857–1871, Jun. 2012.

[66] S. C. Solanki, S. Dubey, and A. Tiwari, "Indoor simulation and testing of photovoltaic thermal (PV/T) air collectors," *Appl. Energy*, vol. 86, no. 11, pp. 2421–2428, Nov. 2009.

[67] S. Dubey, G. S. Sandhu, and G. N. Tiwari, "Analytical expression for electrical efficiency of PV/T hybrid air collector," *Appl. Energy*, vol. 86, no. 5, pp. 697–705, May 2009.

[68] Jin GL, Ibrahim A, Chean YK, Daghigh R, Ruslan H, Mat S, et al. , "Evaluation of Single-Pass Photovoltaic-Thermal Air Collector with Rectangle Tunnel Absorber," *Am. J. Appl. Sci.*, vol. 7, no. 2, pp. 277–282, 2010.

[69] J. I. Rosell, X. Vallverdú, M. A. Lechón, and M. Ibáñez, "Design and simulation of a low concentrating photovoltaic/thermal system," *Energy Convers. Manag.*, vol. 46, no. 18–19, pp. 3034–3046, Nov. 2005.

[70] X. Han, V. Everett, Y. Wang, and L. Zhu, "Numerical analysis of direct liquid-immersed solar cell cooling of a linear concentrating photovoltaic receiver," in *2010 35th IEEE Photovoltaic Specialists Conference (PVSC),Hawaii*, 2010, pp. 003033–003038.

[71] K. Araki, M. Yamaguchi, T. Takamoto, E. Ikeda, T. Agui, H. Kurita, K. Takahashi, and T. Unno, "Characteristics of GaAs-based concentrator cells," *Sol. Energy Mater. Sol. Cells*, vol. 66, no. 1–4, pp. 559–565, Feb. 2001.

[72] M. Y. Hj. Othman, B. Yatim, K. Sopian, and M. N. Abu Bakar, "Performance analysis of a double-pass photovoltaic/thermal (PV/T) solar collector with CPC and fins," *Renew. Energy*, vol. 30, no. 13, pp. 2005–2017, Oct. 2005.

[73] S. Hatwaambo, H. Hakansson, J. Nilsson, and B. Karlsson, "Angular characterization of low concentrating PV–CPC using low-cost reflectors," *Sol. Energy Mater. Sol. Cells*, vol. 92, no. 11, pp. 1347–1351, Nov. 2008.

[74] S. Sharan, S. Mathur, and T. Kandpal, "Economic evaluation of concentrator-photovoltaic systems," *Sol. Wind Technol.*, vol. 2, no. 3–4, pp. 195–200, Jan. 1985.

[75] A. Makki, S. Omer, and H. Sabir, "Advancements in hybrid photovoltaic systems for enhanced solar cells performance," *Renew. Sustain. Energy Rev.*, vol. 41, pp. 658–684, Jan. 2015.

[76] E. C. Kern, Jr. and M. C. Russell, "Combined photovoltaic and thermal hybrid collector systems," in *Proceedings of the 13th ISES Photovoltaic Specialists, Washington*, 1978, pp. 1153–1157.

[77] P. Dupeyrat, C. Ménézo, and S. Fortuin, "Study of the thermal and electrical performances of PVT solar hot water system," *Energy Build.*, vol. 68, pp. 751–755, Jan. 2014.

[78] S. A. Kalogirou and Y. Tripanagnostopoulos, "Hybrid PV/T solar systems for domestic hot water and electricity production," *Energy Convers. Manag.*, vol. 47, no. 18–19, pp. 3368–3382, Nov. 2006.

[79] R. Zakharchenko, L. Licea-Jimenez, S. A. P´erez-Garc´ıa, P. Vorobiev, U. Dehesa-Carrasco, J. F. Perez-Robles, J.Gonzalez-Hern´andez, and Yu. Vorobiev, "Photovoltaic solar panel for a hybrid PV/thermal system," *Sol. Energy Mater. Sol. Cells*, vol. 82, no. 1–2, pp. 253–261, May 2004.

[80] M. Li, G. L. Li, X. Ji, F. Yin, and L. Xu, "The performance analysis of the Trough Concentrating Solar Photovoltaic/Thermal system," *Energy Convers. Manag.*, vol. 52, no. 6, pp. 2378–2383, Jun. 2011.

[81] G.F.Russell, "Uniform temperature heat pipe and method of using the same," ,Patent US4320246,USA, 1982.

[82] W. G. J. H. M. Van Sark, "Feasibility of photovoltaic – Thermoelectric hybrid modules," *Appl. Energy*, vol. 88, no. 8, pp. 2785–2790, Aug. 2011.

[83] Y.-Y. Wu, S.-Y. Wu, and L. Xiao, "Performance analysis of photovoltaic–thermoelectric hybrid system with and without glass cover," *Energy Convers. Manag.*, vol. 93, pp. 151–159, Mar. 2015.

[84] Y. Deng, W. Zhu, Y. Wang, and Y. Shi, "Enhanced performance of solar-driven photovoltaic–thermoelectric hybrid system in an integrated design," *Sol. Energy*, vol. 88, pp. 182–191, Feb. 2013.

[85] Y. Li, S. Witharana, H. Cao, M. Lasfargues, Y. Huang, and Y. Ding, "Wide spectrum solar energy harvesting through an integrated photovoltaic and thermoelectric system," *Particuology*, vol. 15, pp. 39–44, Aug. 2014.

[86] M. Mizoshiri, M. Mikami, and K. Ozaki, "Thermal–Photovoltaic Hybrid Solar Generator Using Thin-Film Thermoelectric Modules," *Jpn. J. Appl. Phys.*, vol. 51, p. 06FL07, Jun. 2012.

[87] D. Yang and H. Yin, "Energy Conversion Efficiency of a Novel Hybrid Solar System for Photovoltaic, Thermoelectric, and Heat Utilization," *IEEE Trans. Energy Convers.*, vol. 26, no. 2, pp. 662–670, Jun. 2011.

[88] H. Najafi and K. A. Woodbury, "Modeling and Analysis of a Combined Photovoltaic-Thermoelectric Power Generation System," *J. Sol. Energy Eng.*, vol. 135, no. 3, p. 031013, Apr. 2013.

[89] Y. Zhang, J. Fang, C. He, H. Yan, Z. Wei, and Y. Li, "Integrated Energy-Harvesting System by Combining the Advantages of Polymer Solar Cells and Thermoelectric Devices," *J. Phys. Chem. C*, vol. 117, no. 47, pp. 24685–24691, Nov. 2013.

[90] K.-T. Park, S.-M. Shin, A. S. Tazebay, H.-D. Um, J.-Y. Jung, S.-W. Jee, M.-W. Oh, S.-D. Park, B. Yoo, C. Yu, and J.-H. Lee, "Lossless hybridization between photovoltaic and thermoelectric devices," *Sci. Rep.*, vol. 3, pp. 1–6, 2013.

[91] S. Mathew, A. Yella, P. Gao, R. Humphry-Baker, B. F. E. Curchod, N. Ashari-Astani, I. Tavernelli, U. Rothlisberger, M. K. Nazeeruddin, and M. Grätzel, "Dye-sensitized solar cells with 13% efficiency achieved through the molecular engineering of porphyrin sensitizers.," *Nat. Chem.*, vol. 6, no. 3, pp. 242–7, Mar. 2014.

[92] G. Min and D. M. Rowe, "Conversion efficiency of thermoelectric combustion systems," *IEEE Trans. Energy Convers.*, vol. 22, no. 2, pp. 528–534, 2007.

[93] M. Elmir, R. Mehdaoui, and A. Mojtabi, "Numerical Simulation of Cooling a Solar Cell by Forced Convection in the Presence of a Nanofluid," *Energy Procedia*, vol. 18, pp. 594–603, 2012.

[94] D. Jing, Y. Hu, M. Liu, J. Wei, and L. Guo, "Preparation of highly dispersed nanofluid and CFD study of its utilization in a concentrating PV/T system," *Sol. Energy*, vol. 112, pp. 30–40, Feb. 2015.

[95] R. A Taylor, T. Otanicar, and G. Rosengarten, "Nanofluid-based optical filter optimization for PV/T systems," *Light Sci. Appl.*, vol. 1, no. 10, p. e34, Oct. 2012.

[96] S. Saroha, T. Mittal, P. J. Modi, V. Bhalla, V. Khullar, H. Tyagi, R. A. Taylor, and T. P. Otanicar, "Theoretical Analysis and Testing of Nanofluids-Based Solar Photovoltaic/Thermal Hybrid Collector," *J. Heat Transfer*, vol. 137, no. 9, p. 091015, May 2015.

[97] A. Kitanovski and P. W. Egolf, "Innovative ideas for future research on magnetocaloric technologies," *Int. J. Refrig.*, vol. 33, no. 3, pp. 449–464, May 2010.

[98] M. F. Al-Saleh and A. E. Yousif, "Properties of the Standard Deviation that are Rarely Mentioned in Classrooms," *Austrian J. Stat.*, vol. 38, no. 3, pp. 193–202, 2009.

[99] P.J. Sebastián, A. Oleac, J. Campos, J.A. Toledob and S.A. Gamboa, "Temperature dependence and the oscillatory behavior of the opto-electronic properties of a dye-sensitized nanocrystalline TiO2 solar cell," *Sol. Energy Mater. Sol. Cells*, vol. 81, no. 3, pp. 349–361, Feb. 2004.

[100] Hashim.Hasan and G. Min, "Enhance the Performance of Hybrid Dye Sensitised Solar Cell /Thermoelectric System," in *Photovoltaic Science applications and Technology, PVSAT-9,10–12 April,Swansea University,UK*, 2013, pp. 141–144.

[101] S. Armstrong and W. G. Hurley, "A thermal model for photovoltaic panels under varying atmospheric conditions," *Appl. Therm. Eng.*, vol. 30, no. 11–12, pp. 1488–1495, 2010.

[102] A. S. Joshi and A. Tiwari, "Energy and exergy efficiencies of a hybrid photovoltaic–thermal (PV/T) air collector," *Renew. Energy*, vol. 32, no. 13, pp. 2223–2241, Oct. 2007.

[103] X. Ju, Z. Wang, G. Flamant, P. Li, and W. Zhao, "Numerical analysis and optimization of a spectrum splitting concentration photovoltaic–thermoelectric hybrid system," *Sol. Energy*, vol. 86, no. 6, pp. 1941–1954, Jun. 2012.

[104] G. Min, "ZT Measurements Under Large Temperature Differences," *J. Electron. Mater.*, vol. 39, no. 9, pp. 1782–1785, Mar. 2010.

[105] G. Min, "TE Module Design Theories," in *CRC Handbook of Thermoelectrics; Micro to Nano*, D.M. Rowe, Ed. Baca Ration: CRC Press, 2006, pp. 11.1–11.15.

[106] D.L. Evans, "Simplified method for predicting photovoltaic array output," *Sol. Energy*, vol. Volume 27, no. no. 6, pp. 555–560, 1981.

[107] *RETScreen International, Photovoltaic Project Analysis*. 2001.

[108] M. D. Rowe, *CRC Handbook of Thermoelectrics*. London: London CRC Press, 1996.

[109] H. O'Hanley, J. Buongiorno, T. McKrell, L-w. Hu (Eds.), "Measurement and Model Correlation of Specific Heat Capacity of Water-Based Nanofluids With Silica, Alumina and Copper Oxide Nanoparticles," in *ASME 2011 International Mechanical Engineering Congress and Exposition. American Society of Mechanical Engineers.*

[110] N. Bozorgan, K. Krishnakumar,and N. Bozorgan, "Numerical Study on Application of CuO-Water Nanofluid in Automotive Diesel Engine Radiator," *Mod. Mech. Eng.*, vol. 02, no. 04, pp. 130–136, 2012.

[111] Kalyanasundaram, K., Ed., Dye-sensitized solar cells, EPFL Press, Lausanne, 2010.

[112] G. R. A. Kumara, S. Kawasaki, P. V. V Jayaweera, E. V. A. Premalal, and S. Kaneko, "Large area dye-sensitized solar cells with titanium based counter electrode," *Thin Solid Films*, vol. 520, no. 12, pp. 4119-4121, April 2012.